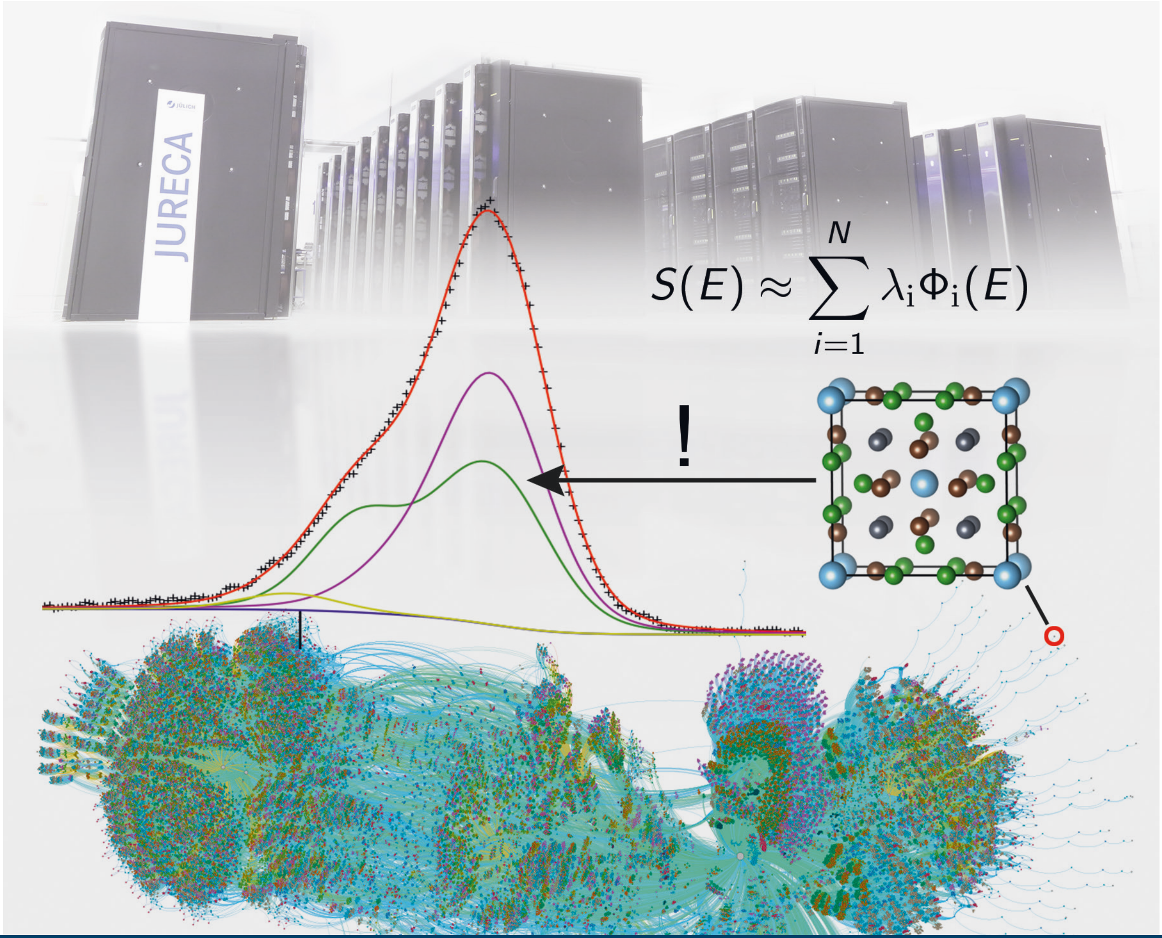

High-throughput All-Electron Density Functional Theory Simulations for a Data-driven Chemical Interpretation of X-ray Photoelectron Spectra

Jens Bröder

Schlüsseltechnologien / Key Technologies
Band / Volume 229
ISBN 978-3-95806-526-0

Mitglied der Helmholtz-Gemeinschaft

JÜLICH
Forschungszentrum

Schriften des Forschungszentrums Jülich
Reihe Schlüsseltechnologien / Key Technologies Band / Volume 229

Forschungszentrum Jülich GmbH
Peter Grünberg Institut (PGI)
Quanten-Theorie der Materialien (PGI-1/IAS-1)

High-throughput All-Electron Density Functional Theory Simulations for a Data-driven Chemical Interpretation of X-ray Photoelectron Spectra

Jens Bröder

Schriften des Forschungszentrums Jülich
Reihe Schlüsseltechnologien / Key Technologies Band / Volume 229

ISSN 1866-1807 ISBN 978-3-95806-526-0

Bibliografische Information der Deutschen Nationalbibliothek.
Die Deutsche Nationalbibliothek verzeichnet diese Publikation in der
Deutschen Nationalbibliografie; detaillierte Bibliografische Daten
sind im Internet über http://dnb.d-nb.de abrufbar.

Herausgeber und Vertrieb: Forschungszentrum Jülich GmbH
Zentralbibliothek, Verlag
52425 Jülich
Tel.: +49 2461 61-5368
Fax: +49 2461 61-6103
zb-publikation@fz-juelich.de
www.fz-juelich.de/zb

Umschlaggestaltung: Grafische Medien, Forschungszentrum Jülich GmbH

Druck: Grafische Medien, Forschungszentrum Jülich GmbH

Schriften des Forschungszentrums Jülich
Reihe Schlüsseltechnologien / Key Technologies, Band / Volume 229

D 82 (Diss. RWTH Aachen University, 2020)

ISSN 1866-1807
ISBN 978-3-95806-526-0

For humanity and its AIs,
therefore most likely for you, the entity,
that is brave enough to be processing this.

— Journey before Destination —
- Brandon Sanderson

If you never fail, you are only trying things that are too easy
and playing far below your level.
- Eliezer, Yudkowsky

We do not only have to think about the future we want to live in,
we also have to lay it out and build it.
- MIT Essential knowledge: The Future

Abstract

Enabling computer-driven materials design to find and create materials with advanced properties from the enormous haystack of material phase space is a worthy goal for humanity. Most high-technologies, for example in the energy or health sector, strongly depend on advanced tailored materials. Since conventional research and screening of materials is rather slow and expensive, being able to determine material properties on the computer poses a paradigm shift. For the calculation of properties for pure materials on the nano scale *ab initio* methods based on the theory of quantum mechanics are well established. **D**ensity **F**unctional **T**heory (DFT) is such a widely applied method from first principles with high predictive power.

To screen through larger sets of atomic configurations physical property calculation processes need to be robust and automated. Automation is achieved through the deployment of advanced frameworks which manage many workflows while tracking the provenance of data and calculations. Through workflows, which are essential property calculator procedures, a high-level automation environment is achievable and accumulated knowledge can be reused by others. Workflows can be complex and include multiple programs solving problems over several physical length scales.

In this work, the open source all-electron DFT program `FLEUR` implementing the highly accurate **F**ull-potential **L**inearized **A**ugmented **P**lane **W**ave (FLAPW) method is connected and deployed through the open source **A**utomated **I**nteractive **I**nfrastructure and **D**atabase for Computational Science (AiiDA) framework to achieve automation. AiiDA is a Python framework which is capable of provenance tracking millions of high-throughput simulations and their data. Basic and advanced workflows are implemented in an open source Python package AiiDA-FLEUR, especially to calculate properties for the chemical analysis of X-ray photoemission spectra. These workflows are applied on a wide range of materials, in particular on most known metallic binary compounds.

The chemical-phase composition and other material properties of a surface region can be understood through the careful chemical analysis of high-resolution X-ray photoemission spectra. The spectra evaluation process is improved through the development of a fitting method driven by data from *ab initio* simulations. For complex multi-phase spectra this proposed evaluation process is expected to have advantages over the widely applied conventional methods. The spectra evaluation process is successfully deployed on well-behaved spectra of materials relevant for the inner wall (blanket and divertor) plasma-facing components of a nuclear fusion reactor. In particular, the binary beryllium systems Be-Ti, Be-W and Be-Ta are investigated. Furthermore, different approaches to calculate spectral properties like chemical shifts and binding energies are studied and benchmarked against the experimental literature and data from the NIST X-ray photoelectron spectroscopy database.

Kurzfassung

Viele Hochtechnologien, wie die Kernfusion sind stark auf maßgeschneiderte hochspezialisierte Materialien angewiesen. Die Ermöglichung von computergestüzter Materialentwicklung ist somit ein lohnenswertes Ziel der Menschheit, um aus dem riesigen Heuhaufen des Materialphasenraumes High-tech Materialien mit gewollten Eigenschaften zu designen. Für reine Materialien auf kleinen Lägenskalen sind etablierte *ab initio* Methoden, welche auf der Theorie der Quantenmechanik basieren, wie die Dichtefunktionaltheorie (DFT) der Stand der Technik, um Materialeigenschaften mit Hilfe des Computers zu bestimmen, bevor diese Materialien im Labor langsam und kostenintensiv überprüft werden.

Für computergestützte Materialentwicklung müssen Prozesse zur Berechnung von physikalischen Eigenschaften robust und automatisiert werden, um Berechnungen an größeren Mengen von Kristallstrukturkonfigurationen durchführen zu können. Die Automatisierung wird durch den Einsatz hochentwickelter Frameworks erreicht, welche die Herkunft von Daten und Berechnungen verfolgen und verwalten. Durch sogennante Workflows, welche Protokolle zur physikalischen Eigenschaftsberechnung darstellen, wird ein hohes Maß an Automatisierung erreicht und Expertenwissen kann in diesen konserviert und von anderen wiederverwendet werden.

In dieser Arbeit wurde das Open-Source DFT-Programm `FLEUR` für die anstehenden Aufgaben ausgewählt, welches alle Elektronen mithilfe der leistungsfähigen, hochpräzisen **L**inearized **A**ugmentierte **P**lane **W**ave (FLAPW) behandelt. Der `FLEUR`-Program wird an das Open-Source **A**utomated **I**nteractive **I**nfrastructure und **D**atenbank für Computational Science (AiiDA) Framework angebunden, um eine hohe Automatisierung mit `FLEUR` erreichen zu können. AiiDA ist ein Python-Framework, das millionen an Hochdurchsatzsimulationen und ihre Daten in einer Datenbank nachverfolgen und verwalten kann. Fundamentale und fortgeschrittene Workflows wurden in einem Open-Source Python-Paket (AiiDA-FLEUR) implementiert, um insbesondere Eigenschaften für die chemische Analyse von Röntgenphotoelektronenspektren zu berechnen. Diese Workflows wurden auf eine Vielzahl von Materialien angewendet, insbesondere auf bekannte, metallische, binäre Verbindungen.

Die genaue Phasenzusammensetzung und andere Eigenschaften eines oberflächennahen Materials können durch die sorgfältige chemische Analyse von hochauflösenden Röntgenphotoelektronenspektren verstanden werden. In dieser Arbeit wird der Spektrenauswertungsprozess basierend auf *ab initio* Simulations Ergebnissen durch die Entwicklung einer Anpassungsmethode für vorerst einfache, Mehrphasenspektren verbessert. Dieses XPS-Auswertungsverfahren mit *ab initio*-Daten wurde erfolgreich auf Spektren von Materialien angewendet, die für die Wandkomponenten eines Kernfusionsreaktors relevant sind, insbesondere für die Berylliumverbindungen (Be-Ti, Be-W, Be-Ta). Weitere Ansätze zur Berechnung der Spektren-Eigenschaften wie chemische Verschiebungen und Bindungsenergien wurden untersucht und mit der experimentellen Literatur, insbesondere der NIST Datenbank für Röntgenphotoelektronenspektroskopie verglichen.

Table of Contents

1. Introduction

Meeting the growing demands of over 9 billion human beings and the transition into a longterm sustainable way of life on earth, while increasing or at least maintaining the status and quality of human civilization and protecting our common goods [1, 2] is the grand challenge of our times. This is formulated by the United Nations general assembly in 17 sustainable development goals to meet by 2030 [3, 4]. Materials production, usage and management play a crucial role in our socioeconomic systems and heavily impact our environment [5].

Many technologies strongly depend on special materials with desired, optimized properties, designed form and economic feasibility [6, 7]. In the energy sector for example, solar cells fully depend on materials with the right optical properties that yield a high quantum efficiency while being inexpensive and durable enough to work for decades or longer [8–12]. Wind turbine blades and turbines in general also consist of optimized high-tech materials to withstand forces and heat [13, 14]. Transitioning to a complete renewable energy mix crucially depends on finding reasonable inexpensive materials for energy storage [15, 16] in large quantities, especially for electric energy [17]. The challenge of making nuclear fusion a reality depends from a technological point of view to a large extent on designing high-tech materials that possess and sustain their desired properties long enough under the extreme operating conditions of such a device [18, 19]. The durability, efficiency and economic feasibility of fuel cells depends strongly on the cells materials [20]. Other challenges worth mentioning are new permanent [21] or special magnets [22, 23], thermoelectrics [24], materials for (green) information technologies, (quantum)computing [25], (high-temperature) superconductors [26], lasers, (space)flight, materials for medical equipment [27], drugs [28], biofriendly materials [29], catalysts [30], 3D printable materials, replacements for toxic, expensive, rare or oil based materials.

The size of material phase space is enormous [31, 32] making it inconvenient and very costly to optimize and screen materials through a pure experimental approach within laboratories, like Edison [33] did for the filament of the electric light bulb, or Haber and Bosch pursued to find a suitable catalyst for ammonia synthesis transforming agriculture worldwide [34]. Since 1993, worldwide computational capabilities increased [35] exponentially by a factor of over 1 million. Given these challenges and opportunities for materials, one worthy longtime goal pursued by mankind is to enable full scale computational/virtual data-driven materials design [36–40]. An exemplary computer-driven process for the advancement or replacement of a functional material is sketched in Fig. 1.1. After the characterization of the device and deciding which properties need to be optimized and how, the discovery of new promising candidates is done to a large extent on the computer deploying software from the materials informatics toolbox [41–43] and utilizing various types of data available on materials. The suggested promising candidate materials are then synthesized, tested in the laboratory, manufactured and finally deployed, if the properties are satisfactory.

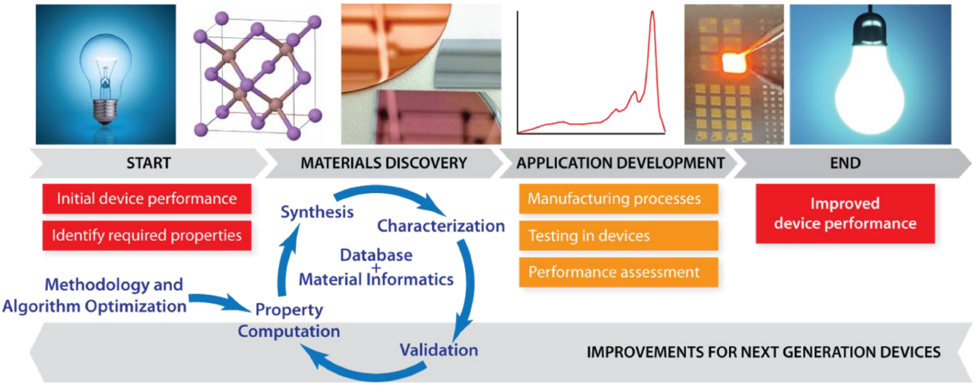

Fig. 1.1.: Materials-design process example for improvement of a high-tech material for a device. Graphic under creative common license 3.0 taken as original from [37].

While the fundamental quantum mechanical equations for materials [44–46] are long known in condensed matter physics and quantum chemistry, calculating material properties accurately, i.e. solving these equations for a real world material like steel, is computationally expensive or even impossible [47]. Since the micro structure (atomic configuration) of a material determines its physical and chemical properties to a large extent, also the size of material configuration space poses a challenge. It is growing exponentially with the number of atoms or protons in a structure. This makes materials design a multi-scale problem. On the one hand materials-informatics software [37, 42, 43, 48–50] has to be robust and automatized to enable screening through many different materials, on the other hand practical models and approximations for all length scales and diverse phenomena have to be created, implemented and interconnected. Furthermore, massive amounts of data of all facets on materials have to be shared and made available for others to harvest and progress [51]. Data repositories like [39, 52–59] enable the deployment of machine learning techniques to discover correlations and develop better models and understanding of the underlying physics [60].

To calculate material properties on the nano scale for molecules and solids established practical *ab initio* methods, based on the theory of quantum mechanics [47], like **D**ensity **F**unctional **T**heory (DFT) [61] are the methods of choice. Archiving some degree of automation in materials design processes is possible through the deployment of software frameworks [62–72] which manage workflows and track the provenance of data and calculations. This ensures the reliability and reproducibility of calculations. With property calculator protocols, so called workflows, a high-level work environment is achievable. Through workflows knowledge can accumulated and be rather easily reused by others. Workflows can involve multiple different software packages connecting multiple physical scales in one solution. Besides depending on the robustness and fidelity of the deployed software packages, a high overall fidelity of a workflow is achievable through optimization and error treatment strategies within the workflow itself.

In material research and quality assessment sample characterization and chemical phase identification play an essential role. The same is true when studying surface and material changes under external influences. For the identification of the crystal structure and large solid periodic phases X-ray diffraction (XRD) [73, 74] is the state of the art technique. Insight into the elemental composition can be provided by different scattering or scanning probes, also through X-ray photoemission spectroscopy (XPS). For the determination of the chemical phase composition of a sample, XPS or formally known as electron spectroscopy for chemical analysis (ESCA) is the method of choice. XPS is a well known and widely applied technique in research and industry [75–77]. The detailed evaluation of multi-phase high-resolution XPS spectra is often challenging in practice [78].

This work advances a solution for the basic chemical material characterization with X-ray photoemission spectroscopy. The underlying models and methods applied are known, but have to be automated, advanced and connected to different tools to provide a low cost solution for a broader set of materials in order to be useful to a broader audience. For the calculation of spectral properties the open source all-electron DFT program, `FLEUR` [79] implementing the powerful, highly accurate **L**inearized **A**ugmented **P**lane **W**ave method (FLAPW) [80, 81] was chosen. For automation the `FLEUR` program was connected to the AiiDA framework [63] and workflows were implemented to calculate a range of material properties. As proof of principle these workflows are deployed within a material screening project on most known binary metals. These *ab initio* results are partly compared to findings of other DFT software packages. In addition, selected *ab initio* results of beryllides (Be-W, Be-Ti, Be-Ta) relevant for the plasma-facing components of a nuclear-fusion reactor [82] like for the International Thermonuclear Experimental Reactor (ITER) are discussed in more detail. These *ab initio* results are compared to experimental X-ray photoelectron spectra data [83] which was measured by

Nicola Helfer and others. The spectra of these beryllide systems are chemically interpreted through *ab initio* core-level shift data obtained within this work.

The thesis is structured as follows. In *Chapter 2* the basic background knowledge and scientific context for this work is covered. The first sections of Chapter 2 describe the nature of the many-body problem. They promote how material properties can be calculated from density functional theory. The FLAPW method and its implementation in the `FLEUR` program are covered in more detail, since `FLEUR` was deployed throughout this work. The challenges of chemical, material configuration space and how these are tackled, among other knowledge, with high-throughput simulations and machine learning is pointed out. A collection of the current *ab initio* simulation databases and repositories is also presented in this chapter.

Developed methods within this thesis are discussed in *Chapter 3*. One section in this chapter discusses the developed open source AiiDA-FLEUR package, which enables high-throughput calculations with the `FLEUR` program using the AiiDA framework. Furthermore, plug-in layouts and implemented workflows around `FLEUR` are described. The description includes the self-consistency field workflow, a density of states, a band structure workflow, a workflow to calculate an equation of states and workflows for the calculation of core-level shifts and core-level binding energies. A deployable small search and visualize application (Jupyter App) and visualization functions for spectral data are discussed in this chapter. Another section introduces how well-behaved mixed X-ray photoelectron spectra can be fitted from constructed spectra of *ab initio* data. From this physically motivated constrained fit the chemical interpretation of the spectra is possible.

In *Chapter 4* selected *ab initio* simulation results, produced with the deployment of the developed methods, are reported. The first sections discuss what needs to be known, in order to enable material screening projects with high all-electron simulation success rates. This involves the control of good FLAPW parameters and knowing the convergence behavior of quantities of interest. The results from a small screening project of most known metal binary materials is discussed. The `FLEUR` simulation results are compared to experimental databases and results from other electronic structure programs. Furthermore, *ab initio* results of beryllides (Be-W, Be-Ti, Be-Ta) relevant for the inner vessel of a nuclear fusion reactor are discussed in this chapter. X-ray photoelectron spectra of these materials are chemically interpreted through *ab initio* data obtained within this work and the developed component-fit method.

A conclusion and outlook of the whole thesis is found in *Chapter 5*. Besides a sum up of the findings, possible ways to continue this work are outlined.

2. Basics: Theory and Scientific Context

Central to non-relativistic quantum mechanics, computational materials science and the theory of condensed matter physics is the many-body problem, which is essentially about solving the Schrödinger equation in some form (in more detail discussed in various text books like [45, 46, 84, 85]). In the case of a material interacting with light, which is a processes with a response over time, the time-dependent Schrödinger equation 2.1 has to be solved. It is given by

$$i\hbar\frac{\partial}{\partial t}|\Psi\rangle = \hat{H}|\Psi\rangle \tag{2.1}$$

where $|\Psi\rangle$ is a general wave function and $\hat{H}$ is an Hamiltonian operator acting on the wave function. As harmless as this first order linear partial differential equation seems, it is proven in [86, 87] to be in various forms fundamentally exponentially hard on even a quantum computer, i.e., it is a QMA-complete problem of the QMA (Quantum Merlin Arthur) complexity class. Being QMA-complete means that if it could be managed to solve this problem efficiently in polynomial time on a (quantum)computer that algorithm would be applied to solve all problems in the QMA complexity class efficiently. The existence of such an algorithm would prove the equality of QMA to the P complexity class, and further QMA=NP=P, solving the N=NP millennium prize problem on the side. The QMA-completeness fact already tells a lot about the many-body problem, in particular that it is very improbable that we will ever[1] manage to solve it, as it stands, for real physical system containing more than a couple of electrons. Until then one has to instead break it down, shift its complexity and hardness, find smart approximate, efficiently computable solutions from which meaningful physical results can be extracted. Or one has to avoid solving the many-body problem at all by finding other models and concepts for a given (macroscopic) phenomenon or length scale. This is known in the community since the early stages of quantum mechanics and was already stressed by Dirac in 1929 with his saying in [44]: "The underlying physical laws necessary for the mathematical theory of a large part of physics and the whole of chemistry are thus completely known, and the difficulty is only that the exact application of these laws leads to equations much too complicated to be soluble. It therefore becomes desirable that approximate practical methods of applying quantum mechanics should be developed, which can lead to an explanation of the main features of complex atomic systems without too much computation."

That not being enough, chemical space, the number of structural configurations one might want to solve the Schrödinger equation for, is also growing exponentially with the number of protons in the system [31]. These difficulties arise from the enormous size of the Hilbert spaces one deals with when solving the Schrödinger equation of systems containing many particles.

The following sections of this chapter provide a brief, selected overview of what many scientists developed together over generations within the last century to practically address the many-body problem on the nano scale. The sections also contain other scientific context and models which are relevant to understand the methods applied and the results of this thesis.

In the first sections the approach to the many-body problem is discussed, leading from the

---

[1] Ever means here: No matter how fast the future (quantum)computer, deploying the currently known computing concepts, will be! Maybe with our computing concepts the solvable problem sizes will increase a bit with higher spatial computational computing power and storage density.

non-relativistic stationary Schrödinger equation, the Born-Oppenheimer approximation over to wave function methods and reduced quantity approaches over to the basics of density functional theory and ending in its implementation in the `FLEUR` program. Other sections show approaches to the explosion of the structural configuration space, state the theory of X-ray photo-electron spectroscopy (XPS) and discuss how to model such XPS spectra to some extent from *ab initio* simulation without explicitly solving the time-dependent Schrödinger equation.

2.1. Interlude: Large Numbers in Perspective

Physicist need to embed numbers in an understandable context to provide meaning and understanding. To clearer understand the problems and providing a perspective on the large numbers occurring in this work, a collection is shown in Table 2.1 with references to relative and absolute physical boundaries in our world.

Quantity	Estimate
Full wave function/Hamiltonian of Fe on 10x10x10 grid	$10^{81}/10^{162}$ byte
Stoichiometries for ≤ 10,000 electron systems	P(10,000) ~10^{106}
Atoms in the observable universe	10^{78}-10^{82}
Atoms in our galaxy	10^{67}
Chemical space subset of small molecules ≤ 30 atoms [28]	10^{60} members
Protons in the sun	10^{55}
Atoms in the earth	10^{50}
Atoms of all humans	10^{37}
Stoichiometries for ≤ 1000 electron systems	P(1000) ~10^{31}
Atoms in a human	10^{27}
Total top 500 computing power in 2018 [35]	$3 \cdot 10^{25}$ FLOPS
Worldwide stored data estimate 2020 [88]	$4.4 \cdot 10^{22}$ byte
Common computer hard drive storage capacity (2018)	10^{12} byte
Stars in our galaxy	10^{11}
Human population	10^{10}
Age of the Earth	$4.54 \cdot 10^{9}$ years
Stoichiometries for ≤ 100 electron systems	P(100) ~10^{8}
Unique substances indexed (CAS registry)[2]	$1.5 \cdot 10^{8}$
Single user AiiDA calculation throughput limit	$10^{7} - 10^{8}$ per year
Computer hard drive file limit	$10^{6} - 10^{8}$ i-nodes
Seconds in a year	$3.15 \cdot 10^{7}$
Average storage for one small (<35 atoms) `FLEUR` run	$10^{6} - 10^{7}$ byte
Total `FLEUR` calculations ever run (before this work)	10^{6}
Experimentally known unique inorganic materials [89]	10^{5}
Unique XPS core-level shifts in NIST database [90]	10^{3}
Manual one year simulation throughput	10^{2}
Files per `FLEUR` simulation	$2 - 10$

Tab. 2.1.: An overview of some large numbers discussed in this work compared to quantities in our world providing relative and absolute physical boundaries. The table points out challenges and the clear impossibility of taking on the many-body problem or chemical space by brute force.

2.2. Massaging the Many-Body Problem

The full quantum many-body non-relativistic Hamiltonian of interacting nuclei and electrons including electro-magnetic radiation (em) would have the following form

$$\hat{H}_{\text{full}} = \hat{H}_{\text{nuclei}} + \hat{H}_{\text{electrons}} + \hat{H}_{\text{em}} + \hat{V}_{\text{nuclei-electrons}} + \hat{V}_{\text{electrons-em}} + \hat{V}_{\text{nuclei-em}}, \tag{2.2}$$

where $\hat{H}_{\text{x}}$ are terms of the subsystems with their kinetic plus potential contributions. $\hat{V}_{\text{x-y}}$ are the interaction contributions of the subsystems to the Hamiltonian. The photoelectric effect and therefore the X-ray photoemission process would be described by such a type of Hamiltonian. Unfortunately, solving the time-dependent Schrödinger equation 2.1 exactly for such a Hamiltonian beyond simple systems is computationally too expensive.

If one is only interested in the ground state of a system without its time dependence, as it is often the case in material science, it is enough to solve the time-independent Schrödinger equation without any external electro-magnetic field,

$$\hat{H}\,|\,\Psi\rangle = E\,|\,\Psi\rangle\,, \tag{2.3}$$

where E is a scalar correspondent to the stationary state $|\,\Psi\rangle$ and $\hat{H}$ is the time-independent many-body Hamiltonian (in atomic units) containing electrons and nuclei

$$\hat{H} = \hat{H}_{\text{nuclei}} + \hat{H}_{\text{electrons}} + \hat{V}_{\text{nuclei-electrons}}, \tag{2.4}$$

$$\hat{H} = -\sum_i \frac{\nabla_i^2}{2} - \sum_\alpha \frac{\nabla_\alpha^2}{2M_\alpha} + \frac{1}{2}\sum_{i\neq j}\frac{1}{|\mathbf{r}_i - \mathbf{r}_j|} + \frac{1}{2}\sum_{\alpha\neq\beta}\frac{Z_\alpha Z_\beta}{|\mathbf{r}_\alpha - \mathbf{r}_\beta|} - \frac{1}{2}\sum_{i,\alpha}\frac{Z_\alpha}{|\mathbf{r}_i - \mathbf{r}_\alpha|}. \tag{2.5}$$

The first two terms are the kinetic contributions of electrons i and nuclei α with the mass ratio $M_\alpha = m_\alpha / m_{\text{e}} \geq 1800$ of the nucleus mass m_α and the electron mass m_{e}. The other three terms are sums of Coulomb interaction potentials. Two terms sum up the electrons and the nuclei of charge Z_α, Z_β interacting with their own kind. The last Coulomb sum couples the electronic degrees of freedom with the ionic degrees of freedom.

A common applied approximation to decouple the fast moving electrons from the slower and heavier nuclei is the Born-Oppenheimer approximation [91]. The new Hamiltonian $\hat{H}_{\text{e}}$ for only the electronic part with N electrons in an external potential V_{ext} from a static configuration of nuclei becomes

$$\hat{H}_{\text{e}} = -\sum_i^N \frac{\nabla_i^2}{2} + \sum_i^N V_{\text{ext}}(\mathbf{r}_i) + \frac{1}{2}\sum_{i\neq j}^N \frac{1}{|\mathbf{r}_i - \mathbf{r}_j|}. \tag{2.6}$$

But also solving the time-independent Schrödinger equation of N interacting electrons with the Hamiltonian $\hat{H}_e$ in equation 2.6 for realistic systems is still out of scope for our computational and data storage capacities. For example, naively storing a wave function of Fe (26 electrons) on a 3D-grid of 10 points in each spatial dimension would require more bits than atoms available in the observable universe.

To overcome this dilemma the scientific community came up with two types of data compression schemes (for an overview see [47]). The first type (wave function type) still explicitly uses the wave function but exploits the advantage that most of the entries of the wave function do not need to be computed or the wave function itself can be approximated. The second solution scheme moves away from the wave function to other reduced quantities from which observables can be calculated directly. In reality, an experiment always measures some observables which depend on probabilities or amplitudes and only implicitly on the wave function itself. In this solution scheme, complexity and hardness of the problem shifts from the wave function to the observable representation (for example the total energy) with the chosen reduced quantity. The wave function methods (first type) can be very accurate, in the limit even exact but do still scale computationally very badly with the number of particles of the system. Well known approximate wave function methods are Hartree-Fock [92], where the wave function is simply approximated by a single Slater-determinant and methods that extend the Hartree-Fock approach like configuration interaction methods (CI) [93] or coupled cluster expansion [94]. These methods are widely applied in chemistry for calculations on molecules, but rarely applicable widely to solid state systems. Since these wave function methods do not play a role in this work they are not further explained. The second scheme, which exploits the usage of reduced quantities to circumvent the wave function leading to a significant reduction in variables. Part of this scheme are Green-function methods and methods deploying some form of a particle density, like the one-body or two-body reduced density matrix, the pair density, or the charge density. The former methods are known as Density Functional Theory (DFT). Since only density functional theory with the electron charge density was applied in this work it is further discussed in more detail.

2.3. Density Functional Theory (DFT)

Density functional theory (DFT) is a very successful and widely applied method [95] for the calculation of ground state properties and beyond [61, 96–98]. The central idea of density functional theory is to shift the complexity of solving the time-independent Schrödinger equation away from the giant wave function Ψ and express every observable $\hat{O}$ as a functional of the ground state charge density $n_0(\mathbf{r})$ as shown in equation 2.7. The charge density is a reduced quantity of the ground state Ψ_{GS} of a system with N electrons, equation 2.8.

$$O[n_0] = \langle \Psi[n_0] \,|\, \hat{O} \,|\, \Psi[n_0] \rangle\,, \tag{2.7}$$

$$n_0(\mathbf{r}) = \langle \Psi_{GS} | \sum_{i=1}^{N} \delta(\mathbf{r} - \mathbf{r_i}) | \Psi_{GS} \rangle \tag{2.8}$$

This would not help if one still has to calculate the full ground-state wave function Ψ_{GS} to calculate the charge density. Here Hohenberg and Kohn have shown in [99] that the total energy of a system is a unique functional of the ground state electron density up to a constant for a given external potential. They have also shown that this ground-state density minimizes the total energy functional.

Theorem 2.3.1: Hohenberg-Kohn Theorem 1 [99]:

For a given external potential $V_{ext}(r)$, the total energy of a system is a **unique** functional of the ground state electron density up to an arbitrary constant.

Theorem 2.3.2: Hohenberg-Kohn Theorem 2 [99]:

If the number of charges is fixed, the ground state electron density is the density which minimizes the total energy functional. $E[n] > E[n_0] \quad \forall n(\mathbf{r}) \neq n_0(\mathbf{r})$

This could be generalized to degenerate ground states. These theorems by Hohenberg and Kohn open the door for finding the ground-state density directly via a minimization principle. The complexity of the overall many-body problem now shifts to determining the form of the total energy functional. For this the total energy functional $E[n]$ is split in terms with a known representation and unknown terms

$$E[n] = E_{\text{ext}}[n] + E_{\text{H}}[n] + E_{\text{kin}}[n] + E_{\text{xc}}[n] \tag{2.9}$$

$$E_{\text{ext}}[n] = \int n(\mathbf{r}) V_{\text{ext}}(\mathbf{r}) d\mathbf{r} \tag{2.10}$$

$$E_{\text{H}}[n] = \frac{1}{2} \int \frac{n(\mathbf{r_1}) n(\mathbf{r_2})}{|\mathbf{r_1} - \mathbf{r_2}|} d\mathbf{r_2} d\mathbf{r_1} \tag{2.11}$$

$E_{\text{ext}}[n]$ accounts for the external potential from the given nuclei configuration, while all other three term correspond to a universal functional form for all systems. $E_{\text{H}}[n]$ is the so called Hartree term from the Coulomb interaction. The term $E_{\text{kin}}[n]$ corresponds to the kinetic energy of the electrons. Everything else with unknown explicit dependence on the charge density is approximated in the so called exchange and correlation term $E_{\text{xc}}[n]$. To now approximate the $E_{\text{xc}}[n]$ term a lot of different functionals evolved [100]. Two very common classes are the local density approximation (LDA) 2.12 or the general gradient approximation (GGA) 2.13, which allows for density gradient dependencies in the exchange and correlation energy ϵ_{xc}.

$$E_{\text{xc}}^{\text{LDA}}[n] = \int \epsilon_{xc}(n(\mathbf{r})) n(\mathbf{r}) \mathrm{d}^3 r \tag{2.12}$$

$$E_{\mathrm{xc}}^{\mathrm{GGA}}[n] = \int \epsilon_{\mathrm{xc}}(n(\mathbf{r}), \nabla n(\mathbf{r})) d^3 r \tag{2.13}$$

In the local density approximation $\epsilon_{xc}(n(\mathbf{r}))$ is the parameterized exchange and correlation energy of the homogeneous electron gas. Several parameterizations for the local density approximation do exist for example [101]. For GGA a variety of completely different GGA functionals exists with different $\epsilon_{\mathrm{xc}}(n(\mathbf{r}), \nabla(n(\mathbf{r})))$. The GGA functional applied throughout the simulations of this work is the Perdew, Burke, and Ernzerhof (PBE) functional [102]. Beyond these two $E_{\mathrm{xc}}[n]$ approximations there is a whole zoo of other functionals, some like hybrid functionals [103] manage to include better strong electronic correlations, or other functionals describe Van der Waals interactions better than GGAs.

Kohn and Sham came up with an efficient way to calculate the total energy of the ground state including the kinetic energy term. For that, an auxiliary Kohn-Sham system [104] is solved self-consistently as follows: Stationary Schrödinger equations 2.14 for single independent particles (i) in a local effective potential V_s, Equation 2.15 are written down for all N electrons,

$$\left[-\frac{\nabla^2}{2} + V_s(\mathbf{r})\right] \psi_i(\mathbf{r}) = \epsilon_i \psi_i(\mathbf{r}) \tag{2.14}$$

$$V_{\mathrm{s}}(\mathbf{r}) = V_{\mathrm{ext}}(\mathbf{r}) + \int \frac{n(\mathbf{r}')}{|\mathbf{r}-\mathbf{r}'|} d\mathbf{r}' + V_{\mathrm{xc}}[n] \tag{2.15}$$

$$V_{\mathrm{xc}}[n] = \frac{dE_{\mathrm{xc}}[n]}{dn} \tag{2.16}$$

$$n(\mathbf{r}) = \sum_i^N |\psi_i(\mathbf{r})|^2 \tag{2.17}$$

where the ψ_i are called Kohn-Sham orbitals and ϵ_i are the corresponding Kohn-Sham single particle energy eigenvalues. The potential $V_{\mathrm{s}}(\mathbf{r})$ consists of a contribution from the external potential, the Hartree potential and the exchange correlation potential $V_{\mathrm{xc}}[n]$, defined by the functional derivative of the exchange and correlation energy with respect to the electron density (2.16). In this way, the effective potential is chosen as such, that the ground-state density of the Kohn-Sham system minimizes the total energy functional of our many-body system. The electron density $n(\mathbf{r})$ is now calculated as the sum of single particle amplitudes. The auxiliary Kohn-Sham system can be solved computational efficiently, since the electron-electron interaction is mimicked in the Kohn-Sham potential leaving single particle equations. Thus one has to solve self-consistently a system of single particle equations.

Summarizing the above, the many-body electron system was mapped onto a system of non-interacting electrons in an effective potential which has the same ground-state density. The Kohn-Sham equations have to be solved in a self-consistent way, as the potential (2.15) in the single particle Schrödinger equation (2.14) is a functional of the electron density (2.17) and the density itself depends on the Kohn-Sham orbitals, which solve the Schrödinger equation (2.14) for each electron. This self-consistency cycle is sketched in Fig. 2.1. After construction of an initial charge density the corresponding potential and Hamiltonian are constructed, solved and a resulting charge density is calculated. Then it is checked whether the new density corresponds to the starting density. If not, the cycle is started all over again with a preconditioned, mixture of old and new density. Among others, common mixing schemes are simple mixing, Broyden mixing [105] or Anderson mixing [106]. Preconditioning of the charge density before mixing avoids charge oscillations and can lead to a smaller amount of iterations needed independent of the system size. A preconditioning method am others is the Kerker method [107].

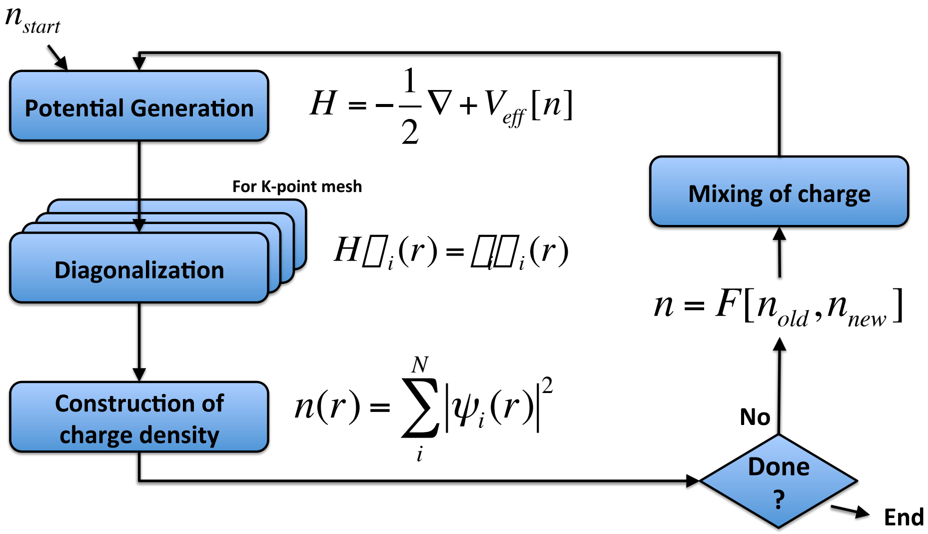

Fig. 2.1.: Self-consistency-cycle for converging the electron density, motivated by an image from [47]. Beginning with a constructed starting density, the corresponding effective potential is calculated, then the eigenvalue problem is solved for the given k-point grid in momentum space and the new charge density is calculated with the resulting Kohn-Sham orbitals. If the old and new density are the same within some distance measure, the calculation is finished. Otherwise the cycle is started all over again with a smart mix F of the new and previous density(ies).

In principle, besides the ground-state density and the total energy, other properties of our auxiliary system (Kohn-Sham orbitals, Kohn-Sham energies, etc.) have no physical meaning for the many-body system. However in practice it turns out that they help to describe some experimental results quite well, as long as strong correlations play no major role in the system. From Fermi-liquid theory [84], where interacting fermions are renormalized to effective free fermions, it is understandable why such a mapping can be a reasonably good one.

To include collinear magnetism in DFT the total charge density is split in a spin up and spin down contribution $n = n_\uparrow + n_\downarrow$, which have to be converged individually in parallel. For non-collinear magnetic systems a three component spin density $m(\mathbf{r})$ which allows for a local quantization axis of each site has to be converged.

So far the treatment of the electrons was non-relativistic. To account for relativistic effects for the core electrons a radial Dirac equation can be solved [108]. For the valence electrons additional terms can be added to the Kohn-Sham Hamiltonian, which can be derived as shown in [109] from the Dirac equation which describes a spin 1/2 particle with mass m conform with relativity in an effective potential V_{eff}. Along [109] this gives rise to correction terms to the Hamiltonian up to $\mathcal{O}\left(m^{-4}\right)$. One important term is called the spin-orbit coupling term and in the absents of and external electrical field it is given by

$$H_{SOC} = -\frac{\hbar}{4m^2c^2}\boldsymbol{\sigma}\cdot\left(\nabla V_{\text{eff}} \times \mathbf{p}\right) \tag{2.18}$$

where m is the electron mass, $\mathbf{p}$ is the momentum operator and σ is a vector of pauli matrices, to describe a spin-1/2. If V_{eff} is a spherical symmetric potential then the gradient can be written as

$$\nabla V_{\text{eff}} = \frac{1}{r}\frac{dV_{\text{eff}}}{dr}\cdot\mathbf{r} \tag{2.19}$$

and one arrives at the well known form of

$$H_{SOC} = -\frac{\hbar^2\xi}{4m^2c^2}\left(\boldsymbol{\sigma}\cdot\mathbf{L}\right) \tag{2.20}$$

where $\mathbf{L}$ is the angular momentum operator, and the spin-orbit coupling constant $\xi = \frac{1}{r}\frac{dV_{\text{eff}}}{dr}$. H_{SOC} couples spin degrees with orbital degrees of freedom and becomes a significant contribution if the gradient of the potential is large, which is the case for heavy nuclei.

A variety of methods is known for solving the Kohn-Sham equations (2.14-2.17). Expanding the Kohn-Sham orbitals $\psi_\nu(\mathbf{r})$ in a set of basis functions $\{\varphi_n(\mathbf{r})\}$

$$\psi_\nu(\mathbf{r}) = \sum_{n=1}^{N} c_\nu^n \varphi_n(\mathbf{r}) \tag{2.21}$$

with expansion coefficients c_ν^n is a widely used method. In this way the eigenvalue problem

$$\hat{H}\psi_\nu(\mathbf{r}) = \epsilon_\nu\psi_\nu(\mathbf{r}) \tag{2.22}$$

is transformed into an algebraic generalized eigenvalue problem of dimension N.

$$\underline{\underline{H}}\underline{c_\nu} = \epsilon_\nu \underline{\underline{S}}\underline{c_\nu} \tag{2.23}$$

where c_ν is the coefficient vector, ϵ_ν is the corresponding eigenvalue, $\underline{\underline{H}}$ is the $N \times N$ Hamilton matrix with elements

$$H^{n,n'} = \int \varphi_n^*(\mathbf{r})\hat{H}(\mathbf{r})\varphi_{n'}(\mathbf{r})d\mathbf{r} \tag{2.24}$$

and the overlap matrix $\underline{\underline{S}}$ with elements

$$S^{n,n'} = \int \varphi_n^*(\mathbf{r})\varphi_{n'}(\mathbf{r})d\mathbf{r} \tag{2.25}$$

It is reasonable to use a basis set which simplifies the matrix diagonalization to be efficient in calculation resources. For orthonormal basis functions, the overlap matrix elements become $S^{n,n'} = \delta^{n,n'}$ and the generalized eigenvalue problem turns into a standard algebraic eigenvalue problem. A localized basis set would lead to a sparse Hamilton matrix and basis functions similar to the Kohn-Sham orbitals $\psi_\nu(\mathbf{r})$, corresponding to a small problem dimension N.

Commonly used basis sets are Gaussians, atomic orbitals or plane waves. Plane waves have the advantage that they are an orthonormal basis set. In addition to the overlap matrix, the kinetic part of the Hamiltonian matrix becomes also diagonal and the potential matrix elements can be calculated via the Fourier transform. But plane waves have a problem with the $1/r$ singularity in the Coulomb potential near the nuclei. The Coulomb potential leads on the one hand to the existence of strongly bound states (core electrons), which are very localized and have eigenvalue energies at least a couple electron volts below the Fermi energy and on the other hand it leads to delocalized states (valence electrons), whose eigenvalue energies are close to the Fermi energy, but whose wave functions oscillate strongly near the nuclei. Treating both adequately with the same basis set would generally require many basis functions and lead to huge problem sizes N. A way out while still using plane waves is to either treat the regions near the nuclei (Coulomb singularity) with another basis set like in the **F**ull-Potential **L**inearized **A**ugmented **P**lane **W**ave Method (FLAPW) [80, 81] (discussed in Section 2.4) or to not treat the core electrons in an exact manner by smoothing the Coulomb potential. The later approaches are so called pseudopotential methods and they are implemented in DFT programs like the Quantum Espresso (QE) package [110] or the VASP software package implementing the projector augmented-wave method (PAW) [111]. The electronic structure community works on common software libraries like the Electronic Structure Library [112] including among other tools, solvers, functionals and community file formats.

Dense eigenvalue solver usually have a computational complexity of $\mathcal{O}(N^3)$ with N being the dimension of the matrix of the eigenvalue problem. Sparse eigenvalue problem solvers, with interest in only a partial spectrum, can scale with $\mathcal{O}(N^2)$ or even $\mathcal{O}(N)$ [113, 114]. Solving the eigenvalue problem is the most time consuming step in most DFT methods, therefore leading to an overall scaling behavior of $\mathcal{O}(N^3)$ for methods needing to solve dense matrices. This is also the case for the FLAPW method, which is the underlying method of the `FLEUR` program used within this work.

2.3.1. Enthalpy of formation from DFT

The enthalpy of formation ΔH_{C} for a compound C is the change of enthalpy if it is formed by its constituent elements per formula unit.

$$\Delta H_{\mathrm{C}} = H_{\mathrm{C}} - \sum_{i=1} \alpha_i H_{\mathrm{i}} \tag{2.26}$$

where α_i is the stoichiometry factor of the element i in the compound C. The enthalpy of formation is per definition for elemental ground-state configurations 0 eV per atom. Compounds with an enthalpy of formation > 0 eV per atom are not stable. From the enthalpies of formation for all stable compounds in a phase digram the enthalpy of change for any reaction for that phase space can be calculated. A way to find the most stable compounds is the convex-hull construction. Compounds which span the convex hull, i.e., lie on the convex hull are the most stable ones. All compounds which lie above the convex hull are energetically metastable or not stable at all. The construction of a convex hull in N-dimension is a solved mathematical problem. A common applied algorithm is the 'Qhull' algorithm [115]. For our 2D-convex-hull construction the implementation contained within Scipy (scipy.spatial) [116] was used. Predicting the enthalpies is valuable for experiments, though there is a difference between stability and synthesizability in the laboratory [117], for example due to kinetic energy contributions, degenerate states and available growth pathways. From density functional theory the enthalpy of formation is estimated from the total energy per atom for the compound and the elemental systems.

$$\Delta E_{\mathrm{tot\,C}} = E_{\mathrm{tot\,C}} - \sum_{i=1} \alpha_i E_{\mathrm{tot\,i}} \tag{2.27}$$

In some cases this is tricky to calculate since total energies are not always comparable [118, 119] for systems which have to be treated computationally differently like in the case of oxides. If done right, the formation energies from DFT are comparable with experimental values, with a reported mean absolute error of 96 meV/atom in one study [120]. Since total energy differences may change with the deployed exchange and correlation functional the convex-hull diagram may also change with the functional.

2.4. The FLAPW method and the FLEUR program

Definition 2.4.1: Some technical terms in `FLEUR`

Element/Isotope: *An Element from the periodic table, with a fixed number of protons.*

(Atomic) Species: *A crystal structure can have several atomic species of the same element. For example due to a magnetic sublattice, with another symmetry as the atomic lattice. Another example would be a core-hole calculation with a species with a core hole and a species of the same element without a core hole. Species can have different FLAPW parameters for the same element. If there is one species of an element in the crystal it is referred to it with the symbol of the element.*

(X) Atom-type: *A group of atoms with the same species X. In crystallography this is also known as '(crystallographic) equivalent atoms'. These species are symmetric equivalent and have the same properties. There can be several atom-types of the same species X in a crystal structure. Different atom-types can still have the same physical properties, like their chemical shift.*

One possibility to overcome the $1/r$ singularity problem with all electrons, is the **F**ull-Potential **L**inearized **A**ugmented **P**lane **W**ave Method (FLAPW) which was in detail studied in [80, 81, 121–123]. The implementation of it in the `FLEUR` program and various features is in more detail described in [79, 124–129]. In the FLAPW method the Kohn-Sham orbitals are expanded in basis functions, which are defined in a piecewise manner. Real space is divided into so called muffin-tin spheres (MT) with a certain radius (r_{MT}) around the atomic nuclei and a region between these spheres, called the interstitial region (IR). This division is conceptually shown in Fig. 2.2, with the interstitial region (in red) and two muffin-tin spheres (in blue) with distinct radii. The basis set functions for the interstitial region are plane waves 2.28 with Bloch vector **k**, a reciprocal lattice vector **G** and a position **r**.

$$\psi_{\mathrm{IR}}^{\mathbf{G}}(\mathbf{k}) = e^{i(\mathbf{k}+\mathbf{G})\mathbf{r}} \tag{2.28}$$

$$\psi_{\mathrm{MT}}^{\mathbf{G}}(\mathbf{k}) = \sum_{\ell m} \left(a_{\ell m}^{\mu,\mathbf{G}}(\mathbf{k})\, u_\ell^\mu(r^\mu, E) + b_{\ell m}^{\mu,\mathbf{G}}(\mathbf{k})\, \dot{u}_\ell^\mu(r^\mu, E) \right) Y_{\ell m}(\hat{\mathbf{r}}^\mu) \tag{2.29}$$

The basis functions within the muffin-tin spheres 2.29 of atom-type μ are a linear combination of spherical harmonics $Y_{\ell m}(\hat{\mathbf{r}}^\mu)$ multiplied with numerical radial functions $u_\ell(r, E)$ on a grid summed up over angular momentum quantum-numbers ℓ and magnetic quantum number m. The numerical radial function $u_\ell(r, E)$ solves the radial Schrödinger equation for a specific

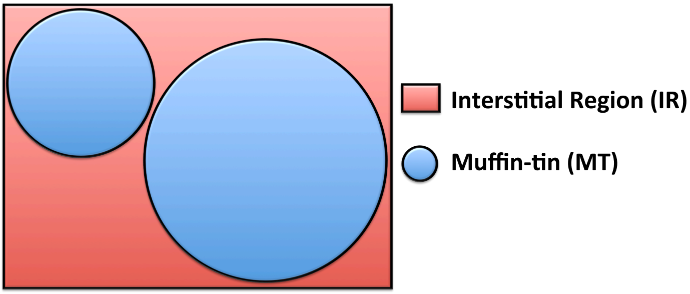

Fig. 2.2.: In the muffin-tin scheme real space is divided in two regions. The muffin-tin spheres and the interstitial region. In each region, a different basis function set is applied.

energy parameter E. The derivative with respect to energy of $u_\ell(r,E)$ is $\dot{u}_\ell(r,E)$. By using a radial function basis set the $1/r$ singularity is taken care of. The a and b matching coefficients are chosen such, that the basis functions and derivatives are continuous on the muffin-tin boundary. In practice a finite number of basis functions is applied and the expansion in spherical harmonics is cut after some ℓ_{max}, which lies usually between 6 and 10. Plane waves are only generated up to a $|k+G| = k_{\text{max}}$, ranging between 3 a_0^{-1} and 6 a_0^{-1}, where a_0 is one bohr radius. Such a basis set can also be constructed for 1D [130] and 2D systems. Leakage of some charge from high lying core states to the interstitial region can by corrected by a core-tail correction. Some materials have semi-core states, which are states still close to the core and often show small dispersion. This states have non-neglectable part of their wave function further away from the core and therefore outside of the muffin-tin radius and the basis functions inside the muffin-tins are not flexible enough to treat them accurately. To treat them correctly and stabilize the algorithms one extents the basis set with local orbital basis functions (LOs) [131]:

$$\psi^{\mu,LO}_{\mathbf{kG}_{LO}}(\mathbf{r}) = \sum_{\ell m} \left(a^{\mu,LO}_{\ell m}\, u^{\mu}_{\ell}(\mathbf{r}^{\mu}, E^{\mu}_{\ell}) + b^{\mu,LO}_{\ell m}\, \dot{u}^{\mu}_{\ell}(\mathbf{r}^{\mu}, E^{\mu}_{\ell}) + c^{\mu,LO}_{\ell m}\, \tilde{u}^{\mu}_{\ell,LO}(\mathbf{r}^{\mu}, \tilde{E}^{\mu}_{\ell}) \right) Y_{\ell m}(\hat{\mathbf{r}}^{\mu}) \qquad (2.30)$$

, where a, b and c are matching coefficients for the basis functions at the muffin-tin boundary and $\tilde{u}^{\mu}_{\ell,LO}(\mathbf{r}^{\mu}, \tilde{E}^{\mu}_{\ell})$ is another solution of the radial Schrödinger equation at another energy parameter $\tilde{E}^{\mu}_{\ell}$. There are also other types of local orbitals described in [132].

The grid points $r[i]$ for the potential inside the muffin-tin radius (r_{MT}) are constructed the following exponential mesh way

$$r[i] = r_{\mathrm{MT}} \cdot e^{(d_x \cdot (1-i))} \tag{2.31}$$

where d_x is a parameter controlling the exponential mesh spacing. As input in the `FLEUR` program the number of grid points for the mesh is specified with the 'jri' parameter. Depending on the muffin-tin radius per default between 400 and 1000 mesh points are created.

2.5. Chemical Configuration Space, the second exponential wall

It was introduced above how to retrieve a ground-state energy of the many-body problem with density functional theory (DFT) for a given configuration of nuclei. The structural configuration is needed to construct the initial state, i.e., the initial potential and the starting density. A different facet of the many-body problem is that the structural configuration space (or chemical compound space (CCS)) is enormous. For us it could be as well infinite and it is not straightforward to theoretically assess how many stable structures there are. Also degenerate ground-states and total energy manifolds with many local minima are a challenge.

An easy and rough estimation for the size of structural configuration space is to look at the number of constructible stoichiometric compositions there are for a given number of protons. This corresponds to a partition function $P(N)$ and therefore the number of possible stoichiometric configurations of the periodic table grows exponentially with the number of protons N in a compound [31]. Some compositions (stoichiometries) will not have a stable ground state while other compositions will have several possible ground states (also besides degeneracy) depending on additional degrees of freedom, like magnetic properties, entropy and external conditions as temperature, pressure or electro magnetic fields. Thus information about metastable structures, surfaces and influences of defects or disorder are also desired, making this estimation rather a lower bound of how many systems might be necessary to calculate. Overall, this crude assessment provides us with an idea about the enormous size of chemical compound space and what is still unknown. For systems with exactly 100 electrons there are more than $P(100) \approx 10^8$ possible stoichiometric configurations. For systems with less or equal 100 electrons (sum of partitions) this number would amount to $1.64 \cdot 10^9$. For 1000 electrons this number is larger than 10^{32}. Quantum chemists estimated in [28], by counting possible spatial arrangements, that there could be more than 10^{60} different molecules with 30 atoms containing only C, N, O and S atoms.

Even with chemical constrains and other estimation methods [32] these numbers are so enormous that it is impossible to straight out explore large parts of structural configuration space in the lab or on the computer. Even if the Schrödinger equation could be solved with some approximate model in a split second for each of these systems physically accurate enough there is still no way to screen brute force such a phase space. Furthermore, it is obvious due to the total and relative amount of atoms in the universe (10^{80}, sun 10^{55}) that only a small amount of stable phases will occur in nature. All other promising materials will have to be discovered and synthesized in the laboratory under the right conditions. Overall, to cope with crystal structure space methods are needed and developed in the community like, structure prediction, down folding, ensemble DFT, structure maps [48], machine learning, cluster expansion, high-throughput experiments and computational screening.

2.5.1. Crystal Structure Sources

How does one find out what configurations need to be calculated? A structural configuration, the starting point for a DFT calculation in the case of solids, contains a list of atom (nuclei) positions and a Bravais matrix of the unit cell plus, if needed, further information like the magnetic configuration. This information is essential for performing electronic structure calculations. When comparing simulation results with experiments it is key to know that the simulated configuration is equivalent to the one under experimental investigation or at least fairly similar. Otherwise one may end up comparing different physical systems. In practice this is often pretty difficult, because real world materials usually are not single crystals and precise knowledge of the measured system is hard to extract, or simply not openly available.

Fig. 2.3b provides an overview of the crystallographic data collected over the ages in databases with more than 100,000 entries that are available in 2019. The database sizes are illustrated through the area of the corresponding circles. Content overlap is roughly indicated by overlapping database circles. The largest circle in the background is the partition functions of 70 as a reference for how many distinct crystal structures there might be for systems with 70 protons (as shown in Fig. 2.3a). Precise high quality crystal structure data experimentally determined with methods like X-ray diffraction (XRD) is very precious and a good starting point. For inorganic structures such data is accumulated from the literature in the commercially available Inorganic Crystal Structure Database (ICSD) [89], created and administrated by FIZ Karlsruhe. There are ~157,000 entries assigned to a structure type in the ICSD, containing ~2,700 elemental crystal, ~38,000 records for binary compounds, ~72,000 records for ternary compounds and ~72,000 records for quaternary plus quintenary compounds. From these entries about 55,000 unique ones are left for computation when sorting out doubles, partial

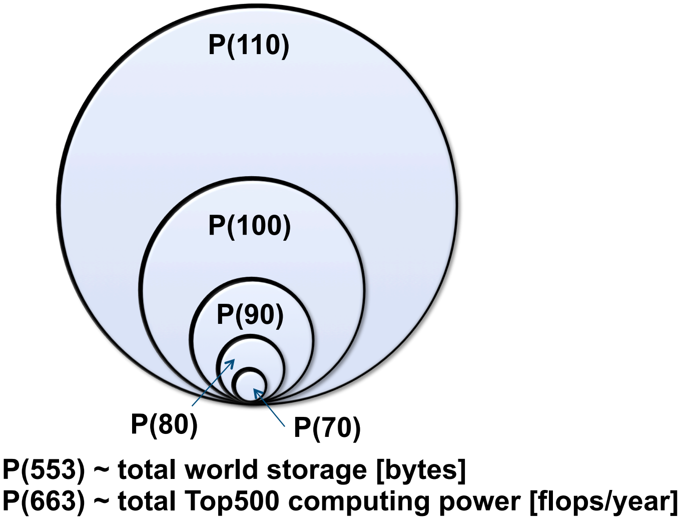

(a)

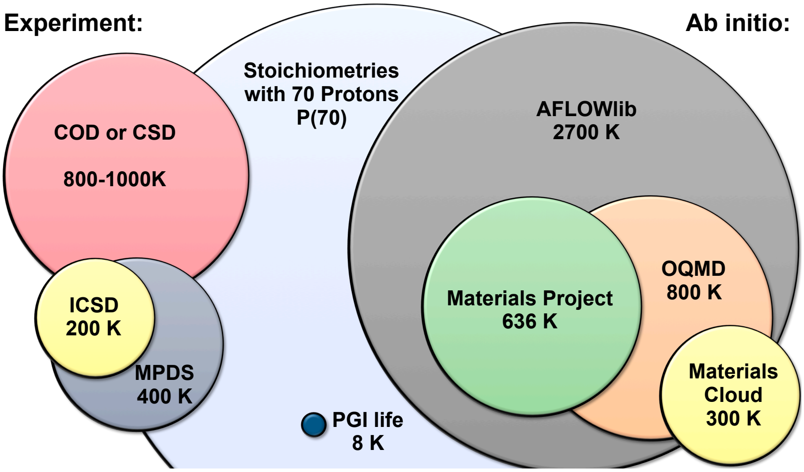

(b)

Fig. 2.3.: Exponential growth of structural configuration space visualized (a). The circle's areas correspond to the partition function (P) counting the number of possible structural stoichiometric configurations for a certain number of protons. An overview of the largest experimental and theoretical crystal structure databases (b). This shows the status from 2018 as some of them are growing fast through automatic frameworks. The larger theoretical databases of non solid state structures like small molecules are not included in this picture.

occupancy and incomplete data. Another commercial inorganic crystal structure database including some additional property information is the Materials Platform for Data Science (MPDS) [53] based on the Pauling file [133] with around 400,000 entires. The Open Crystal Structure Database (COD) [134] is freely available online and open for contributions. Besides inorganic entries it also contains, molecules, molecules on surfaces, organic crystals. It is important to check the data quality for COD entries. Irrelevant for this work, but a treasure for the chemistry community is the CSD [135] containing mainly organic materials and molecules. In addition large publisher companies like Springer Materials [136] are building up databases with structures, materials and properties for a broad scientific community.

On top and out of these experimental structure sources databases evolved which contain theoretically predicted structure data and calculation results. Relevant theoretical based databases for solid state research and relevant for this work are shown in Fig. 2.3b. The largest theoretical structure sets are found in the GDB databases [137, 138] from quantum chemistry containing 977,468,314 small molecules. A database exclusively for theoretical crystal structures is the Theoretical Open Crystal Structure database (TCOD) [139] (not included in Fig. 2.3b). From high-throughput projects, executed mainly with the VASP program, several open databases emerged, which are growing steadily. The American Materials Genome initiative [52] lead to the Materials Project [39]. Its database now contains over 636,000 crystal structure entries. On top of these it contains a range of calculated properties. Among others 60,000 XAS spectra [140], 7,600 elastic tensors, 3,600 piezoelectric tensors and a wide study of electrodes for battery materials can be accessed through the Material Projects API and web apps. The largest collection of over 2.7 million crystal structures (status 04.2019) is found in the AFLOWlib [56] data collection from the group of Stefano Curtarolo at Duke University. Through their automation of VASP calculations and crystal structure prediction in the AFLOW framework, AFLOWlib has more then doubled in recent years and around every 30 seconds calculations on a new structure will be added. On the web ALFLOWlib also provides apps and visualization tools to browse and extract some of the data. Besides a lot of metastable structures it contains structures predicted to be stable but yet unknown to experiments. Another openly available database from the group of Chris Wolverton (America) is the Open Quantum Materials Database (OQMD). The OQMD contains over 300,000 calculated structures from high throughput screenings plus over another 400,000 structure entries of predicted heuslers and combinatorial constructions through structure prototypes. A rather new (since end of 2017) European database for data and simulations run through AiiDA is Materials Cloud [59]. It so far contains data from some individual projects, totaling around 300,000 entries. Currently, it consists mainly of studies on 2D crystal structures predicted to be able to be exfoliated [141], phonon calculations with the quantum espresso package [110] and topological materials. Besides the curated data, Materials Cloud also provides individual project apps to browse and visualize the data. It includes a learning section and a calculation on-demand section if one has an account at the Swiss supercomputing center. These theoretical databases are expected to be growing fast in the coming years.

The small dark blue circle in Fig 2.3b represents an estimate for the number of systems ever investigated by the Peter Grünberg Institute, Quantum Theory of Materials (PGI-1/IAS-1), in order to put material space in perspective to the PGI-1 lifetime simulation output. If assuming that on average the scientists at the PGI treated 200 new systems per year in total, we can estimate that the PGI has investigated around 8,000 different systems over 40 years. If the scientists ran 100 simulations on each of these systems the total amount of simulations performed adds up to 800,000. Such an estimate might be representative for a large number of long term research groups. Unfortunately, none of this data is collected and stored in a structured, accessible form besides the publication of a small subset of results in scientific journals. Also collection of such data in a curated and quality checked way is still a challenge to be solved. From 2015-2018 there was a European center of excellence NOMAD [57], which spent large efforts on collecting *ab initio* simulation data from different groups and software packages in a large online file repository with common meta data information [142]. NOMAD contains 50,236,539 total energy calculations, on 37,376,432 different geometries[3] (status 03.2018). It is unclear to how many unique crystal structures, or stoichiometric compositions this corresponds to, since 37,304,013 are geometries from VASP. 90 percent of these VASP geometries, which make nearly all of the NOMAD repository content, were simulation output files from AFLOWlib, Materials Project and the OQMD. Every tiny difference in the lattice positions stands for a new geometry. Some machine learning studies in material science [143] harvested their data from the NOMAD archive. Overall, most DFT data online so far originates from plane wave basis sets with a pseudopotential method or from similar methods, there is need for more reference data from high-precision all-electron methods including relativistic effects.

2.5.2. Crystal Structure Discovery

Since material and chemical space is enormous there is quite substantial effort going on in discovering and characterizing material phases. From the experimental side this either happens per accident, is done very selectively driven by predictions to find certain pleasant properties, or in a systematic high-throughput way. In automated high-throughput phase

---

[3] `https://metainfo.nomad-coe.eu/nomadmetainfo_public/archive.html`, accessed June 2019

diagram screening like in [144, 145] several chemical elements are simultaneously vapor deposited on large wafers under high vacuum. The adjustments of shutters, deposition heads and environment parameters, create continuously differing concentrations of the elements on the wafer, resulting in the formation of many phases of the corresponding phase diagram. These wafers or so called libraries are then raster scanned and among other things, characterized with X-ray diffraction (XRD) and evaluated with X-ray photoemission spectroscopy (XPS). XRD spectra are rather easy to evaluate and predict. For large enough crystalline structures XRD provides insight into the lattice parameters, making identification of phases easy. Through such methods about 1,000 crystal structure entries are added to the ICSD per year [89, 146]. While XPS is also very sensitive for formation of smaller crystalline structures, it is often tedious to evaluate (for details on this see section 2.9.1). For example the spectra of individual phases do not have to be unique and reference data might be needed for the interpretation. Especially automating the evaluation process for different mixed-phase spectra is hard. Such methods might benefit from the results of this work.

With the increase in computing power, high-throughput capabilities and robustness of electronic structure packages, theoretical structure prediction evolved. To calculate and relax every structure with *ab initio* methods directly is to expensive. For sampling materials space, a zoo of smart methods and algorithms were developed from random sampling over simple replacement algorithms to genetic [147] algorithms, machine learning methods [148, 149] and cluster expansion. Stable and metastable predicted structures are accumulated in open data repositories [39, 56]. Nowadays, the theoretical structure discovery rates outperform the experimental rates by far, but it needs to be stated that there is a non negligible difference in reality between theoretically predicted stability and synthesizability in the laboratory.

2.6. High-throughput Computation in Material Science

Definition 2.6.1: Terms from computer science

High-throughput computing (HTC) *[150]: is a computer science term to describe the use of many computing resources over long periods of time to accomplish a computational task. It is a computing paradigm that focuses on the efficient execution of a large number of loosely-coupled tasks.*

High-performance computing (HPC) *[150]: is a computing paradigm which characterizes the usage of large amounts of computing resources over a relative short period of time for a few computational tasks.*

Many-tasks computing (MTC) *[151]: The boarders of HPC and HTC are blurry. MTC aims to bridge the gap between HTC and HPC. MTC is reminiscent of HTC, but it differs in the emphasis of using many computing resources over short periods of time to accomplish many computational tasks (i.e., including both dependent and independent tasks). MTC denotes high-performance computations (HPC) comprising multiple distinct activities, coupled via file system operations.*

In computational material science high-throughput computing (HTC) has to be understood as having a high temporal simulation density, usually as high as possible, to deal with structural configuration space, or parameter scans. HTC is achieved by utilizing some automation tools. The sizes of computing tasks vary over a wide range depending on the system size or properties to be calculated. Computing tasks rarely run longer than months. The computer science community would classify what the material science community requires rather as many-task computing (MTC), but since the boarders are blurry and the term high-throughput is established in our community it is used throughout this work. In the high-throughput regime, work becomes mainly limited by computational resources plus the capacity and robustness of the computing infrastructure, whereas human labor working time plays a subsidiary role. In the DFT world high-throughput means going from $\mathcal{O}(10^1 - 10^3)$ to $\mathcal{O}(10^4 - 10^7)$ simulations per person per year. The system sizes (number of atoms) which can be simulated depend on the program's scalability on high-performance computing (HPC) systems (supercomputers) and their computing power measured in FLoating point Operations Per Second (FLOPS) and memory bandwidth.

One should keep in mind that high-throughput computations with the same program (for DFT at least) will usually produce more longterm data per CPU time than running one big calculation with the same amount of computing time. Such is the case for the `FLEUR` program, because its algorithm scales cubically $\mathcal{O}(N^3)$ with the system size N. Whereas one DFT simulation results in a constant number of files the sizes of which scale linearly with the system size N (assuming no large matrices are stored longterm). I.e., from the computational side under certain assumptions one can ideally run $\alpha = \frac{N^3}{N'^3}$ simulations on a constant computing time budget. While from a storage bound side one can only run $\alpha = \frac{N}{N'}$ simulations. Realistic maximum system sizes are $\mathcal{O}(1000)$ atoms, while small unit cells contain $\mathcal{O}(10)$ atoms. For example, if the usual system size is $N' = \frac{N_{\mathrm{max}}}{100}$, one could run ideally (ignoring scaling) $\alpha = 100^3 = 1,000,000$ such smaller system calculations with the same computing time but 100 of these simulations already account for the same amount of data as the big one. The small simulations require in total 10,000 times the storage capacity (0.1 GB → 1 TB) and produce 1,000,000 times more files than the large simulation. From this fact obviously different demands arise on the computing, especially the data handling infrastructure for high-throughput runs compared to the large calculation jobs in high-performance computing. In general this is also a dilemma in building supercomputer infrastructure: if one increases the computing power while keeping memory and storage capacities roughly constant some applications (especially with non linear complexity), problem sizes and usage models will be left behind. Also when running HTC simulations the data produced for longterm storage, the number of files and meta data should be reduced to the necessary minimum.

High-throughput studies are not new to the electronic structure community. Single projects and automation through scripts go along with the history of improvements of computing infrastructure and density functional theory capabilities. Early projects are often used to screen an ensemble of crystal structures for certain properties, without much or any data curation. Only a small amount of the data is kept and published in the end, since their interest lay on a few special materials. Examples of such work include and are reviewed in [36, 37].

In recent years the development of more sophisticated frameworks like AFLOW [62], AiiDA [63], ASE [64], ATOMOTE [65], fireworks [66], MatCloud [67], MAST [68], MPInterfaces [69], QuantumATK (commercial) [70], Material Studio (commercial) [71], MeDA (commercial) [72], [17] and others opened up new opportunities. Their management of simulations and curated data allowed for incentives like among others the Materials Project [39, 54] (part of Material Genome Initiative) with pymatgen [152], the OQMD [55, 120], NOMAD [57], ESP [58] and Materialscloud [59] to collect and share data from *ab initio* simulations for conserving and extraction of additional knowledge from it by others. From such projects data-mining has been done as described in [60] to better quantify uncertainties of DFT [153], formation energies plus structure stability [118], to construct phase diagrams [119], or improve the prediction of new crystal structures [149]. Modern material screening studies include a wide range of topics for example finding a material for large-scale carbon dioxide capture and storage (CCS) [154] or battery electrolytes [17].

Quite similar to the scope of this work is a simultaneous high-throughput X-ray absorption spectroscopy (XAS) study from 2017 around the Materials Project [140], in which 500,000 K-edge X-ray absorption near edge (XANES) spectra of 40,000 unique materials were constructed. In addition to this study a small tool utilizing machine learning on the data to provide a turnkey solution to the public [155] was provided.

2.7. The AiiDA framework

In order to automatically manage workflows, simulations, and data the open source 'Automated Interactive Infrastructure and Database for Computational Science (AiiDA)' [63, 156–158] was deployed within this work. The AiiDA framework is completely open source under MIT license and its development efforts started in 2012[4]

AiiDA is designed based on the 4 pillars Automation, Data, Environment, Sharing, short the ADES model for computational science (see Fig. 2.4). The model was also proposed in [63] and specifies desired design criteria important for a computational science work environment including open provenance of data as proposed in the open provenance model [159]. For frameworks implementing the ADES model it becomes straight forward to comply with the international FAIR (Findable, Accessable, Interoperable, Reusable) [160, 161] principles for scientific data and stewardship. In Fig. 2.5 a technical layout of AiiDA is presented. The individual colored components of the layout demonstrate which facet of AiiDA addresses which pillar of the ADES model.

The automation pillar (blue) of the ADES model is realized in AiiDA by a Python application programming interface (API) and the AiiDA daemon. The API provides the user with Python classes for data structures, processes, calculations, utilities, and parsers allowing for different abstraction layers. It is designed to be extendable through plug-in classes among others for data and calculations, which can be more or less code specific. In addition anything from the AiiDA API can be imported as a usual Python package in any Python program, script or notebook allowing for all high-level work of the user to be executed in Python. This transferability allows to even work with several different material science software at once

---

[4] In 2018 AiiDA has contributions from more then 40 people to 35 releases of more than 100,000 lines of AiiDA core Python code without counting any plug-in codes, or support packages.

just in Python. A small program called the AiiDA daemon is running in the background of a workstation taking care of task handling. This handling includes submitting, retrieving, managing job calculations, and workflows. The interaction with schedulers on computing resources is also taken care of by the AiiDA daemon. Therefore, if the daemon is not running, no calculations or processes will be further processed. In order to be event based and scalable to millions of tasks the daemon communicates (since AiiDA version 1.0) with his workers (subprograms) through the established RabbitMQ [162, 163] message broker[5]. A user can interact with the daemon via the custom 'verdi' command line interface provided with AiiDA. The 'verdi' shell provides among many others commands for listing information on running calculations and workflows, and commands for inspecting certain database nodes.

The data pillar of the ADES model is accounted for by tracking the data and logic provenance (data evolution and history). In AiiDA storage has two facets. First certain input and output files of calculations are stored structured in a file repository or an object store. The second storage facet is an SQL (Structured Query Language) database in which certain data from calculation input and output files are parsed and stored. For this work PostgreSQL: "the world's most advanced open source relational database" [164], was deployed. The database allows for complex queries on stored data and calculations. Along the open provenance model [159] the database schema in AiiDA is a directed acyclic graph for data provenance. Data nodes are only connected to data nodes through calculation nodes allowing for clear provenance tracking of all data and calculations without directed cycles. AiiDA has other link types for the tracking of logic from workflows. An example of such a provenance graph is depicted in Fig. 2.6, showing how in the material science case an input structure is connected over several calculations to different result nodes from different calculations. Complexer data node graphs of individual workflows are displayed in the method development results section 3.1.2. Whole database provenance graph visualizations are shown in section B.1 of the appendix. AiiDA also creates a hash table for all calculation, allowing to avoid reruns of the same calculations which are already in the database. This feature is called 'caching' and can save computational resources.

The environment pillar of the ADES model is implemented in AiiDA partially through the AiiDA daemon, the plug-in system and workflow system (discussed in more detail in the subsections 2.7.1 and 2.7.2). Plug-ins contain file parsers, calculation classes, workflows, data

---

[5] In AiiDA version prior to 1.0 the daemon was a 'While True loop' querying the database for certain tasks. Since database queries become slower with growing database size (usually $\mathcal{O}log(N)$, or $\mathcal{O}(N)$), this daemon version slows down for larger databases (> 1 Million nodes). All results of this work are produced with AiiDA-core version <=0.12.3

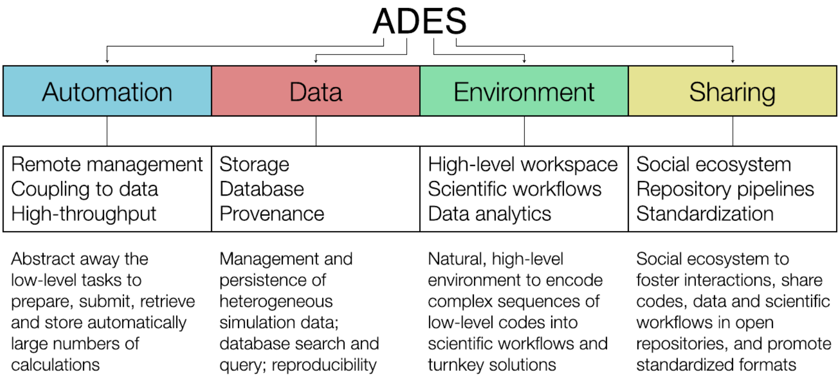

Fig. 2.4.: Automation, data management, a high-level workspace environment and abilities to share protocols plus data with other coworkers and scientists are the four pillars of the ADES model for computational science. Figure reprinted from publication [63] copyright (2016), with permission from Elsevier.

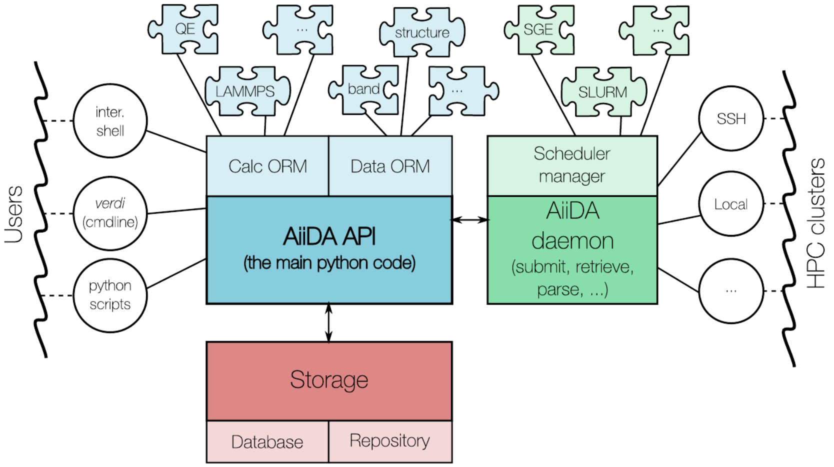

Fig. 2.5.: This sketch shows the components, API, daemon and storage of the AiiDA framework and their interaction. Components include the application programming interface (API) in blue, the AiiDA daemon in green interacting with computing resources and the storage handling in red. Connected plug-ins for calculations, data and schedulers are indicated through puzzle pieces. Figure reprinted from publication [63] copyright (2016), with permission from Elsevier.

structures and verdi command line extensions. Plug-ins are Python packages and can be shared with the public over the Python package index (PYPI [165]). Platforms like github [166], gitlab [167], or bitbucket [168] enable collaborative programming efforts on such open source packages.

For sharing (last ADES pillar) AiiDA provides import export features for simulation results plus data from the repository and the database. In addition sharing small SQL databases without AiiDA is easy, since there exist established commands and tools to do so.

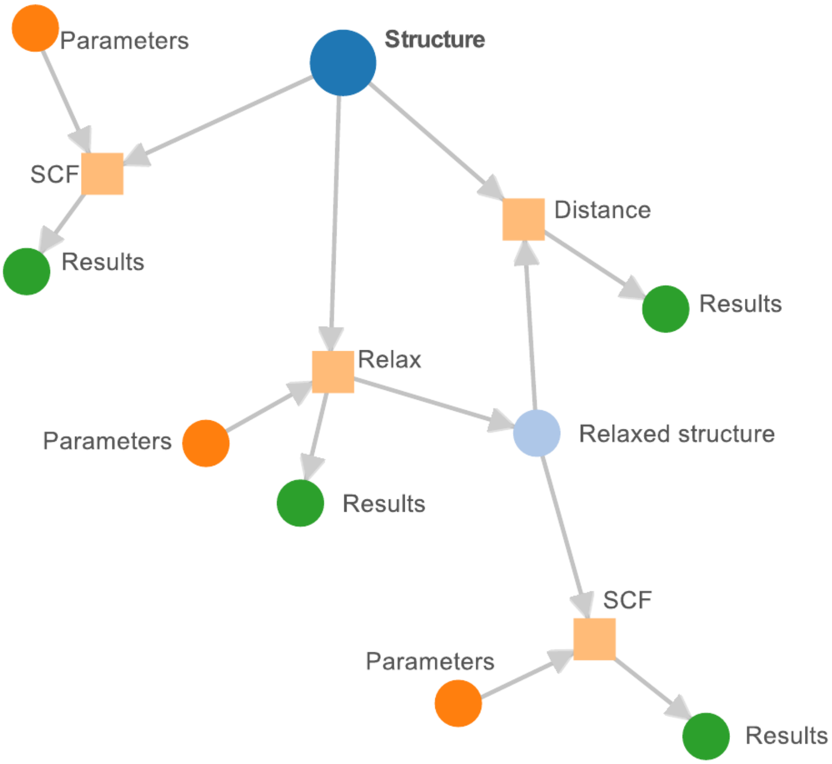

Fig. 2.6.: An example directed acyclic graph that demonstrates how the data provenance is kept in the database. All outputs (green result nodes) are directional connected via calculation nodes (squares) to the calculation inputs. Calculation inputs are structure nodes (blue) and parameter nodes (orange). Figure reprinted from publication [63] copyright (2016), with permission from Elsevier.

2.7.1. Plug-ins in AiiDA

Data structures and file formats of different programs differ a lot. In order to cope with this environment in computational science, AiiDA has a slim base core code and everything around it is organized in plug-ins, or apps. Plug-ins are designed, implemented and maintained by the individual developers in the community. Otherwise maintaining, updating and bug fixing all these individual interfaces would be impossible for a single scientific group. The AiiDA team provides templates for scheduler, command line, data, parser, workflows and calculation plug-ins. Besides these, also plug-ins for different storage back ends like other database software as PostgreSQL and object stores can be implemented.

In order to deploy a program with AiiDA at least a calculation plug-in and a parser plug-in have to be implemented. Parser plug-ins contain parsers for conversion of information from input/output files into data structures. These data structures are stored in the database. Calculation plug-ins tell AiiDA how to launch a calculation for the given code, i.e., how to create the needed code input from given data structures. Since there are several interfaces from external community standards (cif [169], VESTA file formats [170], .xsf XCrySDen file format [171], jmol, VASP input poscar, ASE and pymatgen structure objects) to basic AiiDA data structures, it is convenient to work with the already implemented data structures whenever possible. Though sometimes it is necessary, due to individual code requirements, to implement new data structures for AiiDA which are code or community specific. This is achieved through a data plug-in. Together all plug-ins and utility collection for a given program form an AiiDA extension package. In recent years such packages have been implemented for several well known electronic structure quantum engines (the Quantum Espresso package, VASP, `FLEUR`, Yambo, Siesta, Castep, CP2K, KKR, Lammps, nwchem, phonopy, wannier90, ...). The creation of the package for the `FLEUR` code is part of this work.

AiiDA itself is a rather general framework and not at all limited to material science. It just evolved out of the material science and electronic structure community. All extension package names are collected in the aiida-registry [172], which accounts for AiiDA extension name reservation to avoid collisions. From the registry AiiDA users are provided with a list of available plug-ins (24 in 2018), their content, how they can be installed and if they are compatible with each other in terms of requirements. On top of the registry it is straight forward to build an app store or software manager functionality in the future.

2.7.2. Scientific Workflows (Workchains) in AiiDA

A very powerful feature of the AiiDA framework is the ability to write, run and share workflows. AiiDA workflows/workchains are a way to automatically launch time consuming calculations that logically depend on each other without the user having to wait for each of them. The workflow developer can encode expert knowledge. AiiDA provides the developer with tools to ensure the provenance of data and logic. Workflows are very powerful protocols. Complex series of calculations can be launched through them with a small piece of Python code. In AiiDA, workflows can be submitted to the daemon (run in the background) or executed with ‘run‘ in the Python interpreter, blocking it throughout the whole workflow execution. AiiDA workflows can be made robust and fault tolerant. They allow for seamless integration of knowledge from others with Python. Anyone, also non expert users may deploy them. Workflows become more than advanced bash scripts. They can include expert knowledge about how calculations should be run and converged, reasonable parameters, optimal resource usage, automatic error treatment and restarts. Workflows can expose simple interfaces with optimized default values allowing deployment by non experts. Technically workflows are Python classes which inherit from an AiiDA API base workflow class (WorkChain, WorkFunction). This allows the workflow developer to use Python code and any packages he desires within the workflow. This freedom may be an advantage of AiiDA over other workflow capable frameworks.

```python
from aiida.orm import WorkflowFactory, load_group, Code
from aiida.work.launch import submit
fleur_eos = WorkflowFactory(’fleur.eos’)

inpgen = Code.get_from_string(’inpgen@otherhost’)
fleur = Code.get_from_string(’fleur@cluster’)

# presorted
crystal_strucs = load_group(label=’oqmd_strucs’).nodes.dbnodes
flapw_paras = load_group(label=’oqmd_paras’).nodes.dbnodes

for i,struc in enumerate(crystal_strucs):
    res = submit(fleur_eos, structure=struc,
                 calc_parameter=flapw_paras[i],
                 fleur=fleur, inpgen=inpgen)
```

Code Listing 2.1: Small Python code snippet to launch workflows for a set of crystal structures. This naive but powerful code example spawns a `FLEUR` equation of states workflow for each structure in the Open Quantum Materials Database (OQMD) resulting in over 8 million jobs to be managed by AiiDA in this case. These jobs will have different computation demand and may require different convergence strategies.

The example Python code in Code Listing 2.1 demonstrates how simple it becomes with AiiDA to launch a high-throughput project. Beforehand all structures (more than 800,000 entries) from the Open Quantum Materials Database (OQMD) [55] were imported into an AiiDA database. Then for each crystal structure a node with several specific FLAPW parameters was prepared. With this node some parameters are specifically adjusted beyond the `FLEUR` defaults. The launched workflow in this example could be interchanged with any other workflow exposing a similar Python interface. Furthermore, the code and the machine to run on plus optionally some maximum resources per job among other options have to be specified. With a simple 'for-loop' the user would launch in this code example an equation of states workflow for every crystal structure in the OQMD. This would result in over 8 million DFT self-consistency cycles submitted to some computing resource (in this case 'cluster') and managed by AiiDA. The code piece will execute quite fast (hours to days, depending on the workstation and database speed), but the managed resulting computing jobs of these spawned calculations will take over 10 years on a resource with a throughput of order two thousand jobs per day. It is obvious that this naive demonstrative example will probably result in a very high failure rate. A realistic high-throughput project has to be handled more carefully and more verbosely. Only if the error rate of the infrastructure and the software environment is sufficiently low, the throughput can scale up. It may also be necessary to split the project into smaller parts, to predict plus control the work load and to understand if the deployed quantum engine together with the workflows are robust enough for the project.

2.7.3. The AiiDA Community and the Python Universe

Keeping expert knowledge of the previous generation of scientists available in an adjustable individual high-level work environment is key to longterm progress and knowledge accumulation. AiiDA addresses this goal with its plug-in infrastructure and connectivity to any other Python tool. Why work with Python? Python is one of the world's most popular high-level programming languages today, which allows for very fast development. The Python package system allows for easy installation of software from the Internet through central servers like PyPI [165] and package managers like Pip [173]. The Python community developed advanced tools for writing (sphinx [174]) and hosting code documentation (Readthedocs [175]), style checking (Pylint [176]), unit testing (unittest from the python standard library or pytest [177]), debugging and notebook analysis (Ipython, Jupyter). Because of these capabilities and because Python is rather easy to learn, most software from the material informatics, data science and machine learning communities is written in Python or at least comes with a Python interface. Popular repositories useful for material science (and deployed within this work) are among many others Pymatgen [152], Atomic simulation environment (ASE) [64], Spglib [178], Matminer [179] and Seekpath [180]. Overall, with notebooks (like Jupyter-notebooks [181], Beaker [182], Apache Zeppelin [183]) one does not have to migrate completely to Python, since notebooks are capable of running all kinds of programming languages (not at peak performance) in their code cells. For interactive data visualization in the browser Java-script libraries are often preferable over Python. The developer of a complex scientific workflow can profit and build on the previous work in the community. Thus it is essential to be able to use any Python code or package inside a workflow. This freedom plus throughput scalability makes workflow engines like AiiDA or ASE more powerful compared to other, often graphical workflow tools or extensions with their own implementations like UNICORE [184–186], JuBE [187, 188], Kepler [189], pyiron [190] or others.

2.8. Machine Learning in Material Science

Machine learning in general is a useful toolbox to gain insight on data where the underlying correlations and rules [191–195] are unknown. If one has an analytic expression, rule or algorithm of a problem to produce the data and can apply it on the scale needed, it would not make sense to apply machine learning on this problem. Still in electronic structure theory, since calculations of larger systems are expensive or even impossible, it might make sense to train some machine learning model to predict certain results instead of running expensive *ab initio* simulation. This is especially the case for physical properties which depend only on the local environment in the system, because here the cost for the application of a machine prediction can be expected to scale with $\mathcal{O}(N)$, where N is the system size. Finding a good model or training a model might scale differently, depending on the algorithms.

Beyond this, machine learning methods are of course very helpful to extract knowledge from high-dimensional data, that our community faces [40, 50, 55, 60, 196–198] from theory and experiments. Experimental data is often rather scarce. Various machine learning stories in material science include: Predicting if a structure is a metal or insulator [199], mechanical properties [199, 200], glass formation [201], predicting crystal structures [31, 32, 148, 149, 202, 203], predicting stability [32, 200, 204], predicting nuclear magnetic resonance (NMR) chemical shifts [205, 206], thermoelectrics [24], critical temperatures of superconductors [26] or let the machine learning community on kaggle work on it like in the case of predicting transparent oxides [207]. Also research groups worldwide advancing software packages around machine learning specialized for material science like matminer [179].

Overall it is apparent that before knowledge can be extracted or helpful tools can be built there needs to be a large enough volume of high-quality curated data. Within this work tools and ways are laid out how this goal of generating larger data bases of high-quality all-electron data from *ab initio* methods might be accomplished. For example, with a large enough and diverse data set of core-level shifts, the prediction of chemical shifts of large structures and layered systems may become feasible.

2.9. X-ray Photoelectron Spectroscopy (XPS)

Photoemission spectroscopy (PES), where X-ray photoelectron spectroscopy (XPS) is a special form of, is based upon the photoelectric effect discovered in 1887 by H. Hertz [208] and theoretically explained by Einstein in 1905 [209]. Photons interacting with atoms can cause electrons to be emitted where the kinetic energy of these photo-electrons is given by:

$$E_{\text{kin}} = h\nu - E_{\text{B}} - \Phi_{\text{B}}, \tag{2.32}$$

where $h\nu$ is the energy of the incoming photon which gets lessened by the binding energy E_{B} of the electron and the work function Φ_{B}, which accounts for the energy needed of an photoelectron to leave the sample. The work function depends on the material and may also have an angle and surface dependence.

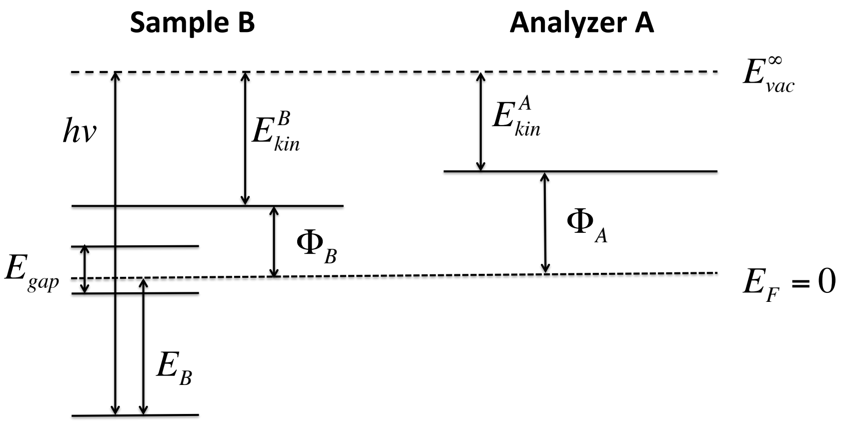

Fig. 2.7.: Visualization of the energy levels in the photoemission process of a sample B and an analyzer A. The energy level of a free electron E_{vac}^{∞} is per definition aligned between the analyzer and the sample. If the Fermi energy E_{F} of the detector aligns with the Fermi energy of the sample through electrical contact, the binding energy E_{B} depends only on Φ_{A} and E_{kin}^{A}. For materials with an energy gap at the Fermi energy, measurements and simulations of binding energies are more challenging. (Figure motivated by [210].)

In Fig. 2.7 the relevant energy level of the photoemission process are shown for a sample B and an analyzer A. The energy level of a free electron E_{vac}^{∞} is per definition aligned between the analyzer and the sample. The binding energy, E_B, is measured in reference to the Fermi energy E_F. As long as the work function of the spectrometer Φ_A is larger then the work function of the sample Φ_B and the Fermi energy E_F of the detector aligns with the Fermi energy of the sample through electrical contact, the binding energy E_B becomes $E_\mathrm{B} = h\nu - E^{A}_\mathrm{kin} - \Phi_\mathrm{A}$ and thus independent of the work function Φ_B of the sample. For non-metals the Fermi energy reference may pose a challenge [210] since impurities and charing effects change the Fermi energy reference within the band gap E_gap.

While photoemission is a charged excitation process there exist also a variety of neutral excitation processes. Depending on the application several photoemission spectroscopy techniques have been developed: ultra-violet spectroscopy (UPS) for valence band spectra, angle-resolved photoemission (ARPES) for band structures measurements and others [76, 211].

The detailed quantum-mechanical description of general photoemission is complex, because the photoemission process involves the excitation of electrons in matter up to ionization via the interaction with photons. These excited electrons have to leave the sample in order to be detected by a detector, making electron transport play an important role in the process. The photoelectrons and their corresponding core-holes in the solid with lifetimes of femto seconds trigger a response from the electronic system, leading to so called 'final-state' effects. Final-state effects and energy loss features include core-hole screening effects, charge transfer, plasmon excitations leading to additional rather broad peak structures, other relaxation processes leading to satellite peaks, variable cross sections, different core-level-line intensity ratios and lifetime effects like Coster-Kronig [212, 213]), shake-up and shake-off of the valence electrons might lead to asymmetric peak shapes, background or additional peaks. Screening effects might lead to additional splittings (multiplet-splittings) of core-level lines, especially for magnetic systems. Contributions from Auger processes are also seen in XPS spectra. A complete description of all this is essentially a time-dependent quantum many-body problem which requires the inclusion of classical or quantum electro dynamics terms. Other X-ray scattering processes contribute to the spectral background. In the literature are several approximations to the photoemission process introduced. The sudden approximation [214, 215] assumes that the primary excitation happens sudden relative to the adjusting of the electron cloud, from this certain matrix element can be neglected. Depending on the level of the approximation there is the one-step [216], or the three-step model [217, 218] of photoemission. Initial-state approximations use ground state properties of the system and neglect final-state effects. It is beyond the scope and interest of this thesis to cover the theory of photoemission in detail, the interested reader is referred to [76, 210, 219, 220]. For the core-level shifts of binary metals we used an initial-state approximation.

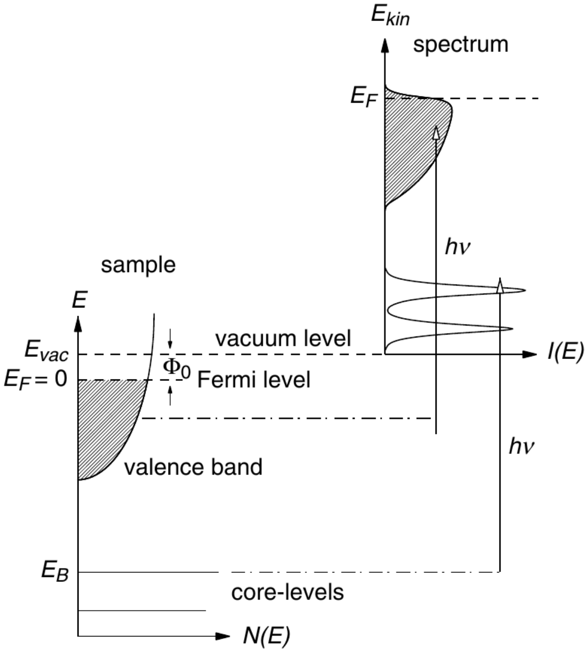

Fig. 2.8.: Schematic single particle view of photoemission spectroscopy (figure from [75]), showing how the density of states corresponds approximately to a measured spectrum. Electrons from the sample with a certain binding energy are excited by photons with sufficiently high energy $h\nu$ into the vacuum and measured by the analyzer. Core electrons from the sample correspond to sharp peaks in the measured spectrum.

A simple schematic of photoemission spectroscopy is shown in Fig. 2.8. Exciting core electrons result in rather narrow peak structures while excitations from the continuous valence states will lead to a more continuous structure in the measured spectrum. The response of valence electrons does not correspond simply to the density of states of the system. Since the focus of this work lies on the chemical interpretation of high-resolution X-ray photoemission spectroscopy of electronic core-level states, we restrict ourself to core-level XPS.

X-ray photoelectron spectroscopy (XPS) also known as electron spectroscopy for chemical analysis (ESCA) is a well known spectroscopy technique for chemical analysis developed since the 1960s. It is in widespread use in research and industrial applications [6] [75–77, 221]. XPS is

---

[6] User list of SDP software in 2004 `https://www.xpsdata.com/user_list_2004.htm`, wikipedia `https://en.wikipedia.org/wiki/X-ray_photoelectron_spectroscopy`,

applied to measure the empirical formula, the electronic state and chemical state of elements contained within the surface area of a sample. The surface sensitivity, originates from the fact that the mean free path of electrons in a material is 1 to 10 nm [222–225], which limits the information depth. The penetration depth of X-ray photons with an energy of 1.5 keV is about 1 to 10 µm [226]. Compared to XPS other surface science methods like X-ray diffraction (XRD) or Rutherford backscattering (RBS) have a 100-1000 fold deeper information depth of several μm. A collection of surface science spectroscopy and microscopy methods is found in [76]. While the extraction of the empirical formula from XPS is most of the time rather straight forward, the chemical interpretation of high-resolution XPS data is often a challenge [78].

The different intensities of the core-electron lines arise strongly from the elemental and orbital depended photoelectron cross-sections. H and He are not directly detectable by XPS, because of their small cross-section for the energies of common X-ray sources. Depending on the chemical environment of the element the core-level peaks shift in their binding energy. These shifts are called chemical shifts, or core-level shifts (CLS) and are of interest because they allow for a chemical interpretation of the system. Chemical shifts do not corresponds to a simple picture of transfered charge between elements due to differences in electronegativity [210].

For an XPS measurement usually ultra-high vacuum ($< 10^{-9}$ mbar) is required to reduce scattering events of electrons with gas particles. In addition, the surface should be fairly empty of adsorbates which might influence the results. Nowadays, there are first ambient pressure XPS systems for some use cases on the market [227, 228]. In Fig. 2.9 the schematic setup of an XPS experiement is shown plus a photograph of a ultra-high vacuum setup for XPS analysis from the IEK-4 of the Forschungszentrum Jülich. From a monochromatic X-ray source photons with energy $E = h\nu$ (for an Al-K$_\alpha$ source E =1486.6 eV, FWHM 0.1 eV) hit the sample under a certain angle ψ. The analyzer collects only electrons exiting the sample at angle Φ within a maximum entrance angle α_{max} and with a kinetic energy according to the photoelectric effect of equation 2.32. The binding energy axis is usually calibrated by measuring and aligning the Au-4f, Ag-3d, Cu-2p, Cu-3p peaks or other narrow known high intensity lines. Through this the work function of the spectrometer (Eq. 2.32) is effectively calibrated out, i.e. set to zero. The analyzer samples the energy of the electrons, by reducing E_{kin} with an internal applied electric field that only electrons with the pass energy E_{pass} are counted at the detector. The setup in the IEK-4 uses a monochromatic aluminium K$_\alpha$ radiation source MX 650 from VG Scienta and a half spherical analyzer from Scienta (R4000

---

user list CasaXPS `http://www.casaxps.com/links/academic_site_licenses.htm`

L2), with an energy resolution as a function of the pass energy [230]

$$\Delta E = \left(\frac{w}{a+b} + \frac{\alpha_{\mathrm{max}}^2}{4} \right) E_{\mathrm{pass}} \tag{2.33}$$

where w is the width of the entrance aperture, α_{max} the entrance angle and a, b are the inner and outer radii of the analyzer. From this arises a trade-off between resolution and signal intensity. The highest practical energy resolution of such a system lies around 0.2 eV for XPS [230]. The resolution also becomes limited by the natural line width of about 0.16 eV of the Al-K_α line [231]. With higher quality and intensity of monochromatic light sources like synchrotron radiation the resolution can be better.

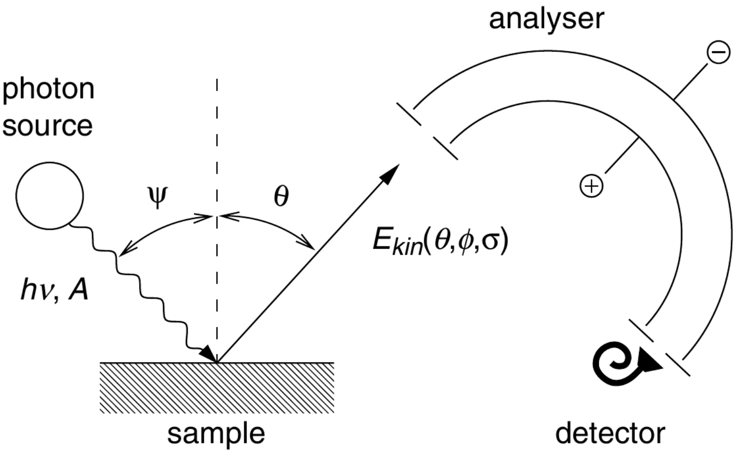

(a)

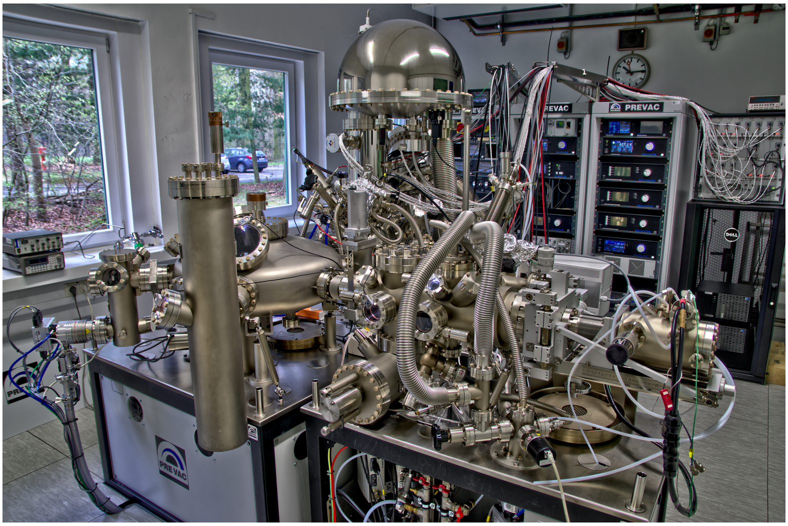

(b)

Fig. 2.9.: Schematic drawing of an XPS experiment is shown in (a) from [75]. An X-ray photon source emits towards a sample, the outgoing photoelectrons are collected and their kinetic energy is sampled by a half spherical analyzer. The photograph in (b) shows the experimental setup with XPS analysis chamber at the IEK-4. For detailed information see [229]. (Photo taken by Tobias Wegener.)

2.9.1. Current Chemical Interpretation of XPS

Different information on a sample is obtainable from XPS spectra. While information of the elements present and their quantity is rather straight forward from a survey XPS spectrum, a detailed chemical interpretation of the exact phase content from a high-resolution XPS spectrum is still a challenge. Usually, in order to do so a multi-peak-function fit including a background function which best approximates the spectral data has to be found first. The fit results may depend on the scientist fitting the spectrum and on his experience [232, 233]. Also it makes a difference if the spectral background fit is adjusted consistently in the fitting procedure [234].

The fit is conducted with statistical methods like least squares, maximum likelihood or others. Notice, that a fit does not correspond to a deconvolution of the spectrum. Finding a good fitting curve is usually not a challenge, while the interpretation of the fit can be hard or the fit may even be unphysical. A variety of standard tools exist to help with the mathematical fitting and justification, among others UniFit [234, 235], CasaXPS [236], SDP [237] and MultiPak [238]. Often Voigt profiles are chosen as peak functions, but in some cases fitting with asymmetric peak functions is necessary. Voigt profiles (Eq. 2.34) are a convolution of a Lorentzian and a Gaussian (Eq. 2.35). The Lorentzian part originates from the usual excitation shape of a process decaying exponential in time from Fermis golden rule [239, 240] broadened by the finite lifetime of core-holes. The Gaussian part accounts for all contributions of additional broadening effects. Broadening effects arise from the natural line-width of the monochromatic photon source (~0.16 eV) [231], the energy resolution of the analyzer, vibrational effects and other sources [218].

$$V(x,\mu,f_{\mathrm{G}},f_{\mathrm{L}}) = G(x-\mu,f_{\mathrm{G}}) \circledast L(x,f_{\mathrm{L}}) = \int_{-\infty}^{\infty} G(x'-\mu,f_{\mathrm{G}}) \cdot L(x-x',f_{\mathrm{L}})dx' \tag{2.34}$$

where the Gaussian G and Lorentzian L are given by

$$G(x-\mu,f_{\mathrm{G}}) = \frac{1}{f_{\mathrm{G}}\sqrt{2\pi}} e^{\frac{(x-\mu)^2}{2f_{\mathrm{G}}^2}} , \quad L(x,f_{\mathrm{L}}) = \frac{f_{\mathrm{L}}}{\pi((x)^2+f_{\mathrm{L}}^2)} \tag{2.35}$$

A Voigt profile $V(x,\mu,f_{\mathrm{G}},f_{\mathrm{L}})$ (Eq. 2.34) has three free parameters, the position μ, Lorentzian broadening f_{L} and the Gaussian broadening f_{G}. The area under a Voigt profile is normalized to one.

When fitting XPS spectra for a certain binding energy region with several Voigt profiles the Lorentzian broadening f_{L} and the Gaussian broadening f_{G} can often be kept the same for all profiles and varied as two fit parameters. Additional the profile positions are optimized each and the area under each peak, which translates into fitting the peak height in most routines. In total this amounts to $N_{\text{fit}} = 2 + 2 \cdot N$ fit parameters for N Voigt profiles. When fitting multiplets, like $4f_{5/2}$ and $4f_{7/2}$ states, constraints on the peak positions can be built into the fit due to an assumed constant peak splitting and on the peak areas by fixing area ratios. Therefore, to fit doublets more peak functions (N) are needed but the number of total fit parameter required reduces to $N_{\text{fit}} = 2 + N$ with the assumptions above. In the case of asymmetric peak shapes additional fit parameters for the asymmetry of the peak function are introduced. Asymmetric peak shapes arise from valence band shake-offs. The theoretical asymmetric form of a main line peak was investigates by Doniach and Sunjic [220]:

$$DS(x-\mu,\alpha,f_{\text{d}}) = \frac{\cos\left[\frac{\pi\alpha}{2} + (1-\alpha)\arctan\left(\frac{x-\mu}{f_{\text{d}}}\right)\right]}{\left(f_{\text{d}}^2 + (x-\mu)^2\right)^{\frac{(1-\alpha)}{2}}}, \tag{2.36}$$

where μ is the position of the main line, f_{d} is a broadening parameter and α tunes the asymmetry. For $\alpha = 0$ the Doniach-Sunjic (DS) shape becomes a Lorentzian. Notice, that the peak maximum of the DS shape is not exactly at μ and depends on α [220]:

$$(x-\mu)_{\text{DS, max}} = f_{\text{d}} \cot\left(\frac{\pi}{2-\alpha}\right). \tag{2.37}$$

The tail of this profile is non-zero for energies far away from the main line, making the profiles area infinite. This leads to fitting problems, since the tail contribution of this form has to be adjusted with the background.

To overcome this problem, other asymmetric peak shapes with finite areas are introduced. A commonly applied [78, 241] shape is an asymmetric Lorentzian convoluted with a Gaussian (LA):

$$LA(x,\mu,f_{\text{L}},f_{\text{G}},\beta,\alpha) = G(x,f_{\text{G}}) \circledast AL(x-\mu,f_{\text{L}},\beta,\alpha) \tag{2.38}$$

$$AL(x-\mu,f_{\text{L}},\alpha,\beta) = \begin{cases} [L(x-\mu,f_{\text{L}})]^{\alpha} & x \le \mu, \alpha \ge 1.0 \\ [L(x-\mu,f_{\text{L}})]^{\beta} & x > \mu, \beta \ge 1.0 \end{cases} \tag{2.39}$$

$$L(x-\mu,f_{\text{L}}) = \frac{1}{4\left(\frac{x-\mu}{f_{\text{L}}}\right)^2 + 1} \tag{2.40}$$

where α and β (≥ 1.0) are parameters for the asymmetric form of the Lorentzian $L(x-\mu, f_{\text{L}})$ of height one at position μ with a full-width half-maximum f_{L}. The fixed height ensures the continuity of the AL function. The AL peak shape is fitted with three to four parameters and has a similar tail as the DS profile, but with a finite area. For curve fitting of transition metal peaks the asymmetric Lorentzian (AL) is convoluted with a Gaussian $G(x, f_{\text{G}})$ with FWHM f_{G} forming the LA peak shape.

For the background of a spectrum the most commonly used fit functions are the Shirley [242, 243] and the Tougaard background [244, 245] functions, also a linear background or

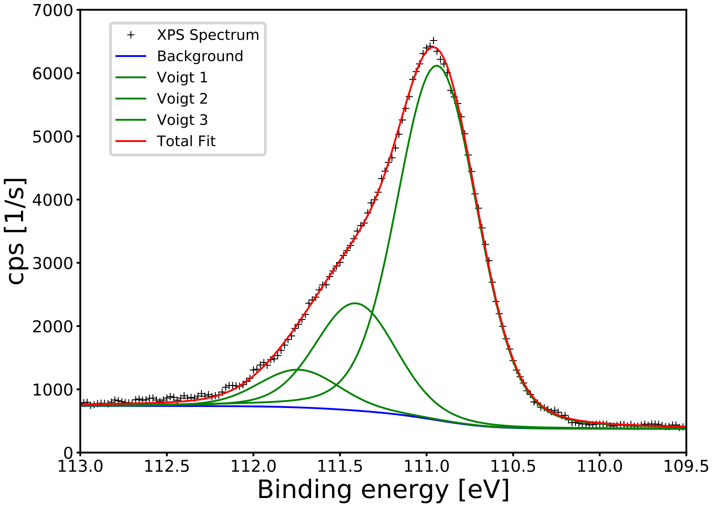

Fig. 2.10.: This figure showns the result of a common fitting procedure. Three Voigt profiles had to be included in order to achieve good agreement with the data points. For the background estimation the Shirely method was applied. The data and fit performed with UniFit are taken with permission of the author from [229].

others functions are sometimes applied [246]. The iterative Shirley background is a special type of Tougaard background and has the form [243]:

$$S_{\mathrm{i}}(E) = k \int_{E}^{\infty} (j(E') - S_{\mathrm{i}-1}(E') dE' \tag{2.41}$$

where $S_{\mathrm{i}}(E)$ is the background at iteration step i and energy E, k is a constant and $j(E')$ is the measured spectrum corrected by other non inelastic loss effects. The initial background S_0 is assumed to be a constant.

An example fit to an experimental XPS spectrum with three Voigt profiles and a Shirley background is shown in Fig. 2.10.

After a successful fit has been found, the fit results have to be interpreted. For the interpretation the positions of the individual peaks have to be related to known positions of possible phases in literature or reference single crystal spectra. This part often fails for several reasons. First, literature data is scarce. The NIST XPS database [90] contains entries for around 6,300 systems, of which 3,000 are oxides and 2,700 contain carbon. The NIST database provides

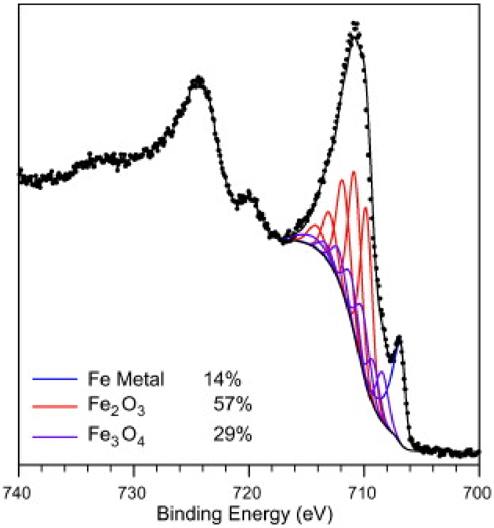

Fig. 2.11.: Interpreted XPS spectra of an Fe-O system with asymmetric peak shapes from Biesinger et al. [78] investigating Fe-based nano particles on a glass substrate. The interpretation was done by fitting Fe-O phases and reusing their fit parameters for mixed systems. This evaluation represents the state of the art. The figure is reprinted from publication [78] copyright (2010), with permission from Elsevier.

28,000 binding energies of which 15,700 are unique plus 7,500 unique core-level shifts. There are other sources for data reviewed by B. Crist in [247], which includes a licensed database with 70,000 non-unique spectra [237] and books [226]. Second, in order for literature data to be accurate enough the energy scales have to be calibrated carefully and other information of the X-ray source and analyzer (resolution, uncertainties) needs to be available. If this is not the case or unclear, it leads to large uncertainties and spread in the data [248]. Third, other effects in XPS spectra need to be accounted for before the fitting procedure or within it like including known satellite positions, plasmons, or other spectral contributions. If the investigated sample was not a metal, it may be necessary to correct the energy scale for charging effects of the sample. Additional data from other surface science methods, like XRD, may support and constrain the spectrum interpretation. Overall, this chemical evaluation way is probably fundamentally limited and only applicable to the simplest material phases. The fundamental limitation arises in detail from the fact that the sum of two (peak) localized functions at different energies lies not in the same (peak) function space. The sum of each unique chemical environment contributes with a different intensity weight to the spectrum.

This makes a fitting with no assumption approach nearly arbitrary for materials (mixtures) with several chemical environments close by. Also binding energies and therefore also binding energy shifts are not unique, since similar chemical environments of an element can exist in different materials. For molecules it is known that sometimes the different C 1s core-level shifts are identifiable by their separated positions and their intensities [249, 250].

With the help of experimental high-resolution reference spectra for certain pure phases it is also partially possible to determine not only phases present but also relative amounts of each phase as demonstrated in [78] for first row transition metals, oxides and hydroxides of Cr, Mn, Fe, Co and Ni. Such a spectrum from the work of Biesinger et al. is shown in Fig. 2.11. Fitting spectra with such complexities is state of the art.

It is known from [251] that satellite positions and intensities do not have to be the same for different chemical environments of the same element. Though it is possible to calculate satellite positions and intensities from *ab initio* [252] or cluster model calculations [251]. Overall, it should be clear that a in detail full chemical interpretation of high-resolution XPS spectra of complex systems is hard and leads often to incomplete evaluations and guesses. A different approach for the chemical analysis of XPS driven by *ab initio* data is discussed in section 3.2.

2.9.2. Quantities for XPS from *ab initio* Simulations

It has been pointed out above that absolute core-level binding energies (BE) and their chemical shifts (CLS), not to be confused with chemical shifts of nuclear magnetic resonances, are valuable for understanding the chemistry of a system. Through the shifts in binding energy chemical phases can be identified. Literature CLS data for materials systems are often rare, and experiments to produce reference data are expensive and time consuming. Without reference data the phases can hardly be identified, making this a kind of chicken and egg problem for complex materials. The data issue could be solved with first principles methods through high-fidelity workflows, by performing high-throughput calculations on every material of interest and deploying machine learning beyond that.

The calculated chemical shifts and binding energies for chemical interpretation need to have a comparable total accuracy of ≈0.1 eV to experiments. Furthermore, the predictions of doublet and multiplet splittings needs to be very exact ≈0.01 eV in order to be useful for fitting and comparing with experiments.

To calculate core-level shifts one needs a method treating all-electrons, including the core electrons, or at least the electrons for the main core-level line of interest. Other approximations for non all-electron methods like the Z+1 [253] approximation or frozen core are not precise enough for core-level shifts [210]. In chemistry and solid state physics scientists have worked on predicting these values and photoemission spectra since the availability of high-resolution XPS measurements [210, 254, 255].

Focusing on *ab initio* methods, there are several methods capable of doing so, with growing computationally hardness as they include more physics and effects of the many-body system ('final state' effects). To save computing resources one wants to use the cheapest method within its scope of application and then climb up the ladder of complexity if necessary.

2.9.2.1. Initial-state Approximation

A rather simple way to calculate core-level shifts ($\Delta E_{\mathrm{B},n\ell j}$) is by comparing the Kohn-Sham energies with respect to the Fermi energy of a standard DFT self-consistent-field ground-state calculation of a system (2) with the respective Kohn-Sham energy in the elemental reference system (1).

$$\Delta E_{\mathrm{B},n\ell j} = \epsilon_{1,n\ell j} - \epsilon_{2,n\ell j} \tag{2.42}$$

where $\epsilon_{1,n\ell j}$ is the Kohn-Sham energy of an atom-type in system 1 of the core-state specified by the quantum numbers n, ℓ, j or other quantum numbers in the full relativistic case with orbital moment and crystal field. Since system 1 and reference system 2 are both in the ground state, this corresponds to an initial-state approximation, neglecting any final-states effects.. This approximation is expected to work for metals as the Fermi energy can be determined and for a grounded sample the reference energy for binding energies in experiments is also the Fermi energy. This approach is reported to be used by several *ab initio* programs [210, 255, 256]. For non-metal systems this approach is expected to give only good results for the relative shifts between different atom-types in the structure since the reference energy is the same. Finding a global reference energy between different phases and to experiment is a challenge here. Also any final-state influences are not included in this approximation.

Influences of FLAPW parameters on Kohn-Sham core-level energies for the `FLEUR` program have been investigated in [257] (section 3.1.3 'Core Level Dependencies' and section 3.1.4). There it was pointed out that the Kohn-Sham energies converge before the charge density is converged and that they depend substantially on the muffin-tin radius and the basis cutoffs. The dependence on the muffin-tin radius varies for individual core levels but this variation can be minimized by calculating with enough (>900) grid points within the muffin-tin spheres. Spin-orbit coupling leads to a constant shift in the Kohn-Sham core-level energies. In contrast a slight increase in cell volume within a ±2 % range has a linear dependence on the Kohn-Sham energies of 100 meV per percent volume change. In [257] it was concluded that the core-level shifts can be converged with respect to the FLAPW parameters within an accuracy below 100 meV, making them comparable to experiments. For this accuracy it is best to choose the same muffin-tin parameters for an element. This was shown for the W 4f core levels of the Be_2W system. Inclusion of spin-orbit coupling lead to a 1%, 10 meV offset for the 4f core-level shifts of W. These findings allow for automation of accurate core-level shift calculations on different structures.

In [132, 258] it was shown that dependencies on the muffin-tin radii can be further reduced by modifying the FLAPW basis set and including more higher local orbitals. This also decreased dependencies of Kohn-Sham energies. It was confirmed for several systems and different core-levels that their core-level shifts can be converged to high accuracy with the FLAPW basis set and independent of FLAPW parameters, if they are the same and reasonable.

2.9.2.2. Binding energies from Core-hole Calculations

Kohn-Sham energies themselves are far off from experimental binding energies and not directly comparable. Absolute binding energies can be calculated with standard DFT via a core-hole calculation. The electronic structure can be relaxed within the presence of core-hole to mimic the 'final state'. Such a core-hole can be calculated as a neutral excitation, i.e. placing the electron in the valence band, or the electron is removed leaving a charged system. To account for induced magnetism of a core-hole, a spin-polarized calculation should be performed. The response to the core-hole accounts for some screening effects of the electron cloud. The binding energy $E_{\mathrm{B,i},n\ell j}$ is calculated as the difference of total energies of systems with a core-hole $E_{\mathrm{tot,1,ch}}$ and without $E_{\mathrm{tot,1}}$.

$$E_{\mathrm{B,i},n\ell j} = E_{\mathrm{tot,1}} - E_{\mathrm{tot,1,ch}} \tag{2.43}$$

From the difference of binding energies ($E_{\mathrm{B,1}}, E_{\mathrm{B,2}}$) a chemical shift $\Delta E_{\mathrm{B},n\ell j}$ can again be estimated.

$$\Delta E_{\mathrm{B},n\ell j} = E_{\mathrm{B,1}} - E_{\mathrm{B,2}} \tag{2.44}$$

These calculations are computational more demanding as for the `FLEUR` program they require super-cell setups in order to converge the binging energies. This is so because the results depends on the number electrons available for the screening, i.e the core-hole impurity density should be small. In order for the core-level shifts to be on the same accuracy level, the binding energies need also be as accurate as 100 meV. This approach is referred to in the literature as ΔSCF.

Oxides, or insulators with a large bandgap are in general from a DFT point in various ways harder to treat correctly. First, oxides come often in a rich phase space (>5 phases), with different configurations, environments and disorder, oxides usually do not grow as single crystals but in multiple configurations. This makes it hard in the first place to chose what to calculate and to decide how to compare to experimental results. Second, oxides are sometimes at the boundaries of applicability of standard DFT functionals, since the bandgap is underestimated and possible strong electron correlations are not accounted for correctly. Calculating with advanced functionals or other methods make comparison of total energies less rigorous. Longer core-hole lifetimes and hole-electron interactions in insulators lead to possible significant excitation effects, matrix effects, final-state features in the spectra, which need to be treated correctly in the method and are beyond standard ground-state DFT. High quality XPS data of insulators are also experimentally harder to obtain, because of sample charging effects which need to be accounted for in the right way. When comparing to theory there is also the problem with the energy reference.

2.9.2.3. Beyond standard DFT and the `FLEUR` Program

Beyond the initial-state and core-hole calculation in standard DFT there exist various computationally more demanding *ab initio* methods to calculate optical responses of a system and time-dependent processes. They are especially required to describe the response of the valence electrons to a strong perturbation or driving force more accurately. These methods can to some extent predict the influence or importance of matrix elements. Most of these methods are state of the art and currently applicable to systems smaller than 100 atoms since have a scaling which is worth than cubical with the system size.

The GW-approximation (GW) [259] is a green function based method which includes explicit many-body effects useful to retrieve response function like the spectral function, or the dielectric function. Core-levels can also be included in GW and absolute binding energies have been calculated within an accuracy of 0.3 eV in [260]. This accuracy might not be accurate enough to compare to experiments.

In time-dependent density functional theory (TDFT) [261] processes can be calculated with DFT over time, allowing for the calculation of processes like photoemission.

To describe the electronic response of neutral excitation more accurately one can solve the Bethe–Salpeter equation (BSE) [262]. By this exciton peak positions, form and magnitude and influence on the electronic structure can be predicted [263, 264], or whole X-ray absorbtion spectra (XAS).

3. Method Development

Some selected results of the method development part of this work are presented in this chapter. One section describes the AiiDA-FLEUR package, which connects the FLEUR code to the AiiDA framework and the developed workflows and Python utilities. Another section deals with the first implemented steps towards a full turn-key solution for the automatic evaluation of well-behaved X-ray photoemission spectra from *ab initio* results.

3.1. The AiiDA-FLEUR Package

The AiiDA-FLEUR Python package[1] enables the usage of the all-electron DFT code `FLEUR` [79]) with the AiiDA framework [63, 156]. The package contains AiiDA plug-ins for the `FLEUR` code itself, its input generator (`inpgen`) and a data structure representing the `FLEUR` input. Furthermore, it contains workflows, property calculator protocols and utilities to create a high-level work environment. The package contains over 6000 lines of Python code, is open source under MIT license and is released on github and PyPI (the Python package index). The package was developed as part of the MaX EU Center of Excellence [265] contribution from the Forschungszentrum Jülich GmbH, (IAS-1/PGI-1), Germany. Since the development of other Python packages for other juDFT codes[2], AiiDA independent utilities were moved to

---

[1] Code: `https://github.com/JuDFTteam/aiida-fleur`
Documentation: `https://aiida-fleur.readthedocs.io`

[2] `https://github.com/JuDFTteam/`

the separate 'masci-tools' (material science tools) repository[3]. This ensures the reusability of file readers, utilities, visualizations and parsers for other purposes, tools and packages. The AiiDA-FLEUR package ships with the plot function *plot_fleur* to quickly gain a default visualization of any database node or nodes produced by `FLEUR` calculations or workflows. Please note that the version of AiiDA-FLEUR (0.6.3) discussed within this work is compatible with AiiDA versions <1.0, since most of the results of this work are produced with this version. For AiiDA versions >1.0 the API is slightly different and AiiDA-FLEUR versions >1.0 have to be used.

3.1.1. Plug-in Layouts

In the following subsections the two individual code plug-ins and the data plug-in of the AiiDA-FLEUR package are presented in more detail. AiiDA calculation plug-ins, as fundamental building blocks, contain instructions on how to create valid input from information in the database and what information to parse from output files and to store in the database. Provenance direct acyclic graphs of data nodes and calculation nodes show what input nodes are needed for a calculation and what output nodes are produced. The calculation plug-ins form the basic building blocks of more complex AiiDA provenance graphs of workflows and a whole provenance network of simulation data. Python code usage examples and details on the output node contents in the database are presented additionally within this section.

3.1.1.1. `FLEUR` Input Generator Plug-in

The input generator plug-in is capable of running the `FLEUR` input generator (`inpgen`) with most of its features. Features like crystal structure modification or creation are not supported on purpose, because they would allow for breaking the data provenance. To initialize a *FleurinputgenCalculation* it is enough to provide a *StructureData* node and a *Code* node as shown in Fig. 3.1. From these inputs a *FleurinputData* object with default FLAPW parameters will be created. Alternatively to the default FLAPW parameters one can provide an additional *ParameterData* node as input with the corresponding parameters. A successful *FleurinputgenCalculation* creates four output nodes in the database. The *FleurinpData* node represents the input files for a *FleurCalculation*. The *RemoteData* node points to the folder where the calculation was run and the *Folder* node points to a local folder like object containing all the retrieved files from an `inpgen` run. Retrieved files include the `FLEUR` input file 'inp.xml', the `inpgen` output file 'out', an 'shell.out' file containing piped shell output and an 'out.error' file with the piped standard error stream.

---

[3] `https://github.com/JuDFTteam/masci-tools`

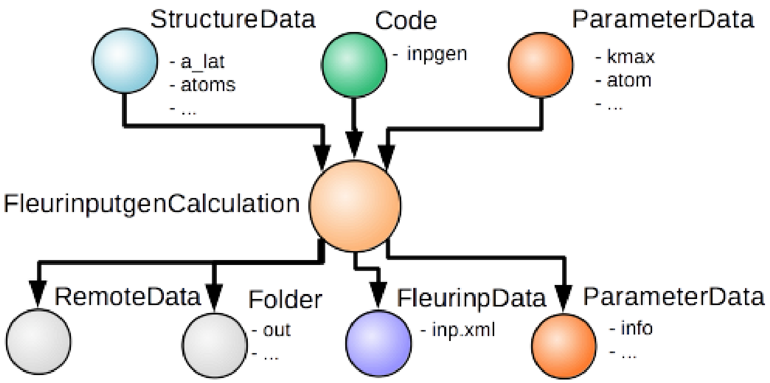

Fig. 3.1.: Database input and output nodes in the directed acyclic provenance graph for a single run of the input generator `inpgen`.

3.1.1.2. `FLEUR` Calculation Plug-in

The calculation plug-in for the `FLEUR` code allows for deployment of the code through AiiDA. Fig. 3.2 shows a node graph of a *FleurCalculation*. Input nodes are a *Code* node, a *FleurinpData* node and an optional *RemoteData* node from a previous parent *FleurCalculation* to continue from its output results. In the *ParameterData* output node of a *FleurCalculation*

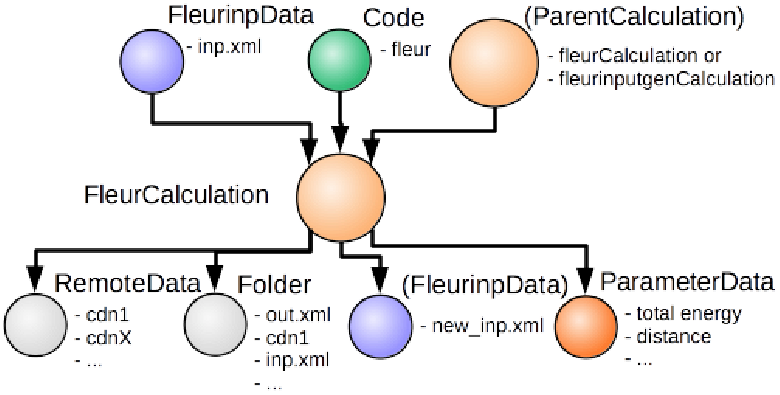

Fig. 3.2.: Database input and output nodes in the directed acyclic provenance graph for a single run of the `FLEUR` code.

basic calculation results are stored, for example the total energy, Fermi energy, band gap, charge distance and meta data information of a single `FLEUR` run.

```
print(fleuroutputnode.get_dict())
{"bandgap": 0.0061037189, "bandgap_units": "eV",
"charge_den_xc_den_integral": −650.251477273, "charge_density1": 9.4019e−06,
"charge_density2": 9.5578e−06, "creator_name": "fleur 27",
"creator_target_architecture": "GEN", "creator_target_structure": " ",
"density_convergence_units": "me/bohr^3", "energy_valence_electrons": −4.20135128,
"end_date": {"date": "2018/08/08", "time": "09:47:40"}, "energy": −879603.931538445,
"energy_core_electrons": −19771.3543364295, "energy_hartree": −32324.8485355339,
"energy_hartree_units": "Htr", "energy_units": "eV",
"fermi_energy": 0.6050871733, "fermi_energy_units": "Htr", "force_largest": 0.0,
"magnetic_moment_units": "muBohr", "magnetic_moments": [0.0105619536, −0.0026848541],
"magnetic_spin_down_charges": [4.8629403112, 4.6137500971],
"magnetic_spin_up_charges": [4.8735022647, 4.611065243],
"number_of_atom_types": 2, "number_of_atoms": 2, "number_of_iterations": 26,
"number_of_iterations_total": 26, "number_of_kpoints": 156, "number_of_species": 1,
"number_of_spin_components": 2, "number_of_symmetries": 8,
"orbital_magnetic_moment_units": "muBohr", "orbital_magnetic_moments": [],
"orbital_magnetic_spin_down_charges": [], "orbital_magnetic_spin_up_charges": [],
"output_file_version": "0.27", "overall_charge_density": 1.88766e−05,
"parser_info": "AiiDA Fleur Parser v0.1", "parser_warnings": [],
"spin_density": 1.7792e−06, "start_date": {"date": "2018/08/08", "time": "09:46:17"},
"sum_of_eigenvalues": −19775.5556877095, "title": "A Fleur calculation with aiida",
"unparsed": [], "walltime": 83, "walltime_units": "seconds",
"warnings": {"debug": {}, "error": {}, "info": {}, "warning": {}}}
```

Code Listing 3.1: Database content of the *ParameterData* output node of a *FleurCalculation*. The node is a dictionary contaning key value pairs. Unit information of values are given by a seperate key with the same name plus a '_units' suffix.

In Code Listing 3.1 such parsed content of a *ParameterData* output node is shown. It contains relevant meta information to understand what was going on in the simulations and should answer the following questions: What system was calculated? Did the calculation succeed? How far did it converge? How long did it take? Have warnings or errors of any kind occurred? In certain run modes of `FLEUR` which change the crystal structure in the calculation, i.e., by execution of relaxation steps, a *FleurinpData* node corresponding to the new input files with the output crystal structure will be returned by a *FleurCalculation*.

Code Listing 3.2 presents a minimum Python code example to run a *FleurinpgenCalculation* with a subsequent *FleurCalculation*. One has to import all relevant Python classes and functions. AiiDA *Factory* methods allow for loading classes from their entry point names. This way the user does not have to remember from where plug-in Python classes have to be imported. All input nodes for the calculations have to be loaded from the database, which were prepared beforehand. To launch a calculation the class and all the input nodes have to be

```
from aiida.orm import load_node, Code, CalculationFactory
from aiida.work.launch import run

inpgen_calc = CalculationFactory(’fleur.inpgen’)
fleur_calc = CalculationFactory(’fleur.fleur’)

inpgen = Code.get_from_string(’inpgen@localhost’)
fleur = Code.get_from_string(’fleur@localhost’)

# prestored Structure and parameters
crystal_struc = load_node(<pk>)
flapw_para = load_node(<pk>)

res = run(inpgen_calc, structure=crystal_struc,
          calc_parameter=flapw_para, inpgen=inpgen)

fleurinp = res.get(’fleurinp’, None)
res_fleur = run(fleur_calc, fleurinp=fleurinp, fleur=fleur)
```

Code Listing 3.2: Minimal Python code example to run the input generator and a follow up `FLEUR` calculation. The crystal structure and FLAPW parameters are loaded from the database in this case. Both calculations are executed with ’run’, thus blocking the Python interpreter.

parsed to the *run* or *submit* launcher functions. In this example the calculation is executed in the Python interpreter with *run* in order to wait for the *FleurinpgenCalculation* to finish before the *FleurCalculation* is executed.

3.1.1.3. Fleurinput Data Structure and Modifier

As a typical `FLEUR` calculation needs a significant amount of additional input parameters beyond the crystal structure represented in AiiDA, functionalities to efficiently manage and manipulate these inputs are wanted. For this the possibility to extend AiiDA by new data structures [63] was utilized. The *FleurinpData* class was implemented, to represent `FLEUR` input files and to provide user friendly methods for processing input or extracting information from it. The input files are stored in the file repository while in the database a part of the full *inp.xml* file is stored for query capabilities. The *FleurinpModifier* class ensures that provenance is kept through all input modifications and allows for previews and undo of changes. In order to be able to undo modifications, the class stores all change requests in a queue. These change requests will only lead to a new *FleurinpData* data node if the *freeze()* method is called.

General class methods of *FleurinpModifier* include:

- *validate()*: Test if the changes in the queue produce valid `FLEUR` input
- *freeze()*: Applies all the changes in the queue (calls the workfunction

modify_fleurinpdata) and returns a new *FleurinpData* object

- *changes()*: Displays the current queue of changes
- *show(display=True, validate=False)*: As a test applies the modifications and displays/prints the resulting *inp.xml* file.

The following change methods have been implemented so far for the *FleurinpModifier* class to ease input file manipulation, while others will follow in the future:

- *xml_set_attribv_occ(xpathn, attributename, attribv, occ=[0], create=False)*: Set an attribute of a specific occurance of xml elements.
- *xml_set_first_attribv(xpathn, attributename, attribv, create=False)*: Set an attribute of first occurance of an xml element.
- *xml_set_all_attribv(xpathn, attributename, attribv, create=False)*: Set an attribute of several xml elements.
- *xml_set_text(xpathn, text, create=False)*: Set the text of first occurance of an xml element.
- *xml_set_all_text(xpathn, text, create=False)*: Set the text of xml elements.
- *create_tag(xpath, newelement, create=False)*: Insert an xml element in the xml tree.
- *delete_att(xpath, attrib)*: Delete an attribute for xml elements from the xpath evaluation.
- *delete_tag(xpath)*: Delete an xml element.
- *replace_tag(xpath, newelement)*: Replace an xml element.
- *set_species(species_name, attributedict, create=False)*: Specific user-friendly method to change parameters of species.
- *set_atomgr_att(attributedict, position=None, species=None,create=False)*: Specific method to change atom group parameters.
- *set_inpchanges(self, change_dict)*: Specific user-friendly method for easy changes of attribute key-value type.
- *set_nkpts(self, count, gamma='F')*: Specific method to set the number of k-points.

Python Code Listing 3.3 demonstrates how to initialize a *FleurinpData* object and how the `FLEUR` input is changed without breaking the provenance by using the *FleurinpModifier* class. In this example the $\mathrm{k}_{\mathrm{max}}$ basis cutoff value is changed and the 'dos' switch is set to 'True'. This operation leaves three linked nodes in the database, a *FleurinpModifier CalcFunction*, a returned new *FleurinpData* node and a generated *ParameterData* node with the applied changes. Since *FleurinpModifier* queues the changes, all input modifications are reduced to this minimal database footprint without spamming the database with uninteresting nodes.

```
from aiida.orm import DataFactory
from aiida_fleur.data.fleurinpmodifier import FleurinpModifier
FleurinpData = DataFactory('fleur.fleurinp')

BeTi_inpxmlfile = './inp.xml'

F = FleurinpData(BeTi_inpxmlfile)
fm = FleurinpModifier(F)
fm.set_inpchanges({'dos' : True, 'Kmax': 3.9 })
fm.show() # display input file with changes
new_fleurinpdata = fm.freeze() # apply changes
```

Code Listing 3.3: Python code example to work with *FleurinpData* and modify input with the *FleurinpModifier* class. This example initializes a *FleurinpData* node and changes some parameters of a species, resulting in a new *FleurinpData* node stored in the database.

3.1.2. Implemented Workflows for `FLEUR`

A powerful feature of the AiiDA framework is the ability to develop, run and share workflows [63]. AiiDA workflows are a way to automatically launch time consuming calculations that logically depend on each other without the user having to wait for each of them. The workflow developer encodes expert knowledge and ensures the provenance of data and logic while having access to the Python universe. The developer should try to keep the database footprint (provenance overhead) as small as necessary for a high-throughput workflow. Workflows are powerful property calculator protocols with complex series of calculations able to be launched with a small snippet of Python code. Additional logic can be encoded in workflows like how to best run and converge calculations, find reasonable parameter sets, determine optimal computing resources, treat errors automatically and enable restarts.

The AiiDA-FLEUR package comes with a set of workflows. The basic ones converge a `FLEUR` calculation, calculate a density of states, an electronic band structure or an equation of state. AiiDA-FLEUR additionally contains more advanced workflows to manage core-hole simulations and calculate core-level electron binding energy shifts. A typical run of the basic `FLEUR` self-consistent field workflow creates about 20 database nodes and around 10 files of different sizes to be stored permanently. Advanced workflows need a few to hundreds of self-consistent field subworkflows.

```
from aiida.orm import WorkflowFactory,load_group, Code, DataFactory
from aiida.work.launch import submit
ParameterData = DataFactory(’parameter’)
workflow_class = WorkflowFactory(’fleur.<wf entrypoint>’)

inpgen = Code.get_from_string(’inpgen@otherhost’)
fleur = Code.get_from_string(’fleur@cluster’)

strucs = load_group(label=’some_strucs’).nodes.dbnodes
calc_paras = load_group(label=’FLAPW_paras_for_strucs’).nodes.dbnodes

# example options node for a cluster running slurm
options = ParameterData(dict={
    ’resources’ : {u’num_mpiprocs_per_machine’: 24, u’tot_num_mpiprocs’: 48},
    ’max_wallclock_seconds’: 5∗60∗60, ’queue_name’ : ’’,
    ’custom_scheduler_commands’ : u’#SBATCH −−partition=batch’,
    ’environment_variables’: {’OMP_NUM_THREADS’ : ’1’}
    })

# launch workflow for all structures
# with default workflow parameter since they are not specified in this case
for i,struc in enumerate(strucs):
    res = submit(workflow_class, structure=struc, options=options,
                 calc_parameters=calc_paras[i], fleur=fleur, inpgen=inpgen)
```

Code Listing 3.4: Generic Python code example how to launch most AiiDA-FLEUR workflows. Most workflows can start either from a *StructureData* node or a *RemoteData* node of a previous `FLEUR` run. Additional *ParameterData* nodes allow for the FLAPW input specification ’calc_parameters’ and additional instructions for the workflow ’workflow parameters’.

The Code Listing 3.4 demonstrates a generic workflow launch example. Most workflows of AiiDA-FLEUR implement and expose the interface demonstrated in the Listing. Input nodes for the workflow have to be prepared. Computational resources for calculations launched by the workflow and anything specific to the computer or the scheduler is tuned with the optional ’options’ *ParameterData* node. The layout and content of this ’options’ node is the same for all workflows within AiiDA-FLEUR. This is also the case for most workflows of other code packages, since the content is what AiiDA exposes for the workflow classes. Hence, this ’options’ node can be reused across different workflow classes and packages. In addition workflow specific control parameters are provided in the ’wf_parameter’ *ParameterData* node. Since every workflow comes with reasonable intrinsic defaults of control parameters, the workflow parameter node is also optional. The more advanced a workflow becomes, the more generic these control parameter nodes do become. All `FLEUR` specific workflows allow to start either from at least a *StructureData* node or from a *FleurinpData* node. *RemoteData* nodes are used to continue from previous `FLEUR` runs. Furthermore, the workflow has to be given the *Code* node(s) of the quantum engine(s) it is deploying. In the following some workflows implemented and deployed as a part of this work are described in more detail.

3.1.2.1. The Self-Consistent Field Workflow: *fleur_scf_wc*

The self-consistent field (SCF) workflow *fleur_scf_wc* is the workhorse and subworkflow for most other workflows, which makes its robustness and flexibility very important. The task of this workflow is to converge the charge density and total energy of a given system. As shown in Fig. 3.3 the workflow runs an *FleurinputgenCalculation* and several *FleurCalculations* in serial if needed. The footprint in the database of a self-consistency workflow with one `inpgen` run and one `FLEUR` calculation looks according to Fig. 3.3b. The input nodes of the workflow are the ones needed for the general `FLEUR` specific workflow interface described before in Code Listing 3.4. Several keys to influence the run behavior of the self-consistency workflow are specifiable in a 'wf_parameters' *ParameterData* node.

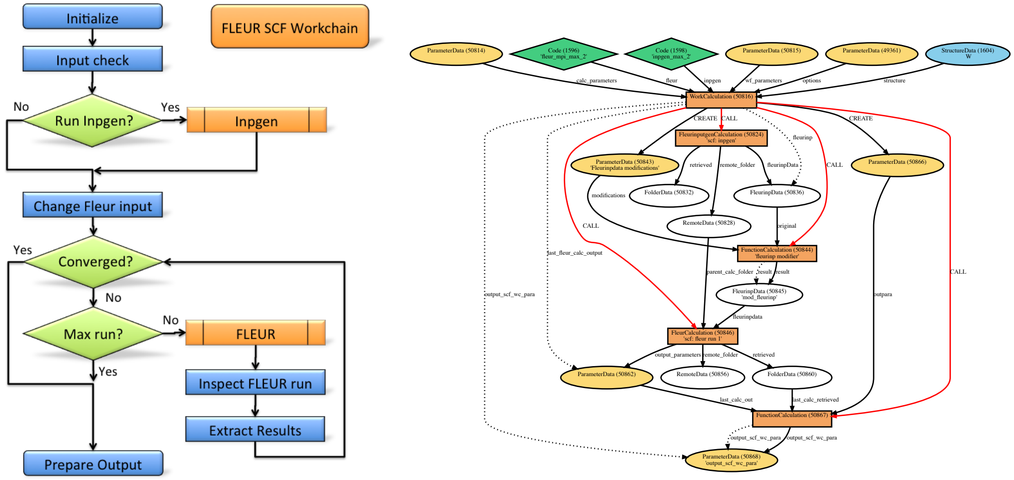

(a) Workflow layout **(b)** Database node graph

Fig. 3.3.: (a) Flowchart of the self-consistency workflow. If needed `inpgen` is run before several `FLEUR` jobs are submitted until convergence or the maximum job submission criterion is reached. (b) Footprint of a `FLEUR` self-consistency workflow in the database graph. Nodes symbolizing calculations and workflows have a rectangular orange shape while data nodes are oval. *StructureData* nodes are blue, *Parameter-Data* nodes are light brawn other data noes are white.

```
wf_parameters_dict = {
  ’fleur_runmax’: 4, # Maximum number of Fleur jobs/starts
  ’itmax_per_run’ : 30, # Maximum iterations run for one Fleur job
  ’density_criterion’ : 0.00002, # Stop if charge denisty is converged below this
  ’energy_criterion’ : 0.002, # Converge the total energy below this
  ’converge_density’ : True, # Converge the charge density (default)
  ’converge_energy’ : False, # Converge the total energy (usually before density)
  #’caching’ : True, # AiiDA fastforwarding (currently not implemented)
  ’serial’ : False, # Execute Fleur with MPI or without
  ’inpxml_changes’ : [], # (expert) List of further changes for the inp.xml after the inpgen run.
  } # Tuples (function_name, [parameters]). Function names need to be known by FleurinpModifier
```

Code Listing 3.5: Default workflow parameter for a self-consistent field workflow with a description of each key. One can specify changes to be applied to the inp.xml after the `inpgen` execution.

Code listing 3.5 shows the default values with some explanation from the documentation of these keys. ’Fleur_runmax’ defines after how many FLEUR jobs the workflow exits as failed if the convergence criterion (specified with ’density_criterion’) is not reached. The key ’itmax_per_run’ sets the number of maximum `FLEUR` self-consistency iterations run per `FLEUR` execution. In some use cases a user wants to change the `FLEUR` input files after the input generator was run. This is enabled by listing all wanted changes according to the *FleurinpModifier* class under the ’inpxml_changes’ key. The self-consistent field workflow always utilizes the ’mindistance’ feature of `FLEUR` and will stop in the next iteration as soon as charge density convergence is reached. The workflow also always parses the walltime to `FLEUR`, allowing `FLEUR` to stop cleanly before running out of walltime. This allows the workflow to relaunch a `FLEUR` calculation, which ran out of walltime until ’Fleur_runmax’ is reached.

```
def choose_resources_fleur(nkpt, natm, max_resources={"num_machines": 1},
                           ncores_per_node=24, memory_gb=120):
    """
    param nkpt: int, number of kpoints
    param natm: int, number of atoms in the cell (for basis estimation)
    param max_resources: dict, maximum computing resource to choose from
    param ncores_per_node, int how many cores are there per node
    param memory_gb: how much memory in GB is there on one node?

    returns nodes, mpi_per_node, openmp, warnings: int, int, int, list

    # TODO: refine for > 1 node systems (larger) systems, memory requirements
    # often too many nodes are currently chosen for a medium system
    """
    from aiida_fleur.tools.decide_ncore import gcd

    ncores_per_node = ncores_per_node
    memory_gb = memory_gb
    warnings = []

```

```
    if natm > 1000:
        nodes = 64*nkpt
        mpi_per_node = 2
        openmp = ncores_per_node/mpi_per_node
    elif natm > 500:
        nodes = 16*nkpt
        mpi_per_node = 2
        openmp = ncores_per_node/mpi_per_node
    elif natm > 200:
        nodes = 4*nkpt
        mpi_per_node = 4
        openmp = ncores_per_node/mpi_per_node
    elif natm > 80:
        if nkpt < 10:
            nodes = 2*nkpt
            mpi_per_node = 4
            openmp = ncores_per_node/mpi_per_node
        elif nkpt < 100:
            nodes = nkpt
            mpi_per_node = 4
            openmp = ncores_per_node/mpi_per_node
        else:
            factor = 2 # TODO
            nodes = nkpt/factor
            mpi_per_node = 4
            openmp = ncores_per_node/mpi_per_node
    elif natm <= 30:
        factor = gcd(ncores_per_node, nkpt)
        nodes = 1
        mpi_per_node = factor
        openmp = ncores_per_node/mpi_per_node
    else:
        if nkpt < 20:
            factor = gcd(ncores_per_node, nkpt)
            nodes = 1
            mpi_per_node = factor
            openmp = ncores_per_node/mpi_per_node
        else:
            factor = gcd(ncores_per_node, nkpt)
            nodes = nkpt/factor
            mpi_per_node = factor
            openmp = ncores_per_node/mpi_per_node

    if max_resources:
        max_numnodes = max_resources.get(’num_machines’, None)
        max_mpiproc = max_resources.get("tot_num_mpiprocs", None)
        if (max_numnodes is not None) and (max_mpiproc is None):
            if max_numnodes < nodes:
                warning = (’The max number of provided compute nodes {} ’
                           ’is less then the recommened {}’
                           ’, consider providing more resouces for this calculation’
                           ’or using less kpoints.’.format(max_numnodes, nodes))
                nodes = max_numnodes
                warnings.append(warning)
        elif max_mpiproc is not None:
```

```
            mpiproc = mpi_per_node*nodes
            if mpiproc >= max_mpiproc:
                nodes = max(max_mpiproc/mpi_per_node,1) # should be at least 1...
            # else everything is fine
        else:
            max_number_total_mpi_proc = max_resources.get('num_machines', None)

    return nodes, mpi_per_node, openmp, warnings
```

Code Listing 3.6: Simple Python 2 code snippet to choose hybrid parallelization strategies for different small system sizes and computing architectures within a maximum amount of given resources.

```
# switch on kerker preconditioning
wf_para = ParameterData(dict={
  'fleur_runmax': 3, 'itmax_per_run' : 80, 'density_criterion' : 0.00005,
  'inpxml_changes' : [['set_inpchanges',
           {'change_dict' : {'preconditioning_param' : 0.8, 'alpha' : 0.40}}
           ]]})

res = submit(fleur_scf_wc, wf_parameters=wf_para, structure=struc,
             calc_parameter=calc_paras, options=options, inpgen=inpgen,
             fleur=fleur, label="test", description="fleur_scf test")
```

Code Listing 3.7: Launch code example for a SCF workflow in the context of the general code example. In this example some specify workflow parameters are specified to switch on Kerker preconditioning.

Diverse system sizes with different cutoff parameters will vary a lot in their computational demands and optimal parallelization strategy. Very small systems might crash or fail if launched with too many resources or with too many MPI processes assigned. Larger systems might not finish the first iteration until running out of walltime. Thus, predicting the job run time, resources and parallelization needed before a simulation launch, is essential to achieving automation and running a high-throughput project. Any workflow launching calculations on very diverse system sizes has to be able to judge if the computational resources it has available are reasonable or not to do the job. Before this work no runtime model or overall parallelization strategy for `FLEUR` on diverse system sizes and architectures existed. In order to be able to run a small HTC project, a crude choice was implemented as shown in Code Listing 3.6 and deployed within the *fleur_scf_wc*. For very large system sizes the parallelization choice was determined by the work of Dr. Uliana Alekseeva on benchmarking the `FLEUR` code for very large systems. For small systems sizes, this parallelization scheme always tries to distribute the k-points evenly among MPI tasks and fill the rest of a compute node with OpenMP tasks. Since it tries to use the compute nodes completely and a prime number of k-points is not so seldom, the parallelization scheme often ends up with using one MPI task per node. This is probably not optimal.

```
{ "distance_charge": 9.5578e-06, "distance_charge_units": "me/bohr^3",
  "distance_charge_all": [9.908865339, ..., 9.5578e-06],
  "errors": [], "warnings": [], "info": [], "iterations_total": 26,
  "loop_count": 1, "material": "W2",
  "last_calc_uuid": "29efcd00-3f8f-4775-a598-95aed5357a65"
    "successful": true, "total_energy": -32324.8485355339,
  "total_energy_all": [-32324.8911239023, ..., -32324.8485355339],
  "total_energy_units": "Htr", "total_wall_time": 83,
  "total_wall_time_units": "hours", "workflow_name": "fleur_scf_wc",
  "workflow_version": "0.2.1"}
```

Code Listing 3.8: 'Output_scf_para' *ParameterData* node example of the SCF workflow. It contains the charge density distance and total energy of all iterations plus additional information about all `FLEUR` runs.

A Python code example on how to submit this workflow is presented in Code Listing 3.7 with the preparation of a non-default workflow parameter node first which switches on Kerker preconditioning for the FLEUR calculation. The self-consistency workflow returns, beside the last *FleurCalculation* output nodes, an own *ParameterData* output node 'output_scf_para', which full content is shown in Code Listing 3.8. This node contains combined information of all `FLEUR` runs including the charge density distance and total energy of the system for each SCF iteration run. The node also contains basic information on the run like the material, basis sizes, total runtime and overall success of the workflow. This single output node or a list of them can be visualized with the 'plot_fleur' function (see Fig 3.4). 'Plot_fleur' will display the convergence of the total energy difference and the charge density on a logarithmic scale over the number of iterations. If a list of SCF workflow nodes or output nodes are given, their results are visualized in one plot together, allowing for a one-shot visual confirmation if all systems converged properly or not. In-browser visualizations via notebooks allows for plots to become interactive. Besides standard convenient interactive features like zooming per mouse or axis changes by Matplotlib, more advanced interactive features are possible through Python, Javascript packages like Bokeh [266]. For example by hovering the mouse over a data point, the crystal structure formula, workflow identifier 'pk', or other properties of the runs can be shown to quickly identify problematic systems within hundreds of calculations.

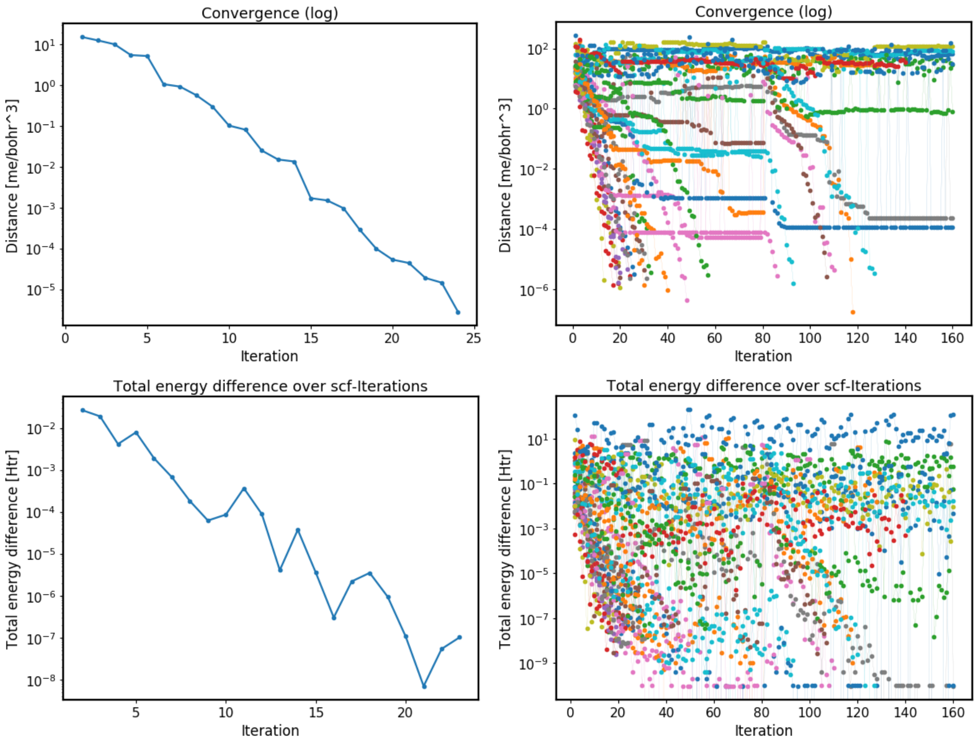

(a) Single SCF node visualization with *plot_fleur(<pk>)*.

(b) Multi SCF nodes visualization with *plot_fleur(list(<pks>))*.

Fig. 3.4.: Default *plot_fleur* visualization for a single SCF workflow node (a) and multiple SCF workflow nodes (b). Two logarithmic graphs are produced each, the convergence of the charge density with respect to the iteration and the convergence behavior of the total energy difference to the previous iteration with respect to the iteration number. The multi node visualization is a collection of these SCF runs condensed in one figure for each property.

3.1.2.2. The DOS and Band Structure Workflows: *fleur_DOS_w* and *fleur_band_wc*

In order to calculate an electronic band structure and a density of states two workflows were implemented. Since their workflow steps and database footprint (as shown in Fig 3.5) are very similar, they are treated together in this subsection. These two workflows are mostly deployed as a post-run on an already converged *FleurCalculation*. As input they therefore need a *RemoteData* node from a previous calculation, a *FleurinpData* node and code nodes. As optional input, similar to all other workflows, they take ’options’ and workflow control parameter (’wf_parameters’) nodes. The content of their workflow parameter nodes as well as a launch code example is shown in Code Listing 3.9. In the corresponding workflow parameters one can adjust the number of k-points, smearing parameters and energy intervals. In the control parameters for the band structure workflow a k-point path can be specified, while for a good density of states calculation one wants to specify the k-point sampling method. A quick *plot_fleur* visualization of a band structure and a density of states is shown in Fig. 3.6. These graphs are meant only for quick examination. More advanced visualizations for band structures, surface state highlighting, combined plots etc. are part of the ’masci-tools’ repository.

```
fleur_dos_wc = WorkflowFactory(’fleur.dos’)
fleur_band_wc = WorkflowFactory(’fleur.band’)
remote = load_node(<pk>)
fleurinp = load_node(<pk>)

wf_para_dos = ParameterData(dict={
    ’tria’ : True, ’nkpts’ : 800, ’sigma’ : 0.005, ’emin’ : −0.30, ’emax’ : 0.80})
wf_para_band = ParameterData(dict={
    ’kpath’ : ’auto’, ’nkpts’ : 800, ’sigma’ : 0.005, ’emin’ : −0.50, ’emax’ : 0.90})

# launch workflows
dos = submit(fleur_dos_wc, wf_parameters=wf_para_dos, fleurinp=fleurinp,
             remote_data=remote, options=options, fleur=fleur, label="test dos",
             description="fleur_dos test")
band = submit(fleur_band_wc, wf_parameters=wf_para_band, fleurinp=fleurinp,
             remote_data=remote, options=options, fleur=fleur, label="test band",
             description="fleur_band test")
```

Code Listing 3.9: Workflow control parameter specification example and launch code for a density of states and a band structure workflow.

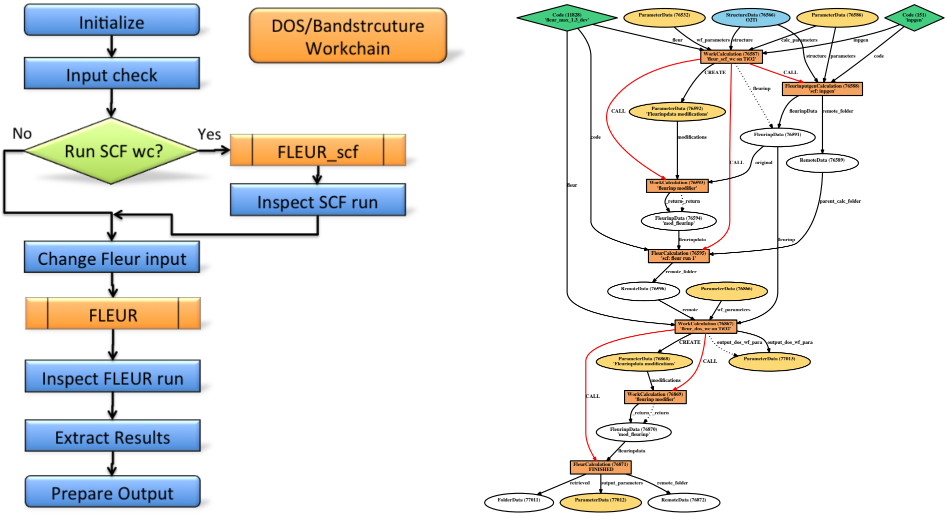

(a) Workflow layout **(b)** Database node graph

Fig. 3.5.: Flowchart of the density of states and the band structure workflows (a). Usually, one `FLEUR` jobs is submitted on top of an already converged FLEUR calculation. The footprint of such a workflow with a `FLEUR` self-consistent field workflow in the database graph is shown in (b). Nodes symbolizing calculations have a rectangular shape while data nodes are oval.

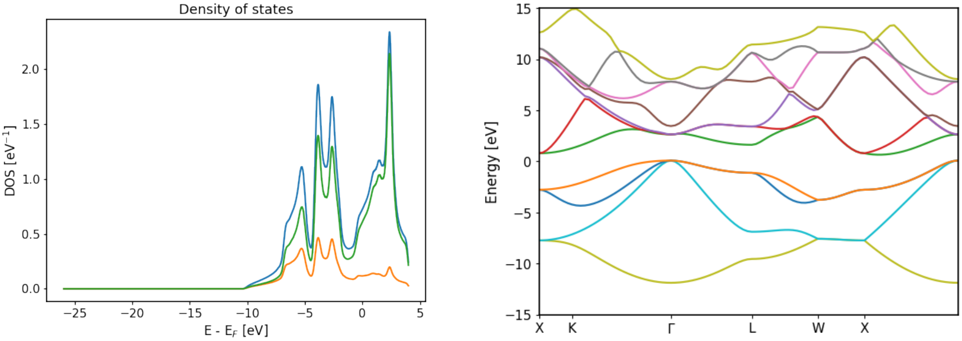

(a) **(b)**

Fig. 3.6.: Default *plot_fleur* visualization of the density of states (DOS) workflow (a) for W and of the band structure workflow (b) for Si.

3.1.2.3. The Equation of States Workflow

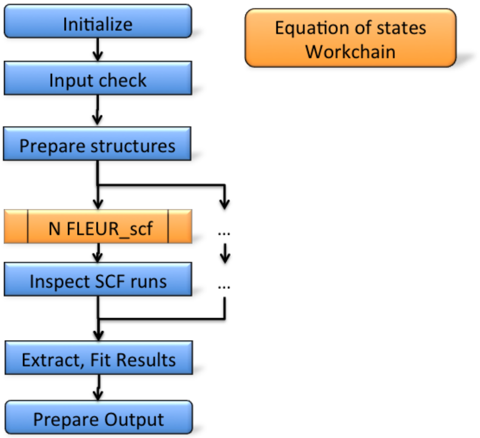

Fig. 3.7.: The equation of states workflow layout, with a `FLEUR` self-consistent field workflow launch for each volume scaling to be calculated, is shown here.

To calculate an equation of states (EOS), total energies for different, scaled volumes of a given crystal structure have to be calculated. In order to do so the *fleur_eos_wc* workflow creates these scaled crystal structures and runs the `FLEUR` self-consistent field (SCF) workflow on each of them with the same FLAPW parameters to ensure comparable total energies. The layout of the workflow is shown in Fig. 3.7 while the database graph of the EOS workflow is shown in Fig. 3.8. The workflow runs the smallest volume structure first, to fail early, or react in the case of non working FLAPW parameters like to small muffin-tin radii. Afterwards all SCFs for the other volumina are calculated in parallel. If every calculation was successful an equation of state is fitted to the resulting total energy per atom data points. To do so fits implemented in ASE [260] and the Birch-Murnaghan fit [267] as performed in the DELTA DFT project [268] are applied. This EOS workflow version executes all SCF workflows in parallel independent of each other. It may be computationally cheaper to run all the SCFs in serial and reuse the last charge density of the previous scaling as a starting density, but this serial design would lead to a longer execution time and most likely to more data transfer because of how the default of the `FLEUR` plug-in works. Newer versions of `FLEUR` have the capability to bundle calculations in one execution, which might be beneficial for EOS type calculations. The provenance graph example from a *fleur_eos_wc* execution in Fig. 3.8 shows how the result node can be tracked back to the cif file the input crystal structure was imported from. The node graphs contains the database footprint of nine SCF workflows run on different scaled crystal structures parallel after the workflow checked the lowest scaling works.

An example for specific control parameters and how to launch a *fleur_eos_wc* in Python is shown in Code Listing 3.10. As input nodes the workflow starts from a crystal structure and optional FLAPW parameters for `inpgen`. In addition to the code nodes it takes the usual options node as optional input . In the workflow control parameters ('wf_parameters') the

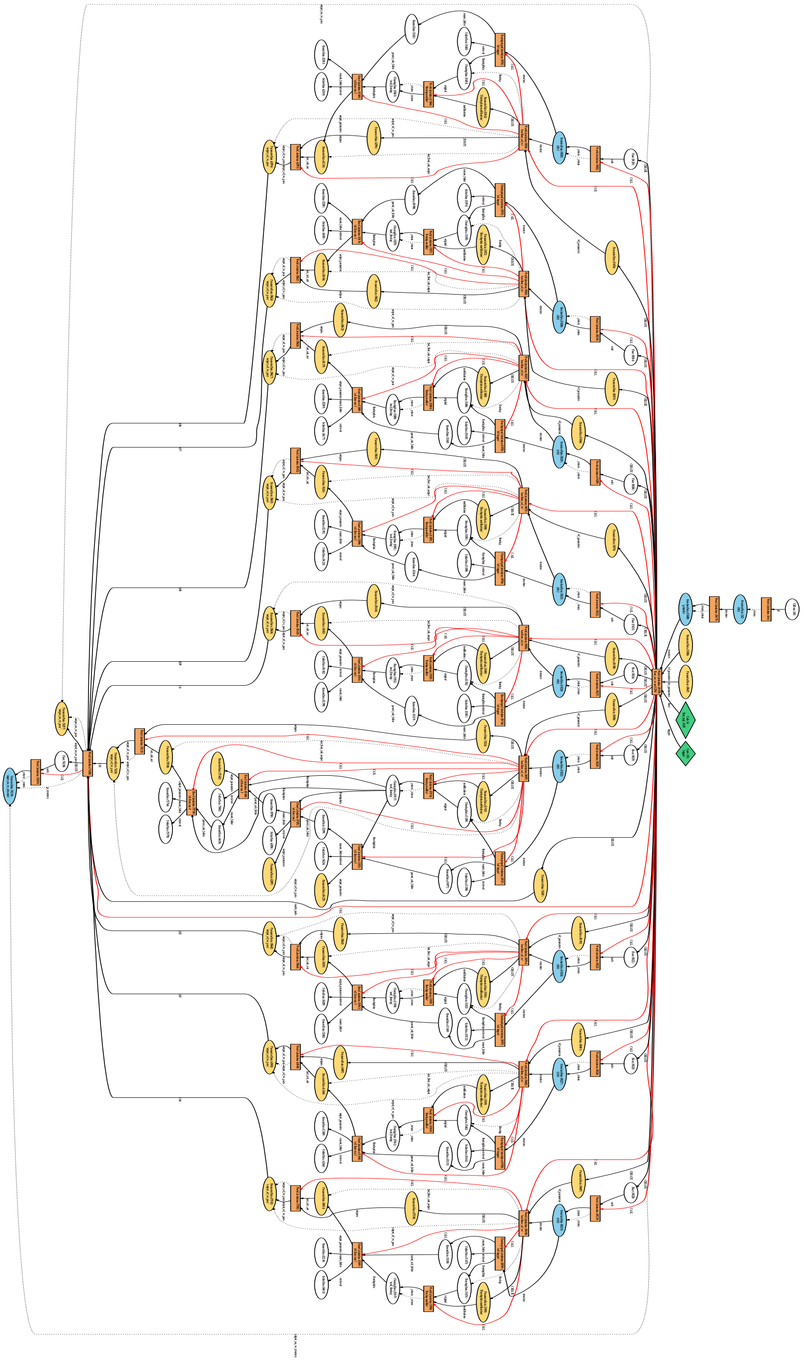

Fig. 3.8.: Provenance graph of the equation of states workflow for `FLEUR` in the database. In this example nine scaling points are calculated with the SCF workflow and afterwards a combined output node with the equation of states results is returned.

user can specify how many scaling points should be calculated, around which initial volume scaling and with what step size the points are distributed. Additional parameters for the underlying SCFs are also specified in the workflow parameter node.

```
fleur_eos_wc = WorkflowFactory(’fleur.eos’)
struc = load_node(<pk>)
flapw_para = load_node(<pk>)

wf_para_eos = ParameterData(dict={
    ’fleur_runmax’: 4, ’points’ : 9, ’step’ : 0.002, ’guess’ : 1.00})

# launch workflow
dos = submit(fleur_eos_wc, wf_parameters=wf_para_eos, structure=struc,
             calc_parameters=flapw_para, options=options, fleur=fleur,
             inpgen=inpgen, label="test eos", description="fleur_eos test")
```

Code Listing 3.10: Workflow control parameter node and launch code example for an equation of states workflow.

```
eos_outputpara.get_dict()
{"bulk_deriv": 2.67215140960889, "bulk_modulus": 127.027293196724,
  "bulk_modulus_units": "GPa", "calculations": [],
  "distance_charge": [1.71247e−05, ... , 1.0709e−05],
  "distance_charge_units": "me/bohr^3", "errors": [], "guess": 1.0, "info": [],
  "initial_structure": "cba2df42−...", "natoms": 6, "nsteps": 9,
  "residuals": [0.00020092833463241], "scaling": [0.96, ... , 1.04],
  "scaling_gs": 0.998197820705052, "scf_wfs": [...], "stepsize": 0.01,
  "structures": ["b1d6c05a−af43−41c2−...", ..., "11cf8599−b6b1−47fb−..."],
  "successful": true, "total_energy": [−25244.2511349729, ..., −25244.2481496444],
  "total_energy_units": "Htr", "volume_gs": 56.5016255389853,
  "volume_units": "A^3","volumes": [54.3394900212401, ..., 58.8677808563436],
  "warnings": [], "workflow_name": "fleur_eos_wc", "workflow_version": "0.3.2"}
```

Code Listing 3.11: Output *ParameterData* node of an equation of states workflow. Among basic information it contains the total energies from all the SCF `FLEUR` runs, the corresponding cell volumes and equation of state fit results.

As the specification of control parameters and a FLAPW parameter node are optional, the workflow can be launched with just some crystal structure and a code node as input. In this case the workflow would use the FLAPW parameters determined by `inpgen` for each SCF, which can lead to a less accurate equation of states results. The output node produced by the equation of state workflow is presented in Listing 3.11. It contains among basic information a collection of total energies, volumes and scalings from all configurations, bulk moduli and the ground state volume results of different equation of state fits. With the current implementation of a uniform scaling of all lattice parameters the bulk moduli are only expected to be physical meaningful for systems with cubic symmetry. For other symmetries in addition the lattice parameters have to be optimized for each fixed scaled volume. Their according default *plot_fleur* visualizations are shown in Fig. 3.9. For the single node the total

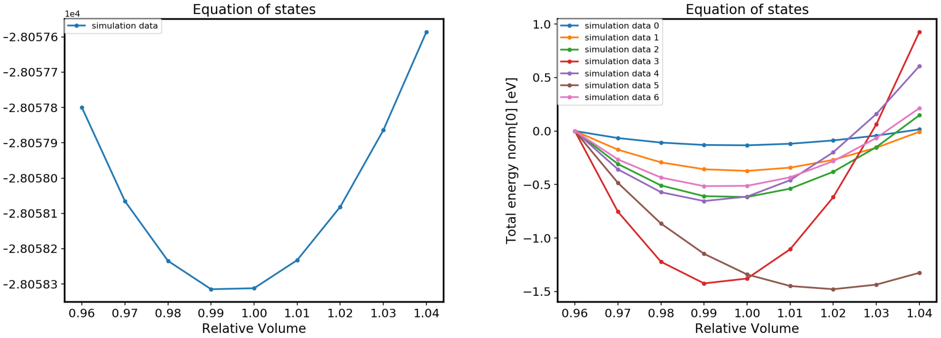

(a) Single EOS node visualization

(b) Multi EOS node visualization

Fig. 3.9.: Simple *plot_fleur* visualization of the equation of states workflow for a single node (a) and a multi node visualization (b). In order to make the equation of state calculations comparable, the total energies are plotted with respect to the total energy of the lowest scaling.

energies for different relative volumes are visualized. In a multi node visualization several equation of state results can be displayed together by plotting total energy differences with respect to the system corespondent total energy of the lowest scaling data point.

3.1.3. Core-level Spectra Turn-key Solution

For the calculation of relevant spectral properties of X-ray photoelectron spectra from *ab initio* as discussed in Section 2.9.2 two advanced workflows were implement. The *initial_cls_wc* workflow for the calculation of initial-state core-level shifts (CLS) of metals and possibly beyond. The second workflow with the potential to utilize a whole super compute cluster is the core-hole workflow[4]. Its objective is to calculate core electron binding energies of a given atomic configuration via core-hole simulations in a super cell setup. The layouts of these two workflows are shown in Fig. 3.10.

In detail, the **initial-state workflow** calculates core-level shifts of a system with respect to the elemental references via normal SCF calculations. If required, the SCF calculations of

---

[4] Some fictitious W-O example: The W-O alloy has 48 atoms in the unit cell with 4 tungsten atom-types by symmetry and 8 oxygen symmetry types. A usual electronic configuration of tungsten has 17 core states and for oxygen there are 2 core states. If one now wants to know the binding energies for all of these, $4 \cdot 17 + 8 \cdot 2 + 1 = 84$ SCF supercell simulations can be deployed. A $2x2x2$ super cell would have 384 atoms which would be reasonable to run on 30 compute nodes each, totaling 2520 compute nodes for 84 jobs.

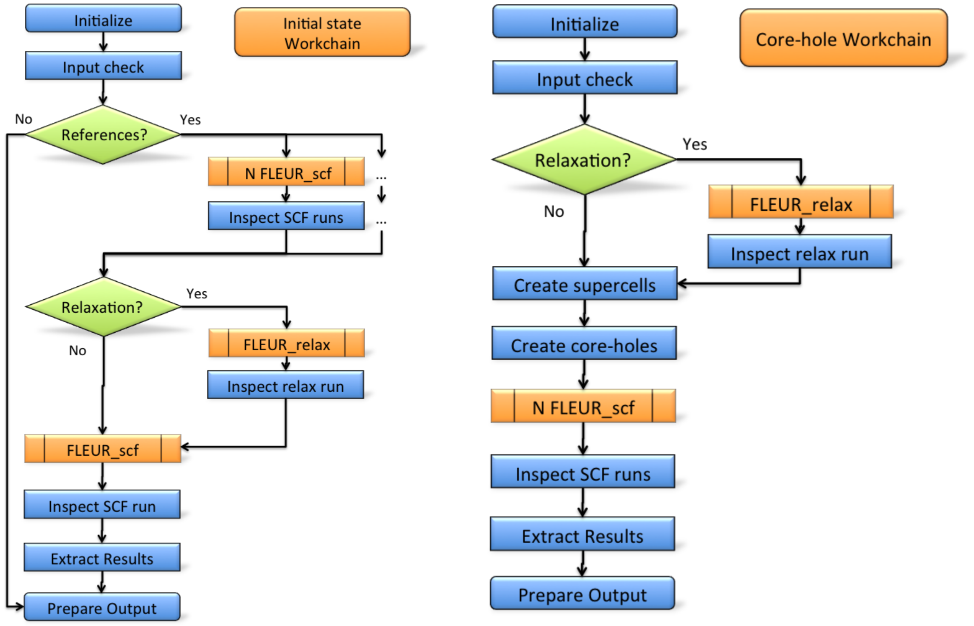

(a) Initial-state workflow layout

(b) Core-hole workflow layout

Fig. 3.10.: (a) Initial-state core-level shift workflow layout and (b) the layout of the core-hole workflow. The initial-state workflow in (a) runs SCFs on the given crystal structure and if needed on all elemental reference crystal structures needed for the calculation of core-level shifts. the core-hole workflow in (b) runs one super cell simulation for a structure without a core hole and compares its total energy to super cell calculations with the core-hole setup of interest.

the corresponding elemental references are also managed by the workflow. Furthermore, the workflow extracts the enthalpy of formation for the investigated compound from these SCF runs. The workflow implements equation 2.42 for the calculation of core-level shifts as the difference of Kohn-Sham core-level energies with respect to the Fermi energy. To minimize uncertainties on CLS it is important that the compound as well as the reference systems are calculated with the same atomic parameters (R_{MT}, radial grid points and spacing, basis cutoff ℓ_{max}). The workflow tests for this equality and tries to assure it, though it does not know what is a good parameter set nor if the present set works well for both systems. Therefore, it is currently best practice to enforce the FLAPW parameters used within the workflow, i.e., provide them as input for the system as for the references. A Python code example for the workflow control parameters and how to launch it is written in Code Listing 3.12.

```
fleur_init_cls_wc = WorkflowFactory(’fleur.initial_cls’)
struc = load_node(<pk>)
flapw_para = load_node(<pk>)

wf_para_initial = ParameterData(dict={
  "references": {"Be": "257d8ae8−32b3−4c95−8891−d5f527b80008",
                 "W": "c12c999c−9a00−4866−b6ef−9bb5d28e7797"},
  "scf_para": {"density_criterion": 5e−06, "fleur_runmax": 3, "itmax_per_run": 80}})

# launch workflow
initial_res = submit(fleur_init_cls_wc, wf_parameters=wf_para_initial, structure=struc,
                     calc_parameters=flapw_para, options=options, fleur=fleur, inpgen=inpgen,
                     label="test initial cls", description="fleur_initial_cls test")
```

Code Listing 3.12: Workflow control parameter example with launch code of an initial-state core-level shift workflow.

Besides control parameters for the launch of the SCF subworkflows the most important parameter is the ’reference’ key. Under this key the source from which the elemental reference should be taken has to be provided. The workflow is quite flexible in its sources for the elemental references. If only a structure is given here, it tries to calculate that structure with the same FLAPW parameters as for the compound, which may not be very robust. If a structure and FLAPW parameters are given for the corresponding element, it calculates the reference from this structure while enforcing the given parameters for the reference. Another option is to provide core-level values or an SCF node or SCF output node. In this case these results are used and no additional calculation for the references are launched by the workflow. For the screening project within this work a fixed elemental set of FLAPW parameters was applied and the elemental references were calculated before the binary compound calculations. In this way the elemental SCF calculations could be reused and they did not need to be recalculated for every binary compound. When designing this workflow another option was to query the database for elemental references or select them from a given group node. This would allow the workflow control parameter node to become optional. But in practice these options were not applied because they do not allow for saving of computational time or the reference choice is not fully transparent to the user. Fig. 3.11 depicts a provenance database graph for an initial-state workflow run on $Be_{12}Ta$. In this case the Be and Ta elemental reference crystals structures are given as input so they were calculated within the workflow besides the SCF run of $Be_{12}Ta$ itself, leading to a database footprint of three SCF workflows. The crystal structure is tracked back to a cif file in the database from which the structure has been refined.

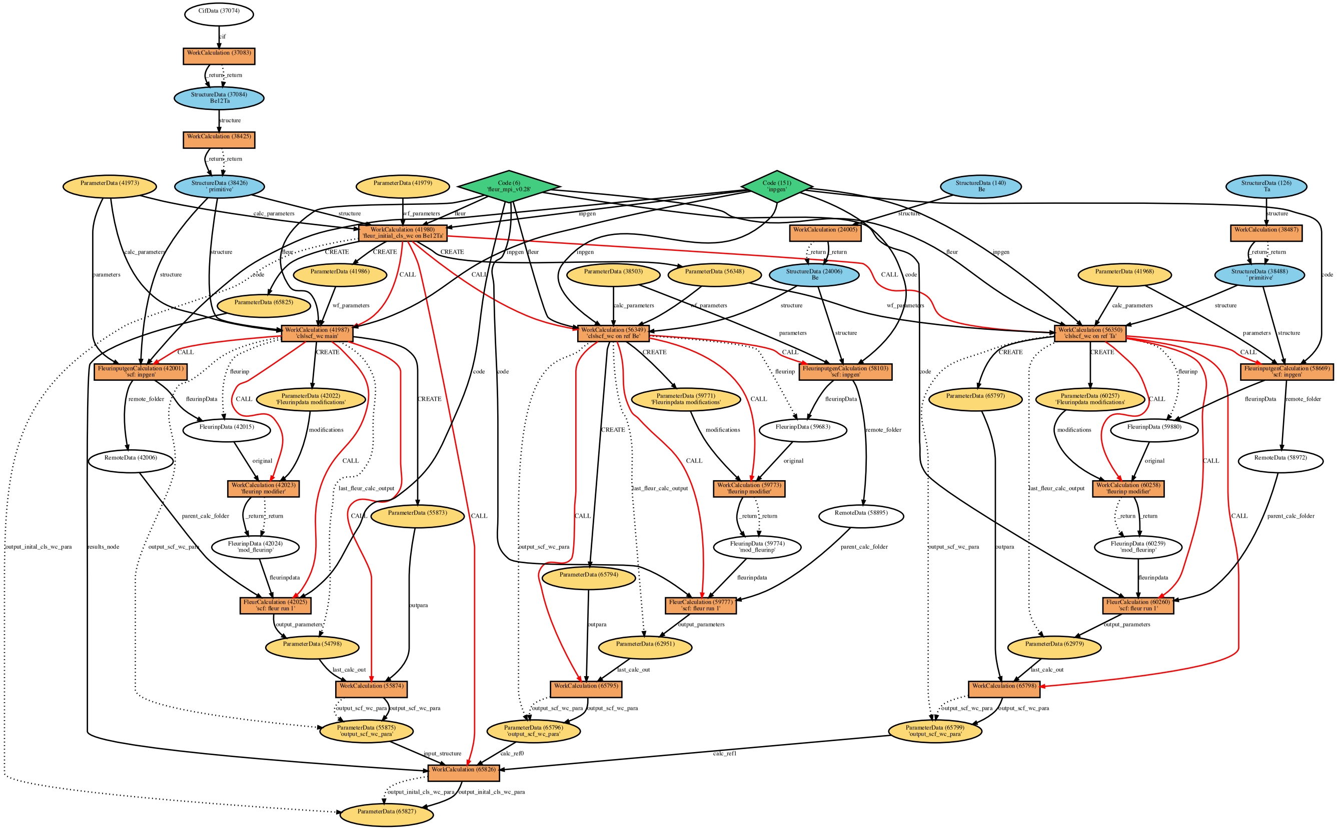

Fig. 3.11.: Provenance graph of the initial-state core-level shift workflow on $Be_{12}Ta$ in the database with data and logic links. In this case the structure is tracked back to a cif file and the Be and Ta references are calculated explicitly, leading to a database footprint of three SCF workflows.

```
initial_outputpara.get_dict()
{"atomtypes": {"Be8W4": [
  {"atomic_number": 4, "coreconfig": "[He]", "element": "Be", "natoms": 2,
   "species": "Be−1", "stateOccupation": [], "valenceconfig": "(2s1/2)"},
  {"atomic_number": 4, "coreconfig": "[He]", "element": "Be", "natoms": 2,
   "species": "Be−1", "stateOccupation": [], "valenceconfig": "(2s1/2)"},
  {"atomic_number": 4, "coreconfig": "[He]", "element": "Be", "natoms": 2,
   "species": "Be−1", "stateOccupation": [], "valenceconfig": "(2s1/2)"},
  {"atomic_number": 4, "coreconfig": "[He]", "element": "Be", "natoms": 2,
   "species": "Be−1", "stateOccupation": [], "valenceconfig": "(2s1/2)"},
  {"atomic_number": 74, "coreconfig": "[Kr] (4d3/2) (4d5/2) (4f5/2) (4f7/2)",
  "element": "W", "natoms": 4, "species": "W−1",
  "stateOccupation": [{"(5d3/2)": ["2.00000000", ".00000000"]},
                      {"(5d5/2)": ["2.00000000", ".00000000"]}],
  "valenceconfig": "(5s1/2) (5p1/2) (5p3/2) (6s1/2) (5d3/2) (5d5/2)"}]},
  "bandgap": 1.29e−08, "bandgap_units": "htr", "binding_energy_convention": "negativ",
  "corelevel_energies": {
    "Be": [[−3.6368105483], [−3.632265731], [−3.6322656557], [−3.6322657313]],
    "W": [[−2550.2147096202, −439.6879734359, −420.4064081902, −370.6879340131,
        −101.1009806871, −92.5245656738, −81.7732545914, −20.6970483776,
        −67.3546082505, −65.0168950274, −17.1416205421, −14.6503698749,
        −8.8167740875, −8.3578324597, −1.0614905309, −0.9792037094]]},
  "corelevel_energies_units": "htr",
  "corelevelshifts": {
    "Be": [[0.04591258769], [0.050457405], [0.0504574803], [0.05045740469]],
    "W": [[0.024640718499, 0.024661266199, 0.024666486, 0.024666188099,
          0.024687366999, 0.0246857361, 0.0246899982, 0.024782819799,
          0.024681577599, 0.024682716499, 0.0247872636, 0.02480582029,
          0.0248186677, 0.0248253974, 0.0248879943, 0.0248955395]]},
  "corelevelshifts_units": "htr", "fermi_energy": 0.4542230019,
  "fermi_energy_units": "htr", "formation_energy": −0.26731670795319,
  "formation_energy_units": "eV/atom", "material": "Be8W4",
  "reference_bandgaps": [0.0019313311, 0.0248201189],
  "reference_bandgaps_des": ["Be2", "W2"],
  "reference_corelevel_energies": {
    "Be": [[−3.682723136]],
    "W": [[−2550.2393503387, −439.7126347021, −420.4310746763, −370.7126002012,
        −101.1256680541, −92.5492514099, −81.7979445896, −20.7218311974,
        −67.3792898281, −65.0415777439, −17.1664078057, −14.6751756952,
        −8.8415927552, −8.3826578571, −1.0863785252, −1.0040992489]]},
  "reference_corelevel_energies_units": "htr",
  "reference_fermi_energy": [0.2722843823, 0.6914067304],
  "reference_fermi_energy_des": ["Be2", "W2"],
  "successful": true, "total_energy": −1762833.35474838,
  "total_energy_ref": [−803.813110785628, −879807.447252371],
  "total_energy_ref_des": ["Be2", "W2"],
  "total_energy_units": "eV", "warnings": [],
  "workflow_name": "fleur_initial_cls_wc", "workflow_version": "0.3.4"}
```

Code Listing 3.13: Output *ParameterData* node content of an initial core-level shift workflow, containing Kohn-Sham core-level energies, shifts, formation energies and additional information.

Code Listing 3.13 displays the content of a resulting output *ParameterData* 'fleur_initial_cls_wc_para' node. The node contains detailed information about the atom-types and their electronic configuration in a nested dictionary list structure for the calculated compound. Additionally, the node contains core-level energies, some basic run information , core-level shifts, total energy, band gap and Fermi energy for the compound and the reference systems. Overall, this node contains all information to construct a relative core-level spectrum or evaluate all shifts for any other reference.

The **core-hole workflow** can be deployed to calculate absolute core-level binding energies. From a computational cost perspective it may be cheaper to calculate all relative initial-state shifts of a structure and then launch one core-hole calculation on the structure to get an absolute reference energy instead of performing expensive core-hole calculations for all atom-types in the structure. The core-hole workflow implements the usual `FLEUR` workflow interface with a workflow control parameter node. The contents of this node and a Python launch code example are shown in Code Listing 3.14.

```
fleur_corehole_wc = WorkflowFactory('fleur.corehole')

struc = load_node(<pk>)
flapw_para = load_node(<pk>)

wf_para_corehole = ParameterData(dict={u'atoms': [u'Be'], #[u'all'],
  u'supercell_size': [2, 2, 2], u'corelevel': ['1s'], #[u'all'],
  u'hole_charge': 1.0, u'magnetic': True, u'method': u'valence', u'serial': False}

# launch workflow
dos = submit(fleur_corehole_wc, wf_parameters=wf_para_corehole, structure=struc,
              calc_parameters=flapw_para, options=options,
              fleur=fleur, inpgen=inpgen, label="test core hole wc",
              description="fleur_corehole test")
```

Code Listing 3.14: Control parameter and launch code example for a core-hole workflow to calculate a full 1s valence core hole for all Be atomtypes in some Beryllide with a $2x2x2$ supercell.

The control parameters contain keys to specify the type of core-hole calculations performed on which atoms and which core levels. With the 'atoms' key a list of atoms is specified on which to place a core hole. They can be specified as strings, as positions, or number in the atom list of the AiiDA *StructureData*. If core-hole calculations on all atomtypes of one element should be deployed, one can specify the element as a string. If the binding energies for all elements and atom-types should be calculated, 'all' can be specified. With the 'corelevel' key the user specifies for which core levels a core-hole calculation should be launched. Possible specifications are 'all', core states like 1s, 2p1/2, etc or an element specification as prefix i.e., 'Be1s'. Furthermore, the core-hole charge ('hole_charge') and the type of the core hole can be specified. The type of the 'method' key can be 'valence' resulting in the core electron to be put into the valence band or ’charge’ which results in a simple removal of the electron leaving a charged system. Core-hole calculations often require the introduction of magnetism into the system, making it important to perform spin polarized calculation, which might be switched off with the ’magnetic’ key. The workflow only launches a series of single core-hole calculations though it can be easily extended to the use case of multiple core holes within one structure. Since the electronic configuration is currently not always written to the ’inp.xml’ by `FLEUR` or `inpgen`, it is important to either enforce an electronic configuration if FLAPW parameters are provided, or to make sure that the electronic configuration is written explicitly in the ’inp.xml’ if a *FleurinpData* node is provided. Otherwise the workflow might struggle preparing the input correctly or `FLEUR` calculations might fail. The super cell size to be calculated is specified with the ’supercell_size’ key as a list of integers in the workflow control parameters. During a workflow run the crystal cells will be adjusted such that the atom with the core hole lies at the coordinate system’s origin to avoid non-symmorphic symmetries. Since we want to compare the total energy of super cell calculations with and without core hole, the workflow first calls the SCF-workflow to convergence a super cell system without core hole. This has two advantages. First, if this SCF already fails, the other expensive calculations are not launched. Second, all the core-hole calculations can start from the converged charge density of the super cell calculation without core hole to save computational time and to make the calculation more stable, at least for small core-hole charges. Then, all core-hole calculations are launched in parallel by the workflow. The database footprint of a deployed core-hole workflow on a simple Si system to calculate 2p binding energies for two atom-types is shown in Fig. 3.12. In total five SCF workflows are run, one for the reference super cell and four core-hole calculations.

```
corehole_outputpara.get_dict()
{"atomtypes": [[
  {"atomic_number": 4, "coreconfig": "(1s1/2)", "element": "Be", "natoms": 1,
   "species": "Be_corehole1", "stateOccupation": [
      {"(1s1/2)": ["1.00000000", ".50000000"]},
      {"(2p1/2)": [".50000000", ".00000000"]}], "valenceconfig": "(2s1/2) (2p1/2)"},
  {"atomic_number": 4, "coreconfig": "[He]", "element": "Be", "natoms": 1,
   "species": "Be−2", "stateOccupation": [{"(2p1/2)": [".00000000", ".00000000"]}],
   "valenceconfig": "(2s1/2) (2p1/2)"},
  {"atomic_number": 4, "coreconfig": "[He]", "element": "Be", "natoms": 1,
   "species": "Be−2", "stateOccupation": [{"(2p1/2)": [".00000000", ".00000000"]}],
   "valenceconfig": "(2s1/2) (2p1/2)"},
  {"atomic_number": 4, "coreconfig": "[He]", "element": "Be", "natoms": 1,
   "species": "Be−2", "stateOccupation": [{"(2p1/2)": [".00000000", ".00000000"]}],
   "valenceconfig": "(2s1/2) (2p1/2)"}]], "bandgap": [0.0004425914],
  "bandgap_units":"eV", "binding_energy": [53.57027767044], "corehole_type": "valence",
  "binding_energy_units": "eV", "binding_energy_convention": "negativ",
  "coreholes_calculated": "Be1s", "coreholes_calculated_details": "", "coresetup": [],
  "errors": [], "fermi_energy": [0.3138075709], "fermi_energy_unit": "eV",
  "reference_bandgaps": [0.0225936434], "reference_coresetup": [],
  "successful": true, "total_energy_all": [−1554.08485250996],
  "total_energy_all_units": "eV", "total_energy_ref": [−1607.6551301804],
  "total_energy_ref_units": "eV", "warnings": [], "hints": [],
  "weighted_binding_energy": [107.14055534088], "weighted_binding_energy_units": "eV",
  "workflow_name": "fleur_corehole_wc", "workflow_version": "0.3.2"}
```

Code Listing 3.15: Output ParameterData node of a simple core-hole workflow run to calculate a spin-polarized half-valence core hole of elemental Be.

The main output result node for a core-hole workflow run on a simple pure Be system is shown in Listing 3.15. On an elemental Be structure a half-valence core-hole calculation was performed with a $2x2x2$ super cell. The output node contains total energies of the core-hole system and the reference system as well as core-level binding energies and the weighted binding energies with charge one. Additional information on the atom-types of each run with details of the core-hole setup are in the output node together with the Fermi energies and bandgaps.

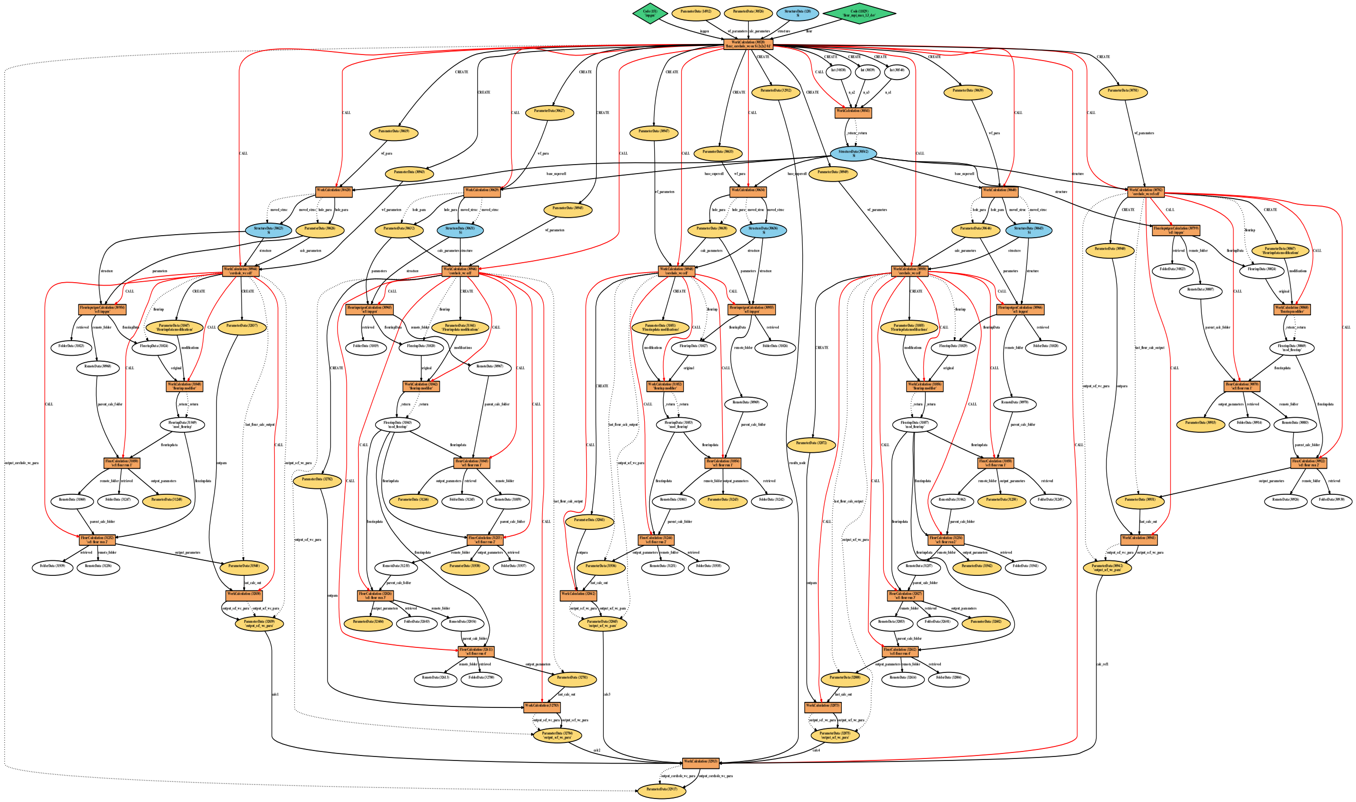

Fig. 3.12.: Core-hole workflow database provenance graph. This graph displays the nodes produced by a run of the core-hole workflow to calculate 2p binding energies of a Si single crystal. Four SCF workflows are run on super cell setups.

3.1.4. XPS Spectra Visualization App

Exposing a large database with different kinds of data to diverse audiences with various interests in the data is a challenge. Enabling everybody to see all the data in all its complexity is not wanted. Surely different target audiences need diverse interfaces to the data. One possible way to accomplished this feat is over little apps, tailored to the target audience which allow for specialized fast queries on a data subset. All larger *ab initio* databases like ALFOWlib, the Materials Project, OQMD, Materials Cloud, NOMAD embed such apps in their web appearances. One way to build up a community-driven open-source app-store like platform would be to use some sort of (notebook) environment which can be interconnected. A first proof principle is here the NOMAD archive which uses beaker notebooks, or AiiDAlab [269] from the work section of Materials Cloud, which deploys Jupyter-notebooks using an app mode extension for Jupyter.

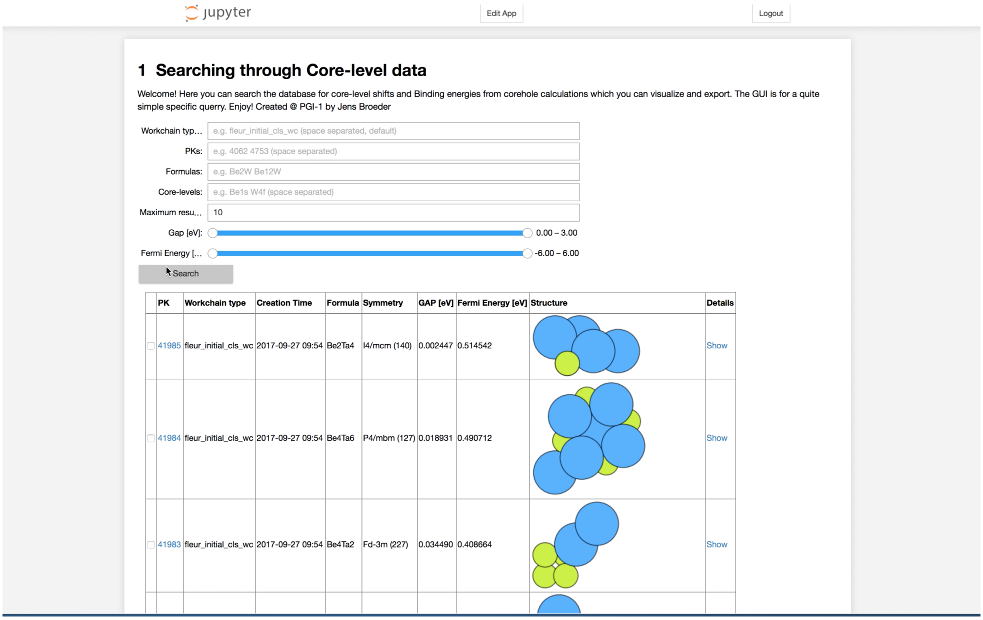

1 Searching through Core-level data

Welcome! Here you can search the database for core-level shifts and Binding energies from corehole calculations which you can visualize and export. The GUI is for a quite simple specific querry. Enjoy! Created @ PGI-1 by Jens Broeder

Workchain typ…: e.g. fleur_initial_cls_wc (space separated, default)
PKs: e.g. 4062 4753 (space separated)
Formulas: e.g. Be2W Be12W
Core-levels: e.g. Be1s W4f (space separated)
Maximum resu…: 10
Gap [eV]: 0.00 – 3.00
Fermi Energy [… -6.00 – 6.00

	PK	Workchain type	Creation Time	Formula	Symmetry	GAP [eV]	Fermi Energy [eV]	Structure	Details
☐	41985	fleur_initial_cls_wc	2017-09-27 09:54	Be2Ta4	I4/mcm (140)	0.002447	0.514542		Show
☐	41984	fleur_initial_cls_wc	2017-09-27 09:54	Be4Ta6	P4/mbm (127)	0.018931	0.490712		Show
☐	41983	fleur_initial_cls_wc	2017-09-27 09:54	Be4Ta2	Fd-3m (227)	0.034490	0.408664		Show

Fig. 3.13.: Jupyter-notebook app to search through core-hole spectra data in the AiiDA database. The small app contains jupyter-widgets to specify a composition content based query that will be executed on the underlying AiiDA database. The output is displayed in an HTML table which allows for selection of results to receive additional insights or to plot them.

As a proof of principle example a small Jupyter-notebook app to explorer core-level shift

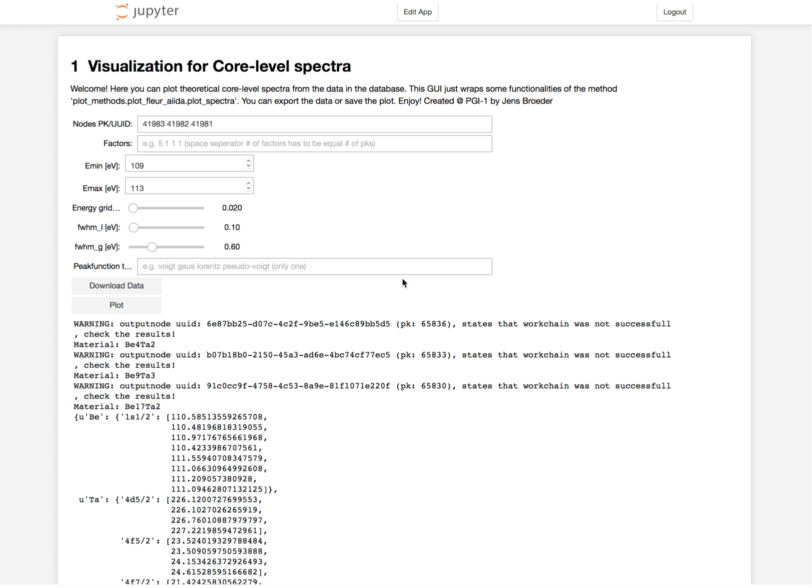

1 Visualization for Core-level spectra

Welcome! Here you can plot theoretical core-level spectra from the data in the database. This GUI just wraps some functionalities of the method 'plot_methods.plot_fleur_aiida.plot_spectra'. You can export the data or save the plot. Enjoy! Created @ PGI-1 by Jens Broeder

Nodes PK/UUID: 41983 41982 41981
Factors: e.g. 5.1 1 1 (space seperator # of factors has to be equal # of pks)
Emin [eV]: 109
Emax [eV]: 113
Energy grid... 0.020
fwhm_l [eV]: 0.10
fwhm_g [eV]: 0.60
Peakfunction t... e.g. voigt gaus lorentz pseudo-voigt (only one)

```
WARNING: outputnode uuid: 6e87bb25-d07c-4c2f-9be5-e146c89bb5d5 (pk: 65836), states that workchain was not successfull
, check the results!
Material: Be4Ta2
WARNING: outputnode uuid: b07b18b0-2150-45a3-ad6e-4bc74cf77ec5 (pk: 65833), states that workchain was not successfull
, check the results!
Material: Be9Ta3
WARNING: outputnode uuid: 91c0cc9f-4758-4c53-8a9e-81f1071e220f (pk: 65830), states that workchain was not successfull
, check the results!
Material: Be17Ta2
{u'Be': {'1s1/2': [110.58513559265708,
                   110.48196818319055,
                   110.97176765661968,
                   110.4233986707561,
                   111.55940708347579,
                   111.06630964992608,
                   111.209057380928,
                   111.09462807132125]},
 u'Ta': {'4d5/2': [226.1200727699553,
                   226.1027026265919,
                   226.76010887979797,
                   227.2219859472961],
         '4f5/2': [23.524019329788484,
                   23.509059750593888,
                   24.153426372926493,
                   24.615285951666682],
         '4f7/2': [21.42425830562279,
```

(a)

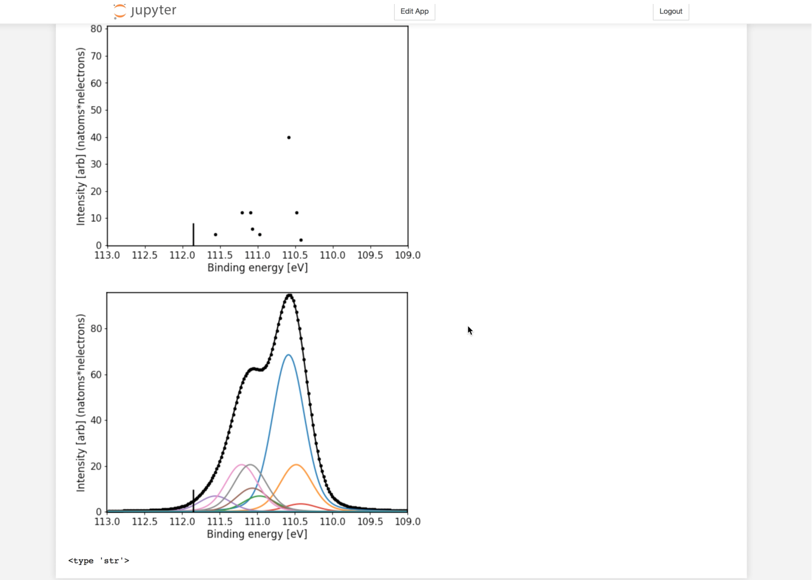

```
<type 'str'>
```

(b)

Fig. 3.14.: Jupyter-notebook app to visualize core-hole spectra data. From the results of different systems any composition of mixed spectra can be constructed with different peak functions, resolution and broadenings. The app displays the constructed spectra as well as the *ab initio* data set from which it was generated and allows for extraction of these data and theoretical spectra.

data was developed and is shown in Fig. 3.13. The first notebook interfaces a small special query of the underlying database for successful core-level workflows and displaying the query results in an HTML table. With Jupyter widgets the user can refine the query. For example the user can decide what elements or formulas he wants to find results for. Furthermore, the workflow type, number of returned results, band gap, Fermi energy and core levels can be specified to refine the query. Through clicking a button the query is executed and the results rendered within an HTML table with some basic information from the database and a preview of the crystal structures. From this table the user can display in detail results about certain runs or select as many results as wanted and construct a theoretical spectrum for them. The spectrum visualization is provided by the functionality of a second notebook shown in Fig. 3.14. This Jupyter-notebook app plots the core-level shifts results from selected database entries. Furthermore, the app displays the raw data and constructs a simple theoretical spectrum from these core-level shifts by the broadening of the shifts through peak functions. Through Jupyter widgets the notebook allows the user to weight results of database entries and to specify the energy range of the plots, the peak function type and parameters of the peak functions like the gaussian or lorentzian broadenings. The data for the constructed spectrum can be downloaded, exported via a download button.

3.2. Fitting XPS Spectra from a Complete *ab initio* Dataset

In the theory sections (2.9.1 and 2.9.2) it was laid-out what challenges lie in the chemical interpretation of X-ray photoelectron spectra and which spectral properties can be calculated from *ab initio* methods, in particular with the `FLEUR` code. In section 3.1.3 the turn-key solution workflows were explained which enable among such spectral properties the calculation of core-level shifts and binding energies.

While comparing simulations results to experimental data we realized that theoretical information on the chemical shifts and the binding energies alone is often not comparable to traditional fit results in the case of most XPS spectra of beryllides. Thus having only theoretical chemical shift data helped little with the chemical interpretation of the spectra. The following reasons for this were identified. One compound can have several different chemical environments of the same element due to the symmetries of the crystal. For example in the case of $Be_{12}Ti$ (I 4/mmm) there are three different Be atom symmetry types with four Be atoms each in a unit cell. These Be atom-types turn out to have each a different core-level shift. Having spectral contributions from several symmetry types per element is not new and long known in the chemistry community for molecules or surface core-level shifts. Though for solids there is mostly one reported shift per compound and element in the numerical XPS databases like NIST [90]. While for molecules the individual chemical environments can be very distinct in their response, for solid state spectra of metals the chemical shifts are often to close together to be fitted separately within the resolution of the experiment. Mathematically the sum of two peak profiles at different means and areas is not a peak profile function again. In general, the sum lies outside of the profile function set and one cannot expect parameters resulting from experimental fits and to some extend reported literature values to be comparable to theoretical predictions of core-level shifts and binding energies for materials with several diverse chemical environments of the same element (at least within the accuracy needed).

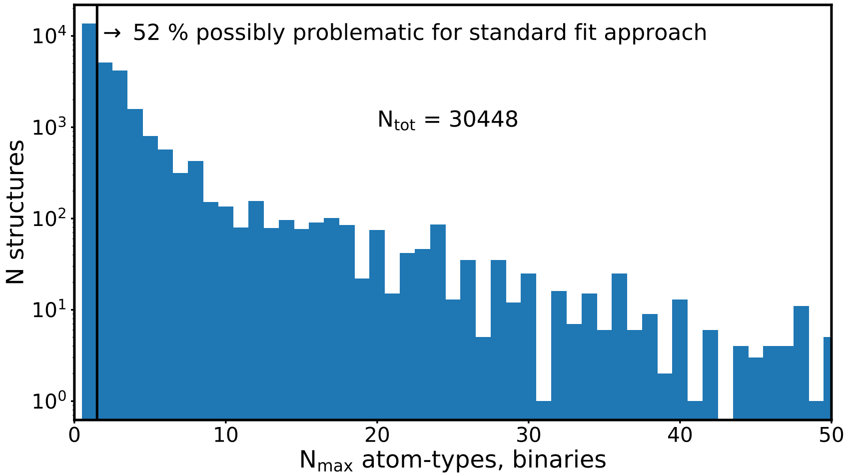

Fig. 3.15.: Number of atom-types by symmetry (non-equivalent atoms) of ~31000 binary structures from the ICSD in an logarithmic histogram. The atom-types are determined with spglib using 'equivalent_atoms'. 52 % of the structures have more than one atom-type per element. A larger number of atom-types increases the complexity and problems of the traditional XPS fitting procedures.

Of the ~31000 structures of the non-unique binary compounds in the ICSD around 52 % have at least one element in several symmetry positions and possible different chemical environments (see Fig. 3.15). This fraction will likely increase for larger and complexer structural configurations like ternary compounds and beyond. The number of atom-types was determined with spglib [178]. While for 48 % of the binaries there is no problem with the traditional fitting approach, for the rest it should be applied more carefully, which is marked by the black line in the histogram. For more precise information on where problems are expected the structures have to be filtered for uniqueness, trash structures have to be sorted out through *ab initio* calculations and the chemical shifts for the atom-types have to be calculated.

Since the fit parameters are often neither comparable to theoretical predictions nor to literature values of individual phase components it can be argued that the interpretation of the traditional experimental fitting approach with nearly no constraints and no a priori knowledge of mixed systems cannot lead to a successful chemical interpretation of phase content for complex spectra. The traditional evaluation approach works well for materials with one effective chemical environment per element and where the chemical shift of a compound is well separated from other chemical shifts in the phase diagram. If the full form of all individual pure phase spectra is experimentally known, the fit parameters can be reused for the evaluation of the phase content [78]. Such a procedure is slow, cost intensive and applied in some specific (industrial) applications where a lot of similar spectra are evaluated.

As a way out of this problem theoretical spectra are constructed within this work and then fitted directly to experimental data with more constraints and a priori knowledge. In order to construct such a theoretical X-ray photoelectron spectrum from chemical shifts and binding energies which can be curve fitted to experimental data directly, two kinds of information are required. First, the absolute binding energies of all chemical environments from all phases that might contribute to the spectrum and second an intensity contribution factor for each chemical environment of these phases to the spectrum. *Ab initio* simulations can provide the binding energies and/or chemical shifts. The chemical shifts are converted into absolute binding energies with respect to an elemental experimental, or theoretical, binding energy reference $E_{\mathrm{B,\,ref}}$ of the core state of interest. The intensity contribution is estimated with the knowledge of the crystal structure via the number of atoms of the same element per non-equivalent atom-type multiplied with the number of electrons from the core level contributing to the spectrum.

A theoretical *ab initio* spectrum fit function $S_{\mathrm{theo}}(E)$ is constructed in detail as follows,

$$S_{\mathrm{exp}}(E) = S_{\mathrm{theo}}(E) + B_{\mathrm{exp}}(E) \tag{3.1}$$

$$S_{\mathrm{theo}}(E) = \sum_{i=1}^{N} \lambda_{\mathrm{i}} \Phi_{\mathrm{comp,\,i}}(E) \tag{3.2}$$

$$\Phi_{\mathrm{comp,\,i}}(E) = \sum_{j=1}^{M} \alpha_j V_j(E, \mu_{\mathrm{j}}, f_{\mathrm{G}}, f_{\mathrm{L}}) \tag{3.3}$$

$$V_j(E, \mu_\mathrm{j}, f_\mathrm{G}, f_\mathrm{L}) = \frac{\mathfrak{Re}\left[\omega\left(\frac{\sqrt{\ln(2)}(2(E-\mu_\mathrm{j})-\mathrm{i}f_\mathrm{L})}{f_\mathrm{G}}\right)\right]}{f_\mathrm{G}\frac{\sqrt{\pi}}{2\sqrt{\ln(2)}}} \tag{3.4}$$

$$\mu_{\mathrm{j},\ell m} = E_{\mathrm{B,\,ref}} - C_{\mathrm{j},\ell m} \tag{3.5}$$

where $B_\mathrm{exp}(E)$ is the spectrum's background from the experiment, which has to be added to the theoretically constructed spectrum $S_\mathrm{theo}(E)$ for fitting (Eq. 3.1). $S_\mathrm{theo}(E)$ is a linear combination of N phases with a concentration fit parameter λ_i for each phase and its corresponding phase spectrum $\Phi_{\mathrm{comp,\,i}}(E)$ (Eq. 3.2). The phase spectra (Eq. 3.3) are constructed by weighting normed peak-functions V_j with an intensity factor α_j for each of the M chemical environments. In this work α_j is the total number of electrons of a core level contributing from all atoms from atom-type j (i.e., for a W 4f 7/2 core-state α_j would be 8 times the number of W atoms of type j). This assumption on the intensity information extracted from the contributing atom-types for solids is only valid if differences in the cross sections, angular dependence, other scattering properties, electron transport properties and the spatial photon density for the same orbitals on all atom-types throughout a unit cell are negligible. This might not be the case anymore for very large unit cells, since XPS is very surface sensitive. Effects like shake ups, satellites, Costa-Kronig may change relative intensity factors of certain core levels.

As peak function Voigt profiles V_j are deployed, while for transition metals the asymmetric LA line shape is applied (see equation 2.38 from section 2.9.1). A very accurate explicit (without convolution integral) representation of a Voigt profiles is possible through the Faddeeva function (ω), as shown by Eq. 3.4, where f_G, f_L are the Gaussian and Lorentzian full width half maxima and the profile mean is μ_j. The Faddeeva function is included in scientific Python packages. The full width half maxima, f_G, f_L, are also optimized in the fitting and are assumed within this work to be the same for all V_j for a certain core-level and for all phases i. The mean μ_j is the binding energy of the chemical environment j. *Ab initio* chemical shifts $C_{\mathrm{j},\ell m}$ are converted into absolute binding energies with respect to an elemental, binding energy value $E_{\mathrm{B,\,ref}}$ of the core state of interest (Eq. 3.5). These theoretical or experimental elemental reference binding energies have uncertainties from ~0.06 eV up to 0.6 eV in the NIST XPS database [90]. Therefore, the reference energy may need to be optimized within its uncertainty. This optimization is also helpful to compensate differences in the energy scale calibration from the experiment to the reference measurement. Furthermore, fitting the reference binding energy allows for compensation of systematic errors of the *ab initio* data. In the fits shown in Section 4.3 only one reference energy per mixed phase core-level spectrum is fitted.

When fitting splitted core states only one peak is constructed with all degrees of freedom the other(s) are fitted with the same parameters and constant offset for the splitting. Phase concentrations of best fits for individual high-resolution spectra of the same sample are not enforced to yield the same results. Several core-level spectra from the same sample can be fitted at once for example the Be 1s and W 4f region of a Be-W alloy. This way the fit is enforced to use the same phase concentration ratios, reducing the degrees of freedom in the fit.

The spectra interpretation with this physically motivated fit can be automated, by beginning to fit all possible phases with the corresponding elements and sort out phases that do not contribute to the spectrum, then reiterate. Contribution is determined by the concentration values and their uncertainty. Chemical shifts of different phases may not be unique. If the intensity factors and chemical shifts are the same, the phase spectra become indistinguishable. This fit method in principle enables to find all these non-unique spectrum interpretations, i.e. linear dependencies. The fitting procedure needs less fit parameters than the current conventional way of fitting an X-ray photoelectron spectrum, making it beneficial and scalable for the interpretation of more complex spectra, with many different chemical environments. For very simple XPS spectra with phases with only one contribution, the number of fit parameters is the same as for the conventional way.

Notice, that still a complete chemical shift database and intensity estimation for the system of interest is necessary for a trustworthy interpretation. However, one advantage is that constraints from experimental knowledge (i.e., measured stoichiometry) can be incorporated into the fit. The proposed spectra construction does not contain any additional physics and features that might occur in XPS spectra as introduced in section 2.9 and described in [218] like satellites, plasmons, shake-up, shake-off, Auger peaks. Also currently a consistent background estimation is also not included in the fit. Overall, the fitting procedure may be advanced in ways to comprehend these needs too. For the fitted well-behaved beryllides spectra examined in detail within this work these issues are not relevant.

In retrospect the method has some similarities to the evaluation of XAS spectra reported in the work of K. Mathew et al. [140] in nature scientific data. The method has also advantages over pure experimental approaches which measure all single phase spectra to determine signal ratios like in [78]. This component-fit method is not the same as a Principal Component Analysis (PCA) [270], because our components are physical motivated, known and not altered or orthogonalized to constructed principal components. If our fit succeeds there is a direct chemical interpretation connected to it. Being pure mathematical a PCA usually goes the other way, to find similarities in a series of XPS spectra [271, 272] (functions), the resulting mathematical orthogonal principle components do not need to have any physical meaning and may not lead to a precise chemical interpretation [273] at all. The resulting principle components can even be partly negative and therefore unphysical. Our evaluation procedure and proof of concept led to a pending international patent application and is on the way to be published in a separate publication.

3.3. Method Development Sum-up

In order to enable provenance tracked *ab initio* all-electron high-throughput simulations the `FLEUR` code was connected to the AiiDA framework. This was accomplished through the implementation of AiiDA plug-ins and workflows. Workflows are powerful simulation protocols, containing expert knowledge. The `FLEUR` plug-ins, workflows and tools form together the AiiDA-FLEUR python package, which is open source under MIT license. Workflows and tools account for a high-level work environment, increase productivity by decreasing the required time to solution drastically. Basic workflows for everyday simulations with the `FLEUR` code were implemented. These workflows form the backbone of more advanced workflows like the implemented workflows to calculate core-level properties for X-ray photoelectron spectroscopy. Since these theoretical core-level properties were hard to compare for complexer chemical environments directly to traditional fit results of experimental spectra, we developed and implemented a first proof of principle tool to fit XPS spectra directly from *ab initio* data alone. This resulted in a pending international patent application and a small app to search and access the simulations results from a database for fitting spectra. The workflows, fitting procedure and the database access app lay out a first version for a scalable turn-key solution for XPS spectra. The spectral fitting has to be advanced in various ways for systems outside of the scope of this work and is not blindly applicable. For example the spectral background is not yet consistently determined within the fit itself. Also special peak area ratios, satellites peaks, shake-up, shake-off, and plasmon excitation contributions have to be removed currently from the spectra before hand, or accounted for somehow.

4. *Ab initio* Simulation Results

In the following sections selected *ab initio* simulation results are presented. The results are produced through the application of the developed methods, discussed in the previous chapter. During the three years of this work the `FLEUR` code evolved. The code robustness was significantly improved, due to vast bug fixes, fine tunning of algorithms and larger testing sets run through AiiDA. The deployment of continuous integration with unit tests avoids the breaking of code features in a fast developing environment. To make all-electron FLAPW high-throughput calculations a reality, besides robustness of the quantum engine, several challenges need to be tackled ranging from the choice of input parameters, over runtime prediction and parallelization, choice of computing resources to convergence strategies. The first sections of this chapter demonstrates how some of these problems are overcome to run a small high-throughput project on 5058 metallic systems to create a core-level shift database for metals. The high-throughput run is discussed in section 4.2. Selected results are discussed and compared to experiments in the later sections of this chapter.

4.1. Lessons from over 800 000 `FLEUR` Input Files

If starting from any structure file or node from any source, the input generator of `FLEUR` (`inpgen`) has to be invoked to generate an input file with some internal default FLAPW parameters. To make `FLEUR` enter the high-throughput highway first the input generator has to be as robust as possible and produce good working parameter defaults for a wide set of structures. Also criteria for reasonable FLAPW input need to be developed for high-throughput simulations.

In order to test and improve `inpgen` robustness, the whole Open Quantum Materials Database (OQMD) [55] was downloaded and all crystal structures stored into an AiiDA database, totaling 824912 structures. Then `inpgen` (version MaX 2 release from 2018) was executed on this structure set. Statistics about the number of atoms and symmetry information of the OQMD structure set is shown in the logarithmic bar charts of Fig. 4.1. Over 90 % of the structures have less than 10 atoms per unit cell and over 80 % belong to a cubical symmetry group. `FLEUR` input files were generated for all these structures. In the `inpgen` version prior of 2016 over 70 % of the executions on a subset failed, due to a variety of reasons. Also some code parts in `inpgen` scaled very badly with the number of atoms in the structure, resulting in run-times of several hours for structures with 500 atoms and more. Most of these issues

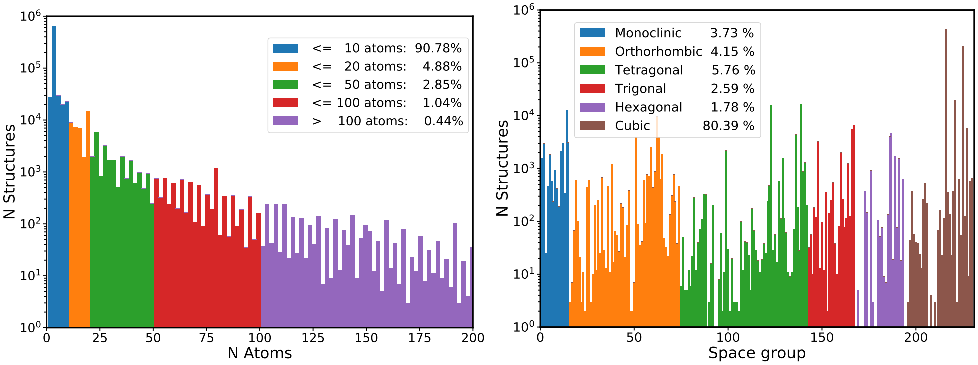

(a) **(b)**

Fig. 4.1.: Open quantum materials database (OQMD) content in terms of structure size (a) and space group number on a logarithmic scale (b). Small structures with less then 10 atoms make up the main database content 90.8 %. The largest structure has 1278 atoms. Also 80.4 % of the structures in the OQMD have a cubic symmetry.

have been fixed by the `FLEUR` developer team. Newer versions of `inpgen` take a couple of seconds at most to execute, tested for structures of up to over 10,000 atoms.

The OQMD structure set is also a simple high-throughout scaling test for AiiDA, since the full launch results in 824912 `inpgen` runs producing around 8 million i-nodes and 5.3 million database nodes to be managed in a short period of time. The current version of the input generator is capable of generating these input files with an error rate below 0.07 % (524 failed). This structure set is rather DFT friendly and has mostly been calculated with another DFT code (VASP). For an other heterogeneous crystal structure database, the Crystallography Open Database (COD) [134] the `inpgen` failure rate is above 1 %. Bringing this error rate closer to 0 is ongoing work. It took around eleven days to generate inputs for all the OQMD structures, and the bottleneck turned out to be the IO-speed of the Postgresql database on the hard disk drive and therefore also the current sequential storing behavior of AiiDA. In actual computing projects bottlenecks are rather the limitation of computational, or data resources and limited throughput capabilities of the computing infrastructure. If the infrastructure permits it, AiiDA is probably capable of managing around 1 million simulations per week.

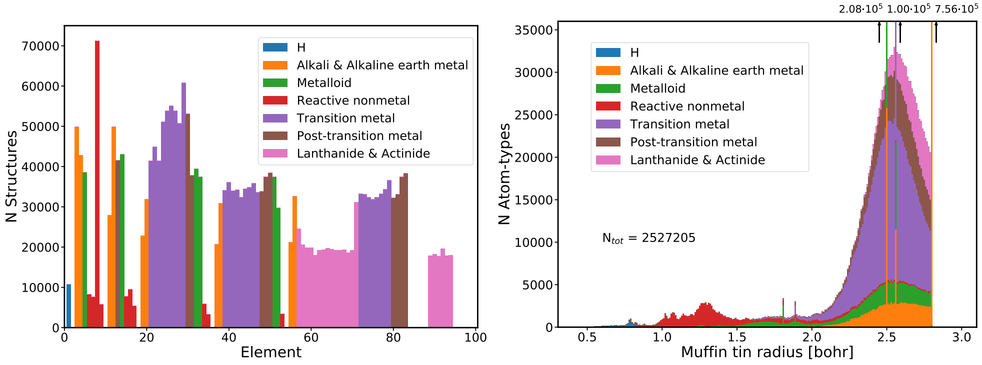

(a) **(b)**

Fig. 4.2.: From (a) is becomes apparent that most of the elements in the periodic table until the Actinides are represented in structures of the OQMD. In (b) the distribution of determined Muffin tin radii for different element types is shown to the fixed maximum muffin tin radius of 2.8 a_0.

From this OQMD input file set one can investigate quantitatively now the default FLAPW parameters chosen by `inpgen` and derive strategies to improve them. The collection of FLAPW parameters, especially muffin-tin radii distributions for the elements, provide helpful guidelines for choosing these parameters in material screening projects, and when comparing total energies or other quantities with an FLAPW parameter dependence. In the first sub figure of Fig. 4.2 a linear distribution of the elemental content in the OQMD structure set is shown. Nearly all elements except the noble gases or very heavy elements (proton number 84-87,>94) are represented non evenly in the set. The different element categories of the periodic table are colored in the histogram. The same coloring is applied to the second sub figure of Fig. 4.2 displaying the overall cumulative distribution of all chosen muffin-tin (MT) radii (in total >2.5 million.). From the distribution of default MT radii it becomes apparent that nearly all very small MT radii, smaller than 1.5 a_0 (bohr radii) come from hydrogen or reactive non-metals like Carbon, Nitrogen, or Oxygen. Intermediate muffin-tin radii (1.5 a_0-2.0 a_0) are from a small mixture of reactive non-metals, metalloids and first transition metals. By far the most chosen default MT radii are (>2.0 a_0), while the distribution peaks around 2.5 a_0. There are three muffin-tin values which stand out from this distribution. The first two at 2.49 a_0 and 2.55 a_0 are probably due to the structure set. The last one at 2.8 a_0 marks the largest MT radius which is chosen by the `FLEUR` code cutting of the distribution.

The resulting average muffin-tin radius determined by `inpgen` with one standard deviation is displayed in Fig. 4.3 for all elements as a periodic table plot. The average muffin-tin radii for all elements is depicted with a color heat-map[1] from blue (smallest) to yellow (largest). These colors underline the same picture as the previous distribution, i.e., that the small MT radii come from H, C, N, O, F, P, S elements and that all heavier elements including the 4f and 5f are very close to the maximum `FLEUR` MT radius of 2.8 a_0. This periodic table of MT radii helps with selecting fixed MT radii for a material screening run. To work for most of the materials one would choose a 2-4 sigma MT radius for each element, if this value is still reasonable. Visualization and exploration of such larger data set are best done interactively in a web visualization, since it is impossible to condense all the information into one plot. For example by clicking on the periodic table one could show the distributions of FLAPW for the respective element with additional information and filter options.

A birds eye perspective on the FLAPW basis set cutoff parameters determined by `inpgen` for the OQMD structure set is shown in Fig. 4.4 by two logarithmic histograms. The histogram in Fig. 4.4a shows the distribution of the atom dependent radial function basis set cutoff ℓ_{max}. From the histogram it becomes apparent that the only values ℓ_{max} is set to are 6, 8 and 10. While for 82.7 % of the OQMD ℓ_{max} is chosen to be 10. This version of `inpgen` never choses odd ℓ_{max} cutoffs and also no smaller cutoffs than 6 or larger cutoffs than 10. The second logarithmic histogram in Fig. 4.4 displays the plane wave basis set cutoff k_{max}. Usual working values of k_{max} lie between 3.5 ${a_0}^{-1}$ and 6 ${a_0}^{-1}$. The minimum chosen plane wave basis set

---

[1] bokeh: Plasma256 palette

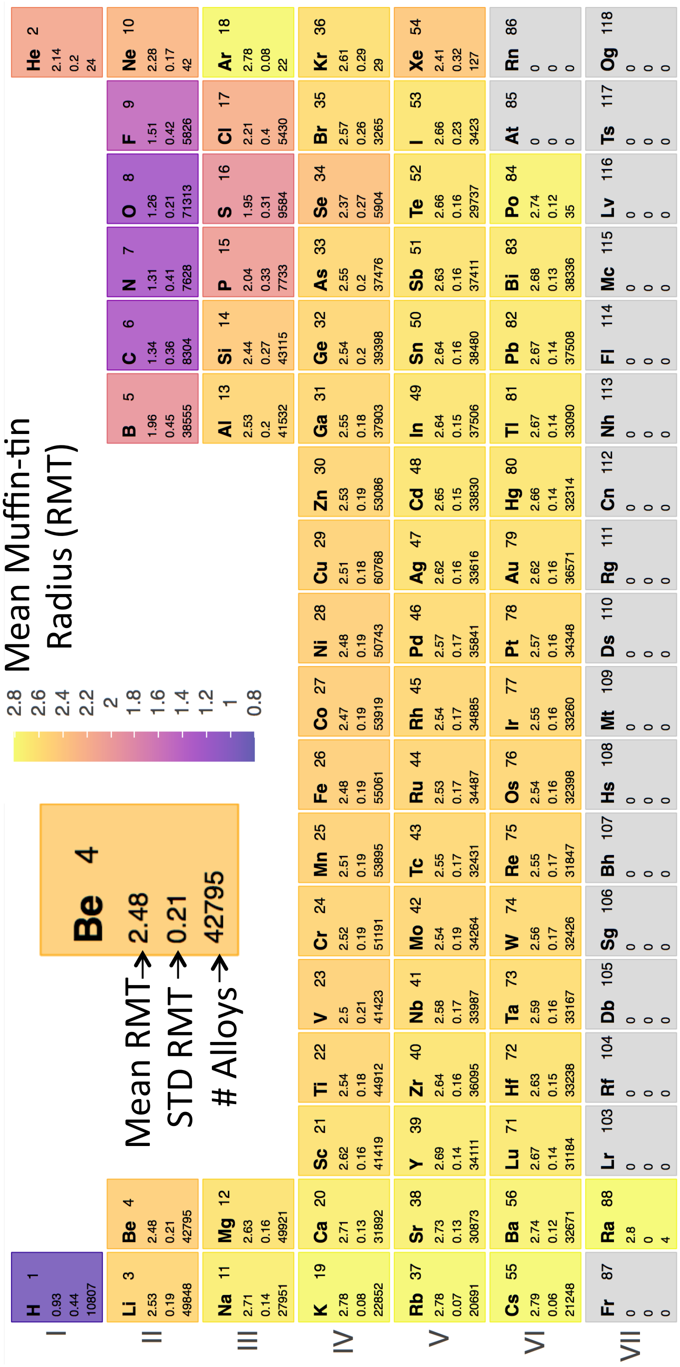

Fig. 4.3.: Mean values of muffin-tin radii (RMT) and standard deviation (STD) determined by `inpgen` for structures in the OQMD.

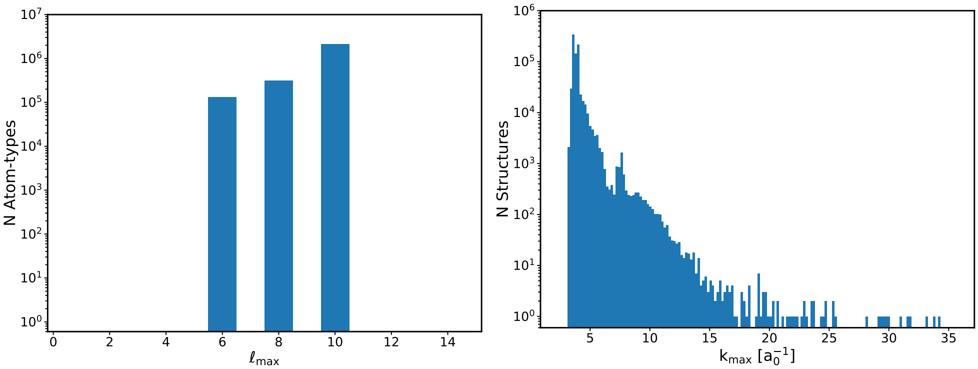

(a) **(b)**

Fig. 4.4.: Two logarithmic histograms showing the default basic cutoff choices for the OQMD structure set. In (a) the distribution of the radial basis cutoff $\ell_{\max}$ makes clear that per default $\ell_{\max}$ is either 6,8, or 10. The cutoff for the plane wave basis $k_{\max}$ clearly varies a lot more as is shown in (b). No $k_{\max}$ smaller than 3.3 $a_0{}^{-1}$ is chosen.

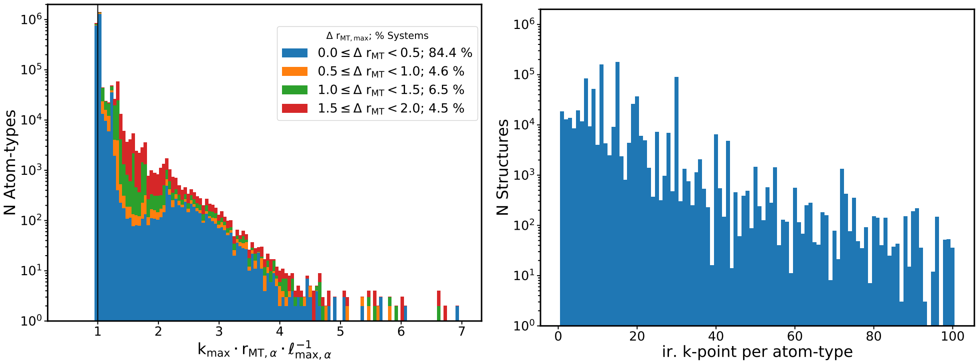

(a) **(b)**

Fig. 4.5.: Number of basis function in the interstitial with respect to number of basis functions in the Muffin tin. Values much large than one or lower than one, might lead to matching problems in the FLAPW method. The default K-point density (1/A) for the structures is shown in (b). It is an important convergence parameter in DFT calculations.

cutoff is 3.3 $a_0{}^{-1}$. Values of $k_{\max}$ larger than 7 $a_0{}^{-1}$ are probably problematic and correlate with smaller MT radii, because `inpgen` tries to fulfill to some extent equation 4.1. In the

FLAPW method it is reasonable for a good matching on the muffin-tin sphere boundaries to have similar sizes in the basis function set inside the spheres and in the interstitial region as explained in [81]. Otherwise the muffin-tin boundary matching equations will be over or under determined.

$$\ell_{\mathrm{max}} = k_{\mathrm{max}} \cdot r_{\mathrm{MT}} \tag{4.1}$$

Equation 4.1 expresses a criterion on the basis cutoffs to achieve this. The criterion is soft, i.e. should be roughly fulfilled. For reasonable FLAPW parameters the basis set inside the sphere should not be larger than the basis set in the interstitial region. It is also not always possible to fulfill this criterion equally well for every elemental species in the structure, because elements can vary largely in their muffin-tin radii and ℓ_{max} cutoffs, but there is only one $\mathrm{k}_{\mathrm{max}}$ for the whole system. Currently `inpgen` determines the $\mathrm{k}_{\mathrm{max}}$ accordingly to the atom-type with the smallest r_{MT} of the system. A logarithmic histogram of this basis size criteria for the OQMD set is shown in sub figure 4.5a. Most systems have a value of 1.0 or close to 1.0, i.e. they have similar basis set sizes in and outside the MT spheres. Values below 1.0 and much larger than 1.0 might lead to stability issues in the FLAPW algorithms.

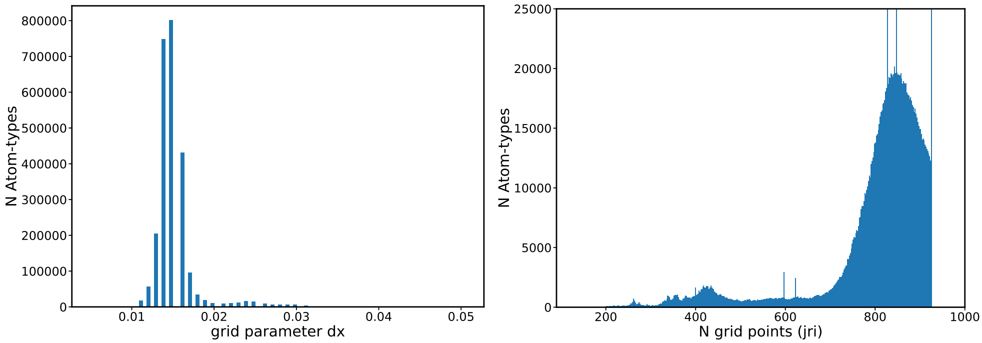

(a) **(b)**

Fig. 4.6.: Histograms for the muffin-tin mesh parameters. In (a) the chosen values for exponential grid spacing factor dx are shown with most of them being between 0.01 and 0.02. The number of grid points chosen for the OQMD set is shown in (b). This distribution correlates with the chosen muffin-tin radii.

Another convergence parameter in DFT calculation is the density of k-points in the irreducible Brillouin zone. It is known that some physical systems or investigated properties require a denser k-mesh then others to yield highly accurate results. In material screening efforts it is well established to use a similar k-point density for all systems and to have different fine-grained mesh levels for certain accuracy levels. For the Materials Project [39] k-point

densities of mostly 500/atom or very high accuracy 1,000/atom are used. The OQMD [55] deploys gamma centered k-point meshes with 4,000 to 8,000 k-points per reciprocal atom (KPPRA). These mesh values are not for the irreducible Brillouin zone.
An indicator for the k-point density produced by the `inpgen` and the `FLEUR` k-point generator for the OQMD set is displayed in sub figure 4.5b. The figure shows all chosen k-point densities in terms of k-points per atom-type in the irreducible wedge of the Brillouin zone (IBZ) in a logarithmic histogram. Apparently there is a wide spread from for the default number of k-points per atom in the irreducible Brillouin zone (IBZ) and probably for the k-point density. The default k-point density should have a similar value for different accuracy levels and should not fall below a certain threshold value. Overall, Fig. 4.5 points to two possible ways where the default parameter choice for `FLEUR` might be improved towards stability.

Since we are interested in core-level shifts the mesh choice within the muffin-tin spheres plays a role. Distributions of muffin-tin grid parameters are displayed in Fig. 4.6. In sub figure 4.6a the chosen values for the exponential grid spacing factor d_x are shown with most of them being values between 0.01 and 0.02. The number of grid points chosen for the OQMD set is shown in the histogram of sub figure 4.6b. The number of grid points distribution correlates with the chosen muffin-tin radius from Fig. 4.2.

Quantity	Value	Comment
Structures from OQMD	824,912	not checked for uniqueness
Successful `inpgen` runs	824,388	does not mean input will work for `FLEUR`
Failed `inpgen` runs	524	problems determining correct symmetries
Total size of all inp.xml files	11 GB	This is once, AiiDA-FLEUR stores twice
Total disk space repository	90 GB	Less overhead in AiiDA versions >= 1.0
Size repository tar.gz	4.6 GB	Took longer than 2 days
i-nodes on disk	19 mio.	Less overhead in AiiDA versions >= 1.0
AiiDA version	0.12.2	
AiiDA database schema	SQL alchemy	compact, because of json fields
AiiDA-FLEUR version	0.6.2	Python 2
Nodes in AiiDA database	4.2 mio.	performance starts to slow
AiiDA database size on disk	13 GB	

Tab. 4.1.: This table sums up some details of the AiiDA, Inpgen scaling test by generating `FLEUR` input for the whole OQMD.

Another lesson from this structure set is that `inpgen` always finds the same amount or less symmetries than spglib. This lies in the algorithm how `inpgen` finds the symmetry operations. There are always numerical cutoff parameters needed in such an algorithm which need tuning. One does not want to find more symmetries then the structure has, less will only waste computational time. Also `inpgen` finds a maximum number of 48 symmetry operations, since super cell structures are not fully symmetrized by `inpgen`.

Collected overview information about this input file investigation for the OQMD database and the resources it took are shown in Table 4.1. Such a project may already be a challenge for storage, because of the number of files and i-nodes on disk it produces with the deployed version of the software stack.

Overall, from the input file investigation can be concluded that AiiDA scales to millions of simulations per week, that the newer `inpgen` versions are very robust but a further fine tuning might still improve the error rate and increase the number of symmetries found. Also it became apparent that the FLAPW default parameters determined by `inpgen` are not always good and should not be blindly trusted for all systems. For FLAPW high-throughput projects there is a necessity to build strategies to improve and check the quality of FLAPW input parameters, before calculations are launched. This dataset might be useful in this regard and a guide for possible places for improvements. Also this study showed that for any high-throughput project on more than 10,000 crystal structures awareness of the underlying data storage infrastructure is needed.

4.2. Material Screening: Creating a Core-Level Shift Database

The developed methods, workflows, knowledge about core-level shifts and FLAPW parameter choices all come together in a small material screening project discussed in this section.

For the project all known stable binary metals from the Materials Project (MP) [39] were extracted to wider test the robustness of the `FLEUR` code (MPI develop version 11.2018) [79] and the initial core-level shifts workflow. The purpose of the project is to create a database of core-level shifts for XPS spectra fitting of binary metals. The criteria are that the compound has to be a stable binary metal, meaning in detail that it has to be predicted to be stable with <50 meV/atom close to the convex hull by the VASP code and its bandgap has to be 0 eV. On the materials Project database this query returned 5058 binary structures. This amounts probably to a large portion of all solid state binary metals experimentally known, since the ICSD contains in total 31000 non-unique binaries, including non metals. Possible formation of additional binaries and ternaries may be found in studies [274] applying the AFLOW framework or the OQMD.

The contents of this extracted structure set is displayed in Fig. 4.7 as an element-element half matrix plot. Elements like noble gases and very heavy radioactive elements for which

Fig. 4.7.: Content overview on all 5058 stable binary metallic phases from the Materials Project. The coloring indicates the number of metallic phases in each binary system, ranging from 0 to 32 phases. Core-level shifts and formation energies have been calculated with the `FLEUR` code for most of these systems.

no binary materials were found in the MP database are not included in the matrix plot. The coloring indicates the number of binary phases, ranging from 0 to 32 for each binary combination in the dataset. Every system with more than 10 phases is colored in dark green. The structures have been relaxed with the VASP code in the MP project. Therefore, they are assumed good enough as they are.

The structures are not further tested within this work to be completely force relaxed or if their cell parameters are optimal, since uncertainties on chemical shifts from a 1-2 % lattice constant mismatch is rather insignificant compared to other uncertainties [257]. Also checking this more carefully would increase the number of SCF to be run within and therefore the run time of this project by a factor 10-40.

In order to calculate initial-state core-level shifts for these binary structures, elemental crystal structure references are also required. For this all 1271 non unique elemental crystal structures at normal pressure were extracted from the ICSD.

To reach high accuracy in the core-level shifts, the same FLAPW parameters have to be used for the reference calculation and the respective element in the compound. For this an FLAPW parameter set was determined which would work for nearly all of the compounds. This parameter set was fixed per element and is displayed in a periodic table plot in Fig. 4.8 including fixed electronic configurations with local orbitals. All compounds with f elements or containing elements to have likely magnetic moments among others Fe, Co, Ni, Cr, Mn for which `FLEUR` switches magnetism on per default, are calculated with collinear magnetism. All calculations are performed with the core tail correction, spin-orbit coupling included and the normal relativistic core solver of `FLEUR`, not the fully relativistic core solver. Therefore, magnetism does not lead to further fine splittings of core levels. The coloring of the periodic table plot has the same color scheme and scale as in Fig. 4.8 and corresponds to the muffin-tin radii values. The muffin-tin radii were selected such that they work for most structures in the binary and elemental data set. Depending on the element this choice corresponds to a muffin-tin radius for the light elements within one standard deviation and for the 4f and 5f elements up to six standard deviations of the default muffin-tin parameters of the OQMD structure set in Fig. 4.8.

The number of grid points within the muffin-tin spheres was fixed for all systems to 981 points. The grid spacing d_x, and the basis cutoff parameters ℓ_{max}, $\mathrm{k}_{\mathrm{max}}$ were not fixed, but determined by `inpgen`. The resulting distributions of ℓ_{max} and $\mathrm{k}_{\mathrm{max}}$ for the binary metals is shown in Fig. 4.9 on a logarithmic scale. The ℓ_{max} for most atom-types is like for the OQMD structure set 6, 8 and mostly 10. The $\mathrm{k}_{\mathrm{max}}$ distribution for the metals with fixed r_{MT} is much more narrow as for the OQMD set. Values for $\mathrm{k}_{\mathrm{max}}$ range from 3.2 $a_0{}^{-1}$ to 7 $a_0{}^{-1}$ with 98.9 % of the systems having a cutoff below 5 $a_0{}^{-1}$ and 70.4 % having a $\mathrm{k}_{\mathrm{max}}$ smaller than 4 $a_0{}^{-1}$, which is quite reasonable. The small amount of systems with $\mathrm{k}_{\mathrm{max}}$ values larger than 5 $a_0{}^{-1}$ correspond again to small r_{MT} like for the elements H, O, N, C. As the muffin-tin radii were fixed, and ℓ_{max} is not much varied by `inpgen` the basis set size cutoff relationship for matching the basis function on the muffin-tin boundaries is less flexible.

The results for the matching criterion from equation 4.1 is shown in Fig. 4.10 as a logarithmic

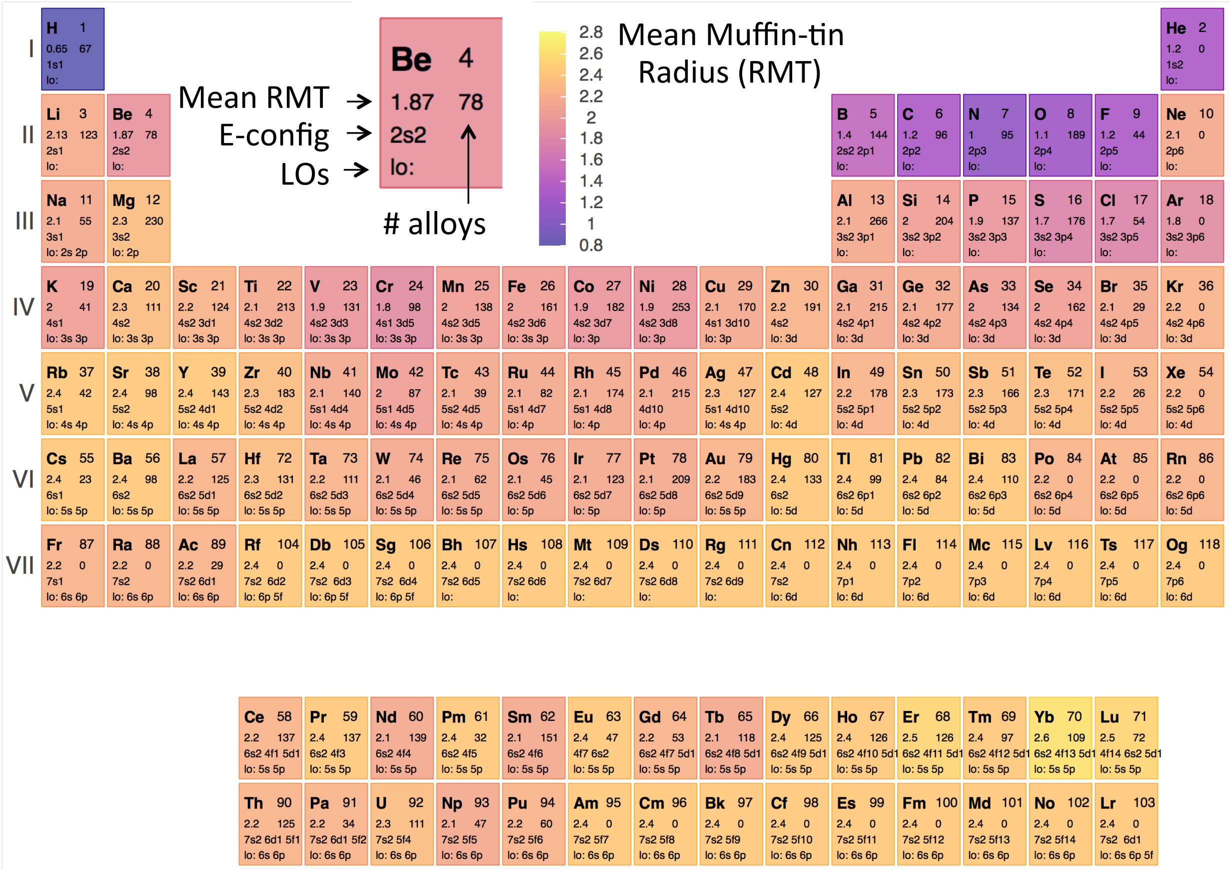

Fig. 4.8.: The chosen muffin-tin radii, electronic configuration and local orbitals for all elements is displayed in a periodic table. This parameter set was applied in the screening with `FLEUR` of the stable binary metallic phases from the Materials Project. The coloring of the elements indicates the muffin-tin radius and the color scale is comparable to Fig. 4.3.

.

distribution along side a logarithmic distribution for the resulting k-point density per atom-type. Most of the system have a value below 1.0 meaning they have more basis function inside the spheres than there are basis functions in the interstitial. Larger difference in muffin-tin radii between elements lead to matching criterion values far away from 1. For the OQMD set before this was different, the criterion for the inpgen defaults was always larger then one. The difference comes from fixing the Muffin-tin radii. This shows that one should be more careful when fixing muffin-tin radii of elements if the basis cutoffs are not flexible enough per default.

The K-point meshes were chosen as Monkhorst packs [275] such that the reciprocal spatial K-point distance is at least 0.2 Å^{-1} in each spatial direction. The resulting number of K-points per atom-type in the irreducible wedge of the Brillouin zone is shown in Fig. 4.10b. Overall this value varies over a wide range.

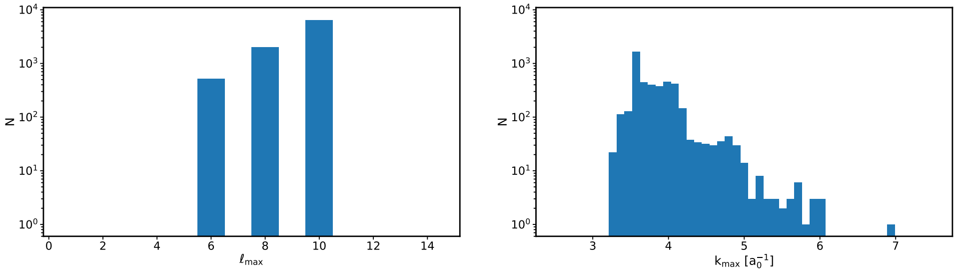

(a) **(b)**

Fig. 4.9.: Two *logarithmic* histograms showing the basis cutoff choices determined by `inpgen` for the binary structure set. In (a) the distribution of the radial basis cutoff $\ell_{\max}$ shows that $\ell_{\max}$ is either 6,8, or 10. The distribution of the cutoff for the plane wave basis $\mathrm{k}_{\max}$ is shown in (b). It varies from 3.2 $a_0{}^{-1}$ to 7 $a_0{}^{-1}$, while 98.9 % of the systems have a cutoff below 5 $a_0{}^{-1}$ and 70.4 % have a $\mathrm{k}_{\max}$ smaller than 4 $a_0{}^{-1}$.

Now, that the FLAPW parameter set is fixed, one shot SCF workflows are launched on all the elemental crystal structures without relaxing the crystal structures. Out of these 1271 elemental SCF simulations 1114 did succeed. The elemental structures with the lowest total energy per atom are used farther as references in the core-level shift and for the formation enthalpy calculations of the binary structures. In the first round of the binary structures a initial-state workflow was run on the 4702 crystal structures containing less than 35 atoms, the others 356 structures contain more then 35 atoms.

For the SCF runs on the small structures the maximum wall-time limit was 20 hours and a maximum of 240 iterations in the self-consistency cycle is allowed. The maximum allowed

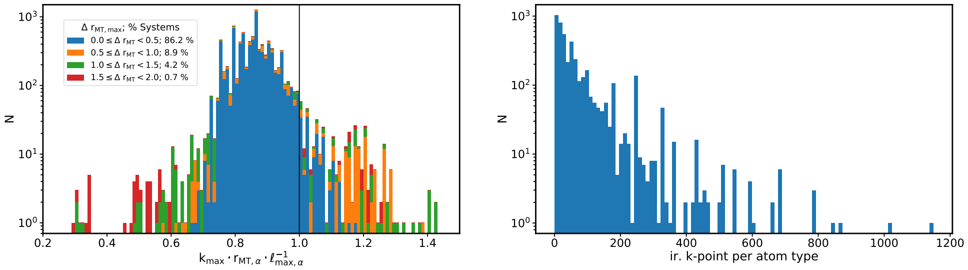

(a) **(b)**

Fig. 4.10.: In (a) the criterion for matching at the muffin-tin boundaries for the chosen FLAPW parameters of the binary metallic structure set is shown. It is optimal if the basis cutoff for the interstitial times the muffin-tin radius of atom-type α is approximately equal to the cutoff for the muffin-tin basis. Values much large than one or lower than one, might lead to matching problems in the FLAPW method. The coloring indicates the differences in muffin-tin radii in the structure. In (b) the resulting number of K-points per atom-type from the chosen K-point density of $0.2\,\text{Å}^{-1}$ for the structures is shown. It is an important convergence parameter in DFT calculations.

computational resources per SCF were 10 nodes on the JURECA supercomputer [276]. Though for most of the small systems the SCF workflow decided to use one compute node. From the 4702 small binary systems 29 (0.6%) failed due to `inpgen`. 171 (3.6%) systems failed with some `FLEUR` error message, 67 (1.4%) failed due to other causes. The most common `FLEUR` failures include an unphysical or broken potential which results in a 'differ' error message. From the non-failed simulation subset not every charge density converged.

In Fig. 4.11 the convergence endpoints of the charge density distance and the total energy difference to the previous iteration on a logarithmic scale are shown for all 4435 binary systems and all 1114 elemental systems. 73.86 % (withing the green box of Fig. 4.11) of all `FLEUR` calculations reached the convergence cutoff criterion of $5\cdot10^{-6}$ me/a_0^{-3} in less then 240 iterations or before running out of granted wall time. The convergence rate of 86.22 % for the 3127 non-magnetic systems is better than the convergence rate of 57.93 % for the 2422 magnetic calculations. 9.93 % of the systems did not converge at all (charge distance >0.5 me/a_0^{-3}, black box of Fig. 4.11), with 82.6 % of these being magnetic calculations. Partially converged systems amount to the other 16.20 % of all systems while non magnetic calculations amount to 37.3 % of the partially converged systems. This should be seen with care and as a snapshot in time. There was a hybrid parallelization resource requesting mistake leading to a

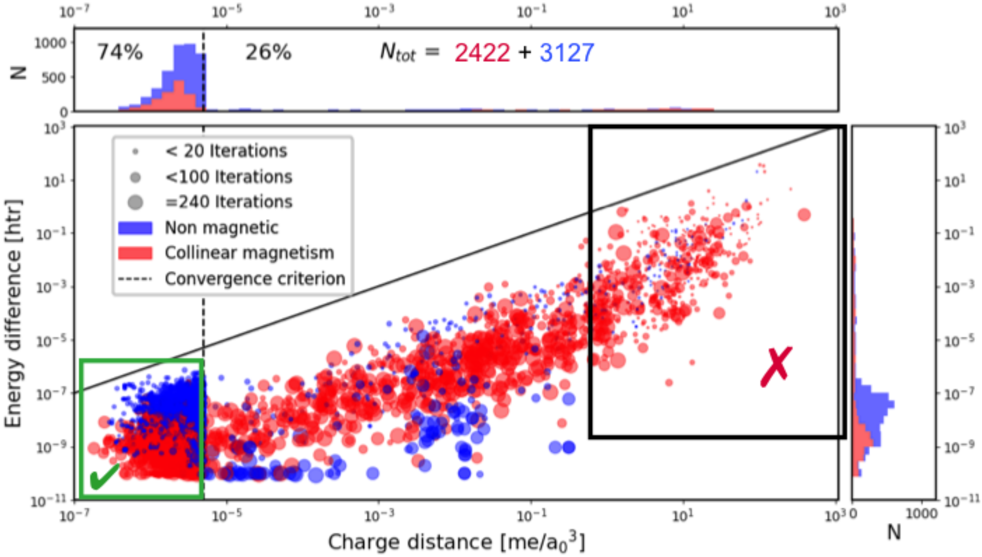

Fig. 4.11.: Charge density and total energy convergence behavior of `FLEUR` calculations on 4435 binary metals from the Materials Project and 1114 elemental structures from the ICSD. Most of the non magnetic (blue) and magnetic systems (red) converge in both quantities (green box). Around 16 % of the systems did converge partial and 10 % not at all (black box). Due to a computational resource assignment mistake, the 'real' converge rate is expected to be much better. Only 5 % of the systems did not converge within 240 iteration. The area of the markers indicate the number of iterations run.

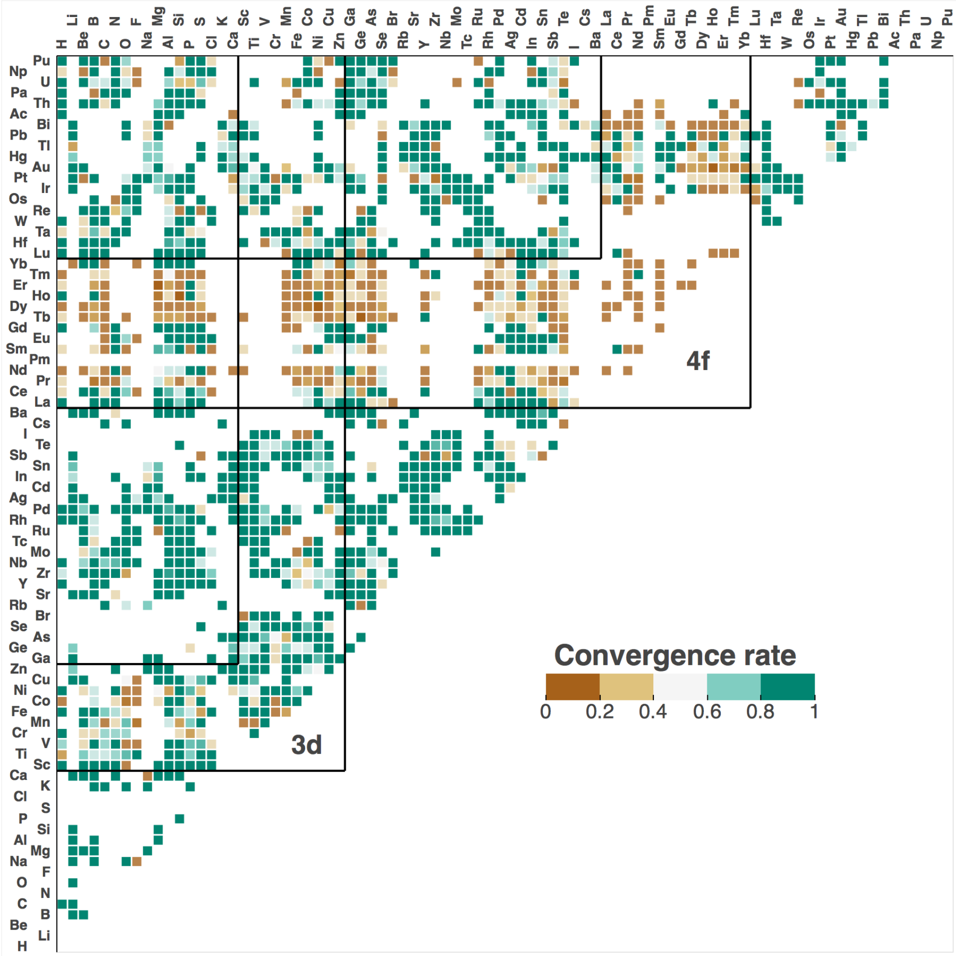

Fig. 4.12.: Matrix visualization of `FLEUR` convergence behavior of the 4435 small (<35 atoms) stable binary metallic phases from the Materials Project. The coloring indicates the relative convergence (brown to green) of the number of metallic phases in each binary phase diagram, with 0 (brown) meaning none and 1 (green) meaning all phases converged. Systems containing partially filled 4f element and to some extent systems with open shell 3d electrons have lower convergence rates.

gravely slowdown of `FLEUR` in certain cases. Therefore, the real convergence rate is probably a lot higher. Only 5.3% of the systems did not converged until they hit 240 iterations. While 17.6% of the systems ran less than 100 iterations and are not converged yet. Therefore, if most of these systems still converge the overall non-converge rate could be around 9% only instead of 26.14%. But this is still unclear until these systems are rerun with if necessary more resources. Collinear magnetic calculations are expected to be harder to converge, since the spin density has to be converged in addition to the charge density. Also the non-convergence of magnetic systems might correlate with the choice of the starting magnetic configuration as well as the fact that many of these systems contain open 4f shells.

A more detailed picture on which of the 4435 binary systems the SCF workflow managed to converge and which not, is gained from the matrix plot in Fig. 4.12. For each binary phase diagram the relative convergence rate from 0 to 1 is depicted. While a rate of 1 (green) means that the charge density converged for all metal phases in the corresponding phase diagram, a rate of 0 (brown) shows that no or a few phases converged. From this representation it becomes apparent that there are mainly convergence problems with magnetic calculation of the 4f systems with the chosen setup. The other cases are more distributed over all phases, while systems with open 3d shells systems which are generally calculated magnetic show also lower convergence rates. It is known in the literature that open 4f systems are challenging to describe correctly in standard DFT, like converging to the right magnetic ground state [277]. Converging the spin-dependent charge density becomes challenging, since the 4f electrons form localized bands close to the Fermi energy, resulting in an energy landscape with many local minima. There are several approaches to treat open f systems. One way within DFT is treating the f or d orbitals with the LDA+U method [254, 278, 279] to split them apart with an occupational dependent energy contribution, or the LDA+HIA approach [280]. It is beyond this work to automatize these approaches and to develop checks if the simulations converged into a physical accurate minimum. From the 1637 binary phase diagrams seen in the matrix visualization of Fig. 4.12 for 55% the diagram all phases converged, forming probably good data sets.

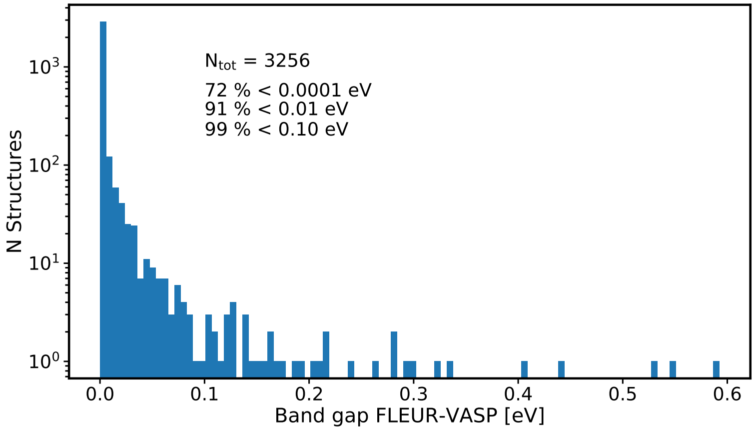

Fig. 4.13.: Logarithmic Histogram of bandgap results of converged `FLEUR` calculations of the small (<35 atoms) stable binary metallic phases compared to the results in the Materials Project database. 91 % of all phases have a bandgap smaller than 0.01 eV.

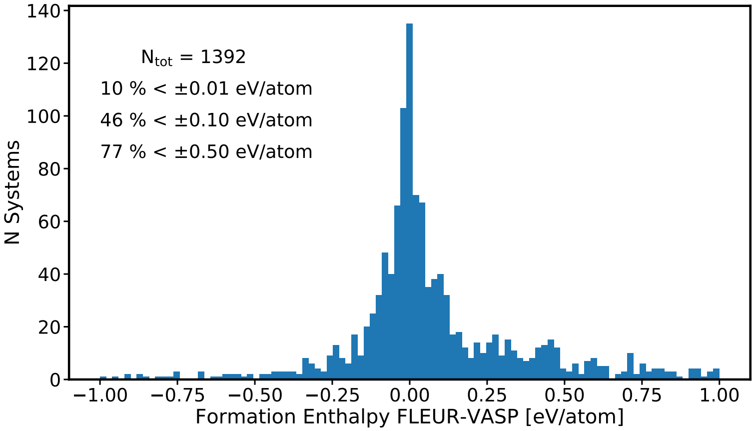

Fig. 4.14.: Histogram of formation energy results from converged `FLEUR` calculations of the small stable binary metal phases compared to the results from the Materials Project. Shown are the averaged enthalpy differences of all phases for each binary systems. For more detail see Fig. 4.15.

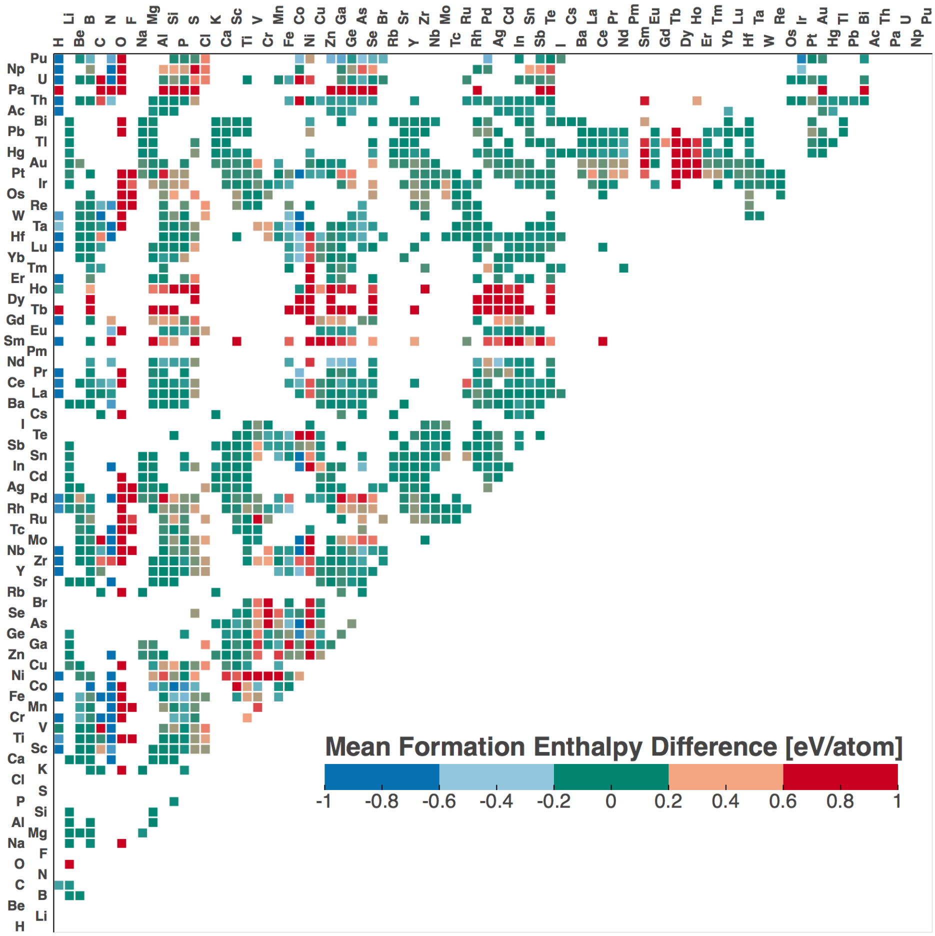

Fig. 4.15.: Matrix overview on `FLEUR` formation energy results of converged small stable binary metallic phases compared to the results from the Materials Project (VASP). The coloring indicates the averaged quantitative agreement in eV per atom of the metallic phases in each binary phase diagram.

To benchmark and understand the quality of the screening results from the binary metals, results of converged systems can be compared to data reported in the Materials Project pro-

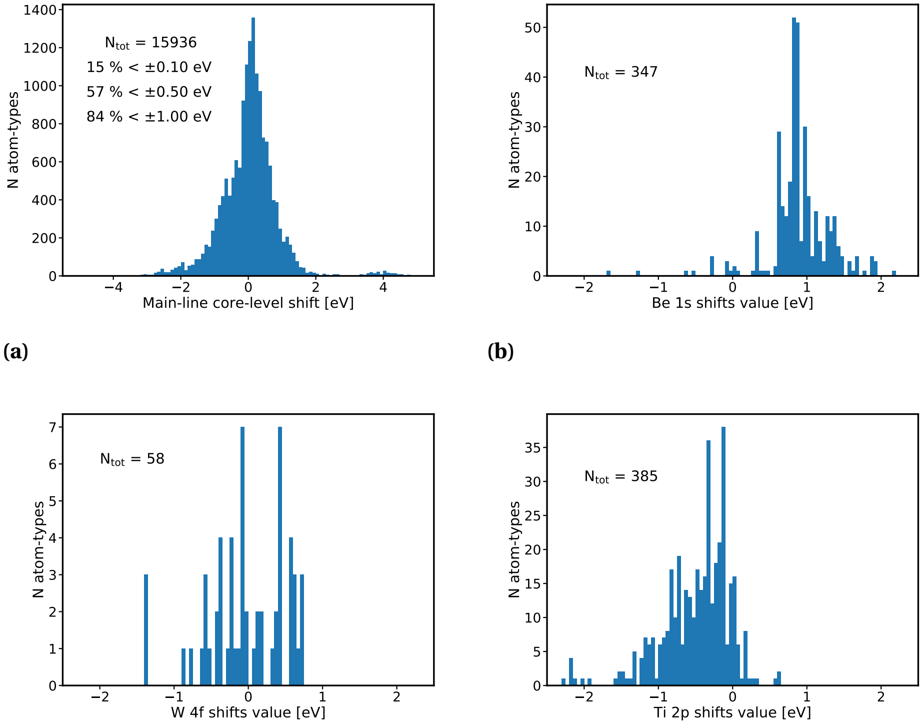

(a) **(b)**

(c) **(d)**

Fig. 4.16.: A birds-eye view on core-level shifts of the chemical environments of the converged binary metals is presented in these histograms. The distribution in histogram (a) contains all main-line core-level shifts for each atom-type. 15 % of all atom-types have a chemical shift smaller then 0.1 eV. The other three histograms (b, c, d) show the core-level shift contributions of the main spectral lines of certain elements. Be 1s core-level shifts (b) are most of the time positive with mostly lie between 0.5 eV and 1.5 eV. For W (c) the 4f doublet shifts show a wide spread, though there are not so many data points. The Ti 2p doublet shifts mostly to lower binding energy values. as is shown in (b).

duced with the VASP DFT program. First, it is checked if all metallic systems predicted by VASP have no bandgap in the `FLEUR` simulations. The bandgap difference for all converged structures is shown in the logarithmic histogram in Fig. 4.13. For 91 % of the 3256 structures the codes agree well and the `FLEUR` bandgap is smaller than 0.01 eV, where 99% of the structures have a `FLEUR` bandgap smaller than 0.1 eV. The other systems with a small bandgap should be investigated in detail. After confirming that no crude mistake was made one could find out if the change was because of the inclusion of spin-orbit coupling, or differences between an all-electron and a pseudo-potential method.

To gain more insight, we compare a more complex quantity like the enthalpy of formation, which value and accuracy depends on DFT simulations on three different structures, like the initial-state core-level shifts. Here systematic errors can occur, if for example the chosen reference structures are not the same. The matrix plot in Fig. 4.15 displays the difference in the enthalpy of formation per atom for each binary system averaged over all metallic phases in it. The formation energies for binaries with gases like H, N, O, Cl and so on are expected to be wrong, because they are not calculated so simple, but need correction terms [119]. From this matrix visualization one can spot the elements where the references is likely problematic since most binary systems containing that element have a large deviation from the VASP results, like for Pa, Ni and elements with open 4f shells. The information in the matrix of Fig. 4.15 is summed up by a histogram in Fig. 4.14. From the histogram it becomes clear that the spread of the distribution is quite large only around 11 % of all systems agree with vasp within 0.01 eV per atom. Half of the systems give the same enthalpy as VASP within 0.1 eV per atom.

The 4435 metals systems correspond to 23939 main line core-level shifts for different atom-types and structures and 208456 calculated core-level shifts in total. The 3256 converged systems yield a dataset of 15936 unique main line core-level shifts for different atom-types and structures with 137651 core-level shifts in total. For the unique main-line core-level shifts this amount is more than twice the number of unique main-line core-level shifts contained in the NIST XPS database [90]. An overview of all the main-line chemical shifts of binary metals is shown in Fig. (a) of Fig. 4.16. Metallic phases often have very small core-level shifts (84% are smaller than ±1 eV), but they can also be larger than ±2 eV for certain chemical environments. Overall, the distributions mean is around 0. and 15% of all core-level shifts are smaller than ±0.1 eV making these chemical environments indistinguishable within the experimental uncertainties from the elemental bulk material. The small visible peaks of core-level shifts of around 4 eV is an artifact of a wrong reference value for the elements Pa, Tb, N, O and F. For different elements the distribution of the chemical shifts can be totally different. In the sub figures (b,c,d) of Fig. 4.16 the chemical shift distributions are shown for the Be, W and Ti main core-level lines. Chemical shifts of 1s states of Be atom-types are likely to have a positive shift and the distribution peaks below 1 eV. In contrast the Ti 2ps rather have a negative chemical shift with a large spread peaking slightly below −0.5 eV. For the W 4f shifts the statistics is not very good, but so far they show a wide spread and contain shifts towards smaller binding energies as well as shifts towards larger binding energies.

To benchmark and understand the quality of the screening results from the binary metals and the quality of the applied core-level shift method, simulated core-level shifts are compared to the experimental literature. For this the XPS NIST database [90] was mined and the overlap to the screening materials determined by chemical formula. Therefore, the crystal structure or even phase content might differ between my results and experiments. From the 6300 unique chemical formulas in NIST the overlap to the screened non failed 4435 binary metals was 62 materials, of which 45 simulations converged. The 45 materials are: AgF, AgMg, Al_3Ti, AlB_2, AlMn, AlNi, AlTi, Au_2Ti, Au_3Cu, $AuCu_3$, AuMg, $AuTe_2$, Bi_2Mg_3, CdO, $CePd_3$, Co_9S_8, $CoSi_2$, Cu_2S, CuS, Fe_3Si, $FeSi_2$, GaNi, $GaNi_3$, HgS, HgTe, In_3Ni_2, $InNi_3$, InSb, MnN, MnSe, MnTe, MnZn, MoN, $MoSi_2$, $NbPd_2$, NbS_2, $NbSe_2$, $NdPd_3$, Ni_2Ta, NiTi, Pd_2Ta, Pd_3Sm, Pd_3Ti, PdSc and Pt_2Si. These materials have entries for 133 core-level shifts in NIST, partially reported directly in the experimental literature. These 133 core-level shifts are compared to the screening results in Fig. 4.17.

The experimental data is quite uncertain and there are known problems with numerical XPS databases [247, 248]. The applied initial-state method with one shot SCF `FLEUR` calculations seems to work quite well for the prediction of small chemical shifts in metals between -1 eV and 1 eV. It seems so far to fail to predict larger core-level shifts in metals right. But with such little data and such a spread in the data it is impossible to conclude that the method predicts metallic shifts well within high accuracy. For a better evaluation of the quality of the data one should compare directly to high resolution experimental spectra, like it is done in section 4.3.

A sum up of resources needed for this small prove of concept screening project is given in Tab. 4.2. Such a small project is not a challenge for AiiDA, the database with 0.5 million nodes is not large yet, but in this AiiDA version with the Django backend the size of the database is already quite large, which is seen in the time needed for queries on the database. The simulations took 2 weeks to execute with the throughput capabilities available to a single user on JURECA. Due to a mistake in resource requesting for hybrid jobs `FLEUR` ran slower than expected and the computational time used is probably a lot larger than what would be needed. With a better performance prediction of `FLEUR` such bottlenecks or suboptimal usage might become detectable. All the files which were stored for longterm from the project took around 1 TB of disk space. Where the 'out.xml' files and 'last_cdn.hdf' take each around 120 GB. This one TB of data could be reduced by further deleting, or grouping smaller files. Keeping only the 'out.xml' files and deleting the 'out' files. Also removing some iterations from the output files or the eigenvalue write outs can decrease the storage footprint further.

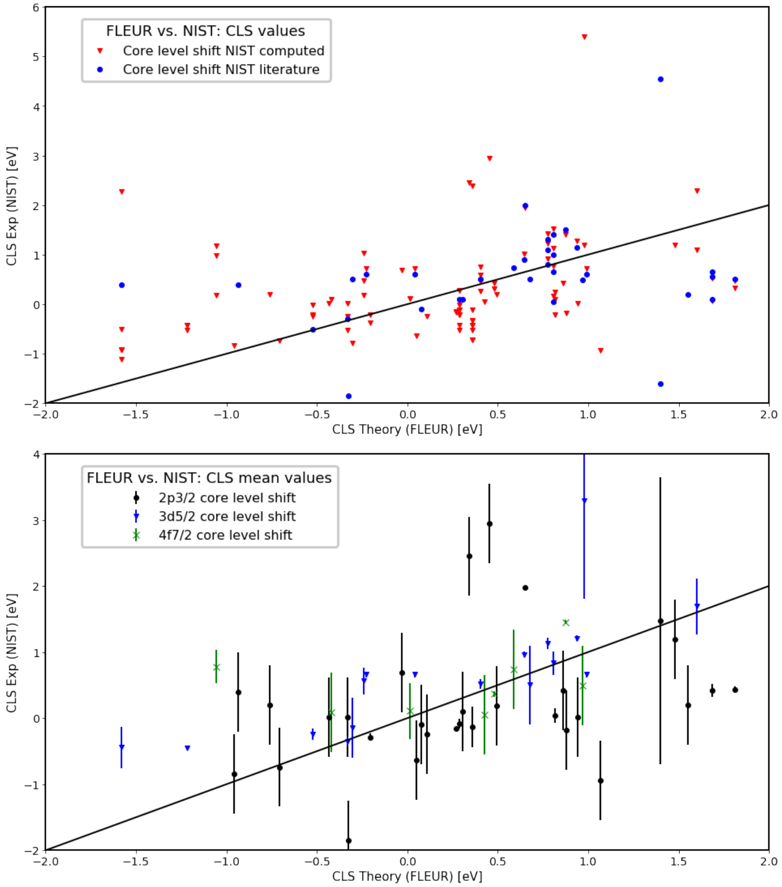

Fig. 4.17.: Comparison of the screening results with overlapping entries of the NIST XPS [90] database. In (top) 133 core-level shifts reported in the literature (blue) and computed from literature reported binding energies (red) are compared to the calculation results with the `FLEUR` code. In (bottom) a comparison of 55 experimental mean values for core-level shifts from NIST XPS entries of 45 binary metallic compounds is shown. Different core-level types differ in color. Data points represent mean values from the NIST database, with the error bar being the standard deviation on the mean value or 0.6 eV for single values.

Quantity	Value	Comment
Elemental structures from ICSD	1271	1132 < 21 atoms, 157 failed
Number of metals from MP	5058	355 contain >35 atoms
Number of initial-state workflows	4702	
Number of SCF workflows run	5973	
Total Convergence rate	68.6%	<=5.0^{-6} me/a_0^3, real prob +15%
Total Non-convergence rate	24.3%	>5.0^{-6} me/a_0^3 within resources
Total Failure rate	7.1%	various causes
Size out.xml files	120 GB	total sum
Total disk space (repo)	990 GB	including other simulations
Total disk space (repo) tar.gz	295 GB	
i-nodes on disk	2.5 mio.	will be less with AiiDA > 1.0
`FLEUR` version	MaX 2 release +	with included bugfixes
AiiDA version	0.12.3	without rabbitMQ
AiiDA database schema	Django	no json filed support yet
AiiDA-FLEUR version	0.6.3	still on python 2
Nodes in AiiDA database	0.5 mio.	less overhead with AiiDA > 1.0
AiiDA database size on disk	34 GB	with json filed might become smaller
Total computational time used	800K core/hours	>80% wasted in wrong parallelization

Tab. 4.2.: This table sums up information of the small screening project of the metallic binaries from the Materials Project. Core-level shifts of these structures were calculated The resulting files from this project for long time storage take about 1 TB of disk space if uncompressed. A large contribution comes from the number of files (2.5 mio. i-nodes). The total execution time of the project was 2 weeks.

4.2.1. Data Quality and Robustness

With powerful frameworks like AiiDA it becomes very easy to produce a lot of data with different quality, precision and even trash. AiiDA itself already tackles this problem at the core by storing the full provenance enabling the implementation of quality checks in workflows or on the database itself, but overall the user has the responsibility. In the electronic structure community there have been efforts in recent years [120, 268] to develop methods for quantifying uncertainties and accuracies between different DFT packages, methods and experiment. In this work this broader issue was not touched, but the convergence behavior of the relevant quantities was investigated or known. Through this knowledge I believe most of the individual calculations to be accurate enough.

One should be skeptical about high-throughput results until quality measures are in place, since there can be systematic errors or biases in calculations or in on top data analysis. For example treating a certain element not in the right way, i.e wrong structure, or electronic starting configuration and so forth, would cause a systematic uncertainty. One source of systematic uncertainty for formation energies and core-level shifts is how the elemental reference structure was chosen. Calculating every elemental structure in the ICSD and using the one with the lowest energy per atom as a reference may not be the best choice. Structures with convergence problems were just excluded, which is certainly not optimal. For example there was a systematic uncertainty found for the reference of Beryllium. Systematic errors from data analysis on top of calculations can be corrected without rerunning all simulations, as long as there is no problem with the individual runs. In this context it might make sense to keep the data analytics part as separate from the calculations and modular as possible.

4.2.2. Conclusion and Outlook Screening

With a small prove of principle project of over 5500 crystal structures it was demonstrated that high-throughput calculation with the FLAPW method and the `FLEUR` code are possible. The results of the project, the performance of `FLEUR` (MPI develop version 11.2018) and the SCF workflow are a snapshot in time and should not be generalized so easily. The stability/robustness of `inpgen`, the `FLEUR` program and the workflow, can still be improved to decrease the failure rate of simulations, which was in total for this project around 7%. Errors need to be properly caught by `FLEUR` or the AiiDA-FLEUR package to avoid any loss of simulation data due to other failures. If certain failures can not be avoided but corrected for the workflow should do so.

Small mistakes can have large consequences in a high-level environment. Due to a one line hybrid parallelization job script mistake over 80 % of the computing time was wasted, making the runtime performance and convergence failure rate way worse than they are in reality.

To archive higher convergence rates of systems and more physical simulation results more expert knowledge of the FLAPW method like from [81] has to be included in the SCF workflow. This includes quality checks for FLAPW input parameters and output results, handling of `FLEUR` errors where possible, predicting the runtime of `FLEUR` and choosing a suitable hybrid parallelization for a given system. The usage of other mixing and preconditioning strategies in the workflow may improve convergence speed. Better starting points and handling of magnetic systems might improve convergence rates of magnetic systems. Automation of LDA+U and other features like smarter local orbital choice will help to improve the description of insulators and open shell f-elements. For physical accurate results measures for fidelity have to be found and implemented. Getting a converged result is the first step, deciding if this result is physical meaningful the next step.

The main line core-level shifts from the 4435 converged systems provide additional reference data for nearly as many systems as are stored in the NIST XPS database and the number of main line core-level shifts is more than double the number of core-level shifts in NIST XPS database. Though not all data is to be trusted as pointed out. As first trustworthy data set one can start with the data subset agreeing well with VASP calculations. What a complete set of core-level shift data of a material system can be used for is demonstrated in the following section.

4.3. Example: Fusion Relevant Materials

In Cadarache, Southern France, the so far largest nuclear fusion experiment is currently under construction. The International Thermonuclear Experimental Reactor (ITER, lat. 'the way') is a tokamak reactor type [281]. The first plasma ignition of ITER is planned to happen in 2025. The way towards the final goal of an industrial fusion reactor for mankind's sustainable CO_2 free energy needs is still long (see the eurofusion road map to 2050 [281, 282]). From the insights gained from ITER an even larger industrial prototype reactor (DEMO) is planned to be build. A fusion reactor is a very complex machine (for an impression see Fig. 4.18), posing profound challenges to science and engineering.

One fundamental aspect is the plasma-wall interaction [283] of the inner fusion reactor vessel and designing materials for withstanding the operation conditions of ITER, DEMO and reactors beyond. One material criterion is a low half-life for all activated isotopes and elements in the decay chain. For ITER the inner plasma-facing wall ('the blanket', $600\,\mathrm{m}^2$, see Fig. 4.19) will be coated with the light metal beryllium, because it features a rather high melting point and low tritium absorption, which is important for radiation safety issues. In

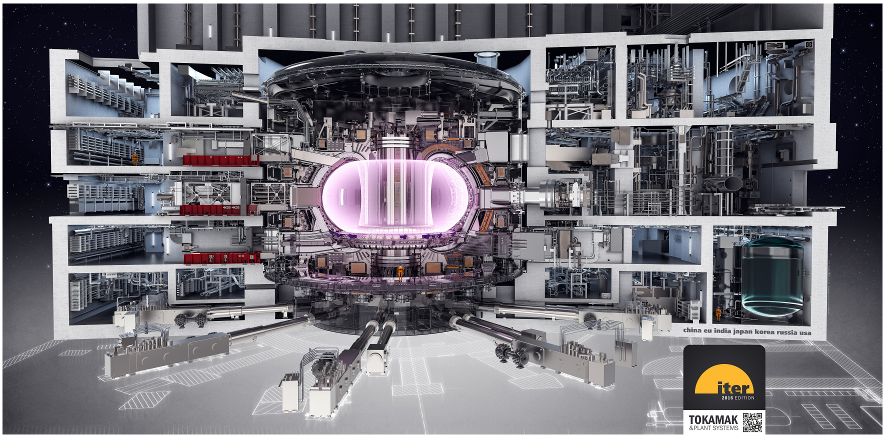

Fig. 4.18.: A computer model of the fusion reactor vessel of ITER with surrounding plant systems is shown. The tokamak type reactor will contain about 1 million parts, weigh roughly 23 000 tons and the vacuum vessel is 11.3 meters tall. The machine's scale can be estimated by comparing to the size of the person in orange standing in front of the reactor vessel. (Information and image taken from the technical section of the ITER website [281])

addition, when atoms from wall materials enter the plasma light element impurities have less impact on the plasma temperature than heavy element impurities [284]. Some parts of the 'divertor', an area at the bottom of the plasma vessel, will be coated with tungsten (see Fig. 4.19). This is necessary, since in the divertor, roughly 15% to 20% of the plasma's radiated heat has to dissipate with a heat load of up to 20 MWm^{-2}. Helium and other gases (fuel impurities) are removed in the divertor from the plasma and the plasma comes intentionally into contact with the divertor tiles [285] leading to high-flux particle bombardment and sputtering. Tungsten is the metallic element with the highest melting point of 3695 K and highest boiling point [286] with reasonable sputtering properties.

The inner wall will be bombarded by neutrons from hydrogen isotopes fusing to helium cores like in the fusion reaction in stars. Additionally the blanket tiles facing the plasma will be bombarded with H, He, Be, N, O and W ions and neutrals. Hydrogen and helium are part of the fusion reaction, nitrogen is inserted as seeding gas and oxygen originates from surface contaminations into the vessel. In principle all potential alloys of the elements involved in this system might form under certain circumstances. To ensure a long and save lifetime of the fusion reactor, it is crucial to understand what materials will form under which conditions

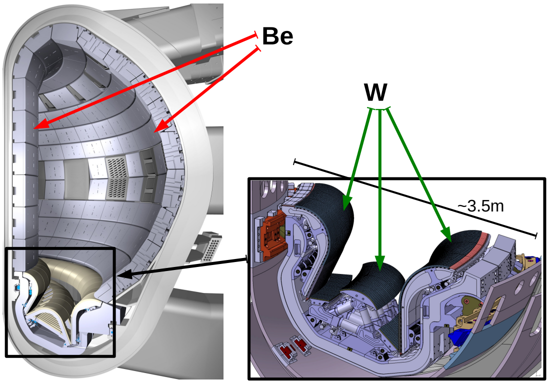

Fig. 4.19.: Vertical slice through a ITER vaccum-vessel computer model (left). The inner wall plates (blanket modules) will consist of beryllium (Be), indicated by the red arrows. The lowest region in the vessel, which is called the divertor (in more detail on the right), will be composed of 54 'cassettes'. Each cassette has target plates made of tungsten (W), indicated by the green arrows, facing the plasma. In the divertor, gases are removed from the plasma, which is accompanied by a lot of heat that has to be dissipated. (Combination of images taken from the technical section of the ITER website [281].)

and to determine their physical properties [281].

In experiments at the IEK-4, Plasma Physics Department of the Institute of Energy and Climate Research at the Forschungszentrum Jülich (FZJ), scientists study plasma-wall interactions among other material topics. With a variety of surface science methods these materials are characterized. For the identification of occurring material phases X-ray photoemission spectroscopy (XPS) is deployed among X-ray diffraction (XRD), ion scattering spectroscopy (ISS), nuclear reaction analysis (NRA) and Rutherford backscattering spectrometry (RBS). In this section *ab initio* results of different selected material systems are shown and the developed fitting method is applied to the chemical interpretation of XPS spectra.

4.3.1. The Be-W System

As mentioned above, Be and W are two interesting materials for a inner fusion reactor wall. Through material transport in a reactor vessel different phases might form over time and operation mode. This makes it crucial for the fusion community to understand the Be-W phase diagram and its physical properties.

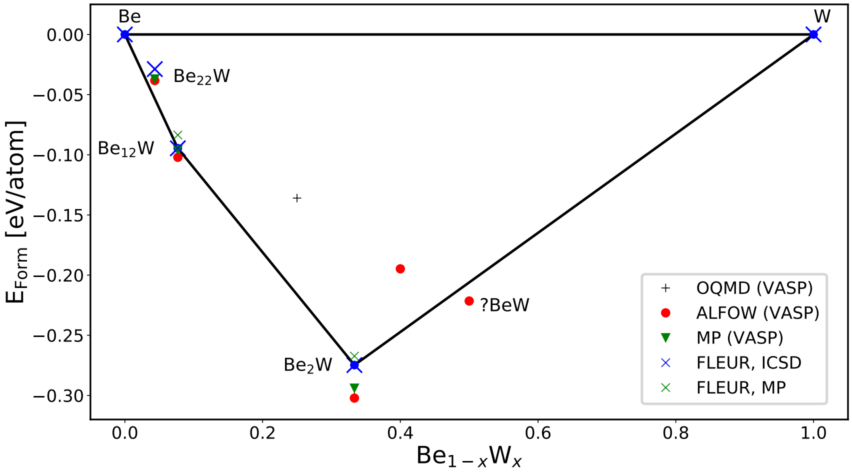

Fig. 4.20.: Convex-hull diagram of the Be-W system. While the Be_2W phase is energetically most stable the $Be_{22}W$ is predicted to be slightly metastable with 25 meV distance from the hull. For all results the PBE functional was used. There may be an additional stable BeW phase predicted by DFT (AFLOWlib [56]), which is currently experimentally unconfirmed.

There are three experimentally known phases Be_2W, $Be_{12}W$ and $Be_{22}W$ in the literature [287] and included in the metal database of this project. In addition, there may be a theoretical phase of BeW (predicted by AFLOWlib with VASP) which is experimentally not reported yet. The Be-W systems was investigated with DFT for various aspects in [288–291]. The most stable W phase has a basic centered cubic (bcc) symmetry and Be crystallizes in the hexagonal close-packed (hcp) structure. The convex hull diagram in Fig. 4.20 from our results makes it clear that Be_2W is the most stable phase predicted by DFT in terms of enthalpy of formation per atom for the Be-W system. Whereas, the reported experimental crystal structure of the $Be_{22}W$ system lies, at least for the PBE functional and the used Be and W crystal structure references, 25 meV above the convex-hull construction. This is in agreement with the experimental observation that it seems harder to synthesize a sample with $Be_{22}W$ than the other two stable phases [292, 293]. $Be_{12}W$ is predicted to be stable and does not lie on the connecting hull line from Be_2W and Be. Hence, making from an energetic viewpoint a pure phase preferable over mixed phases at the 12:1 stoichiometry. This behavior is different for $Be_{12}Ti$ and $Be_{12}Ta$

which lie on the hull line as will be discussed in other subsections. Overall, our formation energies are in agreement with findings from other DFT simulations from various databases. The findings from others are included in Fig. 4.20.

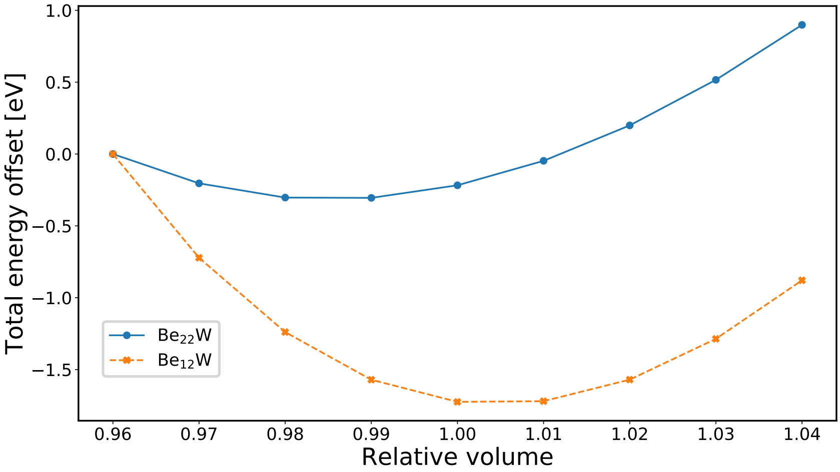

Fig. 4.21.: Equation of states calculated with the `FLEUR` code for all known stable Be-W systems. The bravais matrix was scaled and not the cell optimized under constraint volume. All energy volume curves are calculated using the PBE functional.

In order to check the quality of the experimental crystal structures and if they are well described by the PBE functional a Birch-Murnaghan equation of states for each phase was calculated with `FLEUR` and is shown in Fig. 4.21. The unit cells are scaled without optimizing the lattice parameters for each volume. The resulting ground-state volumes from a Birch-Murnaghan fit of $Be_{22}W$ and $Be_{12}W$ is 2% and 4% underestimated by DFT with the PBE functional. For Be_2W the ground-state volume is slightly overestimated by 1%. The equation of states results are summed up with the enthalpy of formation in Tab. 4.3.

Initial-state core-level shifts of the Be-W system were calculated. These core-level shifts and the number of corresponding electrons in the chemical environment are listed in Tab. 4.4. Core-level shifts on these systems calculated with an older version of the `FLEUR` code were reported in [257]. From the core-level shift and the corresponding atom-type information theoretical spectra can be constructed as proposed in section 3.2. Such theoretical ideal XPS spectra for the Be 1s and W 4f binding energy region are displayed in Fig. 4.22 for all Be-W

database identifier	symmetry group	material formula	enthalpy of formation [eV/atom]	(PBE) volume scale V/V_0
58754	P 63/mmc 194	Be_2W	-0.275	1.0142
109316	I 4/mmm 139	$Be_{12}W$	-0.095	0.9562
58755	F d-3mS 227	$Be_{22}W$	-0.029	0.9835

Tab. 4.3.: *Ab initio* enthalpy of formation for most stable compounds of the Be-W system. Volume scale V/V_0 gives the energetically most favorable unit-cell volume V with respect to the experimental volume V_0, calculated with the PBE functional.

material formula	Be 1s electrons	Be 1s DFT CLSs [eV]	W 4f7/2 electrons	W 4f DFT CLSs [eV]
Be_2W	4,2,2	1.16, 1.16, 1.07	32	0.74
$Be_{12}W$	8,8,8	0.57, 0.47, -0.08	8	0.02
$Be_{22}W$	4,12,24,4	0.65, 0.24, 0.05, -0.39	8	0.74

Tab. 4.4.: *Ab initio* results of all core-level shifts of most stable compounds of the Be-W system and how many 1s electrons contribute per each unit cell of these systems. Depending on the crystal symmetry there are several chemical environments resulting in different chemical shifts. None of these chemical shifts are currently experimentally known in the literature. From this data all XPS spectra containing a mixture of Be-W binary phases can be fitted.

phases. The W 4f spectra have a simple one peak form since each of the three stable phases has one W atom-type per unit cell.

From these theoretical results it becomes apparent, that from an XPS point of view the $Be_{22}W$ phase is predicted to be hardly distinguishable from the other two Be-W phases. Partly because the summed up Be 1s signal does not shift from the Be 1s metal binding energy for the $Be_{22}W$ phase. The 1s peak only becomes broader at the base and a little asymmetric. On top of this the W 4f chemical shifts are similar to the chemical shifts of the Be_2W phase making these two phases non distinguishable by W 4f peak form and position. From this work I recommend to always conduct a careful stoichiometric analysis in addition when looking for these phases. The W 4d doublet separation of 12.49 eV predicted by DFT agrees well with the measured separation of 12.50 eV [90]. The W 4p doublet splitting is calculated to be 67.79 eV is compared to the experimental value in the literature of 67.10 eV [90] overestimated by DFT.

From the Be-W *ab initio* data XPS spectra can be chemically interpreted. I reevaluated raw data from colleagues measured in 2005 which was partly discussed in [292, 293]. The

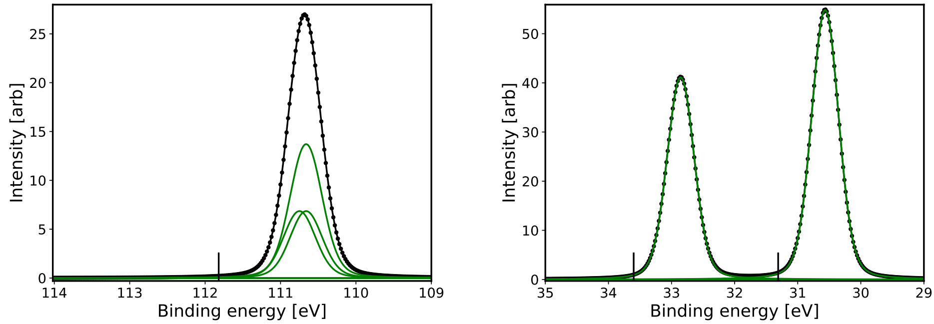

(a) Be_2W, Be 1s

(b) Be_2W, W 4f

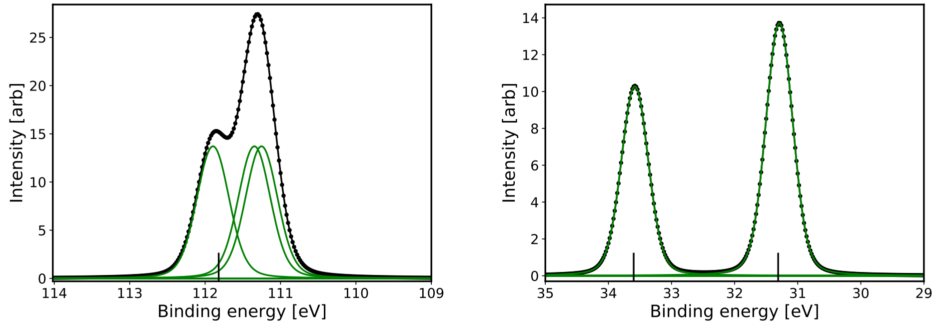

(c) $Be_{12}W$, Be 1s

(d) $Be_{12}W$, W 4f

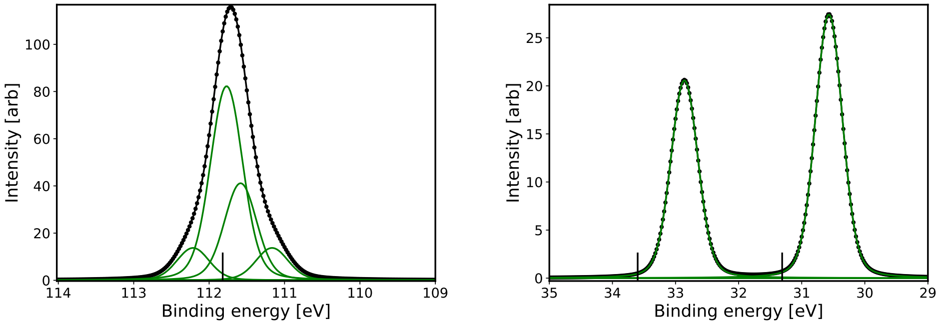

(e) $Be_{22}W$, Be 1s

(f) $Be_{22}W$, W 4f

Fig. 4.22.: Theoretical single-phase XPS spectra of Be 1s and W 4f from the three stable Be-W alloys Be_2W (a), $Be_{12}W$ (b), and $Be_{22}W$ (c). The spectra are constructed from the *ab initio* chemical shifts and the atom-type information in Tab. 4.4 of one computational unit cell. All Voigt profiles have a Lorentzian FWHM of 0.1 eV and a Gaussian FWHM of 0.43 eV. Binding energies of the elemental reference are marked with horizontal lines.

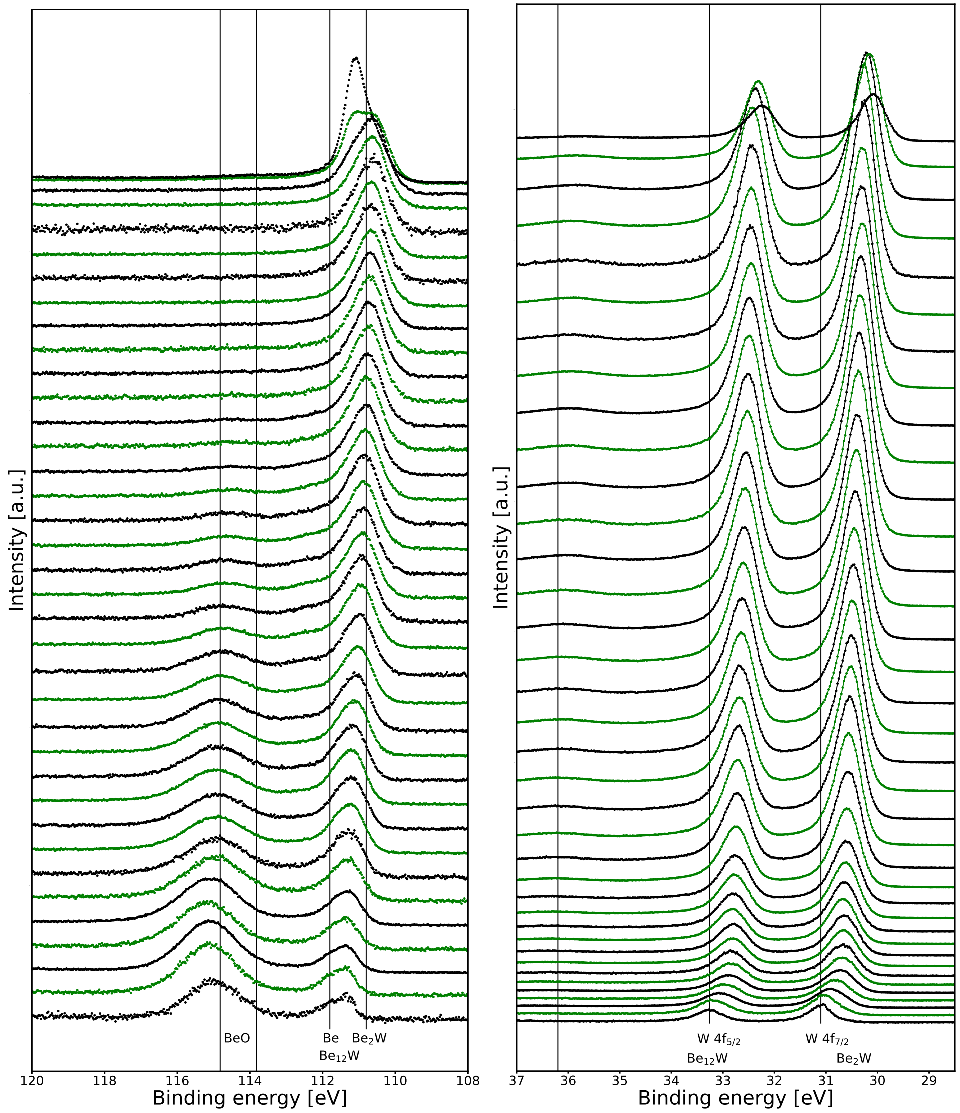

(a) Be 1s spectra

(b) W 4f spectra

Fig. 4.23.: Experimental raw data from a depth analysis with sputter XPS of annealed W on Be. Label positions indicate calculated spectral positions of Be-W alloys. On the left a Be 1s spectra series is shown with different Ar fluxes (from bottom to top). Vertical lines mark Be 1s binding energies from the literature for Be bulk and for beryllium oxide. To show the shifting of spectral, peaks two additional lines with 1 eV difference are added. The spectra series on the right shows high-resolution XPS spectra in the W 4f binding energy region for the same Ar fluxes as on the left. Vertical lines mark the W 4f binding energy positions of W bulk.

XPS data was not completely understood at that time. A few hundred nanometer W were evaporated onto a Be bulk sample. After annealing the sample the formation of a $Be_{12}W$ film was concluded through RBS [292] and XRD [293] measurements. Furthermore, sputter XPS and RBS measurements were performed [292], totaling 37 spectra each. The evaluation of the 1 MeV proton RBS concluded a Be:W stoichiometry of 12:1 below the oxidized surface with an information depth of at least 1 µm for W [294]. In contrast the Be:W stoichiometry determined from the W 4f and Be 1s XPS spectra area ratios corresponds in the 'alloy region' only to 3.3:1. This mismatch of the stoichiometry between XPS and RBS is argued to arise from preferential sputtering of Be over W and because XPS is more sensitive to the surface region than RBS. In their work the Be 1s XPS spectra were fitted with three Gauss-Lorentz functions, one for the 'oxid' peak around 114.4 eV and one named 'metal' and one named 'alloy' with a constant shift of 0.51 eV.

While the stoichiometry determined from XPS was only 3.3:1 they still concluded that this 'alloy' peak in the 'alloy region' corresponds to $Be_{12}W$ as indicated by RBS. This, I now doubt to be the case. At first sight it seems to agree well with the *ab initio* results for $Be_{12}W$, since the initial-state shifts of $Be_{12}W$ suggest that both peaks 'alloy' and 'metal' (from [292]) belong to a clear $Be_{12}W$ spectrum within the 3 µm thick film region. First, because the measured shift of 0.51 eV in the publication [292] would agree with the mean shift of 0.52 eV of the two shifted chemical environments of $Be_{12}W$. Second, because the peak area ratio of the 'metal' and 'alloy' reported in figure 3 of the publication [292] is roughly 1:3 at the beginning of the series and in the 'alloy' region as is also the predicted ratio by DFT for the shifted and non shifted components of pure $Be_{12}W$.

But looking in detail at the raw XPS spectra data of Be 1s and W 4f shown in Fig. 4.23 the picture for the chemical interpretation clearly changes. The raw data shows a clear drift of the Be 1s spectrum over the sputter series (from bottom to top) of the 'alloy' and 'metal' peak together to lower binding energies by nearly 1.0 eV. This shift was corrected in the original evaluation by keeping the Be 1s metal peak fixed. The W 4f spectra also clearly shift with respect to W 4f bulk over the sputter series. Both observations can not be explained theoretically by $Be_{12}W$, which has no chemical shift in the W 4f core levels and the Be 1s spectra are predicted to stay at the same binding energy as long the energy axis is calibrated right throughout the experiment and no sample charging occurs. The BeO 1s signal which would be expected to be at 113.7 eV [90] lies between 114.8 eV-115.0 eV, which might have been their motivation for fixing the Be-O Be bulk Be difference to 3.0 eV and assuming a charging effect. This amount to a 1.0 eV correction of the Be 1s binding energies.

With our evaluation method I can now clarify the chemical interpretation of this sputter XPS series raw data without correcting the binding energy over this series by 1.0 eV. I have

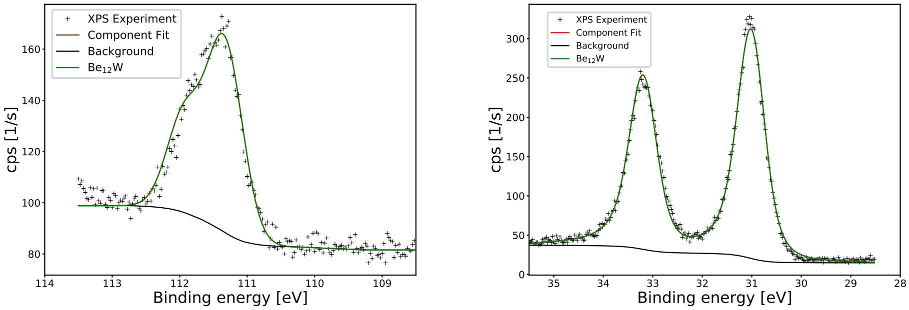

(a) Be 1s Spectrum 2

(b) W 4f Spectrum 2

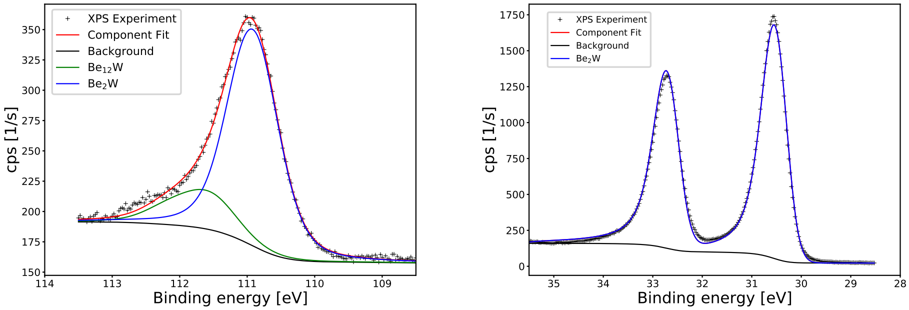

(c) Be 1s Spectrum 16

(d) W 4f Spectrum 16

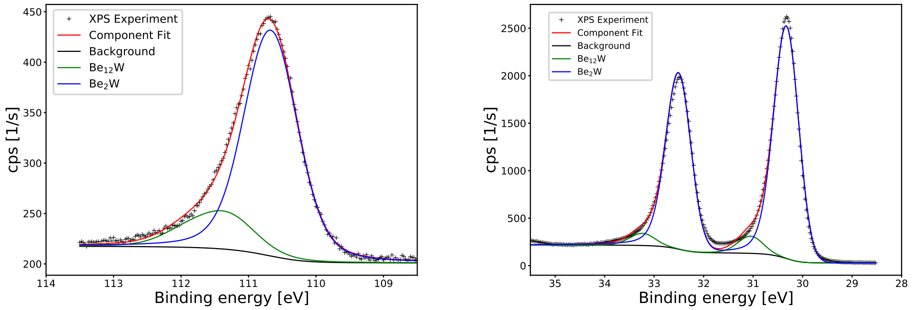

(e) Be 1s Spectrum 29

(f) W 4f Spectrum 29

Fig. 4.24.: A representative subset of the sputter XPS spectra (data sets 2,16,29) on Be-W from [292] is shown with component fits from *ab initio* data. In (a) a Be 1s spectrum at the start of the sputtering is shown yielding only a contribution from $Be_{12}W$. The W 4f (b) can also be matched with $Be_{12}W$ only. The Be 1s spectrum in (c) can be fitted with contributions from $Be_{12}W$ and Be_2W while the component fit of the corresponding W 4f doublet spectrum (d) can be fitted with solely Be_2W. The fits in (e,f) show that the spectra can also be fitted with a small contribution of $Be_{12}W$ in the tail.

component fitted all Be 1s and W 4f spectra. The spectral background was determined with the Shirley method [242, 243]. Since no chemical shifts for Be-O have been calculated and a Be-O would need different broadenings only the region without the Be-O peak was fitted. The Shirley background was determined in the same region compensating partly for the intensity contributions from the oxid peak. I do not think that this changes the principle picture, since the data has quite low statistic. For the Be 1s spectra, Be_2W, $Be_{12}W$, $Be_{22}W$ and Be are included first then phases having no contributions are removed. $Be_{22}W$ is excluded from all fits because of no or only a minor contribution, the measured stoichiometry of 3.3:1 and the Be 1s peak shape.

The W 4f single-phase spectra have linear dependencies. $Be_{22}W$ and Be_2W are hardly distinguishable in the fit. Also $Be_{12}W$ and W are predicted to be not distinguishable. Since $Be_{22}W$ does not contribute to the Be 1s spectra it is excluded directly in the 4f fits. The relative content of W and $Be_{12}W$ could be constrained through knowledge of the stoichiometry. For the fit $Be_{12}W$ is included and not W. Examples of individual component fits of each spectra series is shown in Fig. 4.24. For the fitting of the 4f spectra the experimental 4f-splitting of 2.18 eV was used. The DFT 4f-splitting of all alloys was 2.24 eV which is not close enough to experiment for fitting. In Fig. 4.24 graph (a, b) show one of the first Be 1s and W 4f spectra from the oxidized surface, which could be fitted with a $Be_{12}W$ contribution only. Spectra close or in the 'alloy' region are shown in (c,d) and (f,g). The Be 1s with symmetric Voigt profiles are best matched with a large contribution from Be_2W and a small contribution from $Be_{12}W$. The experimental W 4f spectra can be fitted with Be_2W only. The $Be_{12}W$ in the 4f signal is so small in the tail of the Be_2W peak that it can be covert by the asymmetry parameter of the 4f peak functions. The W 4f reference binding energy varies in these spectra fits by 0.1 eV around 31.1 eV. With a Lorentzian FWHM of 0.1-0.4 eV and a Gaussian FWHM of 0.45-0.8 eV the broadenings are all reasonable.

The resulting interpretation to follow: On the $Be_{12}W$ film surface is some beryllium oxide. What oxide in detail is still unknown, since the peak position is slightly shifted compared to BeO chemical shifts reported in the literature [90, 295]. This shift might be due to constrained growth, or because it arises from some other Be-(W-)O alloy(s). The Be 1s spectrum shows rather small intensity at around 111.8 eV compared to the Be-O contribution. This contribution corresponds to the underlying $Be_{12}W$, the peak form fits very well to $Be_{12}W$. The same picture is seen in the W 4f spectra. The 4f W peaks first do not shift, which is in agreement with $Be_{12}W$ or pure W. During the Ar sputtering the oxide is removed and due to preferential sputtering more Be is removed than W. This is already seen in the intensity increase in the W 4f peaks in the information depth and by the determined Be:W stoichiometry in the 'alloy region'. The stoichiometry from the concentrations of our fit analysis lies between 2.3:1 and 3.3:1 in this region. When sputtering through the 3 µm thick ’alloy’ region the obtained Be 1s and W 4f spectra fit very well the chemical environment of Be_2W. Since Be_2W is the most stable tungsten rich phase in the Be-W phase diagram its formation at a tungsten enriched surface is plausible. Since the information depth of XPS is only a couple of nanometers there is no contradiction to the RBS and XRD results that the bulk material in this film region is $Be_{12}W$. This is also indicated by several XPS spectra at low Ar fluence and steady $Be_{12}W$ contributions in the other Be 1s XPS spectra. This evaluation can be done with the chemical shift data alone and the conventional fit methods. The compound fit needs in these cases 0 two 2 fit parameters less. Our evaluation shows that one has to be careful when evaluating sputter XPS data from a depth composition analysis on a samples containing very different elements, since due to preferential sputtering the surface might be different from the bulk.

4.3.2. The Be-Ti System

Be-Ti alloys are discussed to be used in the breading blanket in fusion reactors because they still yield a high melting point and neutron multiplication while having some other desired properties [296]. Pebbles of these compounds can be mass produced via ’rot rotation’ [297–299] and are studied in detail [300, 301] in facilities in Japan. In [302] V. Bachurin and V. Vladimirov calculated hydrogen vacancy properties in $Be_{12}Ti$ with the VASP code.

The Be-Ti phase diagram contains with five known stable phases more than the previous Be-W system. Known stable phases from experiment include $Be_{12}Ti$, $Be_{17}Ti_2$ α, $Be_{17}Ti_2$ β, Be_3Ti, Be_2Ti, BeTi [303]. Crystal structure data of these is extracted from the ICSD. There are two different crystal structure entries in the ICSD for $Be_{12}Ti$, of which one is known to be incorrect [304, 305]. A convex-hull construction from `FLEUR` calculations on all experimentally known Be-Ti phases plus a Be_5Ti phase predicted by theory is shown in Fig. 4.25. The crystal structure of Be_5Ti is extracted from AFLOWlib [56] (entry: fa032988b6f99f78). The energy of formation data points in blue are calculated with the `FLEUR` code (data also in Tab. 4.5). To compare these results with other DFT simulations, data obtained with the VASP DFT program reported in the Materials Project (MP), AFLOWlib and OQMD databases have been included in the convex-hull plot. The Materials Project calculated with the wrong $Be_{12}Ti$ structure, which lies over 80 meV per atom above the convex hull, this is confirmed by `FLEUR` and was already shown in [305]. The Be-Ti structures from the Materials Project (green triangle) have been included in the binary metal screening and results for the `FLEUR` code on these are shown in green ’x’. The small vertical blue lines mark the determined stoichiometry with one standard derivation for the first Be-Ti sample which is discussed below. Where hull lines are steep a small change in the stoichiometry can change the energetically favored phase composition and the XPS spectrum accordingly. The Ti reference might be a bit problematic since there

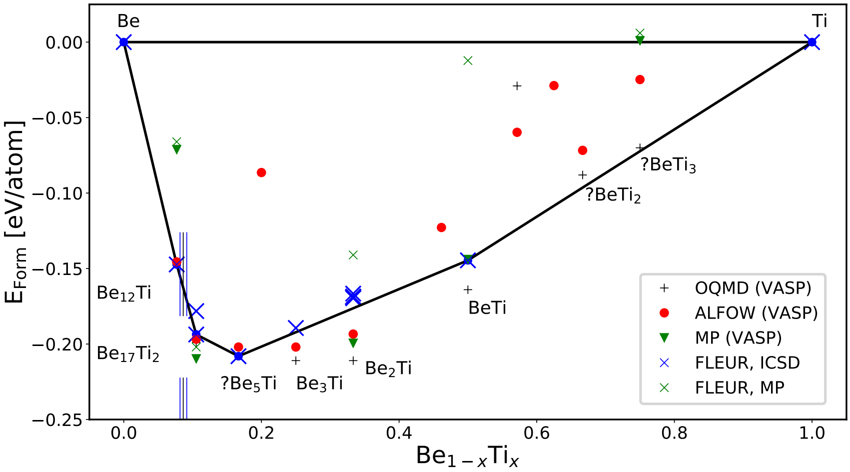

Fig. 4.25.: Convex-hull diagram of the Be-Ti system constructed from `FLEUR` simulations (blue) on known stable phases from the ICSD. The other data points are results from the VASP code from various databases. Theoretical predicted potentially stable phases, experimentally yet unconfirmed, are marked with a prefixed '?'.

are several different Ti crystal structures reported by experiments.

Again, to check if the DFT simulations with PBE agree with the lattice constants reported by experiments an equation of states was calculated for each Be-Ti compound. The resulting total energies for different uniformly volume scalings are shown in Fig. 4.26. The total energies are plotted with respect to the total energy of the smallest volume scaling. To each total energy volume curve a Birch-Murnaghan equation of states curve is fitted to extract the volume scale with the lowest total energy. The results for the optimal volume are collected with the enthalpy of formation in Tab. 4.5. The unit-cell volumes are for all Be-Ti compounds 0.5-2.5% smaller then reported in the experimental literature. GGA functionals and also the PBE functional are known in the literature to overestimate the unit-cell volume [306, 307] which is not the case here. Additional information listed in the table includes the symmetry group and the original identifier in the ICSD or in AFLOWlib.

For the interpretation of XPS spectra initial-state core-level shifts (CLS) for all Be-Ti alloys are calculated with the *fleur_initial_cls_wc* workflow. The Be 1s chemical-shifts results for all atom-types in each alloy are listed in Tab. 4.6. For Ti an often investigated spectral line is the

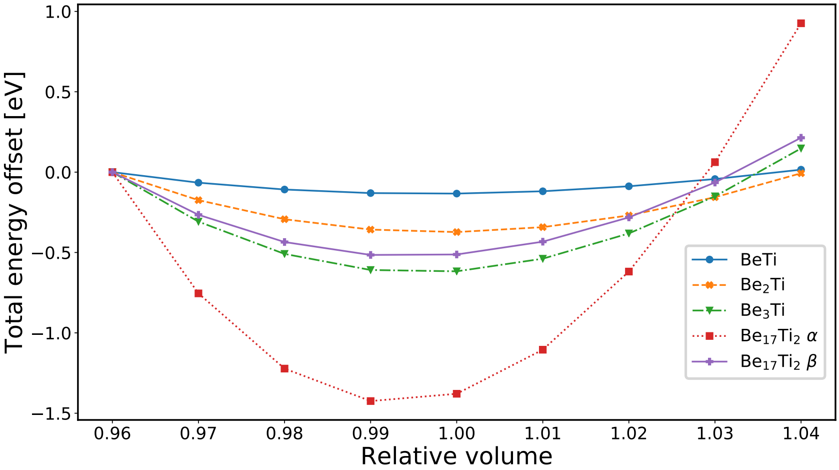

Fig. 4.26.: Equation of states calculated with the `FLEUR` code for all the Be-Ti systems. Just the bravais matrix was scaled and not the cell optimized under constraint volume.

database identifier	symmetry group	material formula	enthalpy of formation [eV/atom]	(PBE) volume scale V/V$_0$
1425	P 63/mmc	Be	0	0.99815
58743	P m-3m 221	BeTi	-0.145	0.98975
58744	F d-3mS 227	Be$_2$Ti	-0.170	0.99475
616451	R -3mH 166	Be$_3$Ti	-0.189	0.98756
fa032988b6f99f78	P6/mmm 191	Be$_5$Ti	-0.208	-
1029217	R -3mH 166	Be$_{17}$Ti$_2$ α	-0.194	0.97489
616452	P 63/mmc 194	Be$_{17}$Ti$_2$ β	-0.178	0.97938
616454	I 4/mmm 139	Be$_{12}$Ti	-0.147	0.9839

Tab. 4.5.: *Ab initio* enthalpy of formation for most stable compounds of the Be-Ti system. The volume scale V/V$_0$ is the energetic most favorable unit-cell volume V with respect to the experimental volume V$_0$, calculated with the PBE functional under uniform compression.

2p doublet. The Ti 2p chemical shifts are also shown in Tab. 4.6. BeTi and Be$_2$Ti have only one Be atom-type in the unit cell with a CLS of 0.88 eV and 1.29 eV, respectively. All other Be-Ti alloys have more chemical environments. Some of them containing a different number of Be atoms.

material formula	Be 1s electrons	Be 1s DFT CLSs [eV]	Ti 2p3/2 electrons	Ti 2p DFT CLSs [eV]
BeTi	2	0.88	4	0.15
Be_2Ti	4	1.29	4	0.43
Be_3Ti	2,12,4	1.52, 1.36, 0.84	16,8	0.48, -0.02
Be_5Ti	6,4	1.29, 1.05	8	-0.09
$Be_{17}Ti_2$ α	6,12,12,4	1.03, 0.97, 0.82, 0.48	16	-0.15
$Be_{17}Ti_2$ β	6,12,12,4	1.08, 0.98, 0.81, 0.65	8,8	-0.16, -0.13
$Be_{12}Ti$	8,8,8	1.02, 0.79, 0.32	8	0.01

Tab. 4.6.: *Ab initio* results of all core-level shifts of most stable compounds of the Be-Ti system and how many electrons contribute for each unit cell of these systems. Depending on the crystal symmetry there are several chemical environments resulting in different chemical shifts. All these chemical shifts are currently experimentally not known in the literature. From this data all XPS spectra containing a mixture of these Be-Ti binary phases can be fitted.

From the core-level shift results in Tab. 4.6 and the information on the number of contributing electrons contributing to the intensity single-phase spectra can be constructed. Such theoretical single-phase spectra for the Be 1s and the Ti 2p1/2 and 2p3/2 binding energy regions are displayed in Fig. 4.27. A full-width half-maximum of 0.1 eV for the Lorentzian and 0.43 eV for the Gausians part in the Voigt profile for each contribution was selected. These broadenings are comparable to what is observed in experiments. The calculated 2p-splitting of 5.77 eV stays constant for all Be-Ti alloys. The reported 2p-splitting from experiments of 6.09 eV [90] is slightly larger then the doublet splitting from DFT. For oxides there are reported 2p-splittings in the range of 5.6-5.7 eV [308]

Because of a Coster–Kronig transition the 2p have a different Lorentz broadening and their area ratio differs from 1:2. The constructued theoretical Ti 2p spectra are thus not expected to be correct. Furthermore, the transition metals are known to have strong asymmetric peak shapes towards higher binding energies from the main peak due to conduction electron shake-ups. Except for Be_3Ti there is only one atom-type contribution to the 2p spectra giving them all simple single doublet profile form. The two Ti environments of Be_3Ti create a double peak structure in each 2p peak.

The theoretical spectra for the Be 1s binding energy region have more complex overall shapes due to several contributing chemical environments. The shape of the $Be_{17}Ti_2$, and

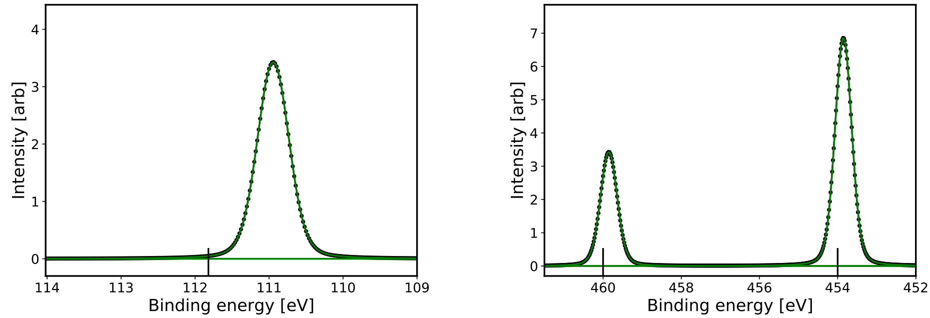

(a) BeTi, Be 1s

(b) BeTi, Ti 2p

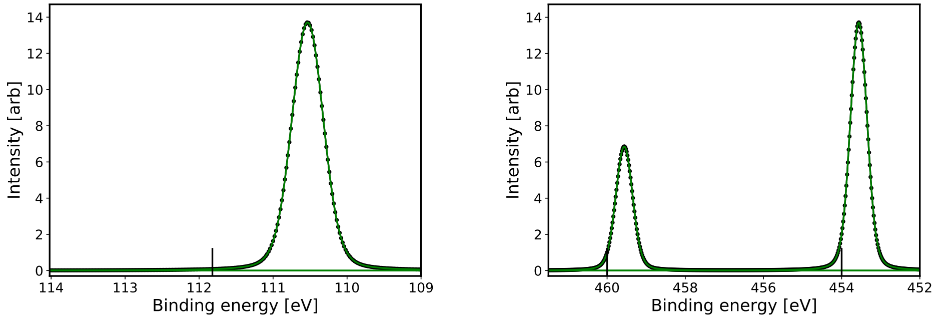

(c) Be_2Ti, Be 1s

(d) Be_2Ti, Ti 2p

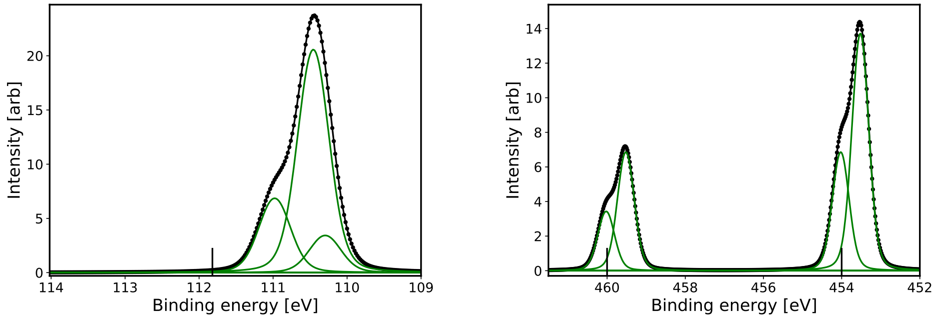

(e) Be_3Ti, Be 1s

(f) Be_3Ti, Ti 2p

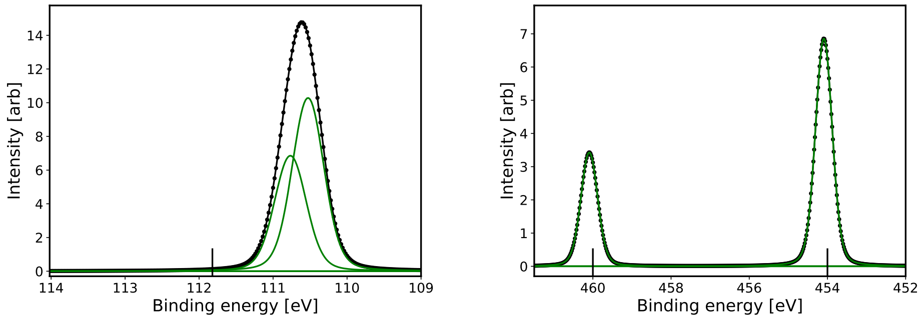

(g) Be_5Ti, Be 1s

(h) Be_5Ti, Ti 2p

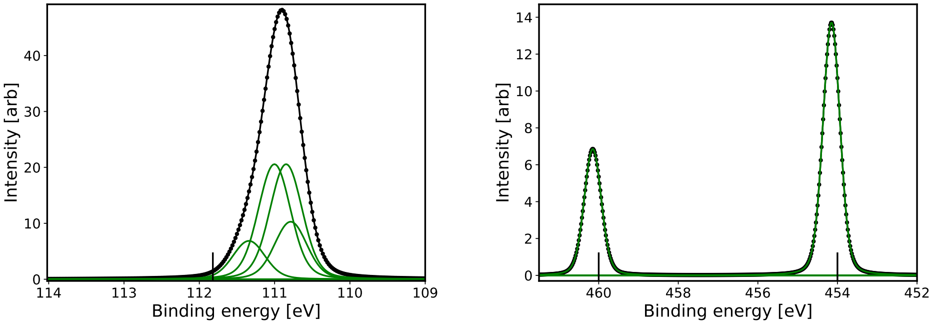

(i) $Be_{17}Ti_2$ α, Be 1s

(j) $Be_{17}Ti_2$ α, Ti 2p

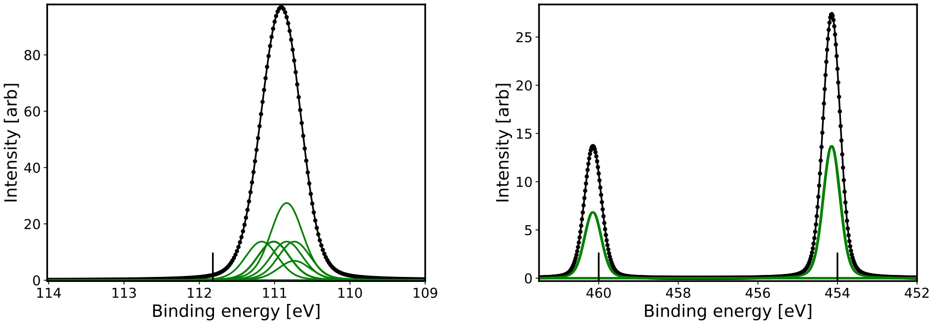

(k) $Be_{17}Ti_2$ β, Be 1s

(l) $Be_{17}Ti_2$ β, Ti 2p

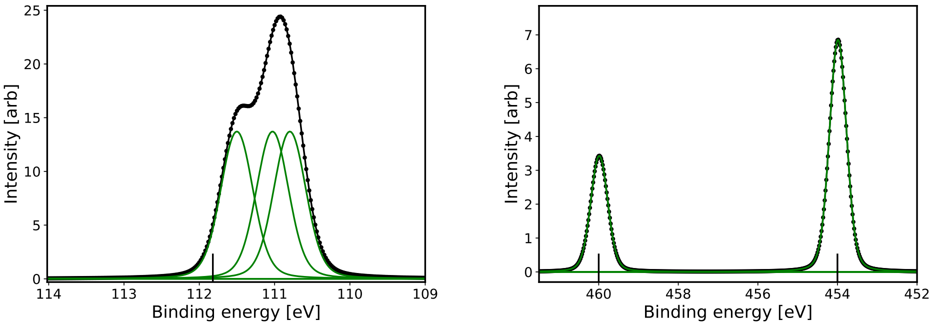

(m) $Be_{12}Ti$, Be 1s

(n) $Be_{12}Ti$, Ti 2p

Fig. 4.27.: Theoretical single phase XPS spectra of Be 1s and Ti 2p from the stable Be-Ti alloys. The spectra are constructed from the *ab initio* chemical shifts and the atom-type information in Table 4.6 of one computational unit cell. All Voigt profiles have Lorentzian FWHM of 0.1 eV and a gaussian FWHM of 0.43 eV.

Be_5Ti spectra is still an overall single peak, but an asymmetric one. The CLS values differ not enough to split the peaks visibly. The $Be_{12}Ti$ and Be_3Ti phase have a broad double-peak shape with more spectral weight towards smaller binding energies. The Be_3Ti shifts collectively more to smaller binding energies then the $Be_{12}Ti$ spectrum. Overall, besides the two $Be_{17}Ti_2$ phases, the Be 1s spectra are well distinguishable by shape, enabling any chemical interpretation.

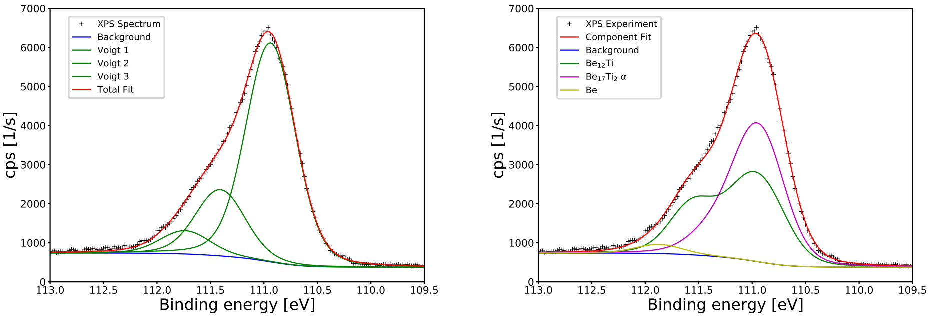

Fig. 4.28.: (left) Measured Be 1s X-ray Photoelectron spectrum at 300 K with a fit (8 fit parameters) of three Voigt profiles with the same Lorentzian and Gaussian broadening (XPS data from [229]). (right) Theoretical phase fit (6 fit parameters) of a mixed spectra with contributions of $Be_{12}Ti$, $Be_{17}Ti_2$ and elemental Be fitted to the same experimental spectrum.

In an experiment at IEK-4 by Nicola Helfer, a commercial sample, produced over 40 years ago by Brush Beryllium [309] was reinvestigated in ultra-high vacuum with XPS. The sample is expected to have a Be:Ti stoichiometry ratio of 12:1. XPS spectra are measured at room temperature after annealing of the sample with temperatures reaching from 300 K to 1100 K. This series was measured at 0 and 40° emission angles of photoelectrons. The sample surface was cleaned with Ar sputtering. One observed a nearly unchanged Be 1s spectral region until a sudden change after annealing with over 1000 K. All XPS data and additional XRD measurements are presented in [229]. Usual approximations with several Voigt profiles to the XPS spectra using UniFit [235] are also presented in [229]. To represent this dataset two spectra are shown in Fig. 4.28 and Fig. 4.29. The traditional evaluation method is compared to the proposed component fit method. In the two graphs of Fig. 4.28 the same experimental data of a XPS spectrum at 300 K with different fits is shown. The left graphs shows a common evaluation which needs three Voigt profiles with a Shirley background to find a good match to the spectral data points in black. This approximation needs eight fit parameters, two for each

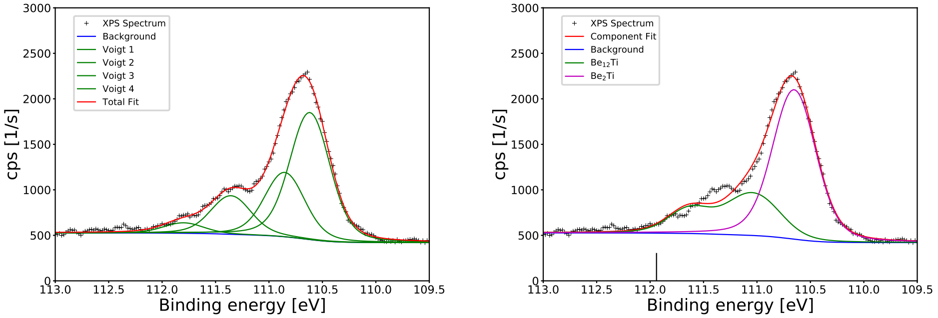

Fig. 4.29.: (left) X-ray Photoelectron spectrum measured at 300 K after heating to 1100 K with a fit (10 fit parameters) of four Voigt profiles with the same Lorentzian and Gaussian broadening (XPS data from [229]). (right) theoretical phase fit (5 fit parameters) of a mixed spectra of $Be_{12}Ti$ with Be_2Ti compared to the same experimental spectrum.

Voigt profile plus the same Lorentzian and Gaussian broadening for all Voigt profiles. Since there is nearly no literature data on Be-Ti binding energies a chemical interpretation could not be concluded from this fit. The reported Voigt profile positions [229] at binding energies of 110.94 eV, 111.40 eV, and 111.74 eV with core-level shifts w.r.t. metallic Be of 0.92 eV,0.45 eV and 0.12 eV do not match the *ab initio* CLS of $Be_{12}Ti$ (1.02 eV, 0.79 eV and 0.3 eV). Only the largest core-level shift is in agreement. Also the area ratios of the three profiles to each other is questionable for a pure $Be_{12}Ti$ spectrum, since from the crystal structure three contributions with the same area are expected. From XRD measurements they concluded that there is mostly $Be_{12}Ti$ in the sample. But the determined Be:Ti stoichiometry by XPS was 12(1):1 in the information depth. This would allow for a phase mixture at the surface within the uncertainty.

Evaluating now the same spectrum with our component fit method I can fit the spectrum very well with only six fit parameters instead of eight. The determined Shirley background was added in the fit. A mixture of 51 % $Be_{12}Ti$, 47 % $Be_{17}Ti_2$ α and a slight amount of 2 % Be in the Be 1s signal match best the experimental data. The determined Be:Ti stoichiometry from the extracted unit cell rations from this is 10.7:1. The fit used a full width half maximum (FWHM) broadening of fixed 0.1 eV for the Lorentzian part and 0.46 eV for the Gaussian part. The reference Be 1s binding energy was 111.88 eV. This fit result can be explained by preferential sputtering of Be over Ti change the surface region a bit.

After annealing to over 1000 K the spectrum changes completely. The evaluations of such a spectrum with the common experimental fitting approach and our component fit is shown in Fig. 4.29. To reach a good agreement to the experimental data four Voigt profiles need to be fitted with ten fit parameters. This fit is shown with the data in the left graph in Fig. 4.29. The best match with the component fit is shown in the plot on the right. It needs only five parameters, but cannot describe the rough features around 111.5 eV very well. The component fit finds still contributions with 33 % from $Be_{12}Ti$ and 67 % from the Ti rich phase Be_2Ti. The formation of Be_2Ti was also confirmed in XRD measurements in [229]. Apparently after a certain temperature Be starts to evaporate from the sample in increasing quantities, depleting the sample of Be. This way Be_2Ti forms in the surface region while there is still $Be_{12}Ti$ bulk left. The system might also end in some other metastable states when it cools down. Remarkably no BeTi is found. The Be 1s binding energy was 111.94 eV in the fit, with a Lorentzian FWHM of 0.13 eV and Gaussian FWHM of 0.41 eV.

spectrum temp.[K]	phases present in fit	relative Be 1s signal content fit result
300, (a)	$Be_{12}Ti$, $Be_{17}Ti_2$ α, Be	8.22(2), 1.45(1), 90.33(2)
600, (b)	Be_2Ti, Be_3Ti, $Be_{12}Ti$, Be	31.06(0), 41.21(0), 23.64(0), 4.1(0)
600. None	Be_2Ti, $Be_{12}Ti$, $Be_{17}Ti_2$ β, Be	54.18(0), 22.15(0), 17.98(0), 5.69(0)
700, (c)	$Be_{12}Ti$, $Be_{17}Ti_2$ α, Be	34.96(0), 58.85(0), 6.19(0)
800, (d)	$Be_{12}Ti$, $Be_{17}Ti_2$ α, Be	64.01(0), 32.47(0), 3.52(0)
900, (e)	$Be_{12}Ti$, Be	82.38(0), 17.62(0)
900, (f)	$Be_{12}Ti$, Be	65.31(0), 34.69(0)

spectrum temp.[K]	Be 1s BE fit [eV]	FWHM Gauss, Lorentz fit [eV]	stoichiometry Be : Ti	iter-ations	χ^2 pdof
300, (a)	111.95	0.42, 0.15	116.9 : 1.0	92	12.11
600, (b)	112.09	0.67, 0.04	3.2 : 1.0	81	6.7
600. None	112.01	0.66, 0.05	3.22 : 1.0	121	7.44
700, (c)	111.87	0.54, 0.08	10.17 : 1.0	71	17.84
800, (d)	111.96	0.53, 0.05	10.92 : 1.0	71	41.32
900, (e)	112.03	0.57, 0.03	14.57 : 1.0	61	38.37
900, (f)	112.01	0.56, 0.01	18.38 : 1.0	67	74.32

Tab. 4.7.: In detail fit results from *ab initio* data of the chemically interpreted Be 1s X-ray photoemission spectra of a Ti on Be bulk experiment at the IEK-4. Besides the values of the fit parameters (concentrations, Be 1s reference FWHM) information on the fit quality and a calculated stoichiometry from the phase content is provided.

Another experiment on a Be-Ti system was performed by Nicola Helfer at the IEK-4. Ti

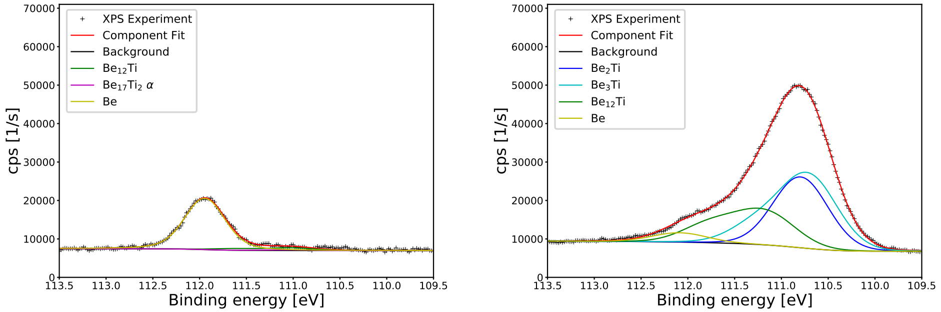

(a) Ti on Be 300 K

(b) Ti on Be 600 K

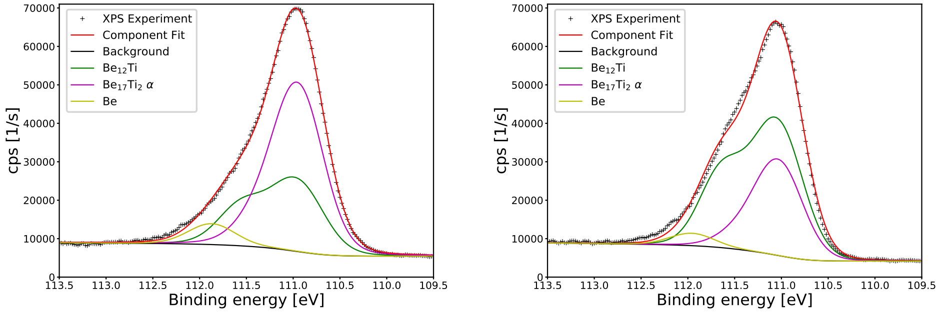

(c) Ti on Be 700 K

(d) Ti on Be 800 K

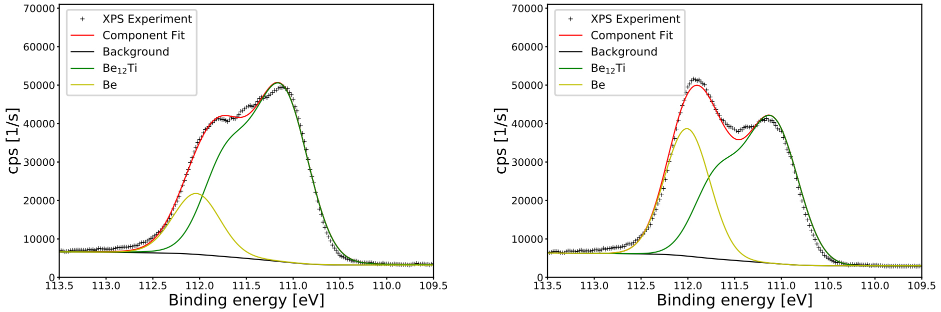

(e) Ti on Be 900 K 1

(f) Ti on Be 900 K 2

Fig. 4.30.: Chemically interpreted Be 1s X-ray photoemission spectra of a Ti on Be bulk experiment conducted by Nicola Helfer at the IEK-4. In the experiment Ti was evaporated onto Be and the sample was heated up to different temperatures. The spectra are all measured at room temperature. The component fit analysis by me works well and provides a full chemical interpretation. Wobbly features in the spectra after heating to 900 K are not well captured by the component fit. Detailed fit results are shown in Tab. 4.7

was evaporated onto a polycrystalline beryllium sample. Then the sample was heated to various increasing temperatures 300 K, 600 K, 700 K, 800 K, 900 K and again 900 K. After each heating the sample was given time to cool down to room temperature and an XPS spectrum was measured. The experimental data from these six high-resolution Be 1s spectra with the resulting component fit analysis by me is shown in Fig. 4.30. The experimental determined Shirley background was added to the overall theoretical spectrum, which is probably not optimal. In a first fit the concentrations of all seven Be-Ti phases plus Be were fitted to the experimental data. The Be 1s binding energy and the FWHMs of the Voigt profiles were allowed to vary in the least squares optimization. All phases with no contributions in the first fit are dropped and a final fit with only contributing phases was performed. The quantitative results do not change, only the fit quality improves. The results of the final fits are in detail documented in Tab. 4.7.

The full chemical analysis picture from the component fits is as follows: At room temperature (Fig. 4.30a) the Ti layers do not react much with the underlying Be, resulting in a rather small intensity Be 1s spectrum dominated by a signal from pure Be with only very small contributions from other phases which are hardly distinguishable from the background noise. The binding energy of 111.95 eV for pure Be is slightly shifted from the values of previous experiments 111.86 ± 0.06 eV or the literature value of 111.82 ± 0.06 eV from NIST XPS [90]. It is not easy to calibrate the binding energy axis in experiments very exactly. In the evaluation of the spectra the fit is now allowed to vary the Be 1s binding energy ± 0.1 eV around the 111.95 eV value. Such a rather large variation for the reference binding energy is still justifiable for the Be-Ti system , since all phases (see Tab. 4.6) are distinguishable within this allowed variation.

After heating the sample to 600 K, the spectrum (Fig. 4.30b) changes notedly and the component fit correlates this to the formation of several other Be-Ti phases, with 31.06% of the 1s signal coming from Be in a Ti rich Be_2Ti chemical environment. The other contributions to the spectrum are assigned as 41.21% Be_3Ti, 23.64 % $Be_{12}Ti$, and 4.1 % pure Be. The area under the Be signal also increased compared to the spectrum at 300 K. Thus, more Be atoms are now within the information depth of the apparatus, due to diffusion of Be or/and Ti. The elements have clearly mixed and most Be in the information depth is now in some chemical environment with Ti, favoring rather Ti rich environments, which is mirrored in the Be:Ti stoichiometry of 3.2:1.0 extracted from the component fit. No BeTi, Be_5Ti or $Be_{17}Ti_2$ are found in the 600 K spectrum. When explicitly excluding the Be_3Ti phase from the fit, the spectrum can also be matched well with the inclusion of $Be_{17}Ti_2$ β phase instead of the more common $Be_{17}Ti_2$ α phase, see Tab 4.7. These two fits might be differentiated by fitting consistently the Ti 2p spectra also.

After heating the sample up to 700 K and 800 K, the spectra (Fig. 4.30c, 4.30c) show an increase in the Be rich phases $Be_{17}Ti_2$ α and $Be_{12}Ti$. No contribution from other phases besides a small Be bulk signal is found. While for the 700 K spectrum the $Be_{17}Ti_2$ α contribution is larger than the contribution from $Be_{12}Ti$ this is flipped for the measurement after heating to 800 K. The area of the Be 1s signal did increase only slightly further compared to the 700 K spectrum, therefore the amount of Be atoms within the information depth stays now roughly the same.

The spectra recorded after heating the sample up to 900 K for the first and 900 K for the second time show the absence of the $Be_{17}Ti_2$ α phase while the signal for bulk Be is growing. The only other phase contributing to the spectra is $Be_{12}Ti$. This may be explained by diffusion of the Ti into the Be bulk, while larger volume of pure Be forms at the surface. This is pictured in the Be:Ti stoichiometric estimation from the phase content of the fit. The Be:Ti stoichiometry first increased to 14.57:1.0 and in the second heating further to 18.38:1.0. The component fit to these two high temperature spectra cannot capture the 'wobbly' features of the double peak. To archive a good match the Be 1s reference binding energy was determined to shift to 112.01 eV, showing a drift to higher binding energies of the overall spectra. In addition, to the fit parameter results Tab. 4.7 contains information on the fit itself. The number of iterations mimics how hard it was for 'scipy.optimize' to find the best match. Fits containing more fit parameters need more iterations. The χ^2 per degree of freedom values extracted from the fit are an indication for the quality of the fit, with a value of 1 meaning the fit matches the data very well. Since no, or very small uncertainties on the experimental data and theoretical data are propagated through the optimization the one sigma uncertainty values on the fit parameters are probably to small and the reduced χ^2 values to large. The approximations can also be performed with less parameters for example by fixing the full width half maximum (FWHM) of the Lorentzian in the Voigt profiles. The Lorentzian broadening should be a property of the X-ray source and line width, which should stay constant throughout all measurements. The FWHM of the Gaussian captures all other contributions which might show a temperature, or disorder dependence. Overall the FWHM do not vary so much between the different spectra and are comparable.

4.3.3. The Be-Ta System

Through radioactive activation and decay of tungsten atoms tantalum may form. It is therefore also of interest for the fusion community to understand the Be-Ta system and being able to identify its phases.

In the Be-Ta phase diagram are six experimental known phases [310, 311]: $Be_{12}Ta$, $Be_{17}Ta_2$, Be_3Ta, Be_2Ta, Be_2Ta_3 and $BeTa_2$. The structure types of the Be rich phases also occurred in the

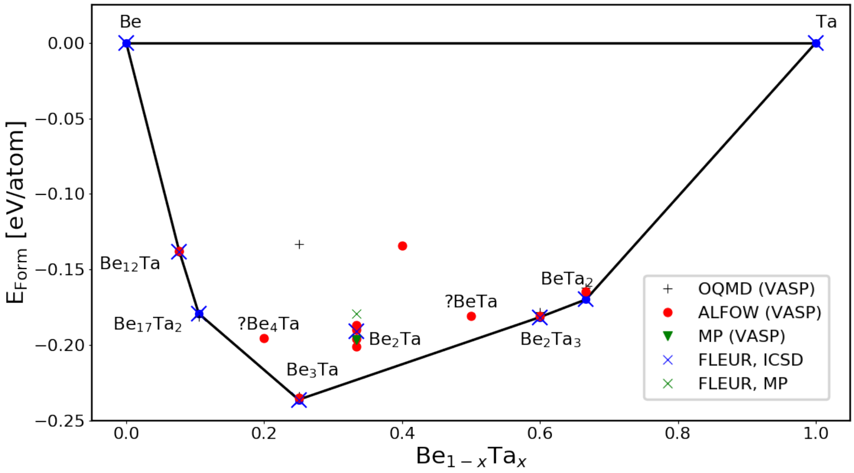

Fig. 4.31.: Convex-hull digram of the Be-Ta system with the six known Be-Ta phases. Be_3Ta is predicted to be the most stable phase, while the calculated Be_2Ta structure is predicted to be metastable. As in the case for the Be-Ti system, $Be_{12}Ta$ lies on the convex-hull line between $Be_{17}Ta_2$ and Be. The results from FLEUR agree very well to data from others produced with the VASP program. There are no additional theoretical predicted stable phases, only metastable ones from ALFOWlib marked with a prefixed '?'.

Be-Ti system. The Ta rich phases differ from the Ti rich phases. All experimentally reported Be-Ta crystal structures have been extracted from the ICSD [89].

The enthalpies of formation for these systems were calculated with `FLEUR`. From these results the convex hull of the Be-Ta system shown in Fig. 4.31 was constructed. The data agrees very well with the calculated enthalpy of formation from the OQMD, Materials Project and ALFOWlib produced with the VASP DFT-program. The spread between VASP and `FLEUR` is for the Be-Ta systems smaller than in the case of Be-Ti and Be-W. DFT predicts the Be_2Ta structure to be metastable with 30 meV per atom above convex hull, as happened with the `FLEUR` code for Be_2Ti. Besides Be_2Ta all experimental known phases span the convex hull and are thus predicted to be stable in terms of formation energy by DFT. Be_3Ta with an enthalpy of formation of −236 meV per atom is the most stable structure in the Be-Ta phase diagram. Two meta-stable structures of Be_4Ta and BeTa are predicted by AFLOWlib. These two theoretical

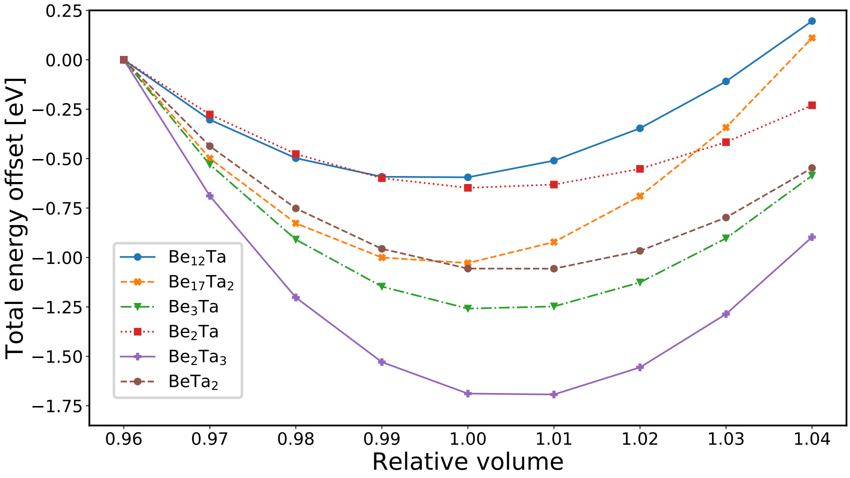

Fig. 4.32.: Equation of states calculated with the `FLEUR` code for all the Be-Ta systems. Just the bravais matrix was scaled and not the cell optimized under constraint volume.

structures are marked with a '?' in the Fig. 4.31. The calculated enthalpies of formation are listed in Tab. 4.8.

In order to check the theoretical agreement of the unit-cell volume Birch-Murnaghan equation of states for each phase have been calculated. Uniformly scaled volume versus total energy curves for the Be-Ta alloys are shown in Fig. 4.32. For each total energy curve the total energies are plotted with an offset of the total energy of the smallest volume. The resulting volumes scales V/V_0 from the fit with the lowest total energy are also listed in Tab. 4.8 along database source and symmetry of the unit cell.

Core-level shifts for the Be-Ta phases were calculated and are listed in Tab. 4.9. The Be rich phases have several chemical environments for different Be atom-types. Be_3Ta and Be_2Ta_3 have two Ta environments, of which the ones from Be_3Ta are predicted to be well separated in XPS spectra. Resulting constructed single-phase spectra from this data are shown in Fig. 4.33.

Samples with a Be:Ta stoichiometry of approximately 12:1 were investigated with XPS by N. Helfer in [229] after annealing at elevated temperatures. After annealing temperatures of over 900 K the Be 1s and Ta 4f spectra show strong changes as in the case of the first Be-Ti sample discussed. Representative experimental data from the series with a first component-fit analysis is shown in Fig. 4.34. Good fits can be found for the Be 1s and Ta 4f spectra. For

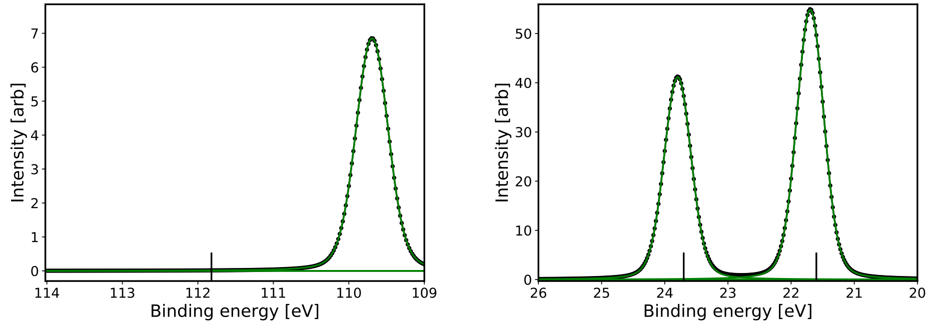

(a) $BeTa_2$, Be 1s

(b) $BeTa_2$, Ta 4f

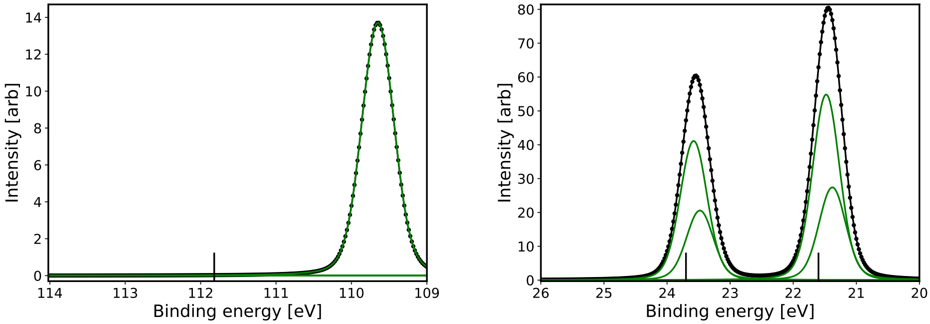

(c) Be_2Ta_3, Be 1s

(d) Be_2Ta_3, Ta 4f

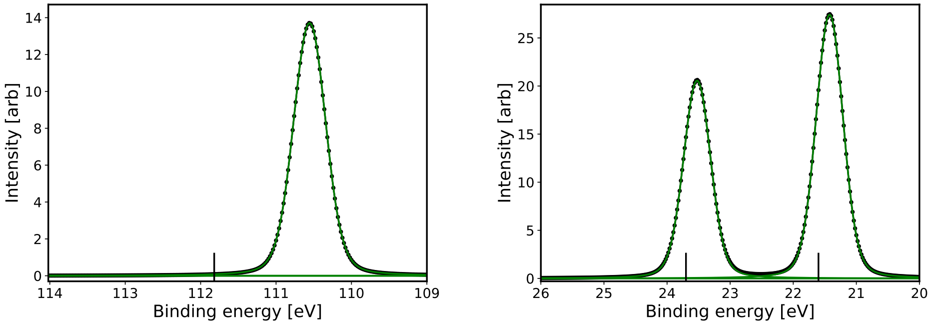

(e) Be_2Ta, Be 1s

(f) Be_2Ta, Ta 4f

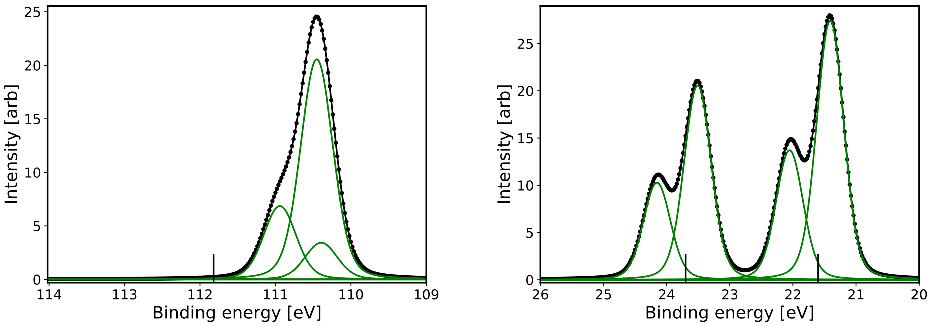

(g) Be_3Ta, Be 1s

(h) Be_3Ta, Ta 4f

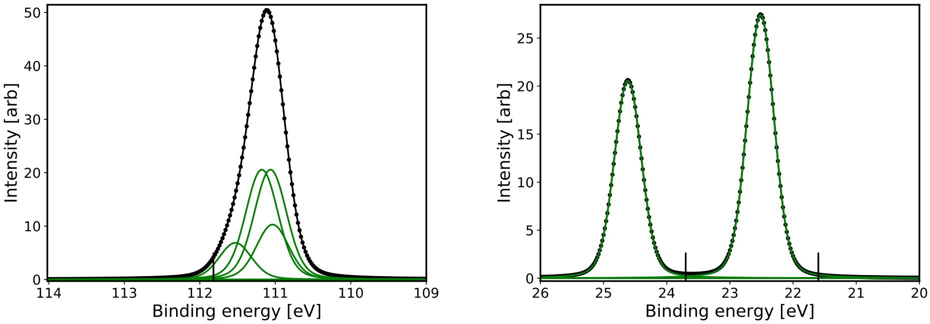

(i) $Be_{17}Ta_2$, Be 1s

(j) $Be_{17}Ta_2$, Ta 4f

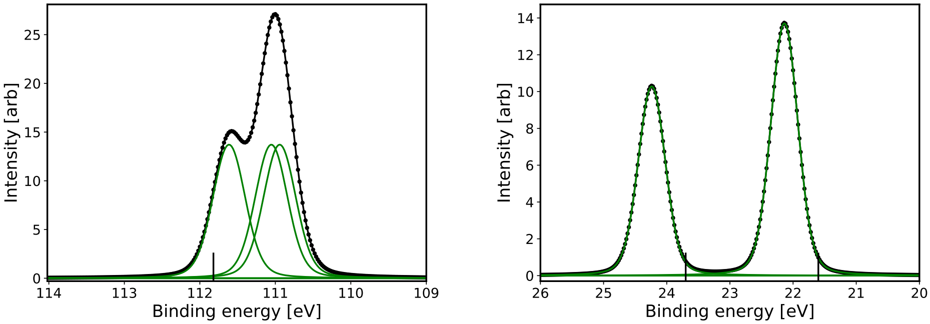

(k) $Be_{12}Ta$, Be 1s

(l) $Be_{12}Ta$, Ta 4f

Fig. 4.33.: Theoretical single phase XPS spectra of Be 1s and Ta 4f from known stable Be-Ta alloys. The spectra are constructed from the *ab initio* chemical shifts and the atom-type information of one computational unit cell, which is listed in Tab. 4.9. All Voigt profiles have a Lorentzian FWHM of 0.1 eV and a gaussian FWHM of 0.43 eV.

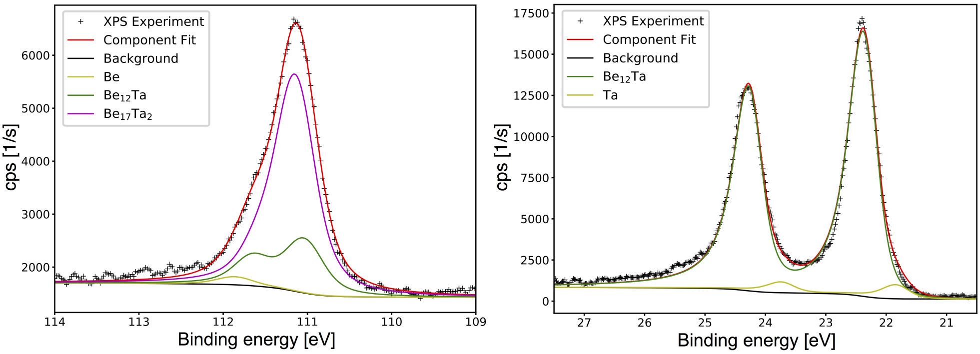

(a) 300 K 0° Be 1s

(b) 300 K 0° Ta 4f

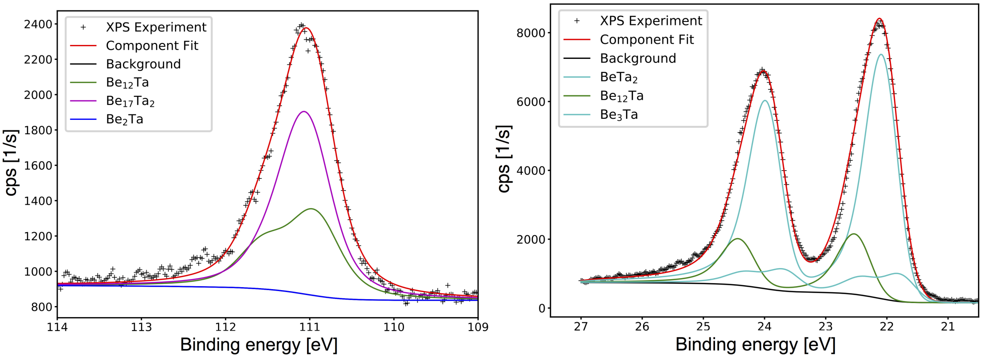

(c) 800 K 40° Be 1s

(d) 800 K 40° Ta 4f

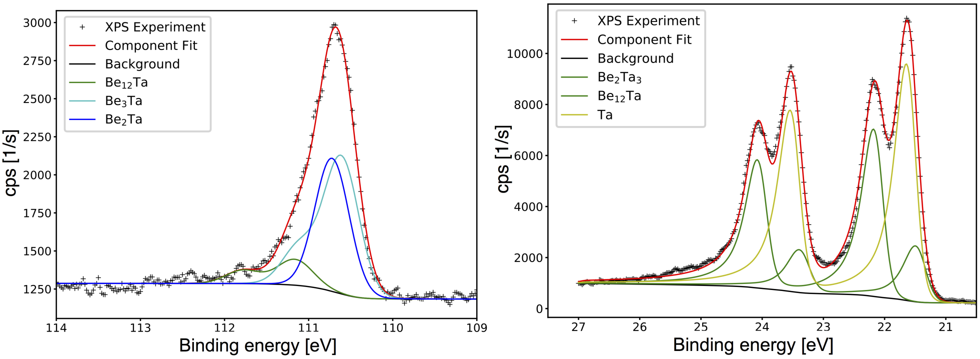

(e) 1000 K 40° Be 1s

(f) 1000 K 40° Ta 4f

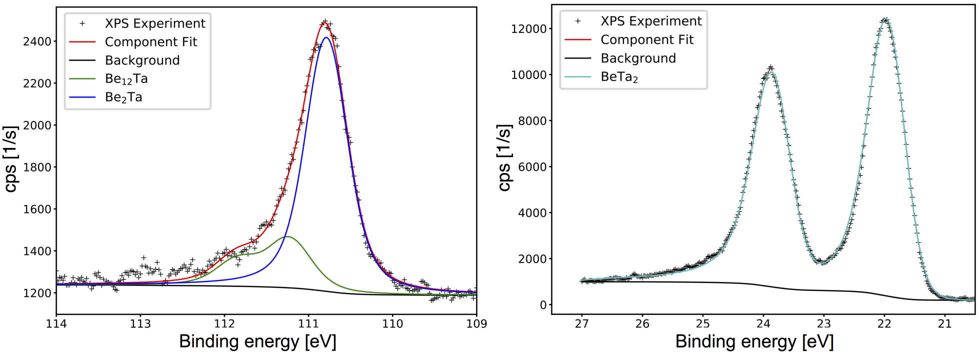

(g) 300 K 0° Be 1s

(h) after heating, 300 K 0° Ta 4f

Fig. 4.34.: Chemical interpretation of Be 1s (left) and Ta 4f (right) XPS spectra with component fits. Each spectrum is fitted *individually*. The fits match the data quite well, only the peak tails cause some trouble. Several phases have only small shifts in the Ta 4f states making the fitting harder, since a slide variation in the 4f reference might lead to completely different phase concentrations. But the resulting phases from the best Be 1s component fits are all inconsistent with their Ta 4f counter parts and therefore physically incorrect.

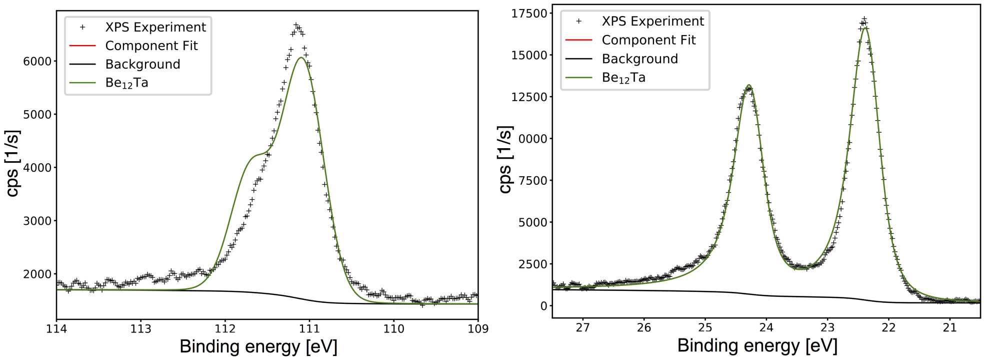

(a) 300 K 0° Be 1s

(b) 300 K 0° Ta 4f

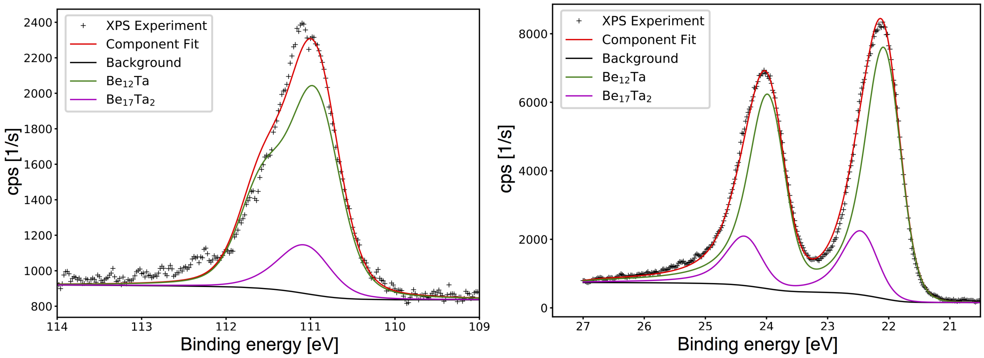

(c) 800 K 40° Be 1s

(d) 800 K 0° Ta 4f

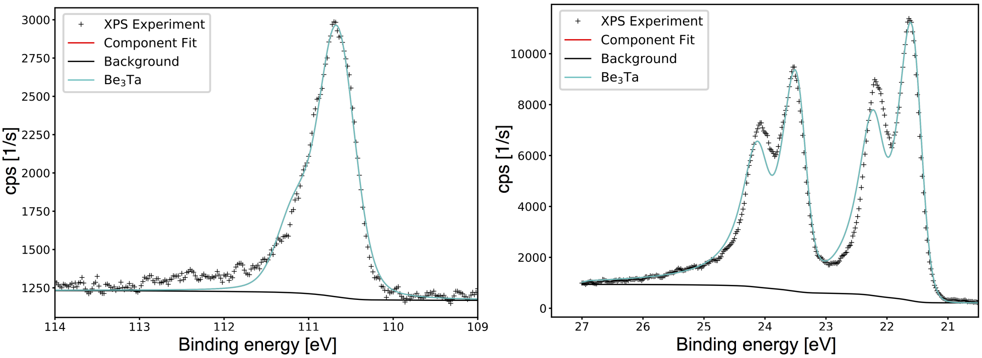

(e) 1000 K 40° Be 1s

(f) 1000 K 40° Ta 4f

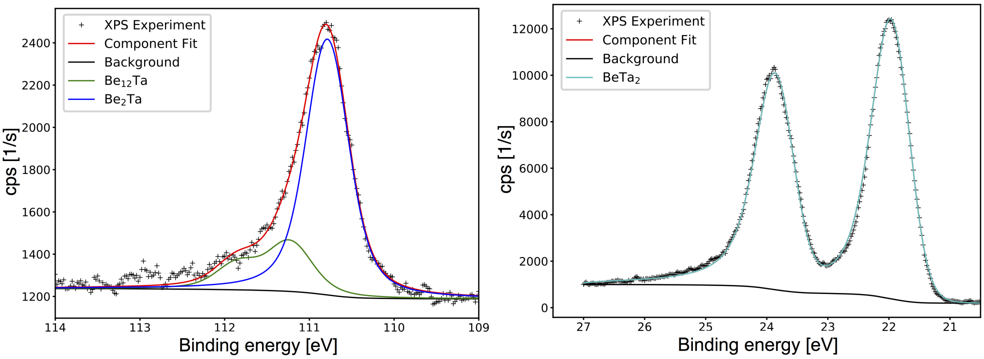

(g) after heating 300 K 0° Be 1s

(h) after heating, 300 K 0° Ta 4f

Fig. 4.35.: Chemical interpretation of the same Be 1s (left) and Ta 4f (right) XPS spectra as in Fig. 4.34, but this time with *consistent constrained* component fits. Both spectral regions, Be 1s and Ta 4f are optimized *at once*, enforcing the same phase concentration ratios. The best fits match the experimental data less as when freely fitting each spectrum on its own. Especially, the shape of the theoretical Be 1s spectrum of $Be_{12}Ta$ is problematic in the fit. While the fits are still not optimal the overall physical interpretation is now intuitive. Starting with a pure $Be_{12}Ta$ ((a, b) sample 1, (c, d) sample 2), while annealing at higher temperature Be evaporates, encouraging the formation of Ta richer phases. Then Be_3Ta seems to dominate at the surface of sample 2 (e,f), but after measuring again after the whole procedure the surface region of sample 2 contains mainly Be_2Ta (g, h).

database identifier	symmetry group	material formula	enthalpy of formation [eV/atom]	(PBE) volume scale V/V_0
58738	I 4/mcm 140	$BeTa_2$	-0.170	1.01557
616431	P 4/mbm 127	Be_2Ta_3	-0.181	1.01627
616428	F d-3mS 227	Be_2Ta	-0.191	1.00725
616429	R -3mH 166	Be_3Ta	-0.236	1.01231
616430	R -3mH 166	$Be_{17}Ta_2$	-0.179	0.99092
109317	I 4/mmm 139	$Be_{12}Ta$	-0.138	0.98561

Tab. 4.8.: *Ab initio* enthalpy of formation for most stable compounds of the Be-Ta system are listed. From a Birch-Murnaghan equation of states fit the unit-cell volume with the lowest total energy for the PBE functional is found. The reported volume scales V/V_0 are with respect to the experimental reported volume V_0 of the unit cell of the crystal.

the Be 1s states Voigt profiles were applied as peak-function form while for the 4f states the asymmetric LA form was used. The asymmetric peak shape introduces one additional degrees of freedom, which makes the least squares fitting harder, taking more iterations. The same asymmetry is assumed for all Ta 4f chemical environments within one 4f spectrum.

The experimental Ta 4f splitting was determined to be 1.92 eV [90]. This splitting is applied in the fitting since the DFT results of 1.98 eV deviates to much from experiment. Other doublet separations predicted by DFT are also slightly larger like 11.56 eV [90] versus measured 11.50 eV for the Ta 4ds and for the Ta 4ps 62.96 eV [90] versus the measured 62.50 eV separation.

Unfortunately, these first concentrations ratios results of Fig. 4.34 and the preferred phases in the Be 1s fits (left) do not compare well to the phases found in the 4f fits (right). These first results are problematic, since we believe both spectra to arise from the same sample area and the same information depth. Furthermore, we also believe that the sample did not change during the measurement time. In the Be-Ta system Be_2Ta and $BeTa_2$ both have only a very small Ta 4f shift, making the variance of the Ta reference problematic. Also these phases have large Be 1s shifts and it should be clear from the Be 1s if they are in the information depth or not.

Fitting first the Be 1s then the Ta 4f with the same phases and constrained concentration ratios did not resolve the mismatch. To overcome this problem both spectral regions are fitted within one optimization enforcing the same phase concentration ratios. This leads in the cases of mixed phases to an additional significant reduction in optimization parameters, which is good. The same spectra with these consistent component fits are shown in Fig. 4.35.

material formula	Be 1s electrons	Be 1s DFT CLSs [eV]	Ta 4f7/2 electrons	Ta 4f DFT CLSs [eV]
$BeTa_2$	4	2.128	32	-0.10
Be_2Ta_3	8	2.170	16,32	0.22, 0.12
Be_2Ta	8	1.265	16	0.18
Be_3Ta	2,12,4	1.427, 1.368, 0.878	16,8	0.19, -0.45
$Be_{17}Ta_2$	6,12,12,4	0.291, 0.641, 0.755, 0.784	8	-0.92
$Be_{12}Ta$	8,8,8	0.877, 0.206, 0.767	8	-0.54

Tab. 4.9.: *Ab initio* results of all core-level shifts of most stable compounds of the Be-Ta system and how many Be 1s electrons contribute per each unit cell of these systems. Depending on the crystal symmetry there are several chemical environments resulting in different chemical shifts. All these chemical shifts are currently experimentally not known in the literature. From this data all XPS spectra containing a mixture of Be-Ti binary phases can be fitted.

These fits match the data not that well overall as the *individual* fits did before, but now the phase content is *consistent*. From this interpretation can be concluded that there is $Be_{12}Ta$ in both samples. Though the Ta 4f can be explained with mainly the $Be_{12}Ta$ phase, the Be 1s results for $Be_{12}Ta$ cannot capture the form of the spectrum. The origin of this form is still to be understood. To gain enough statistics in the Be 1s spectra, it takes hours to measure them. From the experimental side should be checked if the sample does indeed not change, and no averaged out process is seen. From the theory side it should be checked if the chemical shifts for $Be_{12}Ta$ do not change much for the fully relaxed cell within DFT (the ground state PBE lattice volume was 1.5 % smaller). Also with beyond DFT methods it could be checked if the form of the Be 1s peak is indeed not asymmetric at all. The influence of a consistent Shirely background for spectra containing multiple chemical environments should be tested.

After annealing to 1000 K the spectrum clearly changed and the best consistent fit contains only Be_3Ta. This can capture the shift and form of the Be 1s spectrum and the splitting of the Ta 4f. Though the fit fails to match the 4f data exactly. Some intensity is missing in the higher binding energy peaks and overestimating their flanks. Be has evaporated from the sample leaving this stable phase in the transition at the surface.

At higher annealing temperatures or after preferential Ar sputtering mainly the Ta richer Be_2Ta is found at the surface. The Ta 4f spectra can again be very well explained by mainly coming from the Be_2Ta phase, while it is also clearly seen in the Be 1s spectra. Though the overall form of the Be 1s spectra can again not be very well explained by just Be_2Ta.

Comparing the component fit with the traditional fit evaluation of the data by N. Helfer [229] shows that both can fit the spectra well. The component fit always needs less fit parameters as is summed up in Tab. 4.10. Fitting both spectra usually reduces the number of fit parameters again. In the most simple case, a spectrum with a single phase with one contribution, all approaches need the same amount of fit parameters. The problems with the single spectra component fit are expected to also arise in the tradition approach. The component fit enforces a chemical interpretation or leads to a bad or failed fit, which points to missing or wrong information.

XPS spectrum Fig. 4.34, 4.35	N Fit parameters traditional [229]	N Fit parameters individual fits Fig. 4.34	N Fit parameters both in one fit Fig. 4.35
(a+b)	(8+9)=17	(6+6)=12	(4+5)=9
(c+d)	(8+9)=17	(6+7)=13	(5+5)=10
(e+f)	(8+8)=16	(6+8)=14	(5+5)=10
(g+h)	(8+9)=17	(5+5)=10	(5+6)=11

Tab. 4.10.: This table compares the number of fit parameters needed to fit the presented Be-Ta spectra. The traditional evaluation from [229] using UniFit always requires even for these quite simple spectra more fit parameters than the component fit. By fitting the Be 1s and Ta 4f spectra within one optimization enforcing the same phase content the number of fit parameters (last column) is even further reduced. For single phase spectra containing one atom-type no reduction in fit parameters is achievable.

4.3.4. Core-level Shifts of selected other Systems

Materials in nature contain nearly always impurities, and it is cost intensive to purify materials. Here, further core-level shift (CLS) data on metallic binary alloys from the small material screening project is listed. Systems containing Be and W might be of further interest for the fusion community. Be alloys are also used in the aerospace and space flight industries. Tungsten has also various further applications and is for example mixed into some high-tech steels. The Be 1s CLS are collected in Tab. 4.11 while the W 4f CLS are listed in Tab. 4.12. The chosen Be reference structure in the screening differed from the one selected in the detailed investigation. The difference in their Be 1s reference is 211 meV, leading to a systematic difference. An investigation has shown that these structures are very similar in their total energy per atom, to be consistent I have recalculated the core-level shifts from the screening with the high-quality reference used before. For W the difference in the W 4f references was only 17 meV, which I did not correct for. This demonstrates how the choice of the reference structure may introduce systematic biases in the data. This bias could be investigated and estimated by looking at the difference in the Kohn-Sham core levels for different elemental structures. Data discussed in detail in the Be-W, Be-Ti and Be-Ta sections are excluded from the tables. Be rich phases have often several chemical environments while the most W alloys have only one chemical environment of tungsten. In Tab. 4.13 the 1s core-level shifts for converged lithium alloys are listed. The agreement in formation energies with the VASP program was for these compounds also quite good. Li alloys are important for battery research and are also used in the Tritium breeding blanket of a fusion reactor.

MP Database Identifier	Symmetry Group	Material Formula	Be atoms	Be 1s DFT CLSs [eV]
mp-603	227	Be_2Ag	4	-0.29
mp-12761	139	$BeAu_2$	1	-1.5
mp-1220	216	Be_5Au	4, 1	-0.49, -1.87
mp-27757	129	Be_4B	2, 2, 4	0.11, 0.18, 0.23
mp-1432	225	Be_2B	2	1.25
mp-30425	226	$Be_{13}Ba$	2, 12, 12	0.82, 0.4, 0.41
mp-11280	191	$Be_{12}Ti$	2, 6, 2, 2	-0.25, 0.91, -0.19, 0.75
mp-30441	166	$Be_{17}Nb_2$	6, 3, 6, 2	0.83, 0.89, 0.75, 0.38
mp-12648	166	$Be_{17}Ti_2$	2, 6, 6, 3	0.59, 0.9, 0.99, 1.13
mp-2544	166	$Be_{17}Zr_2$	12, 2, 3	0.83, 0.54, 0.92
mp-1845	226	$Be_{13}Ca$	2, 24	0.83, 0.54
mp-457	226	$Be_{13}Ce$	24, 2	0.68, 1.09
mp-1878	226	$Be_{13}Hf$	24, 2	0.68, 1.23
mp-976039	226	$Be_{13}Lu$	2, 24	1.02, 0.6
mp-855	226	$Be_{13}Mg$	24, 2	0.42, 0.75
mp-337	226	$Be_{13}Pu$	2, 24	1.08, 0.75
mp-972891	226	$ScBe_{13}$	2, 24	1.05, 0.65
mp-2080	226	$Be_{13}Sr$	2, 12, 12	0.82, 0.48, 0.49
mp-1562	226	$Be_{13}Th$	12, 12, 2	0.56, 0.55, 1.06
mp-1163	226	$Be_{13}U$	2, 24	1.09, 0.76
mp-865889	226	$Be_{13}Yb$	2, 24	0.95, 0.61
mp-30445	226	$Be_{13}Zr$	2, 24	1.23, 0.71
mp-2553	191	Be_2Hf	2	1.45
mp-1018057	63	BeHf	2	1.38
mp-13453	63	$BePd_3$	2	0.27
mp-978963	194	$BeTi_3$	2	0.94

mp-1252	191	Be_2Zr	2	1.41
mp-983590	221	Be_3Fe	3	0.64
mp-973292	221	Be_3Mn	3	0.89
mp-977552	221	Be_3Tc	3	0.11
mp-2031	227	Be_2Cu	2, 2	0.59, 0.6
mp-2028	227	Be_2Nb	4	1.14
mp-11272	127	Be_2Nb_3	4	1.94
mp-2676	227	Be_2Ta	4	1.2
mp-1025010	216	Be_5Fe	4, 1	1.38, 0.07
mp-2025	191	Be_5Hf	2, 3	0.83, 1.11
mp-650	216	Be_5Pd	4, 1	0.51, -0.83
mp-11277	191	$ScBe_5$	3, 2	1.05, 0.74
mp-11283	191	Be_5Zr	2, 3	0.88, 1.18
mp-984315	194	Be_3Ni	2, 4	0.44, 0.43
mp-864894	194	Be_3Rh	6	0.14
mp-984612	194	Be_3Ru	6	0.39
mp-30438	194	Be_2Cr	2, 6	1.57, 1.68
mp-2225	194	Be_2Fe	2, 6	1.08, 1.25
mp-11270	194	Be_2Mn	6, 2	1.48, 1.36
mp-1677	194	Be_2Mo	6, 2	1.19, 1.11
mp-11275	194	Be_2Re	6, 2	0.51, 0.4
mp-11281	194	Be_2V	2, 6	1.66, 1.72
mp-11282	194	Be_2W	6, 2	1.16, 1.04
mp-2323	221	BeCu	1	-0.2
mp-1033	221	BeNi	1	0.37
mp-11274	221	BePd	1	-0.76
mp-13452	139	$BePd_2$	1	-0.13
mp-11276	221	BeRh	1	0.73
mp-11279	221	BeTi	1	0.9

Tab. 4.11.: Core-level shifts collection of other binary compounds from the screening containing Be. Beryllium rich systems have often several Be atom-types per unit cell. Different atom-types having the same core-level shifts are added together. These shift are calculated with the same reference structure as for the in detail Be-Ti, Be-Ta, Be-W evaluation

MP Database Identifier	Symmetry Group	Material Formula	W atoms	W 4f7/2 DFT CLSs [eV]
mp-30337	182	Al_5W	2	0.43
mp-12524	181	Al_2W	3	0.74
mp-11696	12	As_3W_2	2, 2	-0.03, -0.13
mp-1008487	63	BW	2	-0.59
mp-1113	140	BW_2	4	-0.07
mp-7832	141	BW	4	-0.6
mp-569803	194	B_2W	4	-0.53
mp-11282	194	Be_2W	4	0.68
mp-684602	58	CW_2	4	0.32
mp-567397	162	CW_2	6	0.4
mp-2034	60	CW_2	8	0.41
mp-1894	187	CW	1	0.43
mp-23269	148	WCl_3	6	-1.4
mp-1008274	221	Co_3W	1	-0.43
mp-2157	194	Co_3W	2	-0.26
mp-20868	194	Fe_2W	4	-0.02
mp-542595	139	Ge_2W	1	-0.08
mp-1007761	194	HW	2	0.36
mp-1400	227	HfW_2	4	0.6
mp-30744	51	IrW	2	0.1
mp-30745	194	Ir_3W	2	-0.88
mp-19066	65	O_8W_3	2, 1	-0.06, -0.22
mp-11329	12	P_2W	2	-0.19
mp-11328	36	P_2W	2	-0.09
mp-2420	62	PW	4	-0.42
mp-1018129	71	Pt_2W	1	-0.63
mp-30866	194	Rh_3W	2	-0.78
mp-862655	194	Ru_3W	2	0.12
mp-1620	139	Si_2W	1	0.16
mp-31219	140	Si_3W_5	2, 4, 4	-0.25, -0.39, -0.38
mp-979289	225	W_3Ta	1, 2	0.19, 0.4
mp-22693	31	Te_2W	4	-0.21
mp-675	227	W_2Zr	4	0.58

Tab. 4.12.: Core-level shifts collection of other binary metallic compounds containing W from the screening. Most of the tungsten alloys contain only one W atom-type per unit cell.

MP Database Identifier	Symmetry Group	Material Formula	Li atoms	Li 1s DFT CLSs [eV]
mp-1018026	141	AgLi	2	0.47
mp-977126	194	$AgLi_3$	6	0.37
mp-862716	139	Ag_3Li	1	0.51
mp-2426	221	AgLi	1	0.73
mp-976408	139	$AgLi_3$	1, 2	0.16, 0.42
mp-865875	225	$AgLi_3$	1, 2	0.08, 0.49
mp-1067	141	AlLi	2	-0.3
mp-10890	221	Al_3Li	1	0.47
mp-975906	139	Al_3Li	1	0.51
mp-568404	12	Al_4Li_9	2, 2, 1, 2, 2	0.68, 0.51, 0.52, 0.45, 0.61
mp-975868	139	$AlLi_3$	1, 2	0.65, 0.75
mp-11248	221	Au_3Li	1	0.76
mp-11247	225	$AuLi_3$	2, 1	0.72, 0.14
mp-1001835	194	BLi	2	0.47
mp-16726	62	BLi	4	0.63
mp-210	194	$BaLi_4$	2, 2, 4, 8, 4, 4	-0.02, 0.01, -0.19, -0.09, -0.1, -0.0
mp-22902	123	BiLi	1	-0.56
mp-1021323	191	$C_{12}Li$	1	2.05
mp-1001581	191	C_6Li	1	2.29
mp-11644	227	$CaLi_2$	4	0.13
mp-976272	139	Ca_3Li	1	-0.07
mp-570466	194	$CaLi_2$	4, 4	0.1, 0.11
mp-976075	139	$CaLi_3$	1, 2	0.1, -0.01
mp-975929	225	$CaLi_3$	1, 2	0.16, -0.08
mp-1437	227	CdLi	2	0.08
mp-973940	225	Cd_3Li	1	-0.34
mp-865612	194	Cd_3Li	2	0.01
mp-867343	225	$CdLi_3$	1, 2	0.1, 0.38
mp-975904	139	$CdLi_3$	1, 2	0.25, 0.31
mp-974058	225	Cu_3Li	1	1.43

mp-862658	139	Cu_3Li	1	1.4
mp-975882	139	$CuLi_3$	2, 1	0.63, 0.55
mp-567306	166	Ga_7Li_3	6	-0.8
mp-1307	227	GaLi	2	-0.74
mp-29210	63	$GaLi_2$	2, 2	0.46, 0.71
mp-867205	221	Ga_3Li	1	0.11
mp-976025	139	$GaLi_3$	1, 2	0.54, 0.67
mp-976023	225	$GaLi_3$	2, 1	0.88, 0.45
mp-29631	63	Ge_6Li_{11}	4, 2, 2, 4, 2, 4, 4	0.72, 0.5, 0.21, 0.61, 0.79, 0.52, 0.57
mp-29630	65	Ge_2Li_7	5, 4, 1, 4	0.52, 0.31, -0.35, 0.56
mp-8490	141	GeLi	4, 2	0.1, 0.3
mp-9918	88	GeLi	8	-0.12
mp-973824	225	Hg_3Li	1	-0.74
mp-2012	221	HgLi	1	0.12
mp-1646	225	$HgLi_3$	2, 1	0.44, 0.04
mp-976047	139	$HgLi_3$	2, 1	0.34, 0.19
mp-22460	227	InLi	2	-0.99
mp-31324	63	$InLi_2$	2, 2	0.16, 0.39
mp-973748	139	In_3Li	1	-0.4
mp-867226	225	$InLi_3$	1, 2	0.27, 0.6
mp-976055	139	$InLi_3$	1, 2	0.27, 0.43
mp-30738	44	Ir_3Li	1	1.86
mp-9563	190	$SbLi_2$	6, 6	0.03, 0.27
mp-30769	164	Sn_5Li_{13}	2, 1, 2, 2, 4, 2	-0.02, -0.13, 0.37, 0.58, 0.19, 0.56
mp-30767	65	Sn_2Li_7	4, 1, 4, 1, 4	0.37, 0.25, 0.2, -0.3, 0.38
mp-30768	11	Sn_3Li_7	2, 2, 2, 2, 2, 2, 2	-0.04, -0.03, 0.33, -0.19, -0.23, 0.23, 0.41
mp-672287	55	Si_4Li_{13}	2, 4, 4, 4, 4, 4, 4	0.9, 0.66, 0.62, 0.81, 0.99, 0.75, 0.85
mp-973374	63	Mg_2Li	2	0.28
mp-973455	2	Mg_2Li	2	0.35
mp-1018789	58	O_2Li	2	4.05
mp-728	191	$PdLi_2$	2	0.78
mp-2170	191	$PtLi_2$	2	0.9
mp-30764	227	Pt_2Li	2	0.76
mp-975799	194	Zn_3Li	2	0.65
mp-976139	25	$MgLi_3$	2, 1	0.29, 0.12
mp-976254	221	$MgLi_3$	3	0.33

mp-976256	225	$MgLi_3$	2, 1	0.29, 0.22
mp-976244	8	MgLi	1, 1, 1	0.37, 0.36, 0.31
mp-976262	8	MgLi	2, 1	0.36, 0.35
mp-976239	38	MgLi	1, 1, 1	0.44, 0.4, 0.39
mp-30760	139	$PbLi_3$	1, 2	0.01, 0.5
mp-976281	139	$PdLi_3$	2, 1	0.83, 0.66
mp-11489	225	$PdLi_3$	1, 2	0.45, 1.05
mp-976322	139	$PtLi_3$	1, 2	0.89, 1.18
mp-7396	225	$TlLi_3$	2, 1	0.44, 0.09
mp-976412	225	$ZnLi_3$	1, 2	0.24, 0.58
mp-976414	139	$ZnLi_3$	2, 1	0.51, 0.44
mp-977207	194	$MgLi_2$	4	0.17
mp-976885	155	$MgLi_2$	1, 3	0.2, 0.12
mp-976843	12	$MgLi_2$	2, 2	0.15, 0.26
mp-976982	63	$MgLi_2$	2, 2	0.11, 0.31
mp-982380	8	$MgLi_2$	1, 1, 1, 1	0.1, 0.14, 0.21, 0.22
mp-7924	127	Sn_5Li_2	4	-0.17
mp-977122	38	$MgLi_5$	1, 1, 1, 1, 1	0.16, 0.27, 0.06, 0.18, 0.12
mp-976944	8	$MgLi_5$	1, 1, 1, 2	0.17, 0.09, 0.2, 0.21
mp-865604	189	$MgLi_5$	3, 2	0.17, 0.28
mp-973316	194	$NaLi_3$	6	-0.34
mp-13444	141	SnLi	4, 2	-0.32, -0.21
mp-30761	164	Pb_2Li_7	2, 2, 1, 2	0.24, 0.28, -0.21, 0.41
mp-27587	12	Pb_3Li_8	2, 2, 4	0.02, -0.18, 0.31
mp-795	88	SiLi	8	0.22
mp-7507	136	Sr_3Li_2	8	-0.17
mp-865939	12	Mg_2Li	1	0.38
mp-2744	187	PdLi	1	0.96
mp-861931	221	Pt_3Li	1	1.67
mp-600561	187	RhLi	1	1.38
mp-1001787	44	Rh_3Li	1	1.98
mp-865907	225	Zn_3Li	1	0.36

Tab. 4.13.: Core-level shifts collection of other binary metallic compounds containing Li from the screening. Many of the lithium alloys contain several Li atom-types per unit cell. The crystal structures were extracted from the materials Project (MP).

4.4. *Ab initio* Simulation Results Sum-up

It was demonstrated that material screening with the all-electron FLAPW method, especially with the `FLEUR` code is possible. The challenging part is the automatic choice of FLAPW parameters and electronic setup which is robust while describing the given system right and still allowing for accurate comparisons of total energies between materials. Furthermore, it was demonstrated that the default FLAPW parameters of `FLEUR` are not always ready for this challenge and point to possible ways of improvement, like better determination of muffin-tin radii and further flexibility in the basis cutoffs for good matching criteria. For my rather small proof of principle high-throughput project I have fixed the FLAPW parameters for each element. Similar things were done in past works like for the full-potential linear muffin-tin orbital (FP-LMTO) calculations of the Electronic Structure Project (ESP) [58, 312]. The usual run mode of the exciting FLAPW code [313, 314] uses fixed species parameters stored in files.

Workflows from the AiiDA-FLEUR package have been deployed to calculate the initial-state core-level shifts of known binary metals (4435 out of 5058) from the Materials Project. For elemental references the elemental structures (1271) of the ICSD have been calculated. This small proof of concept one shot project ran for two weeks totaling over 9000 `FLEUR` simulations with different resource requirements managed by AiiDA. The overall success rate was 68.6 % achieved with the SCF-workflow. Overall, 7.1 % failed for various reasons, 24.3 % did not reach convergence. This is to be seen as a snapshot in time. Most of the non-converged systems were f elements which were calculated with collinear magnetism and spin orbit coupling. All systems were calculated with spin orbit coupling included. The actually overall success rate of non f-systems was lowered by a hybrid parallelization specification mistake which lead to long run times. So not only the fidelity of the `FLEUR` code but also the workflow has to improved. Certain easy user mistakes are to be avoided.

For evaluating the quality of the produced data differences and agreements of `FLEUR` and VASP results were pointed out for formation enthalpies and the calculated bandgap. A comparison of chemical shifts with the overlap of 133 entries of the NIST XPS database [90] showed partially agreement but a large spread in the experimental data. Without any quality measures in place, chemical shift results from this run can include systematic uncertainties due to the reference structure choice. To benchmark the chemical shifts in the database it is better to apply them in the evaluation of single crystal XPS spectra.

Results for the Be-W, Be-Ti, Be-Ta systems were presented in more detail including convex-hull constructions and equation of states. From the calculated core-level shifts and atom-type information theoretical predicted single-phase spectra were constructed. With these theoretical spectra experimental XPS spectra measured by colleagues were fitted and chemically interpreted. The developed component fit method was compared to traditional fit procedure.

The Be 1s spectra were fitted with Voigt profile peak shapes for each chemical environment while for the 4f spectra asymmetric peak shapes were necessary. The resulting concentrations from the phases in the Be 1s fits did not correspond well to the best fit of the 4f spectra. This can be overcome by fitting both spectra at once, constraining the phase content.

It becomes clear from these XPS spectra evaluations, that the component fit approach provides new opportunities, but relies on very precise data and experiments. The method should be further benchmarked against high-resolution single crystal spectra with known broadenings and accurately known elemental reference to check the DFT result very precisely. Also the asymmetric LA shape is not optimal, since changing the gaussian broadening does not affect the asymmetry and to increase the tail significantly the Lorentzian broadening has also to become quite large. Additionally trying out other optimizers, besides least squares with gradient-decent, may improve the method, since there may be local minima, dependencies on the starting points and bounds to be dealt with. Also investigation surface effects and surface core-level shifts might complete the picture. The approximation of the spectral background needs to be included consistently in the fit an revised for several chemical environments. The standard background assume one contribution within one main peak which may introduce systematic errors in the background.

5. Conclusion and Outlook

Designing and optimizing materials on the computer is a profound challenge to accelerate and bring down the cost of innovation driven by materials. In condensed matter physics, materials science and chemistry computational methods and tools play an ever growing role when calculating properties of materials. The same is true for designing and predicting new ideal (nano) materials. *Ab initio* methods provide practical computable approximations to the many-body problem of many electrons. Density functional theory is a widely applied *ab initio* method to calculate observables as a functional of the electron density. Through a minimization principle the ground state density of a many-body system can be self-consistently determined by solving an auxiliary Kohn-Sham system. Data from *ab initio* simulations is valuable for many applications and data hubs emerged in the community out of larger projects. However all-electron reference data is rare, most of the data ($\approx 90\%$) available comes from pseudo-potential plane wave methods.

Chemical configuration space is too large to just screen through it by brute force. Practical methods are needed to cope with its size beyond high-throughput computing and automation of tasks. These methods need to determine what configurations are worth calculating in detail, or may yield promising properties. We have demonstrated that with the AiiDA framework high-throughput calculations of around one million calculation tasks per week are possible.

In this thesis the open source AiiDA-FLEUR package was developed, which allows for automation of calculations with the all-electron quantum engine `FLEUR`. The `FLEUR` program as well as many other electronic structure packages can now be deployed together within a single high-level python work environment using AiiDA, allowing to profit from the individual strengths of each package. Workflows are physical property calculator protocols for a given task or sub task. Expert knowledge and strategies can be embedded into workflows allowing for robustness, fault tolerance and fidelity. Within this work workflows to converge a `FLEUR` calculation, to calculate an equation of states, a density of states, a band structure, formation energies, core-level shifts and binding energies have been implemented. Some of these workflows were deployed on larger ($\mathcal{O}(100) - \mathcal{O}(1000)$) sets of crystal structures from various sources.

X-ray photoemission spectroscopy is a powerful tool to gain insight into the chemical composition within the surface region of a sample. It is widely applied in research and industry for material characterization. The exact analysis of high resolution XPS spectra is still an ongoing challenge which poses various difficulties. Core-level shifts provide insight on the chemical environments and are a key component for such analysis. It was argued that a usual fitting approach with only few constraints has fundamental problems with samples containing phases which have multiple not clearly separated chemical environments of the same element. Therefore, the application range of the usual approach is rather limited to simple phases and their simple mixtures. Since some important spectral properties of XPS spectra can be computed via *ab initio* methods, a physically motivated fit built on *ab initio* data was proposed. This data-driven evaluation approach often contains less degrees of freedom and has the potential to scale to complexer systems. Also this evaluation strategy allows to build in additional constraints like an experimentally known stoichiometry or to fit several spectra with the same phase content at once. This way additional degrees of freedom can be eliminated from the fitting. Furthermore, linear dependencies between the phases can be determined and the method allows for the extraction of phase concentrations.

A proof of principle application of this data-driven component-fit approach was demonstrated on ’well behaved’ high-resolution XPS spectra of main core-level lines of Be-W, Be-Ti and Be-Ta systems. ’Well behaved’ meaning without many other physical effects having major contributions to these spectra. The Be-Ti and Be-Ta data was measured at the IEK-4 by Nicola Helfer. These material systems are of interest to the nuclear fusion community. The alloying under certain annealing temperatures could be better understood with this developed analysis, which was not possible to this extent beforehand. The best fit for individual core-level spectra might not be consistent with the best fit results of other core-level lines. Fitting several different core-level spectra of the same sample at once enforces consistency, or may point to sources of inconsistency.

Furthermore, in a small proof of principle screening project with `FLEUR` the initial-state core-level shifts were calculated for 4435 binary metals, out of 5058 stable materials found in the Materials Project. By enabling this project and from executing it, we have learned about the robustness of the `FLEUR` program, data infrastructure and throughput capabilities of computing resources. From this knowledge future high-throughput projects with `FLEUR` may profit. In this project we have calculated more than twice as many main-line core-level shifts than are found in the NIST XPS database, a mature experimental numerical reference database, which is representative for the whole literature. Our data set allows for evaluation of XPS spectra of these metals. The overlap from the materials with the NIST database was only 133 core lines of 45 materials. The comparison of data posed challenges due a wide spread in the NIST data and no in detail uncertainty investigation of our data. Some properties from the binary materials were also quantitatively compared to VASP simulations from the Materials Project. As elemental references the energetically favorable structures from the ICSD were taken. A wrong reference will lead to systematic differences in the core-level shifts and formation energies of systems containing that element. Elements with open 4f and 5f shells still pose a challenge to the SCF workflow as they would need special treatment within DFT.

As an outlook, in the future the tools for computational material design developed in our community and *ab initio* packages become more robust and will bring us closer towards driving materials discovery and materials optimization. Also all-electron programs will enter the high-throughput highway. Individual groups and projects will contribute to curated and searchable data repositories. Larger comparisons and accuracy classification of DFT quantum engines will become feasible. On the way the robustness and scalability of quantum engines and frameworks will improve. Bringing the code packages to a high-level platform will allow to harvest their individual strengths bringing us closer to a materials design infrastructure, saving resources by not redoing things over and over again. Meta workflows which are *ab initio* package agnostic might emerge from community efforts. Online platforms or companies can provide utilities and services with a higher visibility to serve outside communities and industry.

For the `FLEUR` program additional workflows with high-throughput capabilities implementing advanced features will emerge. The current basic workflows and utilities of AiiDA-FLEUR will be reused and refined in these tasks. Workflows and tools from also other *ab initio* packages may become helpful for calculating other important properties of fusion relevant materials, like diffusion properties of materials, thermal conductivity, influence of crystal defects, mechanical properties, or oxidization properties. This may help in the research of finding and characterizing promising materials or their sub components and precipitates.

With a structural symmetry analysis one could check which entries in the NIST database should be seen rather carefully, by checking if the crystal structures of the reported materials in NIST have several atom-types and therefore may give rise to several different core-level shifts.

Through *ab initio* methods a database including all relevant properties of core-level spectra of all known materials and surfaces may be created, forming the foundation for data-driven spectra interpretation. With machine learning this base data may be extrapolated to arbitrary system sizes or collective surface contributions. On top of such data an evaluation program like casaXPS or UniFit deploying advanced smart component-fits may solve large parts of the XPS spectra interpretation problem. Such a tool or service may accelerate materials discovery, material characterization and innovation in industries and laboratories around the world.

Appendices

A. Software Stack

New software is usually only the tip of the iceberg. It depends on a wide range of tools for numerics, data processing and visualization. I can hardly mention and give credit to every piece of software that was useful for my work or depended on, but I tried and compiled the following table (Tab. A.1) of the in my view most important packages and data sources. May it be useful for people continuing this or similar work and save them time.

Software	Code, License	usage, influence
Python based		
AiiDA [63]	OS, MIT	Managing workflows and provenance
AiiDA-FLEUR (this work)	OS, MIT	Using FLEUR with AiiDA
Masci-tools (partly this work)	OS, MIT	Utility, special plotting
Jupyter-notebook [181]	OS, mod BSD	Documenting, developing, executing work
Pandas [315]	OS, BSD	Data evaluation and quick statistics
numpy [316]	OS, BSD	Data processing, handling
Pymatgen [152]	OS, MIT	Structure and other data manipulation
ASE [64]	OS, GNU LGPL	Structure manipulation
matplotlib [317]	OS, PSF	Data visualization
bokeh [266]	OS, BSD	Interactive data visualization
lxml [318]	OS, BSD	XML processing, parsing with python
Spglib [178]	OS, New BSD	symmetry processing of structures
json (python en/decoder)	OS, PSF	Processing of json files
h5py	OS, PSF	Processing of hdf5 files
Other software		
FLEUR code (intel stack) [79]	OS, MIT	Fortran DFT code, this works simulations
Postgresql	OS, PSQL	Data and provenance storage
git (github, gitlab, bitbucket)	OS, GPLv2	Code and work version control
LaTeX, TeXstudio	OS,LPPL	Writing and formating text
Microsoft Powerpoint	commercial	Presentations, talks, workflow layouts
Libre Office	OS,MPL2	Documentation, workflow layouts
CI services, Jenkins, Travis	commercial	Continous integration and testing

sphinx [174]	OS, Sphinx	Code documentation
read the docs [175]	OS, MIT	Hosting code documentation
Graphviz [319–321]	OS, GPL v1.0	Database small graph visualizations
Gephi [322]	OS, GPL	Database large graph visualizations
docker, docker-compose [323]	commercial	AiiDA-FLEUR tutorial and tests
dbbeaver [324]	OS, ASL	Database status, management and changes
postgres app mac [325]	OS, PSQL	PostgreSQL deployment on mac
postico app mac [326]	commercial	Database changes on mac
pgadmin [327]	OS, PSQL	Database status and management
gource [328]	OS,GPL3	Repository visualization
Databases		
ICSD [89]	commercial	Structure data source for this work
Materials Project, API [39, 54]	open data	login needed, structure data source
AFLOWLib [56]	open data	Structure data source for this work
OQMD and its API [55]	open data	Structure data source (mysql db)
NIST XPS [90]	open data	Database of XPS binding energies
Materialscloud [59]	open data	Visualization of data, and data source
COD [134]	open data	Structure data source for this work

Tab. A.1.: Notice: Dependencies of the software packages are not mentioned, only if they have been used extensively as stand alone. Each category is roughly sorted after relevance, with most relevant first. Default software from the Linux and Mac OS infrastructure of the PGI and computing resources are also not mentioned.

B. Code and Data Visualization

B.1. AiiDA Database Overview

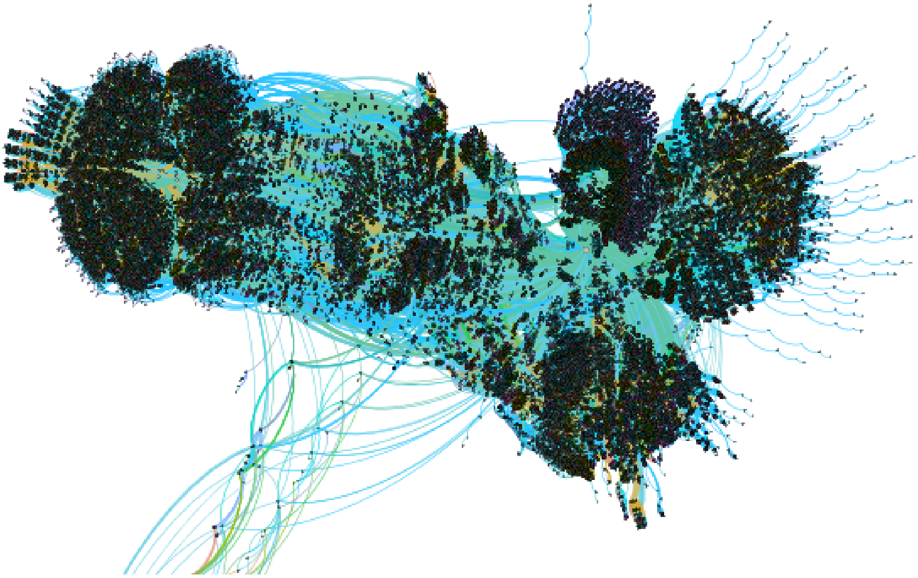

Fig. B.1.: A directed acyclic provenance graph of a small SQL database containing over 4000 self-consistent field cycles of different codes resulting in around 130000 nodes (black dots) to provide a brief impression on complexity and scalability. (Produced with Gephi [322], Multi force-directed graph layout)

When running many complex workflows or a material screening task one ends up with millions of files on disk and databases with easily tens of millions of nodes. A database with one million nodes is about three gigabyte and more in size. In the method development section the footprint in the AiiDA provenance graph of the developed workflows for `FLEUR` were discussed. To get an impression about the complexity of a rather small overall, cumulative AiiDA provenance graph containing some workflows with different codes on various computers is shown in Fig. B.1. The graph depicts about 4000 self-consistent field workflows with different codes, versions and computing resources, resulting in about 130,000 nodes (black dots). The graph is layouted with a parallel multi-force-atlas graph-layout algorithm using Gephi [322]. Clusters of nodes evolve around different highly connected `FLEUR` code nodes on diverse computing resources. Crystallographic Information File (CIF) data nodes from which crystal structures have been extracted dangle loosely connected around the edges. Such a plain full graph visualization is for the extraction of physics or browsing interactively through the data rather not useful. Force graph visualization might be in general helpful to visualize structure property maps, or other higher dimentional complex relationships.

Node type	quantity	relative content	comment
ParameterData	221670	38.68 %	should be less, AiiDA bug
WorkCalculation	147718	25.77 %	should be less, AiiDA bug
StructureData	38259	6.68 %	
RemoteData	34500	6.02 %	`FLEUR` plus `inpgen`
FolderData	34202	5.96 %	`FLEUR` plus `inpgen`
CifData	32232	5.62 %	
FleurinpData	29202	5.10 %	get modified in workflows
FleurinputgenCalculation	17701	3.09 %	
FleurCalculation	17015	2.97 %	
Others	600	0.10 %	

Tab. B.1.: Snapshot of the node content of the database with after the first metal screening results. The (provenance) and input preparation overhead is 33 nodes per `FLEUR` calculation. This overhead depends in detail on the workflows deployed and their design. Under high-throughput conditions, sometimes the tasks of small fast *WorkCalculations* within workflows were executed multiple times (100-1000) for some reason (bug in AiiDA). This causes an excess of *WorkCalculations* and *ParameterData* nodes. The real overhead is probably more around 10-15 nodes. This bug might be fixed in newer AiiDA versions. These double nodes may be cleaned from the database. Also in newer AiiDA and AiiDA-FLEUR version most of the *WorkCalculation* block will largely consist out of *CalcFunctions*.

B.2. Disk footprint Overview

Fig. B.2 displays a birds-eye view on disk usage of a small AiiDA workstation. While the Postgres databases creates files with a certain maximum fixed size, in this case one GB the repository has a lot of files with different sizes. In this case all files are quite small. For `FLEUR` the largest files are the 'out.xml' files and the 'last_cdn.hdf' files, which are for small systems only up to 100 MB. This view should point out the requirements on storage of the database and the repository. When replacing the repository with an object store the AiiDA repository would be one large file, or several smaller files of fixed size as in the database case. Visualization of the screenings data footprint would have taken long and would add nothing special to the picture.

Fig. B.2.: Bird-eye view of disk usage of a small AiiDA workstation (120 GB). The AiiDA repository with many small files is shown on the left. The larger boxes correspond to the charge density files of the last iteration and 'out.xml' files. The disk footprint of the PostgreSQL databases (on the right) are several larger files with around 1 GB in size. This points out the different storage requirements for the repository and the database. Lastest database backups files and files with additional parsed information for evaluation can also become quite large. Most of the rest is data unrelated to AiiDA, or other small environments. (created with GrandPerspective.app [329])

B.3. Repository Code Overview

Software is not static. During the development (2016-2018) of AiiDA-FLEUR and masci-tools also AiiDA and the `FLEUR` program changed significantly. The progress of the source code from the software packages over time is visualized in the following figures to give credit to the developer teams and to provide insight into these ecosystems. The figures have been created from the git history of the packages. Fig. B.3 shows the code development of the `FLEUR` team including all files. Prior to 2016 the code was not openly available within a git repository. The initial commit of the full previous code in Q2 2016 is cut off in the graph. In Fig. B.4 the progress of the python code of the aiida-core package is shown. The masci-tools repository python code development shown in Fig. B.6, it contains utility which is independent of AiiDA and can be reused within the institute. It is a mixed code package. Fig. B.6 documents the status of solely the python code in the AiiDA-FLEUR package. Contributions to AiiDA-FLEUR from Vasily Tseplyaev started in the fourth quarter of 2018. Before 2017 the package was in another repository under a different name, which history is not included.

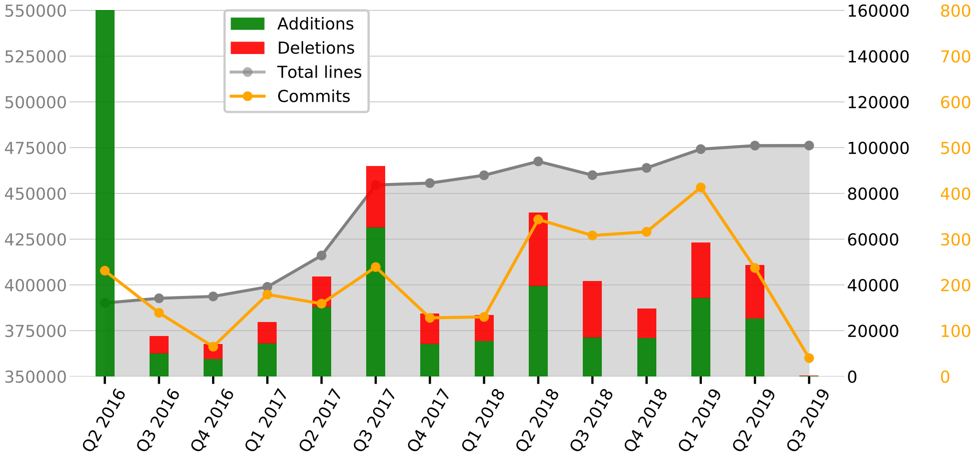

Fig. B.3.: The gitlab repository of `FLEUR` was created in the second quarter of 2016. The graph shows the total changes and activity on all files. The large initial commit of previous code of `FLEUR` in Q2 2016 is cut off. The total lines refer to all file types.

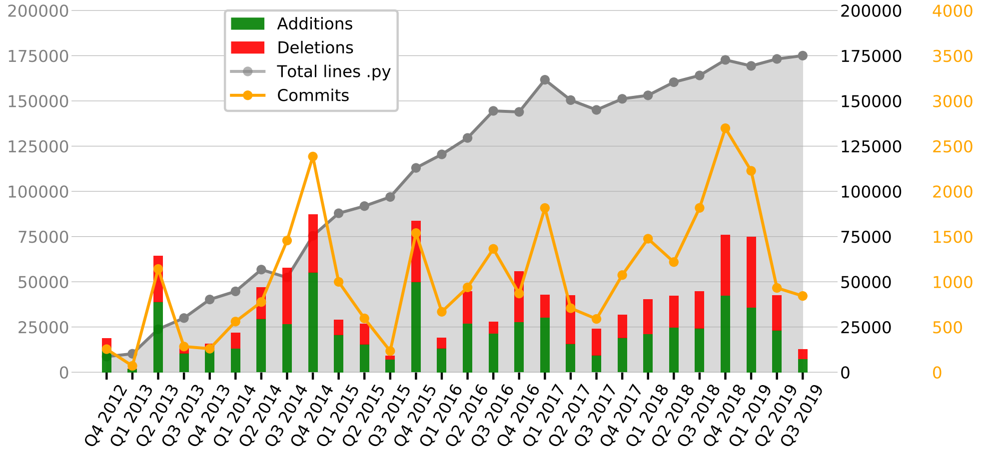

Fig. B.4.: AiiDA-core package development over time is visualized in this graph. The total lines refer to python code files only.

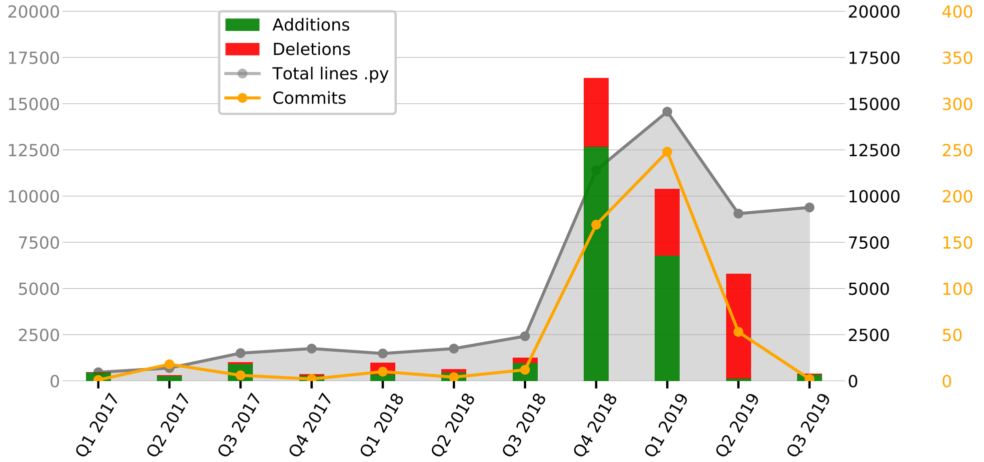

Fig. B.5.: The evolution of the Masci-tools repository, containing AiiDA independent utility and tools applied at the IAS-1 and rather specific to electronic structure.

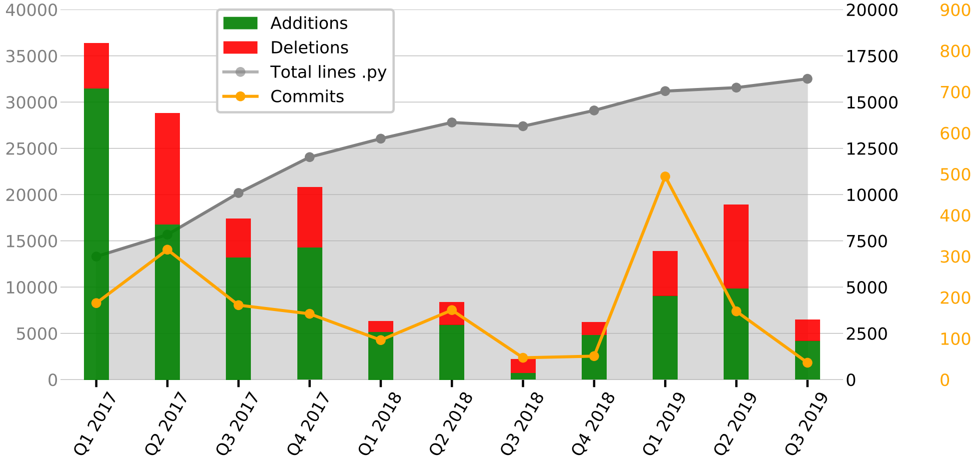

Fig. B.6.: The AiiDA-FLEUR development started at the end of 2015, but the repository was renamed and moved, which is why the history is only visible since Q2 2016 with a large initial changes. The total lines refer to python code files only.

Conventions and Abbreviations

In this work, we stick to the following conventions in mathematical expressions:

Symbol		Explanation
$\mathbf{r}$	bold	3 or 4-dimensional vector
$\hat{\mathbf{r}}$	bold hat	normalized 3-dimensional vector
$\underline{c}$	underline	general vector
$\underline{\underline{M}}$	double underline	general matrix

The following abbreviations and physical constants are used:

Abbr.	Meaning
AI	Artificial Intelligence
API	Application Programming Interface
a_0	Bohr radius
bcc	body-centered cubic
BE	binding energy
BZ	Brillouin zone
CLS	core-level shift
CPU	central processing unit
cps	counts per sweep
DB	data base
DFT	density functional theory
DOS	density of states
EOS	equation of states
ESCA	electron spectroscopy for chemical analysis

fcc	face-centered cubic
FWHM	full-width half-maximum
FLAPW	full-potential linearized augmented-plane-wave (method)
FLOPS	floating point operations per second
FP	full potential
GF	Green function
GGA	general gradient approximation
hcp	hexagonal close-packed
HDD	hard disk drive
HPC	high-performance computing
HTC	high-throughput computing
HTML	Hypertext Markup Language
IAS	Institute of Advanced Simulation
IBZ	irreducible Brillouin zone
IEK	Institute of Energy and Climate Research
IO	input/output
IR	interstitial region
ISS	ion scattering spectroscopy
IT	information technology
ITER	International Thermonuclear Experimental Reactor
LA	asymmetric Lorentz profile
LDA	local density approximation
LO	local orbital
MPI	Message Passing Interface
MT	Muffin tin
MTC	Many-tasks computing
NRA	Nuclear reaction analysis
OS	open source
PBE	PBE exchange-correlation (functional)
PCA	Principle Component Analysis
PES	photoemission spectroscopy
PGI	Peter Grünberg Institute
QMA	Quantum Merlin Arthur complexity class
RAM	random access memory
RBS	Rutherford backscattering spectrometry
RMT	Muffin-tin radius

SCF	self-consistent field
SOC	spin-orbit coupling
SSD	solid state drive
SQL	structured query language
UHV	ultra-high vacuum
UPS	ultraviolet photoelectron spectroscopy
XAS	X-ray absorption spectroscopy
XC	exchange-correlation (functional)
XML	Extensible Markup Language
XRD	X-ray diffraction
XPS	X-ray photoelectron spectroscopy

List of Figures

List of Tables

Bibliography

[1] OECD. *OECD Environmental Outlook to 2050.* 2012, p. 350. DOI: 10.1787/9789264122246-en. (Cit. on p. 1).

[2] United Nations. *Paris Agreement.* 2015 (cit. on p. 1).

[3] United Nations Statistics Division. *The Sustainable Development Goals Report 2019.* 2019 (cit. on p. 1).

[4] United Nations General Assembly. *United Nations General Assembly A/RES/70/1: Transforming our world: the 2030 Agenda for Sustainable Development.* 2015 (cit. on p. 1).

[5] OECD. *Global Material Resources Outlook to 2060.* 2019, p. 212. DOI: 10.1787/9789264307452-en. (Cit. on p. 1).

[6] N. A. of Sciences Engineering and Medicine (cit. on p. 1).

[7] L. Dobrzanski. "Significance of materials science for the future development of societies". In: *Journal of Materials Processing Technology* 175 (06/2006), pp. 133–148. DOI: 10.1016/j.jmatprotec.2005.04.003 (cit. on p. 1).

[8] M. A. Green. *Solar cells: Operating principles, technology, and system applications.* 1982 (cit. on p. 1).

[9] M. A. Green. "Thin-film solar cells: review of materials, technologies and commercial status". In: *Journal of Materials Science: Materials in Electronics* 18.1 (2007), pp. 15–19. ISSN: 1573-482X. DOI: 10.1007/s10854-007-9177-9. (Cit. on p. 1).

[10] A. G. Aberle. "Surface passivation of crystalline silicon solar cells: a review". In: *Progress in Photovoltaics: Research and Applications* 8.5 (2000), pp. 473–487. DOI: 10.1002/1099-159X(200009/10)8:5<473::AID-PIP337>3.0.CO;2-D. (Cit. on p. 1).

[11] G. Chamberlain. "Organic solar cells: A review". In: *Solar Cells* 8.1 (1983), pp. 47 –83. ISSN: 0379-6787. DOI: 10.1016/0379-6787(83)90039-X. (Cit. on p. 1).

[12] G. Niu, X. Guo, and L. Wang. "Review of recent progress in chemical stability of perovskite solar cells". In: *J. Mater. Chem. A* 3 (17 2015), pp. 8970–8980. DOI: 10.1039/C4TA04994B. (Cit. on p. 1).

[13] P. Brøndsted, H. Lilholt, and A. Lystrup. "Composite materials for wind power turbine blades". In: *Annual Review of Materials Research* 35.1 (2005), pp. 505–538. DOI: `10.1146/annurev.matsci.35.100303.110641`. (Cit. on p. 1).

[14] P. Schilke. "Advanced Gas Turbine Materials and Coatings". In: *GE reference Library GER-3569G* (2004), pp. 1–25. URL: `http://www.baaax.ir/Content/media/article/[P.W._Scheke]_Advanced_Gas_Turbine_materials_and_c(BookZZ.org)_0.pdf` (cit. on p. 1).

[15] S. Weitemeyer et al. "Integration of Renewable Energy Sources in future power systems: The role of storage". In: *Renewable Energy* 75 (2015), pp. 14 –20. ISSN: 0960-1481. DOI: `10.1016/j.renene.2014.09.028`. (Cit. on p. 1).

[16] F. Steinke, P. Wolfrum, and C. Hoffmann. "Grid vs. storage in a 100% renewable Europe". In: *Renewable Energy* 50 (2013), pp. 826 –832. ISSN: 0960-1481. DOI: `10.1016/j.renene.2012.07.044`. (Cit. on p. 1).

[17] X. Qu et al. "The Electrolyte Genome project: A big data approach in battery materials discovery". In: *Computational Materials Science* 103 (2015), pp. 56–67. ISSN: 09270256. DOI: `10.1016/j.commatsci.2015.02.050`. (Cit. on pp. 1, 26, 27).

[18] S. J. Zinkle and J. T. Busby. "Structural materials for fission & fusion energy". In: *Materials Today* 12.11 (2009), pp. 12 –19. ISSN: 1369-7021. DOI: `10.1016/S1369-7021(09)70294-9`. (Cit. on p. 1).

[19] M. Rieth et al. "Recent progress in research on tungsten materials for nuclear fusion applications in Europe". In: *Journal of Nuclear Materials* 432.1 (2013), pp. 482 –500. ISSN: 0022-3115. DOI: `10.1016/j.jnucmat.2012.08.018`. (Cit. on p. 1).

[20] B. C. H. Steele and A. Heinzel. "Materials for fuel-cell technologies". In: *Materials for Sustainable Energy*, pp. 224–231. DOI: `10.1142/9789814317665_0031`. (Cit. on p. 1).

[21] A. G. Kusne et al. "On-the-fly machine-learning for high-throughput experiments: search for rare-earth-free permanent magnets". In: *Scientific Reports* 4 (2014), p. 6367. DOI: `10.1038/srep06367`. (Cit. on p. 1).

[22] B Dupé et al. "Engineering skyrmions in transition-metal multilayers for spintronics". In: *Nature Communications* 7 (2016), p. 11779. DOI: `10.1038/ncomms11779`. (Cit. on p. 1).

[23] P. Kurz. "Non-Collinear Magnetism at Surfaces and in Ultrathin Films". In: 0 (2000), p. 219. URL: `http://hdl.handle.net/10068/266501` (cit. on p. 1).

[24] T. D. Sparks et al. "Data mining our way to the next generation of thermoelectrics". In: *Scripta Materialia* 111 (01/2016), pp. 10–15. ISSN: 13596462. DOI: `10.1016/j.scriptamat.2015.04.026`. (Cit. on pp. 1, 34).

[25] R. Waser. *Nanoelectronics and Information Technology: Advanced Electronic Materials and Novel Devices*. Wiley, 2012. ISBN: 9783527409273 (cit. on p. 1).

[26] V. Stanev et al. "Machine learning modeling of superconducting critical temperature". In: (2017), pp. 1–17. arXiv: `1709.02727`. URL: `http://arxiv.org/abs/1709.02727` (cit. on pp. 1, 34).

[27] S. Shrivastava and A. International. *Medical Device Materials: Proceedings from the Materials & Processes for Medical Devices Conference 2003, 8-10 September 2003, Anaheim, California*. ASM International, 2004. ISBN: 9781615032600 (cit. on p. 1).

[28] R. S. Bohacek, C. McMartin, and W. C. Guida. "The art and practice of structure-based drug design: A molecular modeling perspective". In: *Medicinal Research Reviews* 16.1 (), pp. 3–50. DOI: `10.1002/(SICI)1098-1128(199601)16:1<3::AID-MED1>3.0.CO;2-6`. (Cit. on pp. 1, 8, 19).

[29] C. G. Simon Jr. and S. Lin-Gibson. "Combinatorial and High-Throughput Screening of Biomaterials". In: *Advanced Materials* 23.3 (2011), pp. 369–387. DOI: `10.1002/adma.201001763`. (Cit. on p. 1).

[30] J. C. Dellamorte, M. A. Barteau, and J. Lauterbach. "Opportunities for catalyst discovery and development: Integrating surface science and theory with high throughput methods". In: *Surface Science* 603.10 (2009). Special Issue of Surface Science dedicated to Prof. Dr. Dr. h.c. mult. Gerhard Ertl, Nobel-Laureate in Chemistry 2007, pp. 1770 –1775. ISSN: 0039-6028. DOI: `10.1016/j.susc.2008.11.056`. (Cit. on p. 1).

[31] O. A. von Lilienfeld. "First principles view on chemical compound space: Gaining rigorous atomistic control of molecular properties". In: *International Journal of Quantum Chemistry* 113.12 (06/2013), pp. 1676–1689. ISSN: 00207608. DOI: `10.1002/qua.24375`. (Cit. on pp. 1, 6, 19, 34).

[32] D. Davies et al. "Computational Screening of All Stoichiometric Inorganic Materials". In: *Chem* 1.4 (2016), pp. 617 –627. ISSN: 2451-9294. DOI: `10.1016/j.chempr.2016.09.010`. (Cit. on pp. 1, 20, 34).

[33] R. Friedel and P. Israel. *Edison's Electric Light: The Art of Invention*. Johns Hopkins Introductory Studies in the History of Technology. Johns Hopkins University Press, 2010. ISBN: 9780801899447 (cit. on p. 1).

[34] V. Smil. *Enriching the Earth: Fritz Haber, Carl Bosch, and the Transformation of World Food Production*. The MIT Press. MIT Press, 2004. ISBN: 9780262693134 (cit. on p. 1).

[35] Prometeus GmbH. *TOP500*. URL: `https://www.top500.org/statistics/perfdevel/` (visited on 05/24/2019) (cit. on pp. 1, 8).

[36] G. Hautier, A. Jain, and S. P. Ong. "From the computer to the laboratory: materials discovery and design using first-principles calculations". In: *Journal of Materials Science* 47.21 (2012), pp. 7317–7340. ISSN: 0022-2461. DOI: `10.1007/s10853-012-6424-0`. (Cit. on pp. 2, 26).

[37] K. Alberi et al. "The 2019 materials by design roadmap". In: *Journal of Physics D: Applied Physics* 52.1 (2019), p. 013001. URL: `http://stacks.iop.org/0022-3727/52/i=1/a=013001` (cit. on pp. 2, 26).

[38] J. J. de Pablo et al. "New frontiers for the materials genome initiative". In: *npj Computational Materials* 5.1 (2019), p. 41. ISSN: 2057-3960. DOI: `10.1038/s41524-019-0173-4`. (Cit. on p. 2).

[39] A. Jain et al. "Commentary: The materials project: A materials genome approach to accelerating materials innovation". In: *APL Materials* 1.1 (2013). ISSN: 2166532X. DOI: `10.1063/1.4812323` (cit. on pp. 2, 22, 24, 26, 91, 93, 160).

[40] B. Meredig. "Industrial materials informatics: Analyzing large-scale data to solve applied problems in R&D, manufacturing, and supply chain". In: *Current Opinion in Solid State and Materials Science* 21.3 (2017). Materials Informatics: Insights, Infrastructure, and Methods, pp. 159 –166. ISSN: 1359-0286. DOI: `10.1016/j.cossms.2017.01.003`. (Cit. on pp. 2, 34).

[41] K. Rajan. "Materials informatics". In: *Materials Today* 8.10 (2005), pp. 38 –45. ISSN: 1369-7021. DOI: `10.1016/S1369-7021(05)71123-8`. (Cit. on p. 2).

[42] S. Ramakrishna et al. "Materials informatics". In: *Journal of Intelligent Manufacturing* Dean 1990 (2018), pp. 1–20. ISSN: 15728145. DOI: `10.1007/s10845-018-1392-0`. (Cit. on p. 2).

[43] A. Dima et al. "Informatics Infrastructure for the Materials Genome Initiative". In: *JOM* 68.8 (2016), pp. 2053–2064. ISSN: 1543-1851. DOI: `10.1007/s11837-016-2000-4`. (Cit. on p. 2).

[44] P. A. M. Dirac and R. H. Fowler. "Quantum mechanics of many-electron systems". In: *Proceedings of the Royal Society of London. Series A, Containing Papers of a Mathematical and Physical Character* 123.792 (1929), pp. 714–733. DOI: `10.1098/rspa.1929.0094`. (Cit. on pp. 2, 6).

[45] F. Schwabl, ed. *Quantenmechanik (QM I) : eine Einführung*. 7. Aufl. Springer-Lehrbuch. Berlin: Springer, 2007, XV, 430 S. ISBN: 9783540736745 (cit. on pp. 2, 5).

[46] F. Schwabl. *Quantenmechanik für Fortgeschrittene (QM II)*. Springer-Lehrbuch. Springer Berlin Heidelberg, 2008. ISBN: 9783540850762 (cit. on pp. 2, 5).

[47] S. Blügel et al. *Computing solids: Models, ab-initio methods and supercomputing ; lecture notes of the 45th IFF Spring School 2014*. Vol. 74. Schriften des Forschungszentrums Jülich : Reihe Schlüsseltechnologien. Jülich: Forschungszentrum Jülich, 2014. ISBN: 978-3-89336-912-6 (cit. on pp. 2, 3, 10, 13).

[48] O. Isayev et al. "Materials Cartography: Representing and Mining Materials Space Using Structural and Electronic Fingerprints". In: *Chemistry of Materials* 27.3 (2015), pp. 735–743. DOI: `10.1021/cm503507h`. (Cit. on pp. 2, 20).

[49] T. Lookman et al. "Statistical inference and adaptive design for materials discovery". In: *Current Opinion in Solid State and Materials Science* 21.3 (06/2017), pp. 121–128. ISSN: 13590286. DOI: `10.1016/j.cossms.2016.10.002`. (Cit. on p. 2).

[50] L. Ward and C. Wolverton. "Atomistic calculations and materials informatics: A review". In: *Current Opinion in Solid State and Materials Science* 21.3 (06/2017), pp. 167–176. ISSN: 13590286. DOI: `10.1016/j.cossms.2016.07.002`. (Cit. on pp. 2, 34).

[51] A. Jain, K. A. Persson, and G. Ceder. "Research Update: The materials genome initiative: Data sharing and the impact of collaborative ab initio databases". In: *APL Materials* 4.5 (2016), p. 053102. DOI: `10.1063/1.4944683`. (Cit. on p. 2).

[52] J. J. de Pablo et al. "The Materials Genome Initiative, the interplay of experiment, theory and computation". In: *Current Opinion in Solid State and Materials Science* 18.2 (2014), pp. 99 –117. ISSN: 1359-0286. DOI: `10.1016/j.cossms.2014.02.003`. (Cit. on pp. 2, 22).

[53] The PAULING FILE team. *MPDS: Materials Platform for Data Science*. URL: `http://www.mpds.io/` (visited on 05/24/2019) (cit. on pp. 2, 22).

[54] S. P. Ong et al. "The Materials Application Programming Interface (API): A simple, flexible and efficient API for materials data based on REpresentational State Transfer (REST) principles". In: *Computational Materials Science* 97 (2015), pp. 209–215. ISSN: 09270256. DOI: `10.1016/j.commatsci.2014.10.037`. (Cit. on pp. 2, 26, 160).

[55] J. E. Saal et al. "Materials design and discovery with high-throughput density functional theory: The open quantum materials database (OQMD)". In: *Jom* 65.11 (2013), pp. 1501–1509. ISSN: 10474838. DOI: `10.1007/s11837-013-0755-4` (cit. on pp. 2, 26, 32, 34, 86, 92, 160).

[56] S. Curtarolo et al. "AFLOWLIB.ORG: A distributed materials properties repository from high-throughput ab initio calculations". In: *Computational Materials Science* 58 (2012), pp. 227–235. ISSN: 09270256. DOI: `10.1016/j.commatsci.2012.02.002`. (Cit. on pp. 2, 22, 24, 113, 121, 160).

[57] *NOMAD: NOvel MAterials Discovery Laboratory.* URL: `https://www.nomad-coe.eu` (visited on 05/24/2019) (cit. on pp. 2, 23, 26).

[58] C. Ortiz, O. Eriksson, and M. Klintenberg. "Data mining and accelerated electronic structure theory as a tool in the search for new functional materials". In: *Computational Materials Science* 44.4 (2009), pp. 1042 –1049. ISSN: 0927-0256. DOI: `10.1016/j.commatsci.2008.07.016`. (Cit. on pp. 2, 26, 150).

[59] MARVEL, EPFL. *MATERIALSCLOUD: A Platform for Open Science.* URL: `https://www.materialscloud.org` (visited on 05/24/2019) (cit. on pp. 2, 22, 26, 160).

[60] A. Jain et al. "New opportunities for materials informatics: Resources and data mining techniques for uncovering hidden relationships". In: *Journal of Materials Research* 31.08 (2016), pp. 977–994. ISSN: 0884-2914. DOI: `10.1557/jmr.2016.80`. (Cit. on pp. 2, 27, 34).

[61] K. Capelle. "A bird's-eye view of density-functional theory". en. In: *Brazilian Journal of Physics* 36 (12/2006), pp. 1318 –1343. ISSN: 0103-9733. DOI: `10.1590/S0103-97332006000700035`. (Cit. on pp. 3, 10).

[62] S. Curtarolo et al. "AFLOW: An automatic framework for high-throughput materials discovery". In: *Computational Materials Science* 58 (2012), pp. 218 –226. ISSN: 0927-0256. DOI: `10.1016/j.commatsci.2012.02.005`. (Cit. on pp. 3, 26).

[63] G. Pizzi et al. "AiiDA: automated interactive infrastructure and database for computational science". In: *Computational Materials Science* 111 (2016), pp. 218–230. ISSN: 09270256. DOI: `10.1016/j.commatsci.2015.09.013`. arXiv: `1504.01163`. (Cit. on pp. 3, 26, 27, 29, 30, 49, 53, 55, 159).

[64] A. Larsen et al. "The Atomic Simulation Environment—A Python library for working with atoms". In: *Journal of Physics: Condensed Matter* 2.101 (2017) (cit. on pp. 3, 26, 33, 159).

[65] K. Mathew et al. "Atomate: A high-level interface to generate, execute, and analyze computational materials science workflows". In: *Computational Materials Science* 139 (2017), pp. 140–152. ISSN: 09270256. DOI: `10.1016/j.commatsci.2017.07.030`. (Cit. on pp. 3, 26).

[66] A. Jain et al. “FireWorks: a dynamic workflow system designed for high-throughput applications”. In: *Concurrency and Computation: Practice and Experience* 27.17 (2015), pp. 5037–5059. ISSN: 15320626. DOI: `10.1002/cpe.3505`. (Cit. on pp. 3, 26).

[67] X. Yang et al. “MatCloud: A high-throughput computational infrastructure for integrated management of materials simulation, data and resources”. In: *Computational Materials Science* 146 (2018), pp. 319 –333. ISSN: 0927-0256. DOI: `10.1016/j.commatsci.2018.01.039`. (Cit. on pp. 3, 26).

[68] T. Mayeshiba et al. “The MAterials Simulation Toolkit (MAST) for atomistic modeling of defects and diffusion”. In: *Computational Materials Science* 126 (2017), pp. 90 –102. ISSN: 0927-0256. DOI: `10.1016/j.commatsci.2016.09.018`. (Cit. on pp. 3, 26).

[69] K. Mathew et al. “MPInterfaces: A Materials Project based Python tool for high-throughput computational screening of interfacial systems”. In: *Computational Materials Science* 122 (2016), pp. 183 –190. ISSN: 0927-0256. DOI: `10.1016/j.commatsci.2016.05.020`. (Cit. on pp. 3, 26).

[70] Synopsys Inc. *QuantumATK: Atomic-Scale Modeling for Semiconductor & Materials Research.* URL: `https://www.synopsys.com/silicon/quantumatk.html` (visited on 05/24/2019) (cit. on pp. 3, 26).

[71] Dassault Systems Inc. *BIOVIA Materials Studio.* URL: `https://www.3dsbiovia.com/products/collaborative-science/biovia-materials-studio/` (visited on 05/24/2019) (cit. on pp. 3, 26).

[72] Materials Design Inc. *MedeA framework from Materials Design Inc.* URL: `https://www.materialsdesign.com` (visited on 05/24/2019) (cit. on pp. 3, 26).

[73] W. H. Bragg and W. L. Bragg. “The Reflection of X-rays by Crystals”. In: *Proceedings of the Royal Society of London A: Mathematical, Physical and Engineering Sciences* 88.605 (1913), pp. 428–438. ISSN: 0950-1207. DOI: `10.1098/rspa.1913.0040`. (Cit. on p. 3).

[74] Y. Waseda, ed. *X-Ray Diffraction Crystallography [E-Book] : Introduction, Examples and Solved Problems.* Berlin, Heidelberg: Springer-Verlag Berlin Heidelberg, 2011, online resource. ISBN: 9783642166358. URL: `http://dx.doi.org/10.1007/978-3-642-16635-8` (cit. on p. 3).

[75] F. Reinert and S. Hüfner. “Photoemission spectroscopy from early days to recent applications”. In: *New Journal of Physics* 7.1 (2005), p. 97 (cit. on pp. 3, 37, 40).

[76] Paul van der Heide. *X-ray Photoelectron Spectroscopy: An introduction to Principles and Practices.* 2011, p. 264. ISBN: 978-1-118-06253-1. DOI: `10.1002/9781118162897.fmatter` (cit. on pp. 3, 36–38).

[77] ULVAC-PHI Inc. *ULVAC-PHI Inc.* URL: `https://www.ulvac-phi.com/en/` (visited on 05/24/2019) (cit. on pp. 3, 37).

[78] M. C. Biesinger et al. “Resolving surface chemical states in XPS analysis of first row transition metals, oxides and hydroxides: Cr, Mn, Fe, Co and Ni”. In: *Applied Surface Science* 257.7 (2011), pp. 2717 –2730. ISSN: 0169-4332. DOI: `10.1016/j.apsusc.2010.10.051`. (Cit. on pp. 3, 38, 42, 44, 45, 81, 83).

[79] Forschungszentrum Jülich. *FLEUR: The Jülich FLAPW code family.* URL: `http://www.flapw.de` (visited on 05/24/2019) (cit. on pp. 3, 17, 49, 93, 159).

[80] E. Wimmer et al. “Full-potential self-consistent linearized-augmented-plane-wave method for calculating the electronic structure of molecules and surfaces: O_2 molecule”. In: *Phys. Rev. B* 24 (2 1981), pp. 864–875. DOI: `10.1103/PhysRevB.24.864`. (Cit. on pp. 3, 15, 17).

[81] D. J. Singh and L. Nordström. *Planewaves, pseudopotentials, and the LAPW method.* 2nd ed. New York and London: Springer, 2006. ISBN: 978-0-387-28780-5 (cit. on pp. 3, 15, 17, 91, 110).

[82] J. Reimann et al. “Beryllides for fusion reactors”. In: *2009 23rd IEEE/NPSS Symposium on Fusion Engineering.* 2009, pp. 1–4. DOI: `10.1109/FUSION.2009.5226458` (cit. on p. 3).

[83] *Plasma Physics department (IEK-4) of the Institute of Energy and Climate Research at the Forschungszentrum Jülich (FZJ)* (cit. on p. 3).

[84] H. Bruus, K. Flensberg, and O. U. Press. *Many-Body Quantum Theory in Condensed Matter Physics: An Introduction.* Oxford Graduate Texts. OUP Oxford, 2004. ISBN: 9780198566335 (cit. on pp. 5, 14).

[85] P. Dirac. *Lectures on Quantum Mechanics.* Belfer Graduate School of Science, monograph series. Dover Publications, 2001. ISBN: 9780486417134 (cit. on p. 5).

[86] N. Schuch and F. Verstraete. “Computational complexity of interacting electrons and fundamental limitations of density functional theory”. In: *Nature Physics* 5 (08/2009), p. 732. DOI: `10.1038/nphys1370`. (Cit. on p. 6).

[87] Y. K. Liu, M. Christandl, and F. Verstraete. “N-representability is QMA-complete”. In: (2006), pp. 1–6. DOI: `10.1103/PhysRevLett.98.110503`. arXiv: `0609125 [quant-ph]`. (Cit. on p. 6).

[88] International Data Corporation (IDC) (www.idc.com). *IDC document 1678 (2014): The Digital Universe of Opportunities: Rich Data and the Increasing Value of the Internet of Things.* 2014. URL: `https://www.emc.com/leadership/digital-universe/2014iview/executive-summary.htm` (visited on 05/24/2019) (cit. on p. 8).

[89] F. Allen. "Bergerhoff, G. ; Brown, I.D. in „Crystallographic Databases", F.H. Allen et al. (Hrsg.) Chester, International Union of Crystallography, (1987)." In: (1987). URL: `http://www2.fiz-karlsruhe.de/icsd{\_}publications.html` (cit. on pp. 8, 20, 24, 133, 160).

[90] N. Alexander V. et al. *NIST X-ray Photoelectron Spectroscopy Database, NIST Standard Reference Database Number 20, National Institute of Standards and Technology, Gaithersburg MD, 20899.* 2000. DOI: `10.18434/T4T88K`. (Cit. on pp. 8, 43, 80, 82, 105–107, 115, 118, 120, 124, 131, 141, 150, 160).

[91] M. Born and R. Oppenheimer. "Zur quantentheorie der molekeln". In: *Annalen der Physik* 389.20 (1927), pp. 457–484 (cit. on p. 9).

[92] J. C. Slater. "A Simplification of the Hartree-Fock Method". In: *Phys. Rev.* 81 (3 1951), pp. 385–390. DOI: `10.1103/PhysRev.81.385`. (Cit. on p. 10).

[93] P. G. Szalay et al. "Multiconfiguration Self-Consistent Field and Multireference Configuration Interaction Methods and Applications". In: *Chemical Reviews* 112.1 (2012). PMID: 22204633, pp. 108–181. DOI: `10.1021/cr200137a`. (Cit. on p. 10).

[94] I. Shavitt and R. Bartlett. *Many-Body Methods in Chemistry and Physics: MBPT and Coupled-Cluster Theory.* Cambridge Molecular Science. Cambridge University Press, 2009. ISBN: 9780521818322 (cit. on p. 10).

[95] R. Van Noorden, B. Maher, and R. Nuzzo. "The top 100 papers". In: *Nature* 514.7524 (2014), pp. 550–553. ISSN: 0028-0836. DOI: `10.1038/514550a` (cit. on p. 10).

[96] R. O. Jones. "Density functional theory: Its origins, rise to prominence, and future". In: *Reviews of modern physics* 87.3 (2015), p. 897 (cit. on p. 10).

[97] R. O. Jones and O. Gunnarsson. "The density functional formalism, its applications and prospects". In: *Rev. Mod. Phys.* 61 (3 1989), pp. 689–746. DOI: `10.1103/RevModPhys.61.689`. (Cit. on p. 10).

[98] K. Burke. "Perspective on density functional theory". In: *The Journal of Chemical Physics* 136.15 (2012), p. 150901. DOI: `10.1063/1.4704546`. (Cit. on p. 10).

[99] P Hohenberg and W Kohn. "Inhomogeneous Electron Gas". In: *Phys. Rev.* 136.3B (11/1964), B864–B871. DOI: `10.1103/PhysRev.136.B864`. (Cit. on p. 11).

[100] M. A. Marques, M. J. Oliveira, and T. Burnus. “Libxc: A library of exchange and correlation functionals for density functional theory”. In: *Computer Physics Communications* 183.10 (2012), pp. 2272 –2281. ISSN: 0010-4655. DOI: `10.1016/j.cpc.2012.05.007`. (Cit. on p. 11).

[101] S. H. Vosko, L. Wilk, and M. Nusair. “Accurate spin-dependent electron liquid correlation energies for local spin density calculations: a critical analysis”. In: *Canadian Journal of Physics* 58.8 (1980), pp. 1200–1211. DOI: `10.1139/p80-159`. (Cit. on p. 12).

[102] J. P. Perdew et al. “Generalized gradient approximation made simple”. In: *Physical Review Letters* 77.18 (1996), p. 3865. ISSN: 0031-9007. DOI: `10.1103/PhysRevLett.77.3865` (cit. on p. 12).

[103] J. Heyd, G. E. Scuseria, and M. Ernzerhof. “Hybrid functionals based on a screened Coulomb potential”. In: *The Journal of Chemical Physics* 118.18 (2003), pp. 8207–8215. DOI: `10.1063/1.1564060`. (Cit. on p. 12).

[104] W. Kohn and L. J. Sham. “Self-Consistent Equations Including Exchange and Correlation Effects”. In: *Phys. Rev.* 140 (4A 1965), A1133–A1138. DOI: `10.1103/PhysRev.140.A1133`. (Cit. on p. 12).

[105] C. G. Broyden. “A class of methods for solving nonlinear simultaneous equations”. In: *Mathematics of computation* 19.92 (1965), pp. 577–593 (cit. on p. 13).

[106] D. G. Anderson. “Iterative procedures for nonlinear integral equations”. In: *Journal of the ACM (JACM)* 12.4 (1965), pp. 547–560 (cit. on p. 13).

[107] G. Kerker. “Efficient iteration scheme for self-consistent pseudopotential calculations”. In: *Physical Review B* 23.6 (1981), p. 3082 (cit. on p. 13).

[108] D. D. Koelling and B. N. Harmon. “A technique for relativistic spin-polarised calculations”. In: *Journal of Physics C: Solid State Physics* 10.16 (1977), pp. 3107–3114. DOI: `10.1088/0022-3719/10/16/019`. (Cit. on p. 14).

[109] J. Fröhlich and U. M. Studer. “Gauge invariance and current algebra in nonrelativistic many-body theory”. In: *Rev. Mod. Phys.* 65 (3 1993), pp. 733–802. DOI: `10.1103/RevModPhys.65.733`. (Cit. on p. 14).

[110] P. Giannozzi et al. “QUANTUM ESPRESSO: A modular and open-source software project for quantum simulations of materials”. In: *Journal of Physics Condensed Matter* 21.39 (2009). ISSN: 09538984. DOI: `10.1088/0953-8984/21/39/395502`. arXiv: `0906.2569` (cit. on pp. 15, 23).

[111] G. Kresse and D. Joubert. “From ultrasoft pseudopotentials to the projector augmented-wave method”. In: *Phys. Rev. B* 59 (3 1999), pp. 1758–1775. DOI: `10.1103/PhysRevB.59.1758`. (Cit. on p. 15).

[112] Cecam community. *ESL: The Electronic Structure Library*. URL: `https://esl.cecam.org/Main_Page` (visited on 05/24/2019) (cit. on p. 15).

[113] J. M. Soler et al. “The SIESTA method forab initioorder-Nmaterials simulation”. In: *Journal of Physics: Condensed Matter* 14.11 (2002), pp. 2745–2779. DOI: `10.1088/0953-8984/14/11/302`. (Cit. on p. 16).

[114] *OpenMX: Open source package for Material explorer*. URL: `http://www.openmx-square.org` (visited on 05/24/2019) (cit. on p. 16).

[115] C. B. Barber et al. “The Quickhull Algorithm for Convex Hulls”. In: *ACM Trans. Math. Softw.* 22.4 (12/1996), pp. 469–483. ISSN: 0098-3500. DOI: `10.1145/235815.235821`. (Cit. on p. 16).

[116] SciPy developers. *SciPy library, Scientific Python*. URL: `https://www.scipy.org` (visited on 05/24/2019) (cit. on p. 16).

[117] J. J. De Yoreo et al. “Crystallization by particle attachment in synthetic, biogenic, and geologic environments”. In: *Science* 349.6247 (2015). ISSN: 0036-8075. DOI: `10.1126/science.aaa6760`. (Cit. on p. 16).

[118] A. Jain et al. “Formation enthalpies by mixing GGA and GGA + U calculations”. In: *Physical Review B - Condensed Matter and Materials Physics* 84.4 (2011), pp. 1–10. ISSN: 10980121. DOI: `10.1103/PhysRevB.84.045115` (cit. on pp. 16, 27).

[119] G. Hautier et al. “Accuracy of density functional theory in predicting formation energies of ternary oxides from binary oxides and its implication on phase stability”. In: *Physical Review B* 85 (2012), p. 155208. DOI: `10.1103/PhysRevB.85.155208` (cit. on pp. 16, 27, 105).

[120] S. Kirklin et al. “The Open Quantum Materials Database (OQMD): Assessing the accuracy of DFT formation energies”. In: *npj Computational Materials* 1.November (2015). ISSN: 20573960. DOI: `10.1038/npjcompumats.2015.10`. (Cit. on pp. 16, 26, 109).

[121] O. K. Andersen. “Linear methods in band theory”. In: *Phys. Rev. B* 12 (8 1975), pp. 3060–3083. DOI: `10.1103/PhysRevB.12.3060`. (Cit. on p. 17).

[122] D. D. Koelling and G. O. Arbman. “Use of energy derivative of the radial solution in an augmented plane wave method: application to copper”. In: *Journal of Physics F: Metal Physics* 5.11 (1975), pp. 2041–2054. DOI: `10.1088/0305-4608/5/11/016`. (Cit. on p. 17).

[123] M. Weinert, E. Wimmer, and A. J. Freeman. “Total-energy all-electron density functional method for bulk solids and surfaces”. In: *Phys. Rev. B* 26 (8 1982), pp. 4571–4578. DOI: `10.1103/PhysRevB.26.4571`. (Cit. on p. 17).

[124] S. Blügel and B. G. “Full-Potential Linearized Augmented Planewave Method”. In: *Computational Nanoscience: Do It Yourself!* Vol. 31. John von Neumann Institute for Computing, Jülich, 2006, pp. 85–129. ISBN: 3-00-017350-1 (cit. on p. 17).

[125] M. Betzinger et al. “Local exact exchange potentials within the all-electron FLAPW method and a comparison with pseudopotential results”. In: *Phys. Rev. B* 83 (4 2011), p. 045105. DOI: `10.1103/PhysRevB.83.045105`. (Cit. on p. 17).

[126] F. Freimuth et al. “Maximally localized Wannier functions within the FLAPW formalism”. In: *Phys. Rev. B* 78 (3 2008), p. 035120. DOI: `10.1103/PhysRevB.78.035120`. (Cit. on p. 17).

[127] M. Betzinger et al. “Precise response functions in all-electron methods: Application to the optimized-effective-potential approach”. In: *Phys. Rev. B* 85 (24 2012), p. 245124. DOI: `10.1103/PhysRevB.85.245124`. (Cit. on p. 17).

[128] B. Zimmermann et al. “First-principles analysis of a homochiral cycloidal magnetic structure in a monolayer Cr on W(110)”. In: *Phys. Rev. B* 90 (11 2014), p. 115427. DOI: `10.1103/PhysRevB.90.115427`. (Cit. on p. 17).

[129] M. Betzinger, C. Friedrich, and S. Blügel. “Hybrid functionals within the all-electron FLAPW method: Implementation and applications of PBE0”. In: *Phys. Rev. B* 81 (19 2010), p. 195117. DOI: `10.1103/PhysRevB.81.195117`. (Cit. on p. 17).

[130] Y. Mokrousov, G. Bihlmayer, and S. Blügel. “Full-potential linearized augmented planewave method for one-dimensional systems: Gold nanowire and iron monowires in a gold tube”. In: *Physical Review B* 72.4 (2005). ISSN: 0163-1829. DOI: `\url{10.1103/PhysRevB.72.045402}` (cit. on p. 18).

[131] D. Singh. “Ground-state properties of lanthanum: Treatment of extended-core states”. In: *Phys. Rev. B* 43 (8 1991), pp. 6388–6392. DOI: `10.1103/PhysRevB.43.6388`. (Cit. on p. 18).

[132] G. Michalicek et al. “Elimination of the linearization error and improved basis-set convergence within the FLAPW method”. In: *Computer Physics Communications* 184.12 (2013), pp. 2670–2679. ISSN: 00104655. DOI: `10.1016/j.cpc.2013.07.002`. arXiv: `1302.3130`. (Cit. on pp. 18, 47).

[133] P. Villars et al. “The Pauling File, Binaries Edition”. In: *Journal of Alloys and Compounds* 367.1 (2004). Proceedings of the VIII International Conference on Crystal Chemistry of Intermetallic Compounds, pp. 293 –297. ISSN: 0925-8388. DOI: `10.1016/j.jallcom.2003.08.058`. (Cit. on p. 22).

[134] S. Gražulis et al. “Crystallography Open Database (COD): an open-access collection of crystal structures and platform for world-wide collaboration”. In: *Nucleic Acids Research* 40.D1 (2012), pp. D420–D427. DOI: `10.1093/nar/gkr900`. (Cit. on pp. 22, 87, 160).

[135] F. H. Allen. “The Cambridge Structural Database: a quarter of a million crystal structures and rising”. In: *Acta Crystallographica Section B* 58.3 Part 1 (2002), pp. 380–388. DOI: `10.1107/S0108768102003890`. (Cit. on p. 22).

[136] Springer Nature. *SpringerMaterials: The research solution for identifying material properties.* URL: `https://materials.springer.com` (visited on 05/24/2019) (cit. on p. 22).

[137] J.-L. Reymond and et al. *GDB Databases.* URL: `http://www.gdb.unibe.ch/downloads/` (visited on 05/24/2019) (cit. on p. 22).

[138] L. Ruddigkeit et al. “Enumeration of 166 Billion Organic Small Molecules in the Chemical Universe Database GDB-17”. In: *Journal of Chemical Information and Modeling* 52.11 (2012). PMID: 23088335, pp. 2864–2875. DOI: `10.1021/ci300415d`. (Cit. on p. 22).

[139] A. Merkys et al. “A posteriori metadata from automated provenance tracking: Integration of AiiDA and TCOD”. In: *Journal of Cheminformatics* 9.1 (11/15/2017), p. 56. DOI: `10.1186/s13321-017-0242-y`. arXiv: `1706.08704v3 [cond-mat.mtrl-sci]`. (Cit. on p. 22).

[140] K. Mathew et al. “High-throughput computational X-ray absorption spectroscopy”. In: *Scientific Data* 5 (2018), p. 180151. ISSN: 2052-4463. DOI: `10.1038/sdata.2018.151`. (Cit. on pp. 22, 27, 83).

[141] N. Mounet et al. “Two-dimensional materials from high-throughput computational exfoliation of experimentally known compounds”. In: *Nature Nanotechnology* 13.3 (2018), pp. 246–252. ISSN: 1748-3395. DOI: `10.1038/s41565-017-0035-5`. (Cit. on p. 23).

[142] L. M. Ghiringhelli et al. “Towards a Common Format for Computational Material Science Data”. In: July (2016). URL: `http://arxiv.org/abs/1607.04738` (cit. on p. 23).

[143] L. M. Ghiringhelli et al. “Big data of materials science: Critical role of the descriptor”. In: *Physical Review Letters* 114.10 (2015), pp. 1–5. ISSN: 10797114. DOI: `10.1103/PhysRevLett.114.105503`. arXiv: `arXiv:1411.7437v2` (cit. on p. 23).

[144] I. Takeuchi and X.-D. Xiang. *Combinatorial Materials Synthesis*. 2003. ISBN: 0824741196 (cit. on p. 24).

[145] M. L. Green, I. Takeuchi, and J. R. Hattrick-Simpers. “Applications of high throughput (combinatorial) methodologies to electronic, magnetic, optical, and energy-related materials”. In: *Journal of Applied Physics* 113.23 (2013), p. 231101. DOI: `10.1063/1.4803530`. (Cit. on p. 24).

[146] A. Belsky and V. Lynn. “research papers New developments in the Inorganic Crystal Structure Database (ICSD): accessibility in support of materials research and design research papers”. In: (2002), pp. 364–369 (cit. on p. 24).

[147] C. W. Glass, A. R. Oganov, and N. Hansen. “USPEX-Evolutionary crystal structure prediction”. In: *Computer Physics Communications* 175.11-12 (2006), pp. 713–720. ISSN: 00104655. DOI: `10.1016/j.cpc.2006.07.020` (cit. on p. 24).

[148] K. Ryan, J. Lengyel, and M. Shatruk. “Crystal Structure Prediction via Deep Learning”. In: *Journal of the American Chemical Society* 140.32 (2018). PMID: 29874459, pp. 10158–10168. DOI: `10.1021/jacs.8b03913`. (Cit. on pp. 24, 34).

[149] I.-h. Chu et al. “Predicting the volumes of crystals”. In: *Computational Materials Science* 146 (2018), pp. 184–192. ISSN: 09270256. DOI: `10.1016/j.commatsci.2018.01.040`. arXiv: `1712.01321`. (Cit. on pp. 24, 27, 34).

[150] *European Grid Infrastructure (EGI): Glossary V1*. URL: `https://wiki.egi.eu/wiki/Glossary_V1#High_Throughput_Computing` (visited on 05/24/2019) (cit. on p. 25).

[151] I. Raicu. *Many-Task Computing: Bridging the Gap between High Throughput Computing and High Performance Computing*. VDM Verlag, 05/2009, p. 180. ISBN: 978-3639156140 (cit. on p. 25).

[152] S. P. Ong et al. “Python Materials Genomics (pymatgen): A robust, open-source python library for materials analysis”. In: *Computational Materials Science* 68 (2013), pp. 314–319. ISSN: 09270256. DOI: `10.1016/j.commatsci.2012.10.028`. (Cit. on pp. 26, 33, 159).

[153] A. Jain et al. “A high-throughput infrastructure for density functional theory calculations”. In: *Computational Materials Science* 50.8 (2011), pp. 2295–2310. ISSN: 09270256. DOI: `10.1016/j.commatsci.2011.02.023`. (Cit. on p. 27).

[154] M. T. Dunstan et al. “Large scale computational screening and experimental discovery of novel materials for high temperature CO2 capture”. In: *Energy Environ. Sci.* 9.4 (2016), pp. 1346–1360. ISSN: 1754-5692. DOI: `10.1039/C5EE03253A`. (Cit. on p. 27).

[155] C. Zheng et al. “Automated generation and ensemble-learned matching of X-ray absorption spectra”. In: *npj Computational Materials* 4.1 (2018), p. 12. ISSN: 2057-3960. DOI: `10.1038/s41524-018-0067-x`. arXiv: `1711.02227`. (Cit. on p. 27).

[156] AiiDAteam. *AiiDA website.* URL: `https://www.aiida.net` (visited on 05/24/2019) (cit. on pp. 27, 49).

[157] AiiDAteam. *AiiDAteam code repositories on github.* URL: `https://www.github.com/aiidateam` (visited on 05/24/2019) (cit. on p. 27).

[158] AiiDAteam. *AiiDA-core documentation on readthedocs.* URL: `https://www.aiida-core.readthedocs.io/en/stable/` (visited on 05/24/2019) (cit. on p. 27).

[159] L. Moreau et al. “The Open Provenance Model core specification (v1.1)”. In: *Future Generation Computer Systems* 27.6 (2011), pp. 743 –756. ISSN: 0167-739X. DOI: `10.1016/j.future.2010.07.005`. (Cit. on pp. 27, 28).

[160] M. D. Wilkinson. “Comment : The FAIR Guiding Principles for scientific data management and stewardship”. In: *Scientific Data* 3 (2016), pp. 1–9. DOI: `10.1038/sdata.2016.18` (cit. on p. 27).

[161] GO FAIR Initiative. *GO FAIR.* URL: `https://www.go-fair.org` (visited on 05/24/2019) (cit. on p. 27).

[162] Pivotal Software. Inc. *RabbitMQ is the most widely deployed open source message broker.* URL: `https://www.rabbitmq.com` (visited on 05/24/2019) (cit. on p. 28).

[163] RabbitMQ. *RabbitMQ Github account.* URL: `https://github.com/rabbitmq?q=rabbitmq` (visited on 05/24/2019) (cit. on p. 28).

[164] The PostgreSQL Global Development Group. *PostgreSQL: The World’s Most Advanced Open Source Relational Database.* URL: `www.postgresql.org` (visited on 05/24/2019) (cit. on p. 28).

[165] Python Software Foundation. *The Python Package Index (PyPI) is a repository of software for the Python programming language.* URL: `https://www.pypi.org` (visited on 05/24/2019) (cit. on pp. 30, 33).

[166] GitHub, Inc. *GitHub: Build for developers.* URL: `https://www.github.com` (visited on 05/24/2019) (cit. on p. 30).

[167] GitLab Inc. *GitLab: A full DevOps tool.* URL: `https://www.gitlab.com` (visited on 05/24/2019) (cit. on p. 30).

[168] Atlassian. *Bitbucket: Built for professional teams.* URL: `https://www.bitbucket.org` (visited on 05/24/2019) (cit. on p. 30).

[169] S. R. Hall, F. H. Allen, and I. D. Brown. "The crystallographic information file (CIF): a new standard archive file for crystallography". In: *Acta Crystallographica Section A* 47.6 (1991), pp. 655–685. DOI: `10.1107/S010876739101067X`. (Cit. on p. 31).

[170] K. Momma and F. Izumi. "*VESTA3* for three-dimensional visualization of crystal, volumetric and morphology data". In: *Journal of Applied Crystallography* 44.6 (2011), pp. 1272–1276. DOI: `10.1107/S0021889811038970`. (Cit. on p. 31).

[171] A. Kokalj. "XCrySDen—a new program for displaying crystalline structures and electron densities". In: *Journal of Molecular Graphics and Modelling* 17.3 (1999), pp. 176 –179. ISSN: 1093-3263. DOI: `10.1016/S1093-3263(99)00028-5`. (Cit. on p. 31).

[172] AiiDAteam. *AiiDA plug-in registry.* URL: `https://aiidateam.github.io/aiida-registry/` (visited on 05/24/2019) (cit. on p. 31).

[173] Python Packaging Authority (PyPA). *pip - The Python Package Installer.* URL: `https://pip.pypa.io/en/stable/` (visited on 05/24/2019) (cit. on p. 33).

[174] G. Brandl and the Sphinx team. *SPHINX: Python Documentation Generator.* URL: `http://www.sphinx-doc.org/en/master/` (visited on 05/24/2019) (cit. on pp. 33, 160).

[175] Read the Docs Inc. and contributors. *Read the Docs: Technical documentation lives here.* URL: `https://readthedocs.org` (visited on 05/24/2019) (cit. on pp. 33, 160).

[176] Python Code Quality Authority. *Pylint: It's not just a linter that annoys you!* URL: `https://www.pylint.org` (visited on 05/24/2019) (cit. on p. 33).

[177] H. Krekel and et. al. *pytest: helps you write better programs.* URL: `https://docs.pytest.org/en/latest/index.html` (visited on 05/24/2019) (cit. on p. 33).

[178] A. Togo and I. Tanaka. "Spglib : a software library for crystal symmetry search". In: (05/2018). arXiv: `1808.01590`. URL: `https://arxiv.org/abs/1808.01590` (cit. on pp. 33, 81, 159).

[179] L. Ward et al. "Matminer: An open source toolkit for materials data mining". In: *Computational Materials Science* 152.May (2018), pp. 60–69. ISSN: 09270256. DOI: `10.1016/j.commatsci.2018.05.018` (cit. on pp. 33, 34).

[180] Y. Hinuma et al. "Band structure diagram paths based on crystallography". In: *Computational Materials Science* 128 (2017), pp. 140–184. ISSN: 09270256. DOI: `10.1016/j.commatsci.2016.10.015`. (Cit. on p. 33).

[181] Jupyter.org. “Jupyter documentation”. In: (2016) (cit. on pp. 33, 159).

[182] Two Sigma. *BeakerX.* URL: `http://beakerx.com` (visited on 05/24/2019) (cit. on p. 33).

[183] Apache Software foundation. *Apache Zeppelin.* URL: `https://zeppelin.apache.org` (visited on 05/24/2019) (cit. on p. 33).

[184] D. W. Erwin and D. F. Snelling. “UNICORE: A Grid Computing Environment”. In: *Euro-Par 2001 Parallel Processing.* Ed. by R. Sakellariou et al. Berlin, Heidelberg: Springer Berlin Heidelberg, 2001, pp. 825–834. ISBN: 978-3-540-44681-1 (cit. on p. 34).

[185] B. Demuth et al. “The UNICORE Rich Client: Facilitating the Automated Execution of Scientific Workflows”. In: *2010 IEEE Sixth International Conference on e-Science.* 2010, pp. 238–245. DOI: `10.1109/eScience.2010.42` (cit. on p. 34).

[186] A. Streit et al. “UNICORE 6 — Recent and Future Advancements”. In: *annals of telecommunications - annales des télécommunications* 65.11 (2010), pp. 757–762. ISSN: 1958-9395. DOI: `10.1007/s12243-010-0195-x`. (Cit. on p. 34).

[187] S. Lührs et al. “Flexible and Generic Workflow Management”. In: *Parallel Computing: On the Road to Exascale.* Vol. 27. Advances in parallel computing. International Conference on Parallel Computing 2015, Edinburgh (United Kingdom), 1 Sep 2015 - 4 Sep 2015. Amsterdam: IOS Press, 09/01/2015, pp. 431 –438. ISBN: 978-1-61499-620-0. DOI: `10.3233/978-1-61499-621-7-431`. (Cit. on p. 34).

[188] A. Galonska et al. “JuBE-based Automatic Testing and Performance Measurement System for Fusion Codes”. In: *Applications, Tools and Techniques on the Road to Exascale Computing / ed.: K. De Bosschere, E.H. D’Hollander, G.R. Joubert, David Padua, Frans Peters, Mark Sawyer, IOS Press, 2012, Advances in Parallel Computing, Vol. 22. - 978-1-61499-040-6. - S. 465 - 472.* Record converted from VDB: 12.11.2012. 2012. DOI: `10.3233/978-1-61499-041-3-465`. (Cit. on p. 34).

[189] N. Podhorszki et al. “Plasma fusion code coupling using scalable I/O services and scientific workflows”. In: *Proceedings of the 4th Workshop on Workflows in Support of Large-Scale Science - WORKS ’09* August 2016 (2009), pp. 1–9. DOI: `10.1145/1645164.1645172`. (Cit. on p. 34).

[190] J. Janssen et al. “pyiron: An integrated development environment for computational materials science”. In: *Computational Materials Science* 163 (2019), pp. 24 –36. ISSN: 0927-0256. DOI: `10.1016/j.commatsci.2018.07.043`. (Cit. on p. 34).

[191] S. Marsland. *Machine learning: an algorithmic perspective.* Chapman and Hall/CRC, 2014 (cit. on p. 34).

[192] S. Raschka. *Python machine learning.* Packt Publishing Ltd, 2015 (cit. on p. 34).

[193] M. Kirk. *Thoughtful Machine Learning with Python.* 2017, p. 217. ISBN: 9781449374068 (cit. on p. 34).

[194] F. Pedregosa et al. "Scikit-learn: Machine learning in Python". In: *Journal of machine learning research* 12.Oct (2011), pp. 2825–2830 (cit. on p. 34).

[195] M. Abadi et al. "Tensorflow: A system for large-scale machine learning". In: *12th {USENIX} Symposium on Operating Systems Design and Implementation ({OSDI} 16).* 2016, pp. 265–283 (cit. on p. 34).

[196] W. Lu et al. "Data mining-aided materials discovery and optimization". In: *Journal of Materiomics* 3.3 (2017), pp. 191–201. ISSN: 23528486. DOI: `10.1016/j.jmat.2017.08.003`. (Cit. on p. 34).

[197] R. Ramprasad et al. "Machine learning in materials informatics: Recent applications and prospects". In: *npj Computational Materials* 3.1 (2017). ISSN: 20573960. DOI: `10.1038/s41524-017-0056-5`. arXiv: `1707.07294`. (Cit. on p. 34).

[198] E. Gossett et al. "AFLOW-ML: A RESTful API for machine-learning predictions of materials properties". In: (2017), pp. 1–10. DOI: `arXiv : 1711 . 10744v1`. arXiv: `1711.10744`. (Cit. on p. 34).

[199] O. Isayev et al. "Universal fragment descriptors for predicting properties of inorganic crystals". In: *Nature Communications* 8 (2017), pp. 1–12. ISSN: 20411723. DOI: `10.1038/ncomms15679`. arXiv: `1608.04782`. (Cit. on p. 34).

[200] T. Xie and J. C. Grossman. "Crystal Graph Convolutional Neural Networks for an Accurate and Interpretable Prediction of Material Properties". In: *Phys. Rev. Lett.* 120 (14 2018), p. 145301. DOI: `10.1103/PhysRevLett.120.145301`. (Cit. on p. 34).

[201] E. Perim et al. "Spectral descriptors for bulk metallic glasses based on the thermodynamics of competing crystalline phases". In: *Nature Communications* 7 (2016), pp. 1–9. ISSN: 20411723. DOI: `10.1038/ncomms12315`. arXiv: `1606.01162`. (Cit. on p. 34).

[202] S. Curtarolo et al. "Predicting crystal structures with data mining of quantum calculations". In: *Physical Review Letters* 91.13 (2003), pp. 1–4. ISSN: 10797114. DOI: `10.1103/PhysRevLett.91.135503`. arXiv: `0307262 [cond-mat]` (cit. on p. 34).

[203] K. Takahashi and Y. Tanaka. "Material synthesis and design from first principle calculations and machine learning". In: *Computational Materials Science* 112 (02/2016), pp. 364–367. ISSN: 09270256. DOI: `10.1016/j.commatsci.2015.11.013`. (Cit. on p. 34).

[204] W. Ye et al. “Deep neural networks for accurate predictions of crystal stability”. In: *Nature Communications* 9.1 (2018), p. 3800. ISSN: 2041-1723. DOI: `10.1038/s41467-018-06322-x`. (Cit. on p. 34).

[205] F. M. Paruzzo et al. “Chemical shifts in molecular solids by machine learning”. In: *Nature Communications* 9.1 (2018), p. 4501. ISSN: 2041-1723. DOI: `10.1038/s41467-018-06972-x`. (Cit. on p. 34).

[206] F. M. Paruzzo et al. *ShiftML: chemical shifts in molecular solids by machine learning*. URL: `https://www.materialscloud.org/work/tools/shiftml` (visited on 05/24/2019) (cit. on p. 34).

[207] C. Sutton et al. “NOMAD 2018 Kaggle Competition: Solving Materials Science Challenges Through Crowd Sourcing”. In: (2018). URL: `http://arxiv.org/abs/1812.00085` (cit. on p. 34).

[208] H. Hertz. “Ueber einen Einfluss des ultravioletten Lichtes auf die electrische Entladung”. In: *Annalen der Physik* 267.8 (1887), pp. 983–1000. DOI: `10.1002/andp.18872670827`. (Cit. on p. 35).

[209] A. Einstein. “Über einen die Erzeugung und Verwandlung des Lichtes betreffenden heuristischen Gesichtspunkt”. In: *Annalen der Physik* 322.6 (1905), pp. 132–148. DOI: `10.1002/andp.19053220607`. (Cit. on p. 35).

[210] W. F. Egelhoff. “Core-level binding-energy shifts at surfaces and in solids”. In: *Surface Science Reports* 6.6-8 (1987), pp. 253–415. ISSN: 01675729. DOI: `10.1016/0167-5729(87)90007-0` (cit. on pp. 35, 36, 38, 45, 46).

[211] C. S. Fadley. “Angle-resolved x-ray photoelectron spectroscopy”. In: *Progress in Surface Science* 16.3 (1984), pp. 275–388 (cit. on p. 36).

[212] N. Mårtensson and R. Nyholm. “Electron spectroscopic determinations of M and N core-hole lifetimes for the elements Nb—Te (Z= 41- 52)”. In: *Physical Review B* 24.12 (1981), p. 7121 (cit. on p. 36).

[213] R Nyholm et al. “Auger and Coster-Kronig broadening effects in the 2p and 3p photoelectron spectra from the metals 22Ti-30Zn”. In: *Journal of Physics F: Metal Physics* 11.8 (1981), p. 1727 (cit. on p. 36).

[214] R. Manne and T. Åberg. “Koopmans’ theorem for inner-shell ionization”. In: *Chemical Physics Letters* 7.2 (1970), pp. 282 –284. ISSN: 0009-2614. DOI: `10.1016/0009-2614(70)80309-8`. (Cit. on p. 36).

[215] C. Fadley. “Photoelectric cross sections and multi-electron transitions in the sudden approximation”. In: *Chemical Physics Letters* 25.2 (1974), pp. 225 –230. ISSN: 0009-2614. DOI: `10.1016/0009-2614(74)89123-2`. (Cit. on p. 36).

[216] J Braun. “The theory of angle-resolved ultraviolet photoemission and its applications to ordered materials”. In: *Reports on Progress in Physics* 59.10 (1996), p. 1267 (cit. on p. 36).

[217] C. N. Berglund and W. E. Spicer. “Photoemission Studies of Copper and Silver: Theory”. In: *Phys. Rev.* 136 (4A 1964), A1030–A1044. DOI: `10.1103/PhysRev.136.A1030`. (Cit. on p. 36).

[218] S. Hüffner. *Photoelectron Spectroscopy: Principles and Applications*. 3. Auflage. Berlin: Springer, 2003 (cit. on pp. 36, 41, 83).

[219] F. D. Groot and a Kotani. *Core level spectroscopy of solids*. 2008, xx, 490 p. ISBN: 9780849390715 (alk. paper)\r0849390710 (alk. paper). DOI: `10.1201/9781420008425` (cit. on p. 36).

[220] S Doniach and M Sunjic. “Many-electron singularity in X-ray photoemission and X-ray line spectra from metals”. In: *Journal of Physics C: Solid State Physics* 3.2 (1970), pp. 285–291. DOI: `10.1088/0022-3719/3/2/010`. (Cit. on pp. 36, 42).

[221] S. Hofmann. *Auger-and X-ray photoelectron spectroscopy in materials science: a user-oriented guide*. Vol. 49. Springer Science & Business Media, 2012 (cit. on p. 37).

[222] M. P. Seah and W. Dench. “Quantitative electron spectroscopy of surfaces: A standard data base for electron inelastic mean free paths in solids”. In: *Surface and interface analysis* 1.1 (1979), pp. 2–11 (cit. on p. 38).

[223] S Tanuma, C. Powell, and D. Penn. “Calculations of electron inelastic mean free paths. IX. Data for 41 elemental solids over the 50 eV to 30 keV range”. In: *Surface and Interface Analysis* 43.3 (2011), pp. 689–713 (cit. on p. 38).

[224] S. Tanuma, C. J. Powell, and D. R. Penn. “Calculations of electron inelastic mean free paths for 31 materials”. In: *Surface and Interface Analysis* 11.11 (1988), pp. 577–589 (cit. on p. 38).

[225] H. Kanter. “Slow-electron mean free paths in aluminum, silver, and gold”. In: *Physical Review B* 1.2 (1970), p. 522 (cit. on p. 38).

[226] J. F. Moulder. *Handbook of X-Ray Photoelectron Spectroscopy*. Eden Prairie, 1995, pp. 230–232. URL: `https://ci.nii.ac.jp/naid/10025039885/en/` (cit. on pp. 38, 44).

[227] M. Salmeron and R. Schlögl. “Ambient pressure photoelectron spectroscopy: A new tool for surface science and nanotechnology”. In: *Surface Science Reports* 63.4 (2008), pp. 169 –199. ISSN: 0167-5729. DOI: `10.1016/j.surfrep.2008.01.001`. (Cit. on p. 38).

[228] A. Jürgensen, N. Esser, and R. Hergenröder. “Near ambient pressure XPS with a conventional X-ray source”. In: *Surface and Interface Analysis* 44.8 (2012), pp. 1100–1103. DOI: `10.1002/sia.4826`. (Cit. on p. 38).

[229] N. Helfer. “Komparative Untersuchungen von Berylliden mit Photoelektronen-Spektroskopie”. MA thesis. 2017, 61 pp (cit. on pp. 40, 43, 127–129, 134, 142, 143).

[230] D. Briggs. “Practical surface analysis”. In: *Auger and X-Ray Photoelecton Spectroscory* 1 (1990), pp. 151–152 (cit. on p. 39).

[231] M. Cardona and L. Ley. “Photoemission in solids. Vol. 1: General principles; Vol. 2: Case studies”. In: *Topics in Applied Physics, Berlin: Springer, 1978, edited by Cardona, M.; Ley, L.* (1978) (cit. on pp. 39, 41).

[232] J. Conny, C. Powell, and L. Currie. “Standard test data for estimating peak–parameter errors in x ray photoelectron spectroscopy. I. Peak binding energies”. In: *Surface and interface…* 956.July (1998), pp. 939–956. URL: `http://onlinelibrary.wiley.com/doi/10.1002/(SICI)1096-9918(199811)26:12{\%}3C939::AID-SIA441{\%}3E3.0.CO;2-V/abstract` (cit. on p. 41).

[233] J. Conny and C. Powell. “Standard test data for estimating peak parameter errors in x-ray photoelectron spectroscopy: II. Peak intensities”. In: *Surface and interface analysis* 459.March (2000), pp. 444–459. URL: `http://onlinelibrary.wiley.com/doi/10.1002/1096-9918(200007)29:7{\%}3C444::AID-SIA888{\%}3E3.0.CO;2-M/abstract` (cit. on p. 41).

[234] R. Hesse, T. Chassé, and R. Szargan. “Peak shape analysis of core level photoelectron spectra using UNIFIT for WINDOWS”. In: *Fresenius’ Journal of Analytical Chemistry* 365.1 (1999), pp. 48–54. ISSN: 1432-1130. DOI: `10.1007/s002160051443`. (Cit. on p. 41).

[235] R. Hesse. *UNIFIT for Windows.* Version. 2016, p. 2016 (cit. on pp. 41, 127).

[236] Casa Software Ltd. *CasaXPS: Processing Software for XPS, AES, SIMS and More.* URL: `http://www.casaxps.com` (visited on 05/24/2019) (cit. on p. 41).

[237] XPS International Inc. *Spectral Data Processor.* URL: `https://www.xpsdata.com/` (visited on 05/24/2019) (cit. on pp. 41, 44).

[238] PHI, Multipak. *XPS Basic Data Analysis, Multipak Manual.* 6, pp. 1–16 (cit. on p. 41).

[239] P. A. M. Dirac and N. H. D. Bohr. “The quantum theory of the emission and absorption of radiation”. In: *Proceedings of the Royal Society of London. Series A, Containing Papers of a Mathematical and Physical Character* 114.767 (1927), pp. 243–265. DOI: `10.1098/rspa.1927.0039`. (Cit. on p. 41).

[240] E. Fermi. University Of Chicago Press, 1974, p. 264. ISBN: 9780226243658 (cit. on p. 41).

[241] Casa Software Ltd. *Lorentzian Asymmetric Lineshape.* URL: http://www.casaxps.com/help_manual/manual_updates/LA_Lineshape.pdf (visited on 05/24/2019) (cit. on p. 42).

[242] D. A. Shirley. "High-Resolution X-Ray Photoemission Spectrum of the Valence Bands of Gold". In: *Phys. Rev. B* 5 (12 1972), pp. 4709–4714. DOI: 10.1103/PhysRevB.5.4709. (Cit. on pp. 42, 120).

[243] J. Végh. "The Shirley background revised". In: *Journal of Electron Spectroscopy and Related Phenomena* 151.3 (2006), pp. 159–164. ISSN: 03682048. DOI: 10.1016/j.elspec.2005.12.002 (cit. on pp. 42, 43, 120).

[244] S. Tougaard. "Quantitative analysis of the inelastic background in surface electron spectroscopy". In: *Surface and Interface Analysis* 11.9 (1988), pp. 453–472. ISSN: 1096-9918. DOI: 10.1002/sia.740110902. (Cit. on p. 42).

[245] S. Tougaard. "Universality Classes of Inelastic Electron Scattering Cross-sections". In: *Surface and Interface Analysis* 25.3 (1997), pp. 137–154. ISSN: 1096-9918. DOI: 10.1002/(SICI)1096-9918(199703)25:3<137::AID-SIA230>3.0.CO;2-L. (Cit. on p. 42).

[246] M. Repoux. "Comparison of background removal methods for XPS". In: *Surface and Interface Analysis* 18.7 (1992), pp. 567–570. DOI: 10.1002/sia.740180719. (Cit. on p. 43).

[247] B. V. Crist. "A Review of XPS Data-banks". In: *XPS Reports* 1 (2007), pp. 1–52. URL: https://www.researchgate.net/profile/Amol{_}Singh/post/Is{_}there{_}any{_}database{_}where{_}natural{_}XPS{_}FWHM{_}of{_}all{_}the{_}elements{_}are{_}listed/attachment/59d62392c49f478072e9987a/AS:272128522293248@1441891903209
download/XPS+Review.pdf (cit. on pp. 44, 106).

[248] B. V. Crist. "Journal of Electron Spectroscopy and XPS in industry — Problems with binding energies in journals and binding energy databases". In: *Journal of Electron Spectroscopy and Related Phenomena* 231 (2019), pp. 75–87. ISSN: 0368-2048. DOI: 10.1016/j.elspec.2018.02.005 (cit. on pp. 44, 106).

[249] B. D. Silverman et al. "Molecular orbital analysis of the XPS spectra of PMDA-ODA polymide and its polyamic acid precursor". In: *Journal of Polymer Science Part A: Polymer Chemistry* 24.12 (1986), pp. 3325–3333. DOI: 10.1002/pola.1986.080241216. (Cit. on p. 45).

[250] J. Leiro et al. “Core-level XPS spectra of fullerene, highly oriented pyrolitic graphite, and glassy carbon”. In: *Journal of Electron Spectroscopy and Related Phenomena* 128.2 (2003), pp. 205 –213. ISSN: 0368-2048. DOI: `10.1016/S0368-2048(02)00284-0`. (Cit. on p. 45).

[251] T. Fujii et al. “In situ XPS analysis of various iron oxide films grown by NO_2-assisted molecular-beam epitaxy”. In: *Phys. Rev. B* 59 (4 1999), pp. 3195–3202. DOI: `10.1103/PhysRevB.59.3195`. (Cit. on p. 45).

[252] M. Guzzo et al. “Valence Electron Photoemission Spectrum of Semiconductors: Ab Initio Description of Multiple Satellites”. In: *Phys. Rev. Lett.* 107 (16 2011), p. 166401. DOI: `10.1103/PhysRevLett.107.166401`. (Cit. on p. 45).

[253] B. Johansson and N. Mårtensson. “Core-level binding-energy shifts for the metallic elements”. In: *Physical Review B* 21.10 (1980), pp. 4427–4457. ISSN: 01631829. DOI: `10.1103/PhysRevB.21.4427` (cit. on p. 45).

[254] V. I. Anisimov et al. “Density-functional theory and NiO photoemission spectra”. In: *Phys. Rev. B* 48 (23 1993), pp. 16929–16934. DOI: `10.1103/PhysRevB.48.16929`. (Cit. on pp. 46, 101).

[255] L. Triguero et al. “Separate state vs. transition state Kohn-Sham calculations of X-ray photoelectron binding energies and chemical shifts”. In: *Journal of Electron Spectroscopy and Related Phenomena* 104.1-3 (1999), pp. 195–207. ISSN: 03682048. DOI: `10.1016/S0368-2048(99)00008-0`. arXiv: `1512.00567`. (Cit. on p. 46).

[256] N. Pueyo Bellafont et al. “Predicting core level binding energies shifts: Suitability of the projector augmented wave approach as implemented in VASP”. In: *Journal of Computational Chemistry* 38.8 (2017), pp. 518–522. ISSN: 1096987X. DOI: `10.1002/jcc.24704` (cit. on p. 46).

[257] J. Broeder. “Density Functional Theory Simulations on Tungsten and Beryllium Alloys for ITER”. MA thesis. 2015, 58 pp (cit. on pp. 46, 95, 114).

[258] G. Michalicek. “{E}xtending the precision and efficiency of the all-electron full-potential linearized augmented plane-wave density-functional theory method.” Dr. Jülich: Aachen, Techn. Hochsch., 2015, 195 S. : Ill., graph. Darst. ISBN: 978-3-95806-031-9. URL: `http://publications.rwth-aachen.de/record/464499` (cit. on p. 47).

[259] F Aryasetiawan and O Gunnarsson. “The GW method”. In: *Reports on Progress in Physics* 61.3 (1998), pp. 237–312. DOI: `10.1088/0034-4885/61/3/002`. (Cit. on p. 48).

[260] M. J. Van Setten et al. “Assessing GW Approaches for Predicting Core Level Binding Energies”. In: *Journal of Chemical Theory and Computation* 14.2 (2018), pp. 877–883. ISSN: 15499626. DOI: `10.1021/acs.jctc.7b01192` (cit. on pp. 48, 65).

[261] E. Runge and E. K. U. Gross. “Density-Functional Theory for Time-Dependent Systems”. In: *Phys. Rev. Lett.* 52 (12 1984), pp. 997–1000. DOI: `10.1103/PhysRevLett.52.997`. (Cit. on p. 48).

[262] N. Nakanishi. “A General Survey of the Theory of the Bethe-Salpeter Equation”. In: *Progress of Theoretical Physics Supplement* 43 (01/1969), pp. 1–81. ISSN: 0375-9687. DOI: `10.1143/PTPS.43.1`. (Cit. on p. 48).

[263] W. Olovsson et al. “All-electron Bethe-Salpeter calculations for shallow-core x-ray absorption near-edge structures”. In: *Physical Review B - Condensed Matter and Materials Physics* 79.4 (2009), pp. 2–5. ISSN: 10980121. DOI: `10.1103/PhysRevB.79.041102` (cit. on p. 48).

[264] C. Vorwerk, C. Cocchi, and C. Draxl. “Addressing electron-hole correlation in core excitations of solids: An all-electron many-body approach from first principles”. In: *Physical Review B* 95.15 (2017). ISSN: 24699969. DOI: `10.1103/PhysRevB.95.155121`. arXiv: `1612.02597` (cit. on p. 48).

[265] MaX Centre of Excellence. *MaX - Materials design at the Exascale a European centre of excellence*. URL: `www.max-center.eu` (visited on 05/24/2019) (cit. on p. 49).

[266] Bokeh Development Team. *Bokeh: Python library for interactive visualization*. 2018. URL: `https://bokeh.pydata.org/en/latest/` (cit. on pp. 61, 159).

[267] F. D. Murnaghan. “The Compressibility of Media under Extreme Pressures”. In: *Proceedings of the National Academy of Sciences* 30.9 (1944), pp. 244–247. ISSN: 0027-8424. DOI: `10.1073/pnas.30.9.244`. (Cit. on p. 65).

[268] K. Lejaeghere et al. “Reproducibility in density functional theory calculations of solids”. In: *Science* 351.6280 (2016). ISSN: 0036-8075. DOI: `10.1126/science.aad3000`. (Cit. on pp. 65, 109).

[269] AiiDAteam. *AiiDAlab*. URL: `https://www.materialscloud.org/work/menu` (visited on 05/24/2019) (cit. on p. 77).

[270] I. Jolliffe. “Principal Component Analysis”. In: *International Encyclopedia of Statistical Science*. Ed. by M. Lovric. Berlin, Heidelberg: Springer Berlin Heidelberg, 2011, pp. 1094–1096. ISBN: 978-3-642-04898-2. DOI: `10.1007/978-3-642-04898-2_455`. (Cit. on p. 83).

[271] J. P. Holgado, R. Alvarez, and G. Munuera. “Study of CeO2 XPS spectra by factor analysis: reduction of CeO2”. In: *Applied Surface Science* 161.3 (2000), pp. 301 –315. ISSN: 0169-4332. DOI: `10.1016/S0169-4332(99)00577-2`. (Cit. on p. 83).

[272] M. Ni and B. D. Ratner. “Differentiating calcium carbonate polymorphs by surface analysis techniques—an XPS and TOF-SIMS study”. In: *Surface and Interface Analysis* 40.10 (2008), pp. 1356–1361. DOI: `10.1002/sia.2904`. (Cit. on p. 83).

[273] S. Oswald and W. Brückner. “XPS depth profile analysis of non-stoichiometric NiO films”. In: *Surface and Interface Analysis* 36.1 (2004), pp. 17–22. DOI: `10.1002/sia.1640`. (Cit. on p. 83).

[274] S. Curtarolo et al. “The high-throughput highway to computational materials design”. In: *Nature Materials* 12.3 (2013), pp. 191–201. ISSN: 14761122. DOI: `10.1038/nmat3568`. (Cit. on p. 93).

[275] H. J. Monkhorst and J. D. Pack. “Special points for Brillouin-zone integrations”. In: *Phys. Rev. B* 13 (12 1976), pp. 5188–5192. DOI: `10.1103/PhysRevB.13.5188`. (Cit. on p. 97).

[276] J. S. Centre. “JURECA: Modular supercomputer at Jülich Supercomputing Centre”. In: *Journal of large-scale research facilities* 4 (2018), A132. DOI: `10.17815/jlsrf-4-121-1` (cit. on p. 98).

[277] P. Kurz, G. Bihlmayer, and S. Blügel. “Magnetism and electronic structure of hcp Gd and the Gd (0001) surface”. In: *Journal of Physics: Condensed Matter* 14.25 (2002), p. 6353 (cit. on p. 101).

[278] V. I. Anisimov, J. Zaanen, and O. K. Andersen. “Band theory and Mott insulators: Hubbard U instead of Stoner I”. In: *Physical Review B* 44.3 (1991), p. 943 (cit. on p. 101).

[279] A. B. Shick, A. I. Liechtenstein, and W. E. Pickett. “Implementation of the LDA+U method using the full-potential linearized augmented plane-wave basis”. In: *Physical Review B* 60.15 (1999), pp. 10763–10769. ISSN: 0163-1829. DOI: `\url{10.1103/PhysRevB.60.10763}` (cit. on p. 101).

[280] A. B. Shick et al. “Electronic structure and spectral properties of Am, Cm, and Bk: Charge-density self-consistent LDA+ HIA calculations in the FP-LAPW basis”. In: *Physical Review B* 80.8 (2009), p. 085106 (cit. on p. 101).

[281] ITER organisation. *Website of the fusion experiment ITER*. URL: `http:www.iter.org` (visited on 05/24/2019) (cit. on pp. 110–112).

[282] K. H. Nordlund et al. “European research roadmap to the realisation of fusion energy”. In: (2018) (cit. on p. 110).

[283] G Federici et al. “Plasma-material interactions in current tokamaks and their implications for next step fusion reactors”. In: *Nuclear Fusion* 41.12 (2001), pp. 1967–2137. DOI: `10.1088/0029-5515/41/12/218`. (Cit. on p. 110).

[284] R. V. Jensen, D. E. Post, and D. L. Jassby. “Critical Impurity Concentrations for Power Multiplication in Beam-Heated Toroidal Fusion Reactors”. In: *Nuclear Science and Engineering* 65.2 (1978), pp. 282–289. DOI: `10.13182/NSE78-A27157`. (Cit. on p. 111).

[285] L. Pranevičius, L. Pranevičius, and D. Milčius. *Tungsten Coatings for Fusion Applications.* VMU Press, 2009 (cit. on p. 111).

[286] Y. Zhang, J. R. G. Evans, and S. Yang. “Corrected Values for Boiling Points and Enthalpies of Vaporization of Elements in Handbooks”. In: *Journal of Chemical & Engineering Data* 56.2 (2011), pp. 328–337. DOI: `10.1021/je1011086`. (Cit. on p. 111).

[287] H. Okamoto and L. E. Tanner. *The Be-W (Beryllium-Tungsten) system.* 1986. DOI: `10.1007/BF02873019` (cit. on p. 113).

[288] A. Allouche and Ch. Linsmeier. “Quantum study of tungsten interaction with beryllium (0001)”. In: *Journal of Physics: Conference Series* 117.1 (2008). ISSN: 17426596. DOI: `10.1088/1742-6596/117/1/012002` (cit. on p. 113).

[289] A. Allouche, A. Wiltner, and Ch. Linsmeier. “Quantum modeling (DFT) and experimental investigation of beryllium-tungsten alloy formation”. In: *Journal of Physics Condensed Matter* 21.35 (2009). ISSN: 09538984. DOI: `10.1088/0953-8984/21/35/355011` (cit. on p. 113).

[290] C. Björkas et al. “A Be-W interatomic potential”. In: *Journal of Physics Condensed Matter* 22.35 (2010). ISSN: 09538984. DOI: `10.1088/0953-8984/22/35/352206` (cit. on p. 113).

[291] M. Gyoeroek et al. “Surface binding energies of beryllium/tungsten alloys”. In: *Journal of Nuclear Materials* 472 (2016), pp. 76–81. ISSN: 00223115. DOI: `10.1016/j.jnucmat.2016.02.002`. (Cit. on p. 113).

[292] Ch. Linsmeier et al. “Binary beryllium-tungsten mixed materials”. In: *Journal of Nuclear Materials* 363-365.1-3 (2007), pp. 1129–1137. ISSN: 00223115. DOI: `10.1016/j.jnucmat.2007.01.224` (cit. on pp. 113, 115, 118, 119).

[293] A. Wiltner et al. “Structural investigation of the Be-W intermetallic system”. In: *Physica Scripta T* T128 (2007), pp. 133–136. ISSN: 02811847. DOI: `10.1088/0031-8949/2007/T128/026` (cit. on pp. 113, 115, 118).

[294] J. F. Ziegler, M. Ziegler, and J. Biersack. “SRIM – The stopping and range of ions in matter (2010)”. In: *Nuclear Instruments and Methods in Physics Research Section B: Beam Interactions with Materials and Atoms* 268.11 (2010). 19th International Conference on Ion Beam Analysis, pp. 1818 –1823. ISSN: 0168-583X. DOI: `10.1016/j.nimb.2010.02.091`. (Cit. on p. 118).

[295] C. F. Mallinson, J. E. Castle, and J. F. Watts. “The chemical state plot for beryllium compounds”. In: *Surface and Interface Analysis* 47.10 (2015), pp. 994–995 (cit. on p. 120).

[296] C. K. Dorn, W. J. Haws, and E. E. Vidal. “A review of physical and mechanical properties of titanium beryllides with specific modern application of TiBe12”. In: *Fusion Engineering and Design* 84.2-6 (2009), pp. 319–322. ISSN: 09203796. DOI: `10.1016/j.fusengdes.2008.11.009` (cit. on p. 121).

[297] P. Kurinskiy et al. “Production of Be-Ti and Be-Zr rods by extrusion and their characterization”. In: *Fusion Engineering and Design* August (2018), pp. 1–4. ISSN: 09203796. DOI: `10.1016/j.fusengdes.2017.12.022`. (Cit. on p. 121).

[298] Y. Mishima et al. “Recent results on beryllium and beryllides in Japan”. In: *Journal of Nuclear Materials* 367-370 B.SPEC. ISS. (2007), pp. 1382–1386. ISSN: 00223115. DOI: `10.1016/j.jnucmat.2007.04.001` (cit. on p. 121).

[299] P. Vladimirov et al. “Current status of beryllium materials for fusion blanket applications”. In: *Fusion Science and Technology* 66.1 (2014), pp. 28–37. ISSN: 15361055. DOI: `10.13182/FST13-776` (cit. on p. 121).

[300] E. Alves et al. “Characterization and stability studies of titanium beryllides”. In: *Fusion Engineering and Design* 75-79.SUPPL. (2005), pp. 759–763. ISSN: 09203796. DOI: `10.1016/j.fusengdes.2005.06.145` (cit. on p. 121).

[301] P. Kurinskiy et al. “X-ray study of surface layers of air-annealed Be12Ti and Be12V samples using synchrotron radiation”. In: *Fusion Engineering and Design* 87.5-6 (2012), pp. 872–875. ISSN: 09203796. DOI: `10.1016/j.fusengdes.2012.02.047`. (Cit. on p. 121).

[302] D. V. Bachurin and P. V. Vladimirov. “Ab initio study of Be and Be12Ti for fusion applications”. In: *Intermetallics* 100.February (2018), pp. 163–170. ISSN: 09669795. DOI: `10.1016/j.intermet.2018.06.009`. (Cit. on p. 121).

[303] H. Okamoto. “Be-Ti (Beryllium-Titanium)”. In: *Journal of Phase Equilibria and Diffusion* 29.2 (2008), pp. 202–202. ISSN: 1547-7037. DOI: `10.1007/s11669-008-9265-4`. (Cit. on p. 121).

[304] E. Gillam, H. P. Rooksby, and L. D. Brownlee. “Structural relationships in beryllium–titanium alloys”. In: *Acta Crystallographica* 17.6 (1964), pp. 762–763. DOI: `10.1107/S0365110X64001906`. (Cit. on p. 121).

[305] M. L. Jackson, P. A. Burr, and R. W. Grimes. “Resolving the structure of $TiBe_{12}$”. In: *Acta Crystallographica Section B* 72.2 (2016), pp. 277–280. DOI: `10.1107/S205252061600322X`. (Cit. on p. 121).

[306] A. Dewaele, P. Loubeyre, and M. Mezouar. “Equations of state of six metals above 94 GPa”. In: *Phys. Rev. B* 70 (9 2004), p. 094112. DOI: `10.1103/PhysRevB.70.094112`. (Cit. on p. 122).

[307] J. E. Jaffe et al. “LDA and GGA calculations for high-pressure phase transitions in ZnO and MgO”. In: *Phys. Rev. B* 62 (3 2000), pp. 1660–1665. DOI: `10.1103/PhysRevB.62.1660`. (Cit. on p. 122).

[308] M. C. Biesinger et al. “Resolving surface chemical states in XPS analysis of first row transition metals, oxides and hydroxides: Sc, Ti, V, Cu and Zn”. In: *Applied surface science* 257.3 (2010), pp. 887–898 (cit. on p. 124).

[309] *An Investigation of Tntermetallic Compounds for Very High Temperature Applications - Part I.* Tech. rep. (cit. on p. 127).

[310] P. Villars and H. Okamoto, eds. *Be-Ta Binary Phase Diagram 0-100 at.% Ta: Datasheet from “PAULING FILE Multinaries Edition – 2012” in SpringerMaterials).* Copyright 2016 Springer-Verlag Berlin Heidelberg & Material Phases Data System (MPDS), Switzerland & National Institute for Materials Science (NIMS), Japan. URL: `https://materials.springer.com/isp/phase-diagram/docs/c_0900414` (cit. on p. 132).

[311] R. W. Cahn. “Binary Alloy Phase Diagrams–Second edition. T. B. Massalski, Editor-in-Chief; H. Okamoto, P. R. Subramanian, L. Kacprzak, Editors. ASM International, Materials Park, Ohio, USA. December 1990. xxii, 3589 pp., 3 vol., hard- back. $995.00 the set”. In: *Advanced Materials* 3.12 (1991), pp. 628–629. DOI: `10.1002/adma.19910031215`. (Cit. on p. 132).

[312] M. Klintenberg. *The Electronic Structure Project - Identifying New/Novel Functional Materials.* URL: `http://gurka.fysik.uu.se/ESP/` (visited on 05/24/2019) (cit. on p. 150).

[313] A. Gulans et al. “exciting: a full-potential all-electron package implementing density-functional theory and many-body perturbation theory”. In: *Journal of Physics: Condensed Matter* 26.36 (2014), p. 363202. DOI: `10.1088/0953-8984/26/36/363202`. (Cit. on p. 150).

[314] *The exciting Code.* URL: `http://exciting-code.org` (visited on 05/24/2019) (cit. on p. 150).

[315] AQR Capital Management and LLC, Lambda Foundry Inc. and PyData Development Team. *pandas: Python Data Analysis Library.* URL: `https://pandas.pydata.org` (visited on 05/24/2019) (cit. on p. 159).

[316] NumPy developers. *NumPy is the fundamental package for scientific computing with Python.* URL: `https://www.numpy.org` (visited on 05/24/2019) (cit. on p. 159).

[317] J. D. Hunter. "Matplotlib: A 2D graphics environment". In: *Computing In Science & Engineering* 9.3 (2007), pp. 90–95. DOI: `10.1109/MCSE.2007.55` (cit. on p. 159).

[318] S. Behnel, M. Faassenet, and et. al. *lxml: the most feature-rich and easy-to-use library for processing XML and HTML in the Python language.* URL: `https://lxml.de` (visited on 05/24/2019) (cit. on p. 159).

[319] J. Ellson et al. "Graphviz and dynagraph – static and dynamic graph drawing tools". In: *GRAPH DRAWING SOFTWARE.* Springer-Verlag, 2003, pp. 127–148 (cit. on p. 160).

[320] E. R. Gansner and S. C. North. "An open graph visualization system and its applications to software engineering". In: *SOFTWARE - PRACTICE AND EXPERIENCE* 30.11 (2000), pp. 1203–1233 (cit. on p. 160).

[321] AT&T labs. *Graphviz - Graph Visualization Software.* URL: `https://graphviz.gitlab.io` (visited on 05/24/2019) (cit. on p. 160).

[322] M. Bastian, S. Heymann, and M. Jacomy. "Gephi: An Open Source Software for Exploring and Manipulating Networks". In: *Third International AAAI Conference on Weblogs and Social Media* (2009), pp. 361–362. ISSN: 14753898. DOI: `10.1136/qshc.2004.010033`. (Cit. on pp. 160–162).

[323] Docker Inc. *Enterprise Container Platform for High-Velocity Innovation.* URL: `https://www.docker.com` (visited on 05/24/2019) (cit. on p. 160).

[324] DBeaver community. *DBeaver: Universal Database Tool.* URL: `https://dbeaver.io/` (visited on 05/24/2019) (cit. on p. 160).

[325] J. Egger, C. Pastl, and M. Thompson. *Postgres.app: The easiest way to get started with PostgreSQL on the Mac.* URL: `https://postgresapp.com` (visited on 05/24/2019) (cit. on p. 160).

[326] J. Egger. *Postico: A Modern PostgreSQL Client for the Mac.* URL: `https://eggerapps.at/postico/` (visited on 05/24/2019) (cit. on p. 160).

[327] The pgAdmin Development Team. *pgAdmin: the most popular and feature rich Open Source administration and development platform for PostgreSQL.* URL: `https://www.pgadmin.org` (visited on 05/24/2019) (cit. on p. 160).

[328] A. Caudwell. *Gource: software version control visualization.* URL: `https://gource.io/` (visited on 05/24/2019) (cit. on p. 160).

[329] E. Bonsma. *GrandPerspective.* URL: `http://grandperspectiv.sourceforge.net` (visited on 05/24/2019) (cit. on p. 163).

Publications

Parts of this thesis and results from this work have already been published, or a manuscript for publication is currently in preparation:

- The contents of chapter 3, The from ab initio data chemical interpreation process for spectra with sub phase spectra. are published in
  International Patent application (05.2018): J. Broeder, Daniel Wortmann, *Verfahren zur Auswertung von Rumpfelektronenspektren*
- Parts of chapter 3, The AiiDA-FLEUR package has been published: J. Bröder, D. Wortmann, and S. Blügel *Using the AiiDA-FLEUR package for all-electron ab initio electronic structure data generation and processing in materials science*, In Extreme Data Workshop 2018 Proceedings, 2019, vol 40, p 43-48
- Source code of the AiiDA-FLEUR package has been released under MIT license on github and pypi: https://github.com/JuDFTteam/aiida-fleur ; https://pypi.org/project/aiida-fleur/
- Data of the high-throughput screening of the binary metals (chapter 4) including the provenance and meta data has been published: J. Bröder, D. Wortmann, and S. Blügel, *JuCLS database of core-level shifts from all-electron density functional theory simulations for chemical analysis of X-ray photoelectron spectra.*, Materials CLoud Archive, 2020, doi: 10.24435/materialscloud:3j-p3
- Parts of the results from chapter 3 and 4 are in preparation for publication. Journal article: manuscript in preparation

Acknowledgements

Arriving here at this state and point in time was a long journey, which was influenced directly or indirectly by many wonderful and incredible people, to whom I am grateful for being part of this journey.

First my gratitude goes to Prof. Dr. Stefan Blügel for enabling me to go on this journey at the outstanding PGI-1/IAS-1. I am thankful for his supervision of my PhD, guidance and support. Through the participation in the European center of excellence, 'MaX-Materials design at the Exascale' together with the various conferences and workshops I was allowed to attend, I was provided with many chances to broaden my horizon and engaging in scientific collaborations across borders.

I want to thank Prof. Dr. Christian Linsmeier for his guidance at the outstanding IEK-4, reviewing and always supporting my work. Without him the cooperation with the IEK-4 and this work would be totally different.

Furthermore, I thank Prof. Dr. Riccardo Mazzarello for reviewing my work.

Then I thank Dr. Daniel Wortmann for his supervision and guidance throughout my work at the IAS/PGI and for his efforts on the `FLEUR` code. I have always enjoyed our discussions, providing me valuable feedback and further insights.

I also want to thank Dr. H. Rudolf Koslowski, Dr. Nabi Aghdassi, Dr. Timo Dittmar, Nicola Helfer and Petra Hansen from the IEK-4 for their nice cooperation on the chemical interpretation of XPS spectra, which motivated me a lot. Through them I received useful insights from the experimental perspective in our weekly 'friends of surface science' meetings and their feedback helped to improve this work. I also thank Dr. Martin Köppen for his discussions on XPS related to his work.

I thank the `FLEUR` developer team, for spendings months after months fixing issues related to my work, Dr. Uliana Alekseeva, Matthias Redis, and especially Dr. Gregor Michalicek, who I thank also for his friendship, many wonderful discussion and proofreading.

Further I thank Dr. Gustav Bihlmayer for his helpful discussions and for the sharing of his wisdom and computational resources.

I also want to thank all institute members, including our secretary Ute Winkler and members of the PGI IT, for the wonderful working atmosphere, many seminars with many fruitful discussions, out of work events, working with and aside you made this a great time.

Also I like to acknowledge the AiiDA developer team, especially Dr. Giovanni Pizzi, Dr. Martin Uhrin, Dr. Leopold Talirz and Dr. Sebastiaan Huber but also the plugin developers of other DFT codes for their professional hard work. It was a pleasure to see some of my ideas and suggestions advance and finding their way implemented in the AiiDA code base over the years. Thanks for all the wonderful coding weeks, workshops, brainstorming discussions.
I extend my thanks to other colleagues that I met at scientific events, or corresponded via email, for their interested, skeptical questions and fruitful discussions concerning this work. I am also thankful to all the programmer communities out there that write good software especially open source software from which we all profit a lot. Thanks for your daily work and efforts, without you my work could only be a shadow of itself. Hereby I thank the national and international funding agencies for providing us with the resources required to hold up the status of knowledge and technology and push out further.
In particular, I acknowledge support from European Union H2020-EINFRA-2015-1 programme under grant agreement No. 676598 project "MaX - materials at the exascale" and its successor a H2020-INFRAEDI-2018-1 funded project Grant Agreement n. 824143.
For computing resources I furthermore acknowledge JARA, project jara0172, for computing time on CLAIX 2016/2017/2018 and JURECA, besides computing time on in-house PGI clusters.

Finally, I am deeply grateful to my loving wife, to my parents, to my wonderful son, siblings and friends for their endless support with all their heart and understanding. Without you I would have never arrived at this point.

Eidesstattliche Erklärung

Ich, Jens Bröder erklärt hiermit, dass diese Dissertation und die darin dargelegten Inhalte die eigenen sind und selbstständig, als Ergebnis der eigenen originären Forschung, generiert wurden. Hiermit erkläre ich an Eides statt

1. Diese Arbeit wurde vollständig oder größtenteils in der Phase als Doktorand dieser Fakultät und Universität angefertigt;
2. Sofern irgendein Bestandteil dieser Dissertation zuvor für einen akademischen Abschluss oder eine andere Qualifikation an dieser oder einer anderen Institution verwendet wurde, wurde dies klar angezeigt;
3. Wenn immer andere eigene- oder Veröffentlichungen Dritter herangezogen wurden, wurden diese klar benannt;
4. Wenn aus anderen eigenen- oder Veröffentlichungen Dritter zitiert wurde, wurde stets die Quelle hierfür angegeben. Diese Dissertation ist vollständig meine eigene Arbeit, mit der Ausnahme solcher Zitate;
5. Alle wesentlichen Quellen von Unterstützung wurden benannt;
6. Wenn immer ein Teil dieser Dissertation auf der Zusammenarbeit mit anderen basiert, wurde von mir klar gekennzeichnet, was von anderen und was von mir selbst erarbeitet wurde;
7. Ein Teil oder Teile dieser Arbeit wurden zuvor veröffentlicht, siehe Publications Auflistung

Forschungszentrum Jülich, Sep 2019

Jens Bröder

Band / Volume 217
Detection and Statistical Evaluation of Spike Patterns in Parallel Electrophysiological Recordings
P. Quaglio (2020), 128 pp
ISBN: 978-3-95806-468-3

Band / Volume 218
Automatic Analysis of Cortical Areas in Whole Brain Histological Sections using Convolutional Neural Networks
H. Spitzer (2020), xii, 162 pp
ISBN: 978-3-95806-469-0

Band / Volume 219
Postnatale Ontogenesestudie (Altersstudie) hinsichtlich der Zyto- und Rezeptorarchitektonik im visuellen Kortex bei der grünen Meerkatze
D. Stibane (2020), 135 pp
ISBN: 978-3-95806-473-7

Band / Volume 220
Inspection Games over Time: Fundamental Models and Approaches
R. Avenhaus und T. Krieger (2020), VIII, 455 pp
ISBN: 978-3-95806-475-1

Band / Volume 221
High spatial resolution and three-dimensional measurement of charge density and electric field in nanoscale materials using off-axis electron holography
F. Zheng (2020), xix, 182 pp
ISBN: 978-3-95806-476-8

Band / Volume 222
Tools and Workflows for Data & Metadata Management of Complex Experiments
Building a Foundation for Reproducible & Collaborative Analysis in the Neurosciences
J. Sprenger (2020), X, 168 pp
ISBN: 978-3-95806-478-2

Band / Volume 223
Engineering of *Corynebacterium glutamicum* towards increased malonyl-CoA availability for polyketide synthesis
L. Milke (2020), IX, 117 pp
ISBN: 978-3-95806-480-5

Band / Volume 224
Morphology and electronic structure of graphene supported by metallic thin films
M. Jugovac (2020), xi, 151 pp
ISBN: 978-3-95806-498-0

Band / Volume 225
Single-Molecule Characterization of FRET-based Biosensors and Development of Two-Color Coincidence Detection
H. Höfig (2020), XVIII, 160 pp
ISBN: 978-3-95806-502-4

Band / Volume 226
Development of a transcriptional biosensor and reengineering of its ligand specificity using fluorescence-activated cell sorting
L. K. Flachbart (2020), VIII, 102 pp
ISBN: 978-3-95806-515-4

Band / Volume 227
Strain and Tool Development for the Production of Industrially Relevant Compounds with *Corynebacterium glutamicum*
M. Kortmann (2021), II, 138 pp
ISBN: 978-3-95806-522-2

Band / Volume 228
Complex magnetism of nanostructures on surfaces: from orbital magnetism to spin excitations
S. Brinker (2021), III, 208 pp
ISBN: 978-3-95806-525-3

Band / Volume 229
High-throughput All-Electron Density Functional Theory Simulations for a Data-driven Chemical Interpretation of X-ray Photoelectron Spectra
J. Bröder (2021), viii, 169, XL pp
ISBN: 978-3-95806-526-0

Weitere ***Schriften des Verlags im Forschungszentrum Jülich*** unter
http://wwwzb1.fz-juelich.de/verlagextern1/index.asp

Schlüsseltechnologien / Key Technologies
Band / Volume 229
ISBN 978-3-95806-526-0

Mitglied der Helmholtz-Gemeinschaft

JÜLICH
Forschungszentrum